



FLUIDS ENGINEERING DIVISION

Editor

J. KATZ (2009)

Assistant to the Editor

L. MURPHY (2009)

Associate Editors

M. J. ANDREWS (2009)

E. M. BENNETT (2012)

S. L. CECCIO (2009)

O. COUTIER-DELGOSHA (2012)

D. DRIKAKIS (2012)

P. DURBIN (2012)

I. EAMES (2010)

C. HAH (2010)

T. J. HEINDEL (2011)

J. KOMPENHANS (2009)

YU-TAI LEE (2009)

J. A. LIBURDY (2011)

R. MITTAL (2010)

T. J. O'HERN (2009)

N. A. PATANKAR (2011)

H. PEERHOSSAINI (2011)

U. PIOMELLI (2010)

Z. RUSAK (2010)

D. SIGINER (2009)

M. STREMLER (2012)

P. VLACHOS (2012)

M. WANG (2011)

St. T. WERELEY (2011)

Y. ZHOU (2009)

PUBLICATIONS COMMITTEE

Chair, B. RAVANI

OFFICERS OF THE ASME

President, AMOS E. HOLT

Executive Director, THOMAS G. LOUGHLIN

Treasurer, WILBUR MARNER

PUBLISHING STAFF

Managing Director, Publishing

P. DI VIETRO

Manager, Journals

C. MCATEER

Production Coordinator

A. HEWITT

Transactions of the ASME, Journal of Fluids Engineering
(ISSN 0098-2202) is published monthly by
The American Society of Mechanical Engineers,
Three Park Avenue, New York, NY 10016,
Periodicals postage paid at New York, NY
and additional mailing offices.

POSTMASTER: Send address changes to Transactions of the
ASME, Journal of Fluids Engineering, c/o THE AMERICAN
SOCIETY OF MECHANICAL ENGINEERS,
22 Law Drive, Box 2300, Fairfield, NJ 07007-2300.

CHANGES OF ADDRESS must be received at Society
headquarters seven weeks before they are to be effective.
Please send old label and new address.

STATEMENT from By-Laws. The Society shall not be
responsible for statements or opinions advanced in papers
or printed in its publications (B7.1, Par. 3).
COPYRIGHT © 2009 by the American Society of
Mechanical Engineers. Authorization to photocopy material for
internal or personal use under those circumstances not falling
within the fair use provisions of the Copyright Act, contact
the Copyright Clearance Center (CCC), 222 Rosewood Drive,
Danvers, MA 01923, tel: 978-750-8400, www.copyright.com.
Request for special permission or bulk copying should be
addressed to Reprints/Permission Department.
Canadian Goods & Services Tax Registration #126148048.

Journal of Fluids Engineering

Published Monthly by ASME

VOLUME 131 • NUMBER 9 • SEPTEMBER 2009

RESEARCH PAPERS

Flows in Complex Systems

- 091101 Pharyngeal Airflow Analysis in Obstructive Sleep Apnea Patients Pre- and Post-Maxillo-mandibular Advancement Surgery
John Huynh, Ki Beom Kim, and Mark McQuilling
- 091102 Flow Characteristics in a Curved Rectangular Channel With Variable Cross-Sectional Area
Avijit Bhunia and C. L. Chen
- 091103 Measurements of a Wall Jet Impinging Onto a Forward Facing Step
D. C. Langer, B. A. Fleck, and D. J. Wilson

Fundamental Issues and Canonical Flows

- 091201 Large-Eddy Simulation of Wake and Boundary Layer Interactions Behind a Circular Cylinder
S. Sarkar and Sudipto Sarkar
- 091202 On the Pulsed and Transitional Behavior of an Electrified Fluid Interface
Paul R. Chiarot, Sergey I. Gubarenko, Ridha Ben Mrad, and Pierre E. Sullivan
- 091203 Curved Non-Newtonian Liquid Jets With Surfactants
Jamal Uddin and Stephen P. Decent
- 091204 Circulation Generation and Vortex Ring Formation by Conic Nozzles
Moshe Rosenfeld, Kakani Katija, and John O. Dabiri

Multiphase Flows

- 091301 Measurements of High Velocity Gradient Flow Using Bubble Tracers in a Cavitation Tunnel
Bu-Geun Paik, Kyung-Youl Kim, and Jong-Woo Ahn
- 091302 Thermodynamic Effect on Rotating Cavitation in an Inducer
Yoshiki Yoshida, Yoshifumi Sasao, Mitsuo Watanabe, Tomoyuki Hashimoto, Yuka Iga, and Toshiaki Ikohagi
- 091303 Transition of Bubbly Flow in Vertical Tubes: New Criteria Through CFD Simulation
A. K. Das, P. K. Das, and J. R. Thome
- 091304 Transition of Bubbly Flow in Vertical Tubes: Effect of Bubble Size and Tube Diameter
A. K. Das, P. K. Das, and J. R. Thome

(Contents continued on inside back cover)

This journal is printed on acid-free paper, which exceeds the ANSI Z39.48-1992 specification for permanence of paper and library materials. ©™

♻️ 85% recycled content, including 10% post-consumer fibers.

TECHNICAL BRIEFS

- 094501 Analytical Solution for Newtonian Laminar Flow Through the Concave and Convex Ducts
M. Firouzi and S. H. Hashemabadi

The ASME Journal of Fluids Engineering is abstracted and indexed in the following:

Applied Science & Technology Index, Chemical Abstracts, Chemical Engineering and Biotechnology Abstracts (Electronic equivalent of Process and Chemical Engineering), Civil Engineering Abstracts, Computer & Information Systems Abstracts, Corrosion Abstracts, Current Contents, Ei EncompassLit, Electronics & Communications Abstracts, Engineered Materials Abstracts, Engineering Index, Environmental Engineering Abstracts, Environmental Science and Pollution Management, Excerpta Medica, Fluidex, Index to Scientific Reviews, INSPEC, International Building Services Abstracts, Mechanical & Transportation Engineering Abstracts, Mechanical Engineering Abstracts, METADEX (The electronic equivalent of Metals Abstracts and Alloys Index), Petroleum Abstracts, Process and Chemical Engineering, Referativnyi Zhurnal, Science Citation Index, SciSearch (The electronic equivalent of Science Citation Index), Shock and Vibration Digest, Solid State and Superconductivity Abstracts, Theoretical Chemical Engineering

John Huynh

Resident
e-mail: jhuynh1@slu.edu

Ki Beom Kim

Assistant Professor
e-mail: kkim8@slu.edu

Graduate Orthodontic Program,
Center for Advanced Dental Education,
Saint Louis University,
St. Louis, MO 63104

Mark McQuilling¹

Assistant Professor
Department of Aerospace and Mechanical
Engineering,
and Center for Fluids at All Scales,
Saint Louis University,
3450 Lindell Boulevard,
St. Louis, MO 63103
e-mail: mmcquill2@slu.edu

Pharyngeal Airflow Analysis in Obstructive Sleep Apnea Patients Pre- and Post-Maxillomandibular Advancement Surgery

The purpose of this study was to evaluate pharyngeal airflow in obstructive sleep apnea (OSA) patients following maxillomandibular advancement (MMA) surgery using computational fluid dynamics (CFD). Computerized models of four OSA patients, pre- and postsurgery, were created using cone beam computed tomography scans. CFD was used to model airflow at inspiration rates of 340 ml/s, 400 ml/s, and 460 ml/s. The relative pressure, eddy viscosity coefficient, and total area-averaged pressure drops were selected for comparison. Results show a decrease in airway resistance of over 90% for three out of four patients. In these three patients, the MMA surgery reduced the constriction along the airway, which resulted in reduced drag and therefore reduced pressure drop required to move a constant volumetric flow between pre- and postsurgery models. CFD analyses on airways of OSA patients provide data that suggest an improvement in airflow following MMA surgery with less effort required for maintaining constant flow.

[DOI: 10.1115/1.3192137]

1 Introduction

It is estimated that obstructive sleep apnea affects 2% of middle aged women and 4% of middle aged men in the United States [1]. Sequelae for this condition include a disturbance of normal sleep patterns, excessive daytime sleepiness, cognitive dysfunction, headaches, systemic hypertension, dysrhythmias, depression, stroke, and angina [2,3]. Risk factors for obstructive sleep apnea include smoking [4], obesity [5], excessive alcohol consumption [4], respiratory depressing drugs [2], nasal congestion, snoring, and increased neck circumference [6].

Anatomically, when compared with normal patients, apneic patients have a large and/or retropositioned tongue, an elongated soft palate, enlarged pharyngeal tonsils, large parapharyngeal fat pads, retrognathic maxilla and/or mandible, short anterior cranial bases, long anterior facial heights, inferiorly placed hyoid bones, narrow posterior airway spaces, or narrow lateral pharyngeal spaces [2,7–15]. In obstructive sleep apnea patients, the balance of constricting factors (i.e., negative inspirational pressure, collapsing soft tissues, and retropositioned structures) outweigh the dilating factors (i.e., dilating forces of the pharyngeal musculature and increased tone in pharyngeal structures), thus, resulting in increased upper airway resistance [7]. A problem however is that the sites of airway collapse and constriction are not identical in all patients, while some may have multiple sites of obstruction [16].

Treatment modalities for obstructive sleep apnea include non-surgical and surgical treatments. A treatment that has been increasing in popularity is maxillomandibular advancement surgery (MMA). Maxillomandibular advancement surgery has traditionally been considered a Phase II surgical treatment, which is used when Phase I treatments have been unsuccessful [17]. However, in patients who are diagnosed with obstructions at multiple levels along the airway or those with craniofacial anomalies, MMA surgery has been recommended as the first surgical option rather than other Phase I treatments [2,7,17–20].

Recent studies using three-dimensional (3D) imaging have evaluated the effects of MMA surgery on pharyngeal airway volume. Fairburn et al. [21] used helical CT scans to evaluate 3D changes in the upper airways of obstructive apnea patients following MMA surgery. Their results showed that there was a significant increase in the lateral and anteroposterior dimensions of the airway at all levels that measurements were taken at. In a study done by Burgess [22] evaluating airway volumetric changes following MMA surgery using cone beam computed tomography (CBCT), she observed that there was a significant change in airway volume in the long term following MMA surgery.

While these studies show that there is an increase in airway volume following MMA surgery, there are few studies showing how this change in volume affects airflow through the airway. A reason for this is that studying airflow in the airway can be very invasive. As a result, airflow studies have been accomplished using indirect methods to evaluate the airflow. Methods such as anemometry, particle image velocimetry (PIV), and computational fluid dynamics (CFD) have been used to simulate real life airflows. Although each method has its advantages and disadvantages, the use of CFD is becoming more prominent because it can allow more detailed and comprehensive information to be obtained when compared with the other methods.

Sung et al. [23] suggested that the major contributor to the pathophysiology of obstructive sleep apnea is the reduced cross-sectional area of the velopharyngeal (retropalatal) area. In their study, they simulated the upper airway of a patient with obstructive sleep apnea using CFD. Their results showed that the maximum airflow velocity and maximum negative pressure occurred within the velopharyngeal area meaning that this was the most constricted and, thus, flow limiting area of the airway in that patient.

Shome et al. [24] performed numerical modeling of an anatomically accurate model of the human pharynx using CFD. In their study, they examined the effects of cross-sectional area of the airway on the relative pressure drop within the airway in response to different treatments for obstructive sleep apnea. In response to mandibular advancement, Shome et al. found that there was a decrease in the relative pressure in relation to the increase in cross-sectional area of the airway. While this study shows that air

¹Corresponding author.

Contributed by the Fluids Engineering Division of ASME for publication in the JOURNAL OF FLUIDS ENGINEERING. Manuscript received December 17, 2008; final manuscript received June 27, 2009; published online August 13, 2009. Assoc. Editor: Rajat Mittal.

pressure in the airway is affected by surgical treatment, it does not show how air velocity is affected. There are limited studies showing the effects of MMA surgery on airflow through the airway in terms of air velocity and pressure changes.

The purpose of the study is to evaluate the pharyngeal airflow of obstructive apnea patients who have undergone MMA surgery. Computational fluid dynamics methods will be used to evaluate both air velocity and pressure changes in these patients following surgery.

1.1 Current Study. Previous studies have shown the ability of CFD in analyzing airflows through the upper airways of patients with or without obstructions [23–34]. However, most of the studies were based on one single model and few showed the effects of treatment on airflow post-treatment. Some studies used simplified nonanatomically correct airway models in their CFD analysis instead of anatomically correct models [30,31]. On the other hand, some studies used anatomically correct anatomy, but did not use a turbulence model to model their airflow [35].

In the present study, pharyngeal airflow in patients with obstructive sleep apnea is shown before and after treatment with maxillomandibular advancement surgery. Using cross-sectional CT scans to construct the airway models ensure that the models are anatomically correct. The RNG $k-\epsilon$ turbulence model is also used to simulate turbulence due to the higher Reynolds numbers occurring in the airways.

2 Computational Models

Sections 2.1 and 2.2 detail the method used to create and analyze CFD models starting from CBCT scans.

2.1 Sample and Imaging. Records of four patients who have undergone combined orthodontic treatment and MMA surgery were selected. The sample was comprised of one female and three males. The mean age was 40.0 years. The inclusion criteria for these patients included having a history of obstructive sleep apnea, being treated with a combination of orthodontic treatment and orthognathic surgery, had MMA surgery, and had presurgical CBCT scans taken within a week prior to surgery (T_0) and a scan at least a minimum of 7 weeks following surgery (T_1). The exclusion criteria were patients with craniofacial syndromes and patients who had surgical expansion of their upper jaws. All surgeries were performed by one of two oral surgeons utilizing similar surgical techniques. For the mandibular advancement surgeries, a bilateral sagittal split osteotomy technique was utilized. A nonsegmental Le Fort I osteotomy was utilized for the maxillary advancements. Bone grafts were placed in areas where large surgical movements were performed and rigid fixation was used to fixate both jaws. Prior to fixation, the mandibular condyles were seated in centric relation in all patients.

The CBCT scans of the patients were performed using the same i-CAT CBCT machine at both pre- and postsurgical time points. The field of view used was $23 \times 19 \text{ cm}^2$. The voxel size of the CBCT scans taken was 0.4 mm. All scans were taken with the condyles seated in centric relation. *v-WORKS* 3D software and *DOLPHIN* 3D were used view and analyze the CBCT scans.

The amount of surgical movement in the anteroposterior (AP) direction was determined using the pre- and postsurgical CBCT scans. The head position was oriented with Frankfort Horizontal parallel to the horizontal plane (x -axis). The facial midline was then centered on the vertical plane (z -axis). A plane perpendicular to Frankfort Horizontal, passing through nasion, was created to represent the y -axis. These three planes are displayed in Fig. 1. Four skeletal landmarks (basion, nasion, point A, and point B) were identified along the z -axis plane; these are shown in Fig. 2. The AP surgical movement was calculated using the z -axis coordinate for each jaw. Basion was used as a reference point to evaluate the reliability of the position of the other landmarks. The rela-

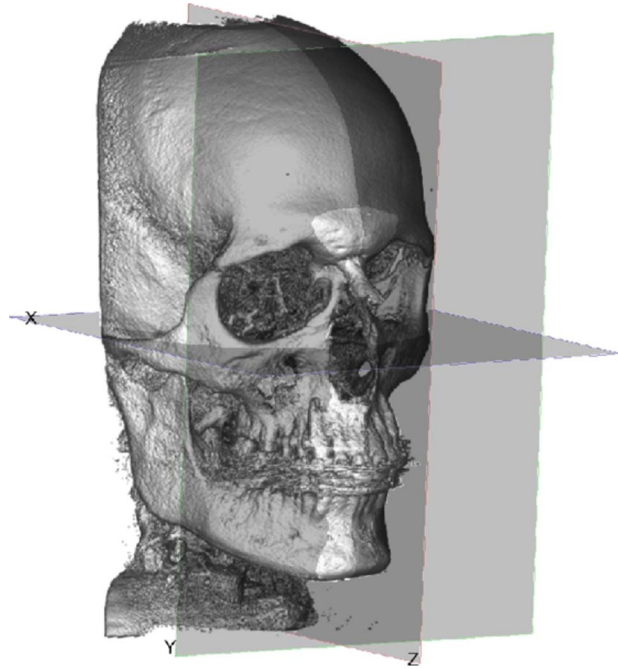


Fig. 1 3D skull depicting X, Y, and Z axes

tive positions of points A and B in relation to nasion were recorded to determine the amount of advancement for the upper and lower jaw, respectively.

The scanned images were imported into *v-WORKS* to generate the volumetric image of the scanned region. Once the volumetric image was produced, the area of interest could be isolated. The superior border was defined as the scan that corresponded with a horizontal line drawn through PNS. The inferior border was defined as the scan that corresponded with a horizontal line drawn tangent to the lowest point on the third cervical vertebra. Typical border positions are shown in Fig. 3.

2.2 3D Model and CFD. Using *v-WORKS*, the scan corresponding with the most superior border of the area of interest was saved as a picture file for future processing. Using a slice thickness of 1.2 mm, successive scans were saved as picture files until the most inferior border of the area of interest was reached. Once these picture files were obtained, they were imported into *IMAGEJ* for further processing. Here, airway slice coordinate sets were generated by clicking on the outline of the airway, as can be seen in Fig. 4. The coordinate sets were then used to create slices of the airway in a solid modeling program, *PRO/ENGINEER*. The slices were then blended together at distances of 1.2 mm apart to form the three-dimensional airway, as seen in Fig. 5. Next, a box was created around the joined slices to produce a hollowed out tunnel in the shape of the airway. The box was then exported as an *stl* file for input into the geometry cleanup software and CFD program, *CADTHRU* and *SC/TETRA*, respectively. *SC/TETRA* is a finite volume flow solver based on the *SIMPLEC* method [36] and *MUSCL* [37] differentiation technique for solving the Navier–Stokes equations. *SC/TETRA* employs an unstructured tetrahedral mesh [38] and contains all pre- and postprocessing required for CFD analysis. Typical screenshots from the geometry cleanup process are shown in Fig. 6. After appropriate geometry cleaning, the model was exported into the CFD software to configure the simulation.

A grid convergence test was done to determine an appropriate grid size for the mesh models. Grid convergence was determined when a number of velocity profiles at various locations along the airway showed minimal difference after further grid refinement. The resulting grid size input into the simulation was based on an octree size of 0.5 mm. The final mesh models of the airway had

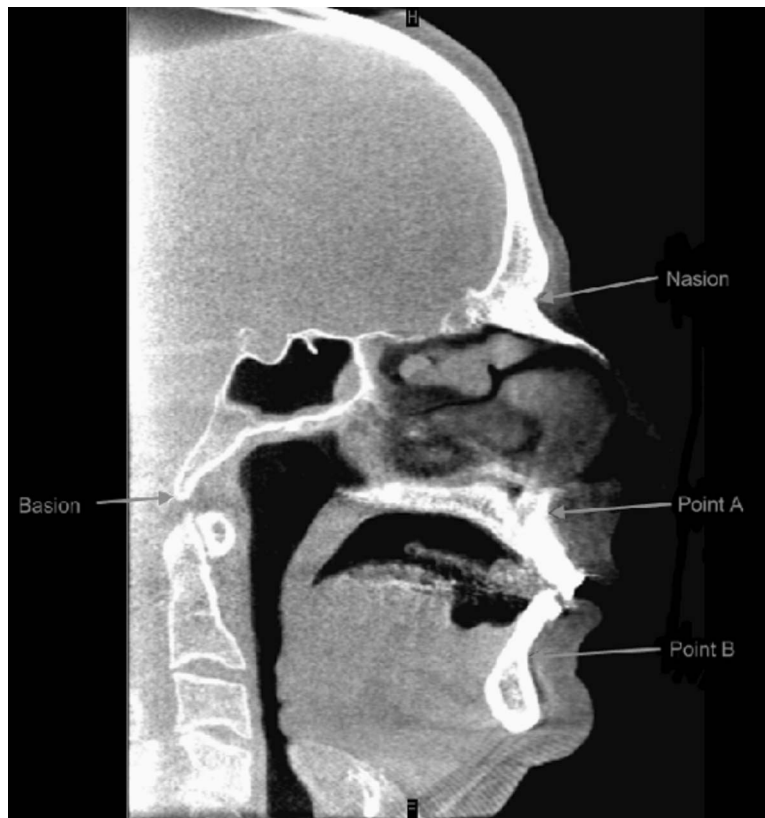


Fig. 2 Landmarks used to determine surgical movement

between 118,878 and 319,193 tetrahedral elements depending on the size of the airways; a typical model is shown in Fig. 7. The surface mesh h -ratio, which is the ratio of radii of the inscribed circle and the circumscribed circle of a surface mesh triangle, was

between 0.43 and 0.46 for all models. This h -ratio describes the quality of surface triangulation, with the best h -ratio equal to 0.5 for an equilateral triangle. The tetrahedral volume mesh quality is similarly described by its h -ratio, which is the ratio of radii of the inscribed sphere and the circumscribed sphere of a tetrahedral element. The tetrahedral h -ratio was between 0.26 and 0.27 for all models in this study, where a value of 0.333 is the best possible h -ratio. These numbers indicate the meshes used for the simulations described herein are of high quality.

In order to model turbulent flow within the pharyngeal airway, the RNG k - ϵ turbulence model was used, as suggested by Sung et al. [23] for simulations on similar geometries. Therefore, no other turbulence closure models were compared. The inlet boundary velocity was set as uniform and was determined for each model to

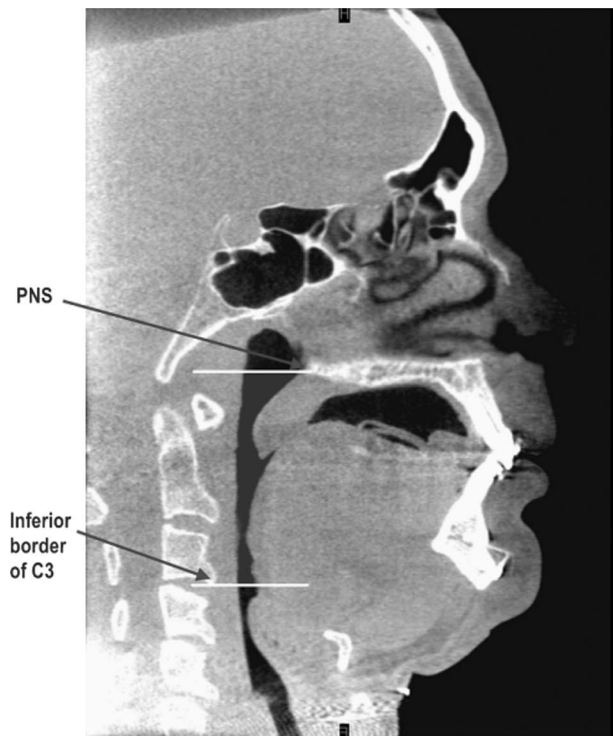


Fig. 3 Typical superior and inferior borders of pharyngeal airway

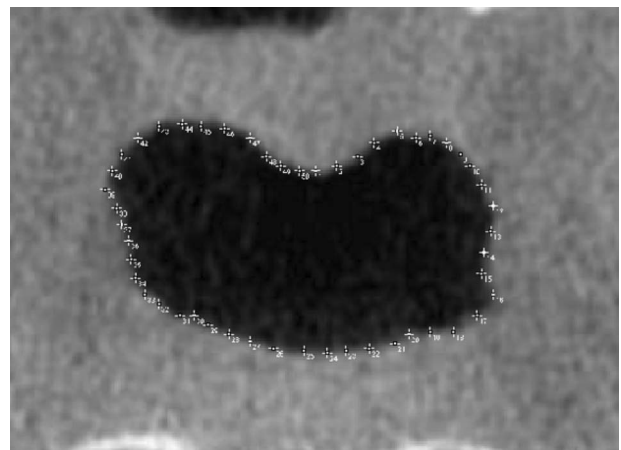


Fig. 4 Outline of airway using IMAGEJ

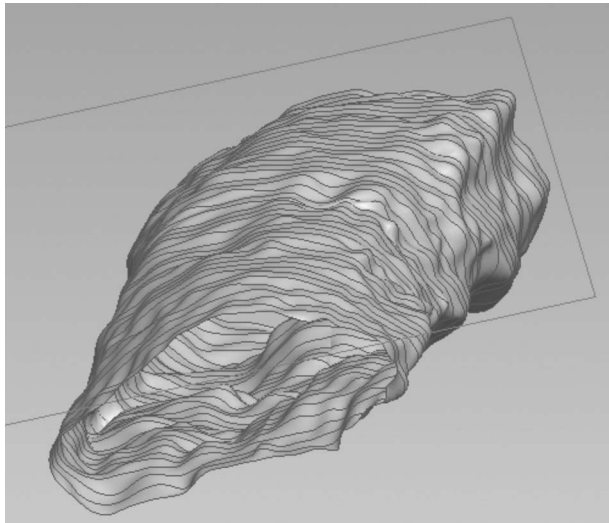


Fig. 5 PRO/ENGINEER model of the airway

correspond with the volumetric flow rates of 340 ml/s, 400 ml/s, and 460 ml/s using the equation $Q=AV$. The inlet areas, A , were computed from the solid modeling program. The outlet boundary was set to a static pressure of 0 Pa for incompressible flow. A no slip condition was set for the walls of the airway, which were also assumed to be rigid and noncompliant. The simulations were performed on a PC with an AMD Athlon™64 X2 Dual Core Processor 6400+ (3.21 GHz) with 8 GB of RAM. Typical simulation times were between 5 min and 8 min.

3 Results

The quantity of maxillary and mandibular surgical advancement is shown in Table 1 for all patients. Maxillary advancement refers to the change in point A between pre- and postsurgery, while mandibular advancement refers to the change in point B between pre- and postsurgery. Of particular note is the minimal amount of advancement for patient 3 as compared with the other patients. As described herein, postsurgery patient 3 behaves differently than the other patients, and this small amount of advancement is believed to be one of the causes for the differences.

Figure 8 shows the change in hydraulic diameter across the airway for all four patients. The hydraulic diameter is a measure of the effective flow area at each location, and is defined as $D=4A/P$, where A is the cross-sectional area and P is the perimeter [24]. This figure again shows how patient 3 results are unlike the

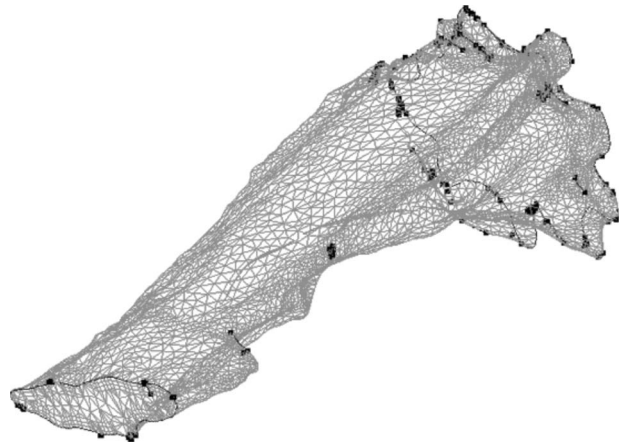
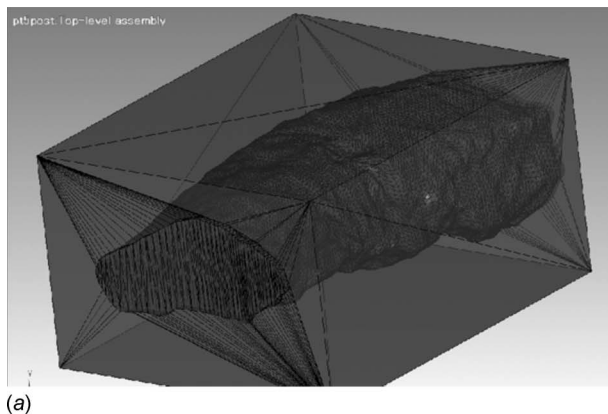


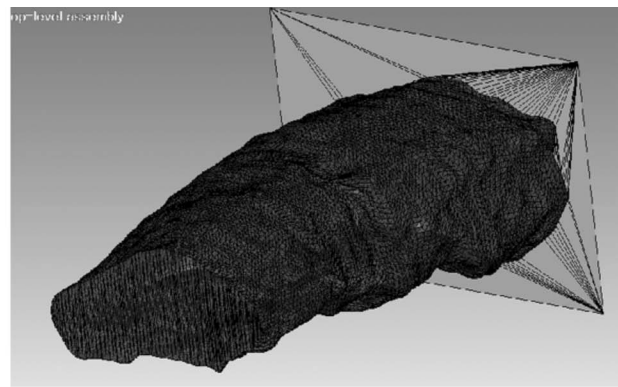
Fig. 7 3D mesh model showing tetrahedral elements

others, where the MMA surgery creates more constriction in several locations of the airway by reducing the effective flow area, represented here by the negative change in hydraulic diameter. The other three patients experience an increase in hydraulic diameter throughout the airway. The authors suspect the local decreases in hydraulic diameter for patient 3 are the primary reason for the difference in flow behavior when compared with the other patients.

The Reynolds number is a dimensionless number used to characterize different types of fluid flow as laminar, transitional, or turbulent. For laminar flows, the Reynolds number is <2000 , while turbulent flows have a Reynolds number >4000 ; in between those two ranges lies the transitional phase of fluid flow [39]. The equation used to calculate the Reynolds number is $Re=\rho VD/\mu$, where ρ is the density of air= 1.2 kg/m^3 , V is the mean fluid velocity, D is the hydraulic diameter, and μ is the fluid viscosity= $1.8\times 10^{-5}\text{ N s/m}^2$. The volumetric flow rate, Q , is equal to $Q=AV$, where A is the cross-sectional area and V is the mean fluid velocity [40]. Substituting these quantities transforms the Reynolds number equation into $Re=4\rho Q/P\mu$. This equation for the Reynolds number illustrates how for a constant volumetric flow rate, the flow can become more laminar in nature due to increasing the perimeter of a cross section in the airway, as done with the advancement surgeries. Figures 9–12 show the variation in Reynolds number throughout the pharyngeal airways for each patient at T_0 (presurgery) and T_1 (postsurgery) for all three flow rates. The Reynolds numbers observed for all patients at T_0 showed there were significant areas of reduced perimeter, or



(a)



(b)

Fig. 6 Typical CADTHRU models used for geometry cleanup. (a) Model after importing into CADTHRU. (b) Model with some surfaces removed in cleanup process.

Table 1 Quantity of surgical advancement (mm)

	Pt 1	Pt 2	Pt 3	Pt 4	Mean
Maxillary	6.1	4.6	3.3	2.0	4.0
Mandibular	5.8	8.5	5.3	11.3	7.7

stenosis, along the airway, noted by peaks in the Re plots. For patients 1, 2, and 4, the Reynolds numbers increased over 2000 in the areas of stenosis, meaning the laminar flow was changing over to turbulent flow. Patient 3 also showed smaller margin increases in Reynolds number in stenotic areas but the values did not go above 2000. Thus, airflow in this patient was predominantly laminar in nature. As the airflow was increased, there was a corresponding increase in Reynolds number. This was expected as a

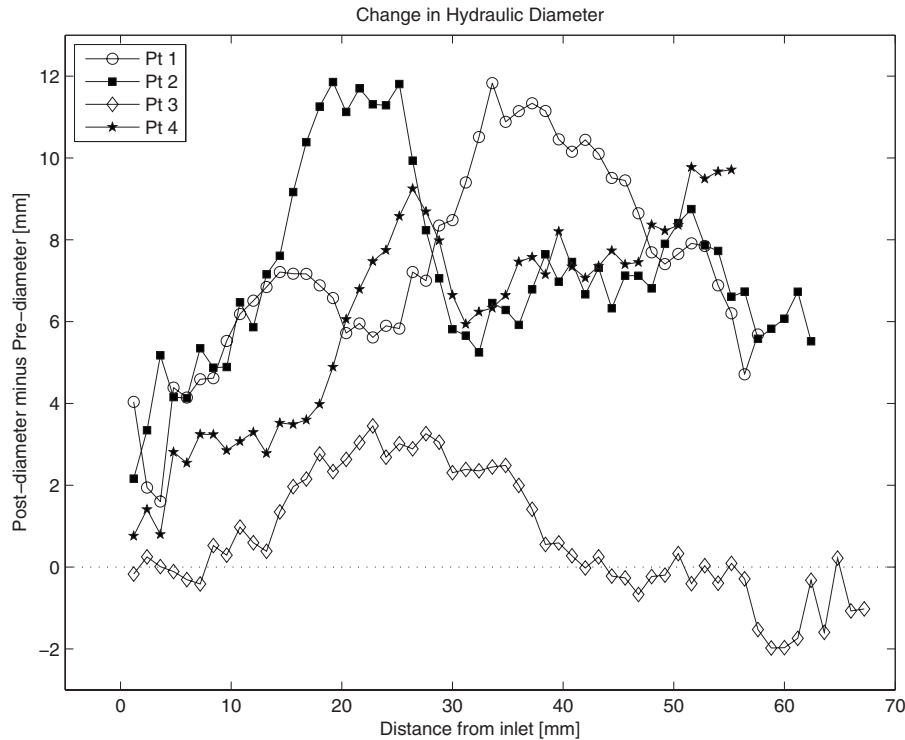


Fig. 8 Change in hydraulic diameter along pharyngeal airway

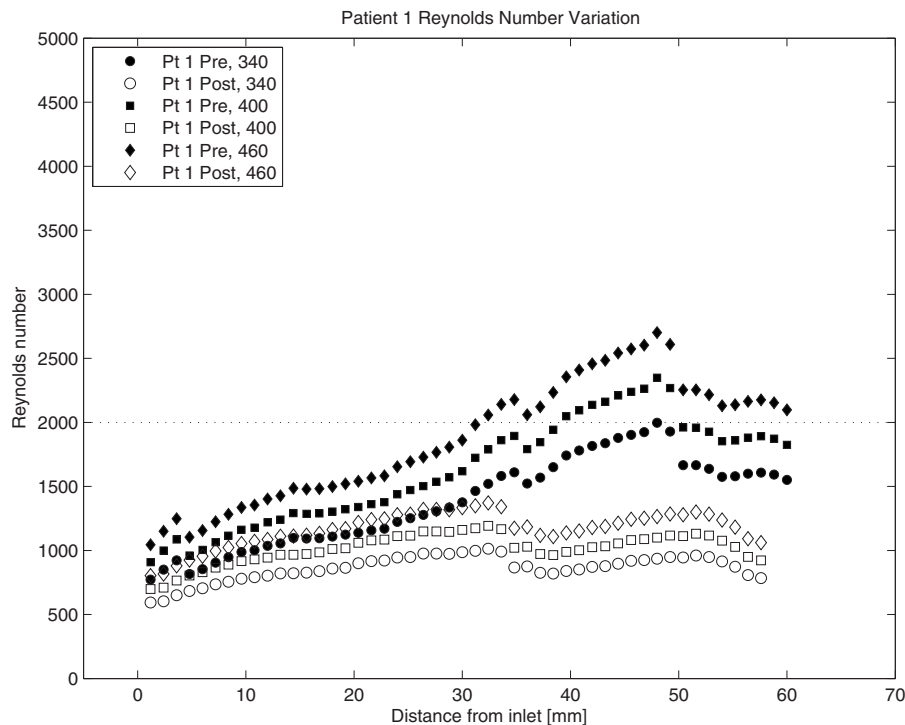


Fig. 9 Reynolds number along pharyngeal airway of patient 1

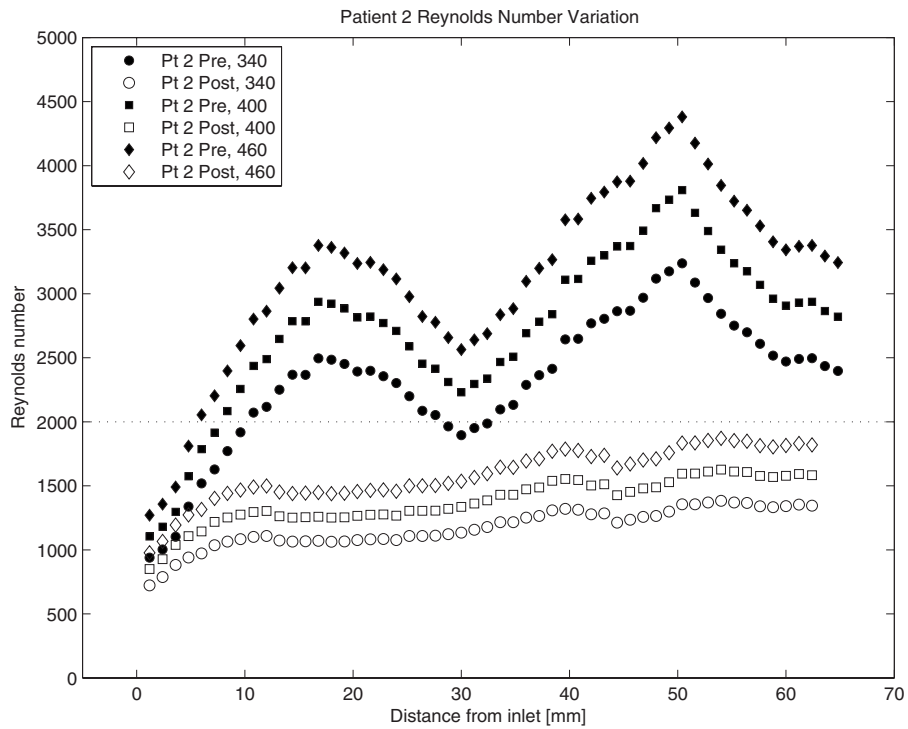


Fig. 10 Reynolds number along pharyngeal airway of patient 2

larger volume of air is trying to pass through a confined space. In general, an increase in Re signifies more turbulent energy, but again patient 3 Reynolds numbers did not change appreciably like the others. Comparing pre- and postsurgery Reynolds numbers show how the advancement surgeries remove stenotic sections of the airway. Following surgery, the Reynolds numbers decreased for all patients due to the increase in perimeter. As a result, the airflow postsurgically tends to be more laminar in nature. In tur-

bulent flow, there is increased mass and energy transfer normal to the surface the airflow is passing over. As a result, the surface friction is increased as turbulence increases. Thus, if turbulence is decreased (Reynolds number is lowered), the respiratory force needed to breathe is also decreased because of the reduction in friction caused by turbulence [41]. As the perimeter was increased along with the hydraulic diameter after the surgery, the driving force necessary to respire decreases. The increase in hydraulic

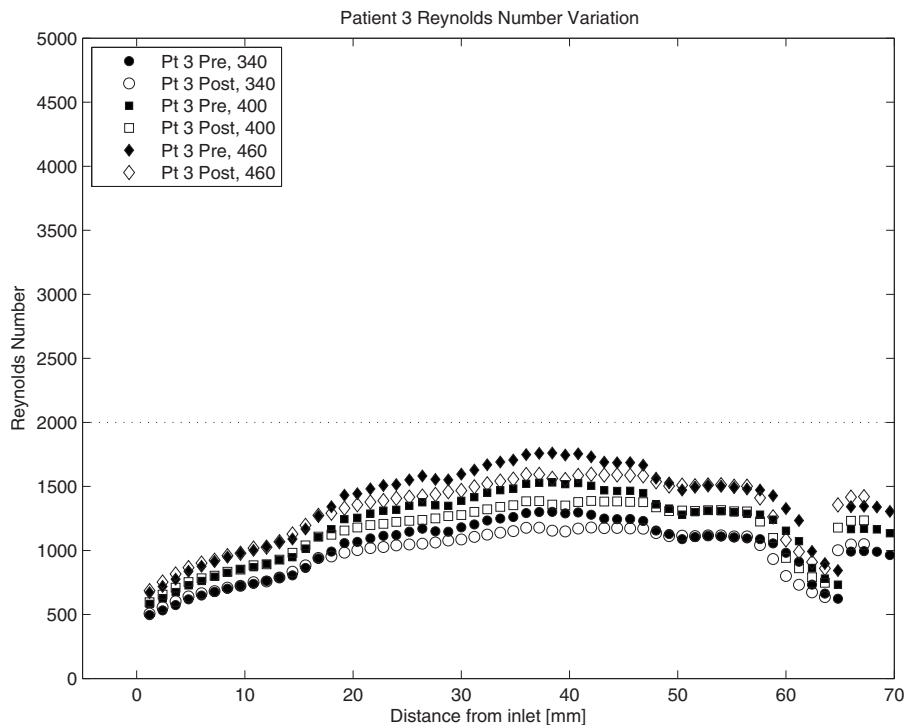


Fig. 11 Reynolds number along pharyngeal airway of patient 3

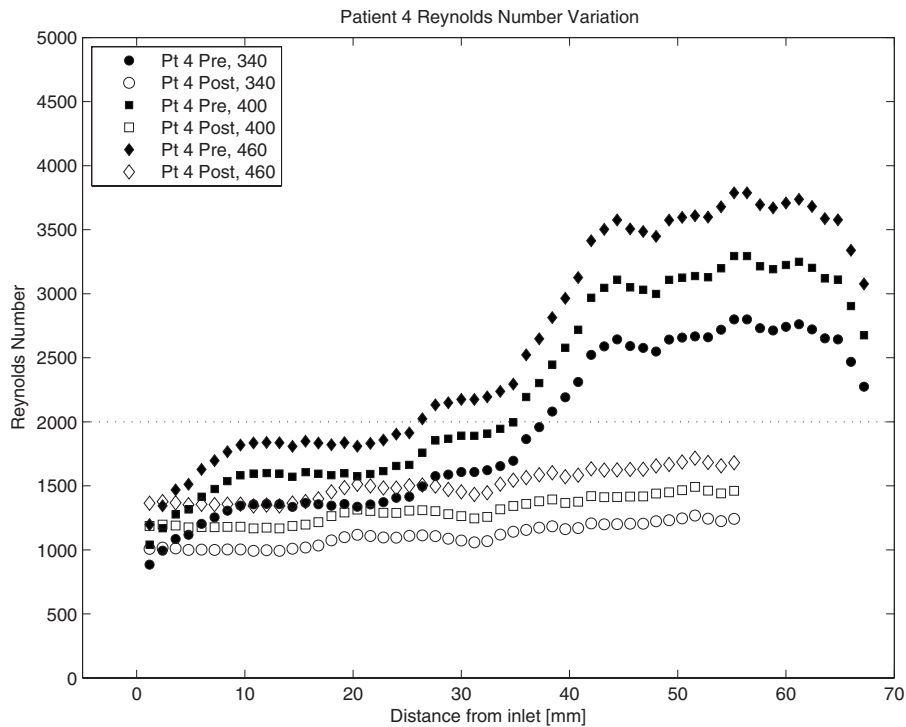


Fig. 12 Reynolds number along pharyngeal airway of patient 4

diameter opens up constricted areas and reduces the pressure drag forces, while the increase in perimeter lowers the Reynolds number, thus reducing the turbulence and resulting skin friction drag.

Figures 9–12 show how patients 1 and 4 behave similarly, while there are significant differences in Reynolds number behavior between 1, 2, and 3. The effects of Reynolds number changes between patients 1 and 2 are also similar; therefore, in the interest of remaining concise, no additional figures from patients 1 or 4 will be presented as results are qualitatively similar to patient 2. It should also be noted that quantitative comparisons drawn in this paper are between pre- and postsurgery behaviors for a single patient, and only qualitative comparisons are drawn between different patients. Therefore, figure scales and colorbars are identical for pre- and postsurgery results for a single patient and are not the same across patients; they were selected in order to illustrate the differences between T_0 and T_1 .

As mentioned earlier, two mechanisms act to reduce the pressure force required to drive a constant volumetric flow through the airway—an increase in hydraulic diameter to reduce pressure drag, and an increase in perimeter to decrease the Reynolds number and thereby decreasing the skin friction drag. Figure 13 shows the eddy viscosity coefficient with streaklines along the midsagittal plane for a typical patient having stenotic regions in the passage and illustrates why this is true. The eddy viscosity coefficient was selected for comparison herein since it contains effects of both turbulent production and turbulent diffusion. The eddy viscosity coefficient rises in regions with increased turbulence, seen near the right wall in the figure. Increased swirling motions indicated by the streaklines are also seen in the turbulent regions. Thus, some of the kinetic energy is no longer in the direction of flow, and its interaction with the bulk fluid movement dissipates some of its energy, thereby requiring more pressure force to drive the volume of fluid through the passage. This deviation from laminar flow can also result in increased shear stresses on the walls of the airway.

Contours presenting the eddy viscosity coefficient along the midsagittal plane for T_0 and T_1 are presented in Figs. 14–17 for patients 2 and 3 at all flow rates. Higher values for the eddy

viscosity coefficient were found in areas of stenosis, as well as along the anterior and posterior walls of the airway. Figure 14 shows how increasing the flow rate causes a corresponding increase in eddy viscosity, as the faster freestream supplies more energy into the turbulence process. This trend is true for all patients at T_0 and T_1 , and regions near the walls show more of an

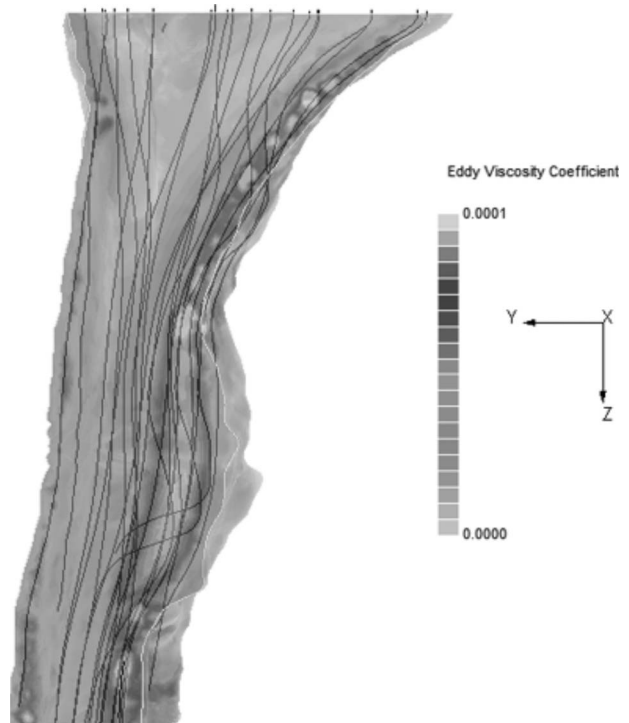


Fig. 13 Eddy viscosity coefficient contour with streaklines

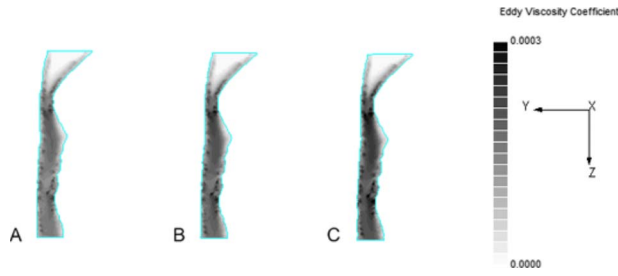


Fig. 14 Contour of eddy viscosity coefficient for patient 2 along midsagittal plane at T_0 . Three flow rates shown: (a) 340 ml/s, (b) 400 ml/s, and (c) 460 ml/s.

increase in turbulent activity than regions near the middle of the passage. Comparing Fig. 14 to Fig. 15 shows how the advancement surgery decreases the turbulence near the walls and out into the passage, which agrees well with the decreases in Reynolds number as presented earlier; similar trends are seen with patients 1 and 4. Patient 3, however, shows only minimal difference in eddy viscosity between T_0 and T_1 , as seen in Figs. 16 and 17, respectively. Only the middle of the passage changes appreciably, with higher turbulence remaining near the walls. As will be seen later, the changes in hydraulic diameter and perimeter due to the surgery and the resulting decrease in passage turbulence seen here actually requires an increase in total pressure to drive the volume

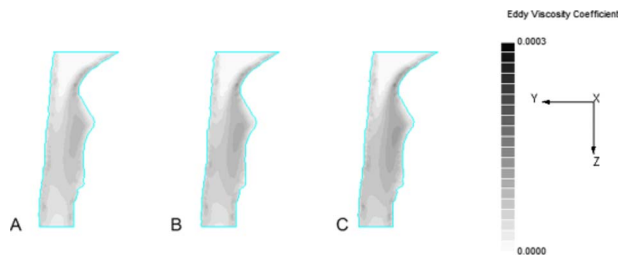


Fig. 15 Contour of eddy viscosity coefficient for patient 2 along midsagittal plane at T_1 . Three flow rates shown: (a) 340 ml/s, (b) 400 ml/s, and (c) 460 ml/s.

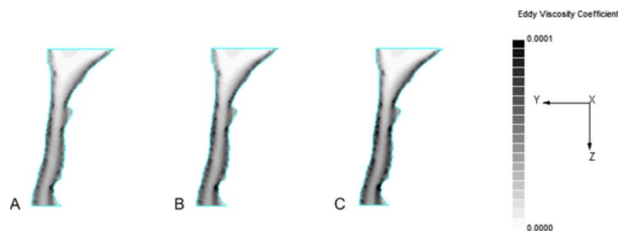


Fig. 16 Contour of eddy viscosity coefficient for patient 3 along midsagittal plane at T_0 . Three flow rates shown: (a) 340 ml/s, (b) 400 ml/s, and (c) 460 ml/s.

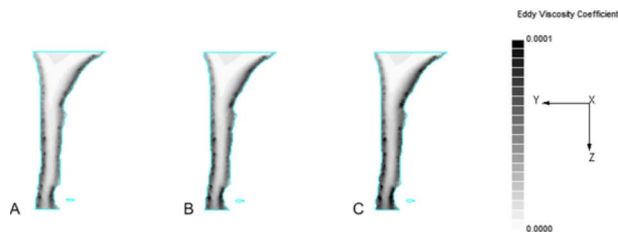


Fig. 17 Contour of eddy viscosity coefficient for patient 3 along midsagittal plane at T_1 . Three flow rates shown: (a) 340 ml/s, (b) 400 ml/s, and (c) 460 ml/s.

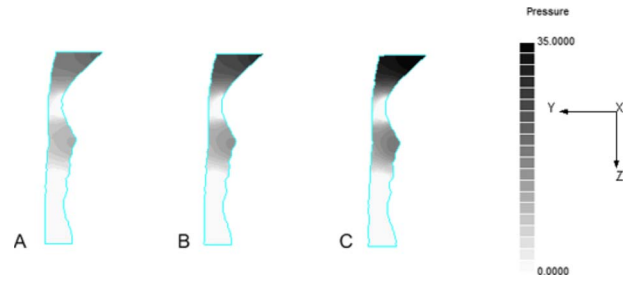


Fig. 18 Contour of relative pressure (Pa) for patient 2 along midsagittal plane at T_0 . Three airflow speeds shown: (a) 340 ml/s, (b) 400 ml/s, and (c) 460 ml/s.

of fluid through the passage. Hence, lowering turbulence is not the only factor to consider when deciding if the surgery was effective or not.

Contours presenting the relative pressure along the midsagittal plane for T_0 and T_1 are presented in Figs. 18–21 for patients 2 and 3 at all flow rates. As expected, all patients experience an increase in relative pressure with an increase in flow rate because a greater driving force is required to move more air through the same passage. Figure 18 for patient 2 at T_0 shows how areas of stenosis not only increase turbulence, but also decrease the local pressure. This is due to conservation of mass; since the flow rate $Q=VA$ must be

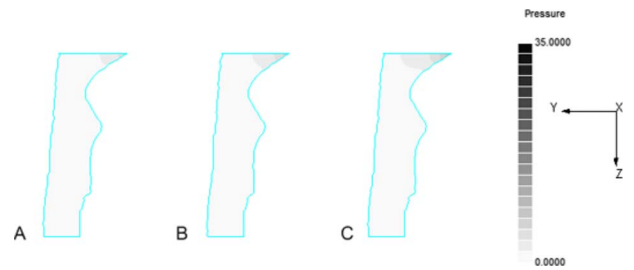


Fig. 19 Contour of relative pressure (Pa) for patient 2 along midsagittal plane at T_1 . Three airflow speeds shown: (a) 340 ml/s, (b) 400 ml/s, and (c) 460 ml/s.

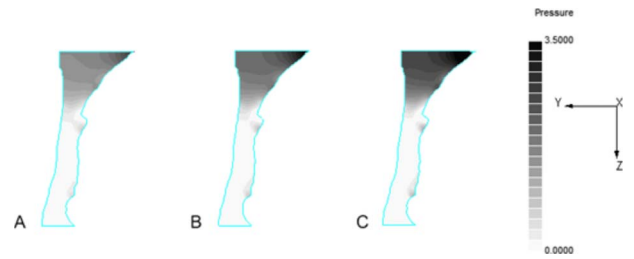


Fig. 20 Contour of relative pressure (Pa) for patient 3 along midsagittal plane at T_0 . Three airflow speeds shown: (a) 340 ml/s, (b) 400 ml/s, and (c) 460 ml/s.

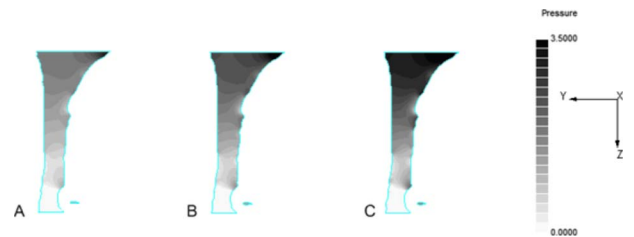


Fig. 21 Contour of relative pressure (Pa) for patient 3 along midsagittal plane at T_1 . Three airflow speeds shown: (a) 340 ml/s, (b) 400 ml/s, and (c) 460 ml/s.

Table 2 Total pressure drop (Δp) at three flow rates for T_0 and T_1 (Pa)

	340 ml/s	400 ml/s	460 ml/s
Pt 1, T_0	12.7	17.1	22.3
Pt 1, T_1	1.1	1.5	1.9
Pt 2, T_0	23.6	31.9	41.4
Pt 2, T_1	2.3	3.1	4.0
Pt 3, T_0	2.1	2.8	3.5
Pt 3, T_1	2.4	3.2	4.1
Pt 4, T_0	43.5	59.3	77.7
Pt 4, T_1	1.1	1.4	1.8

conserved at all locations along the airways, if the flow area A decreases, then the mean velocity V must increase, requiring a greater difference in pressure to drive the flow. Toward the end of the stenosis, however, the pressure recovers until a decrease toward the next stenosis or the outlet. For patient 2, comparing pre- and postsurgery in Figs. 18 and 19, respectively, shows how the surgery causes a reduction in relative pressure all along the airways; the same is true for patients 1 and 4. In contrast, patient 3 in Figs. 20 and 21 displays an increase in relative pressure along the airway between T_0 and T_1 .

Table 2 shows the total area-averaged pressure drop along the airway, Δp , for all patients pre- and postsurgery at all flow rates. As expected for all patients, there is an increase in the total pressure drop along the airway as the flow rate is increased. Patients 1, 2, and 4 have significant decreases in the Δp required from T_0 to T_1 , meaning it takes much less pressure force after the surgery to drive the same volume of air through the passage. Patient 3, however, has an increase in the Δp value from T_0 to T_1 .

The total area-averaged pressure drop, Δp , can also be used to calculate the airway resistance, R , using the equation $R = \Delta p / \dot{m}$, where \dot{m} is the mass flow rate [25]. The mass flow rate, \dot{m} , can be determined using the equation $\dot{m} = \rho Q$, where Q is the volumetric flow rate and ρ is the density of air. The percentage change in this resistance from T_0 to T_1 is shown in Table 3. Patients 1, 2, and 4 showed a minimal tenth of a percent decrease in airway resistance as flow speed was increased. Patient 3 showed a larger magnitude increase in resistance with flow rate at 1.2% and 1.4%. For patients 1, 2, and 4, the decrease in resistance from T_0 to T_1 was higher than 90% with patient 4 showing the largest decrease in airway resistance following the surgery. Patient 3 had an increase in airway resistance from T_0 to T_1 . Considering the amounts of surgical advancements shown earlier in Table 1 and the negative changes in hydraulic diameter seen in Fig. 8, this result is not surprising. It is also noted that while patient 3 had less surgical advancement, the total pressure drop required to drive the presurgery flow is on the order of magnitude of all other patients postsurgery where significant improvement was seen. Quite possibly, patient 3 may be in a range of pharyngeal geometries where the MMA surgery cannot produce results as optimal as others.

4 Conclusions

In this study, CFD modeling illustrated the effects maxillomandibular advancement surgery had on flow characteristics in the pharyngeal airway of obstructive sleep apnea patients. This paper

Table 3 Percentage change in airway resistance

	340 ml/s	400 ml/s	460 ml/s
Pt 1	-91.2	-91.3	-91.4
Pt 2	-91.2	-91.3	-91.4
Pt 3	+11.1	+12.5	+13.7
Pt 4	-97.5	-97.6	-97.7

demonstrated a method to use cone beam computed tomography scans to create a three-dimensional model suitable for CFD analysis. The results presented in this paper lead to the following conclusions.

1. Following surgery, the airway resistance decreased by over 90% for three out of the four patients studied. This is a result of increasing the cross-sectional areas in stenotic regions with the MMA surgery, thereby increasing the hydraulic diameter and reducing the Reynolds number to require less total pressure force to drive the flow for a constant volumetric flow rate.
2. If one assumes the pharyngeal airway is similar to a tube, a generalization using the laminar flow equation $\Delta p = 128\mu LQ / \pi d^4$ can be used to relate Δp with volumetric airflow, where μ is the fluid viscosity, L is the tube length, Q is the volumetric flow rate, and d is the tube diameter [40]. If an average diameter is used for d and all other variables remain equal, and the Δp required for inspiration in the presurgical model was applied to the postsurgical model, then at least ten times as much air can be moved in the postsurgical model with equal effort for the three patients reporting improvements.
3. Isono et al. [42] reported that in obstructive sleep apnea patients there is progressive narrowing of the velopharyngeal airway in flow limited inspirations. This paper showed how areas of stenosis cause a lower local relative pressure, and these lower local pressures in the segments distal to the stenotic area could result in further collapse of the airway if the tissues are highly compliant in that area.
4. Patient 3 did not exhibit the favorable characteristics seen in the other three patients between the pre- and postsurgery models. The authors believe this is due to three reasons: the small quantities of maxillary and mandibular surgical advancement, the airway regions having a negative change in hydraulic diameter, and the small change in Reynolds number behavior throughout the pharyngeal passage. This may suggest that patients having a certain range of pharyngeal geometry may not benefit from MMA surgery. This could only be proven with continued discussion with patients and possible testing after the surgery to see if their apnea conditions have improved.

Acknowledgment

The authors wish to thank George Huang of Wright State University and David Welsh of Software Cradle Co. for their guidance with the computational modeling.

Nomenclature

- A = cross-sectional area (m^2)
- D = hydraulic diameter, $D = 4A/P$ (m)
- \dot{m} = mass flow rate, $\dot{m} = \rho Q$ (kg/s)
- P = perimeter (m)
- Δp = total area-averaged pressure drop (Pa)
- Q = flow rate, $Q = VA$ (m^3/s)
- R = flow resistance, $R = \Delta p / \dot{m}$ (Pa s/kg)
- Re = Reynolds number, $Re = \rho VD / \mu$
- T_0 = time denoting one week prior to surgery
- T_1 = time denoting seven weeks after surgery
- V = mean flow velocity (m/s)

Greek Symbols

- ρ = density of air (kg/m^3)
- μ = viscosity of air ($kg/m \cdot s$)

References

- [1] Young, T., Palta, M., Dempsey, J., Skatrud, J., Weber, S., and Badr, S., 1993, "The Occurrence of Sleep-Disordered Breathing Among Middle-Aged

- Adults," *N. Engl. J. Med.*, **328**, pp. 1230–1235.
- [2] Fleisher, K., and Krieger, A., 2007, "Current Trends in the Treatment of Obstructive Sleep Apnea," *J. Oral Maxillofac Surg.*, **65**, pp. 2056–2068.
- [3] Padma, A., Ramakrishnan, N., and Narayanan, V., 2007, "Management of Obstructive Sleep Apnea: A Dental Perspective," *Indian J. Dent. Res.*, **18**, pp. 201–209.
- [4] Young, T., Skatrud, J., and Peppard, P., 2004, "Risk Factors for Obstructive Sleep Apnea in Adults," *JAMA, J. Am. Med. Assoc.*, **291**, pp. 2013–2016.
- [5] Tangugsorn, V., Krogstad, O., Espeland, L., and Lyberg, T., 2001, "Obstructive Sleep Apnea: A Canonical Correlation of Cephalometric and Selected Demographic Variables in Obese and Nonobese Patients," *Angle Orthod.*, **71**, pp. 23–35.
- [6] Davies, R., Ali, N., and Stradling, J., 1992, "Neck Circumference and Other Clinical Features in the Diagnosis of the Obstructive Sleep Apnea Syndrome," *Thorax*, **47**, pp. 101–105.
- [7] Prinsell, J., 1999, "Maxillomandibular Advancement Surgery in a Site-Specific Treatment Approach for Obstructive Sleep Apnea in 50 Consecutive Patients," *Chest*, **116**, pp. 1519–1529.
- [8] Guilleminault, C., Riley, R., and Powell, N., 1984, "Obstructive Sleep Apnea and Abnormal Cephalometric Measurements: Implications for Treatment," *Chest*, **86**, pp. 793–794.
- [9] Lowe, A., Santamaria, J., Fleetham, J., and Price, C., 1986, "Facial Morphology and Obstructive Sleep Apnea," *Am. J. Orthod. Dentofacial Orthop.*, **90**, pp. 484–491.
- [10] Lyberg, T., Krogstad, O., and Djupesland, G., 1989, "Cephalometric Analysis in Patients With Obstructive Sleep Apnoea Syndrome: II. Soft Tissue Morphology," *J. Laryngol. Otol.*, **103**, pp. 287–297.
- [11] Lyberg, T., Krogstad, O., and Djupesland, G., 1989, "Cephalometric Analysis in Patients With Obstructive Sleep Apnoea Syndrome: I. Skeletal Morphology," *J. Laryngol. Otol.*, **103**, pp. 287–292.
- [12] Prachartam, N., Nelson, S., Hans, M., Broadbent, B., Redline, S., and Rosenberg, C., 1996, "Cephalometric Assessment in Obstructive Sleep Apnea," *Am. J. Orthod. Dentofacial Orthop.*, **109**, pp. 410–419.
- [13] Riley, R., Guilleminault, C., Herran, J., and Powell, N., 1983, "Cephalometric Analyses and Flow-Volume Loops in Obstructive Sleep Apnea Patients," *Sleep*, **6**, pp. 303–311.
- [14] Rodenstein, D., Dooms, G., Thomas, Y., Liistro, G., Stanesco, D., and Culee, C., 1990, "Pharyngeal Shape and Dimensions in Healthy Subjects, Snorers, and Patients With Obstructive Sleep Apnea," *Thorax*, **45**, pp. 722–727.
- [15] Schwab, R., Gefter, W., Hoffman, E., Gupta, K., and Pack, A., 1993, "Dynamic Upper Airway Imaging During Awake Respiration in Normal Subjects and Patients With Sleep Disordered Breathing," *Am. Rev. Respir. Dis.*, **148**, pp. 1385–1400.
- [16] Hoffstein, V., and Wright, S., 1991, "Improvement in Upper Airway Structure and Function in a Snoring Patient Following Orthognathic Surgery," *J. Oral Maxillofac Surg.*, **49**, pp. 656–658.
- [17] Prinsell, J., 2002, "Maxillomandibular Advancement Surgery for Obstructive Sleep Apnea Syndrome," *J. Am. Dent. Assoc.*, **133**, pp. 1489–1497.
- [18] Prinsell, J., 2000, "Maxillomandibular Advancement (MMA) in a Site-Specific Treatment Approach for Obstructive Sleep Apnea: A Surgical Algorithm," *Sleep Breath.*, **4**, pp. 147–154.
- [19] Prinsell, J., 2000, "Maxillomandibular Advancement Surgery for Obstructive Sleep Apnea," *J. Med. Assoc. Ga.*, **89**, pp. 54–57.
- [20] Conradt, R., Hochban, W., Brandenburg, U., Heitmann, J., and Peter, J., 1997, "Long-Term Follow-Up After Surgical Treatment of Obstructive Sleep Apnea by Maxillomandibular Advancement," *Eur. Respir. J.*, **10**, pp. 123–128.
- [21] Fairburn, S., Waite, P., Vilos, G., Harding, S., Bernreuter, W., and Cure, J., 2007, "Three-Dimensional Changes in Upper Airways of Patients With Obstructive Sleep Apnea Following Maxillomandibular Advancement," *J. Oral Maxillofac Surg.*, **65**, pp. 6–12.
- [22] Burgess, B., 2004, "Pharyngeal Airway Volume Following Maxillomandibular Advancement Surgery Utilizing Cone Beam Computed Tomography," MS thesis, Saint Louis University, Saint Louis, MO.
- [23] Sung, S., Jeong, S., Yu, Y., Hwang, C., and Pae, E., 2006, "Customized Three-Dimensional Computational Fluid Dynamics Simulation of the Upper Airway of Obstructive Sleep Apnea," *Angle Orthod.*, **76**, pp. 791–799.
- [24] Shome, B., Wang, L., Santare, M., Prasad, A., Szeri, A., and Roberts, D., 1998, "Modeling of Airflow in the Pharynx With Application to Sleep Apnea," *ASME J. Biomech. Eng.*, **120**, pp. 416–422.
- [25] De Backer, J., Vanderveken, O., Vos, W., Devolder, A., Verhulst, S., and Verbraecken, J., 2007, "Functional Imaging Using Computational Fluid Dynamics to Predict Treatment Success of Mandibular Advancement Devices in Sleep-Disordered Breathing," *J. Biomech.*, **40**, pp. 3708–3714.
- [26] Xu, C., Sin, S., McDonough, J., Udupa, J., Guez, A., and Arens, R., 2006, "Computational Fluid Dynamics Modeling of the Upper Airway of Children With Obstructive Sleep Apnea Syndrome in Steady Flow," *J. Biomech.*, **39**, pp. 2043–2054.
- [27] Vos, W., Backer, J. D., Devolder, A., Vanderveken, O., Verhulst, S., and Salgado, R., 2007, "Correlation Between Severity of Sleep Apnea and Upper Airway Morphology Based on Advanced Anatomical and Functional Imaging," *J. Biomech.*, **40**, pp. 2207–2213.
- [28] Croce, C., Fodil, R., Durand, M., Sbirlea-Apiou, G., Caillibotte, G., and Papon, J., 2006, "In Vitro Experiments and Numerical Simulations of Airflow in Realistic Nasal Airway Geometry," *Ann. Biomed. Eng.*, **34**, pp. 997–1007.
- [29] Wen, J., Inthavong, K., Tu, J., and Wang, S., 2008, "Numerical Simulations for Detailed Airflow Dynamics in a Human Nasal Cavity," *Respir. Physiol. Neurobiol.*, **161**, pp. 125–135.
- [30] Heenan, A., Matida, E., Pollard, A., and Finlay, W., 2003, "Experimental Measurements and Computational Modeling of the Flow Field in an Idealized Human Oropharynx," *Exp. Fluids*, **35**, pp. 70–84.
- [31] Huang, Y., White, D., and Malhotra, A., 2005, "The Impact of Anatomic Manipulations on Pharyngeal Collapse: Results From a Computational Model of the Normal Human Upper Airway," *Chest*, **128**, pp. 1324–1330.
- [32] Huang, Y., White, D., and Malhotra, A., 2007, "Use of Computational Modeling to Predict Responses to Upper Airway Surgery in Obstructive Sleep Apnea," *Laryngoscope*, **117**, pp. 648–653.
- [33] Jeong, S., Kim, W., and Sung, S., 2007, "Numerical Investigation on the Flow Characteristics and Aerodynamic Force of the Upper Airway of Patient With Obstructive Sleep Apnea Using Computational Fluid Dynamics," *Med. Eng. Phys.*, **29**, pp. 637–651.
- [34] Ishikawa, S., Nakayama, T., Watanabe, M., and Matsuzawa, T., 2006, "Visualization of Flow Resistance in Physiological Nasal Respiration: Analysis of Velocity and Vorticities Using Numerical Simulation," *Arch. Otolaryngol. Head Neck Surg.*, **132**, pp. 1203–1209.
- [35] Wang, K., Denney, T., Morrison, E., and Vodyanov, V., 2005, "Numerical Simulation of Air Flow in the Human Nasal Cavity," *Conf. Proc. IEEE Eng. Med. Biol. Soc.*, **6**, pp. 5607–5610.
- [36] Patanker, S., 1980, *Numerical Heat Transfer and Fluid Flow*, Hemisphere, New York.
- [37] van Leer, B., 1977, "Towards the Ultimate Conservation Difference Scheme 4: A New Approach to Numerical Convection," *J. Comput. Phys.*, **23**, pp. 276–299.
- [38] Rhie, C., and Chow, W., 1983, "Numerical Study of the Turbulent Flow Past an Airfoil With Trailing Edge Separation," *AIAA J.*, **21**, pp. 1525–1532.
- [39] White, F., 2006, *Viscous Fluid Flow*, McGraw-Hill, Singapore.
- [40] Fox, R., McDonald, A., and Pritchard, P., 2006, *Introduction to Fluid Mechanics*, Wiley, Hoboken, NJ.
- [41] Collins, J., Shapiro, A., Kimmel, E., and Kamm, R., 1993, "The Steady Expiratory Pressure-Flow Relation in a Model Pulmonary Bifurcation," *ASME J. Biomech. Eng.*, **115**, pp. 299–305.
- [42] Isono, S., Feroah, T., Hajduk, E., Brant, R., Whitelaw, W., and Remmers, J., 1997, "Interaction of Cross-Sectional Area, Driving Pressure, and Airflow of Passive Velopharynx," *J. Appl. Physiol.*, **83**, pp. 851–859.

Flow Characteristics in a Curved Rectangular Channel With Variable Cross-Sectional Area

Avijit Bhunia

e-mail: abhunia@teledyne.com

C. L. Chen

Teledyne Scientific Company,
1049 Camino Dos Rios,
MC A10,
Thousand Oaks, CA 91360

Laminar air flow through a curved rectangular channel with a variable cross-sectional (c/s) area (diverging-converging channel) is computationally investigated. Such a flow passage is formed between the two fin walls of a 90 deg bend curved fin heat sink, used in avionics cooling. Simulations are carried out for two different configurations: (a) a curved channel with long, straight, constant c/s area inlet and outlet sections (entry and exit lengths); and (b) a short, curved channel with no entry and exit lengths. Formation of a complex 3D flow pattern and its evolution in space is studied through numerical flow visualization. Results show that a secondary motion sets in the radial direction of the curved section, which in combination with the axial (bulk) flow leads to the formation of a base vortex. In addition, under certain circumstances the axial and secondary flow separate from multiple locations on the channel walls, creating Dean vortices and separation bubbles. Velocity above which the Dean vortices appear is cast in dimensionless form as the critical Dean number, which is calculated to be 129. Investigation of the friction factor reveals that pressure drop in the channel is governed by both the curvature effect as well as the area expansion effect. For a short curved channel where area expansion effect dominates, pressure drop for developing flow can be even less than that of a straight channel. A comparison with the flow in a constant c/s area, curved channel shows that the variable c/s area channel geometry leads to a lower critical Dean number and friction factor. [DOI: 10.1115/1.3176970]

1 Introduction

With the ever increasing trend of power density of electronic devices, thermal management is becoming a growing challenge, particularly when the application platform precludes liquid cooling. Various fin structures and surface modifications have been considered in the past few decades to improve air cooling convection heat transfer, as reviewed by Garimella [1]. Certain special structure heat sinks have gained popularity in recent years, particularly for high end applications. Curved fin heat sink, such as the one shown in Fig. 1, is an example from the avionics electronics industry. Air impingement on a curved fin heat sink has also been considered for high performance computer chip cooling [2]. Flow in a curved fin heat sink is significantly more complex than in a traditional, straight fin sink. The fundamental difference arises due to the formation of secondary flow in the curved section. The secondary flow is beneficial as it alters the boundary layer formation bringing in cold fluid from the core of the channel toward the curved walls, thereby enhancing heat transfer [3]. However, curved flow passages also experience a higher pressure drop, compared with straight channels of similar length. An overall system figure of merit (FOM) of curved channel over straight channel may be defined as the ratio of heat transfer enhancement to pressure drop increase. A thermal designer strives to achieve a high FOM, where the benefit of a curved channel over a straight channel is realized by significant heat transfer enhancement without excessive rise in pressure drop. An important tool in the design process is a knowledge base on the fundamental flow and thermal characteristics in the individual curved flow passages between fins, as it forms the building block of the overall heat sink performance. Keeping this in mind we have carried out a study of air

flow through a single passage formed between two curved fins of the heat sink shown in Fig. 1. The passage has a constant c/s area straight inlet section, followed by a variable c/s area curved section (a 90 deg bend), and another constant c/s area, straight outlet section. The present paper is the first part of the study that focuses solely on the flow characteristics. The heat transfer aspects of the problem will be published in a separate article.

In a curved channel, the fluid elements are subject to centrifugal force. To balance this extra body force and the local viscous stresses, a radial (inward) pressure gradient ($\partial P/\partial r$) develops from the outer curvature wall (OCW) or the concave wall toward the inner curvature wall (ICW) or the convex wall. However, a perfect balance is not achieved over the entire c/s area. For example, within the boundary layers close to the walls, where local velocity is significantly less than the bulk fluid, the centrifugal force is weak and $\partial P/\partial r$ cannot be balanced. The local imbalance results in a radial or secondary flow from OCW to ICW. The dimensionless number characterizing flow in a curved channel is the Dean number (De), defined as $De = Re \sqrt{D_h/R}$, where Re is the Reynolds number, D_h is the channel hydraulic diameter, and R is the radius of curvature of the inner curvature wall. The structure and strength of the secondary flow depend on the channel geometry and flow velocity (V_i). Figure 2(a) shows the schematic of a typical secondary flow created as $\partial P/\partial r$ exceeds the centrifugal force within the velocity boundary layers near the top and bottom walls of the curved channel. The resulting secondary flow is from OCW to ICW near the walls, and back toward the OCW around the midheight of the channel. This is representative of a low axial channel flow (bulk) velocity condition (V_i), when only one pair of secondary flow cells develops and remains conformal to all the channel walls. Conventionally this is termed as the *main secondary flow*. With increasing V_i , as the secondary flow strengthens, it has a tendency to separate from one or more walls. For example, in the schematic of Fig. 2(b), the secondary flow detaches from the top wall (TW), attaches to the ICW, and then again detaches from the ICW. Each secondary flow separation creates a local

Contributed by the Fluids Engineering Division of ASME for publication in the JOURNAL OF FLUIDS ENGINEERING. Manuscript received September 10, 2008; final manuscript received May 29, 2009; published online August 13, 2009. Assoc. Editor: Rajat Mittal. Paper presented at the 2008 ASME International Mechanical Engineering Congress (IMECE2008), Boston, MA, October 31–November 6, 2008.

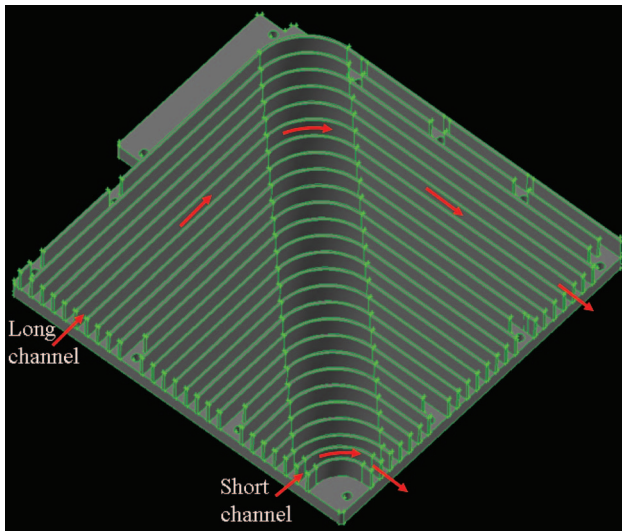


Fig. 1 A schematic of curved fin heat sink. Representative air flow paths between two sets of fins are shown by red arrows.

recirculation cell as shown in Fig. 2(c). For higher velocity conditions, in addition to the main secondary flow, multiple secondary flow structures are formed, commonly known as *Dean vortices*, after the first analysis by Dean [4]. The nondimensional number characterizing the onset of Dean vortices is called the critical Dean number (De_{crit}).

The curved channel/duct flow is widely encountered in many engineering applications, such as bent tube heat exchangers, turbine blades, air conditioning ducts, the condenser area of solar collector heat pipes, passages in biological systems, etc. A significant amount of prior research has investigated the flow and thermal fields of a curved channel. Since this article focuses on the flow characteristics, we only cite the flow related literature for the sake of brevity. Cheng et al. [5] experimentally visualized the secondary flow pattern in curved rectangular channels, 25 mm wide (b), curvature ratio (CR) of 5, and the aspect ratio (AR) varying between 1 and 12. CR is defined as the ratio of radius of curvature (R) and the channel width (b), while AR is the ratio of channel height (H) and width (b). Sugiyama et al. [6] reported flow visualization at the end of 180 deg turn in channels, 20 mm wide, CR varying between 5 and 8, and AR varying from 0.5 to 2.5. Ligrani and Niver [7] experimented with a nearly 2D channel ($AR=40$) for De varying between 40 and 220, and showed the formation of secondary flow patterns at various angular positions along the curved section. Effort on the numerical front dates back to the early 80s. Cheng and Akiyama [8] reported a 2D model of fully developed laminar flow entering a curved rectangular channel, while Ghia and Sohkey [9] and Humphrey et al. [10] investigated the developing flow. In these calculations, AR varied in the range of 0.2–5, and De was limited to ~ 100 . Hwang and Chao [11] investigated fully developed laminar flow in a curved square duct under isothermal condition. More recently, Chandratilleke and Nursubyakto [12] presented a 3D computational model of flow through a curved rectangular channel with uniform heating at the outer (concave) wall. They considered parametric ranges of $1 \leq AR \leq 8$ and $20 \leq De \leq 500$, and included the effect of buoyancy. To summarize the findings of these research works—The De_{crit} value; the main secondary flow and the Dean vortices (for $De > De_{crit}$ condition) all depend on several geometric and thermal conditions, such as the channels, (AR) and (CR) location along the curved section and the wall heating pattern.

In spite of 3 decades of research, most prior works report flow pattern at a specific cross section. Literature on the evolution of multiple vortices in a curved channel remains scarce. In an experi-

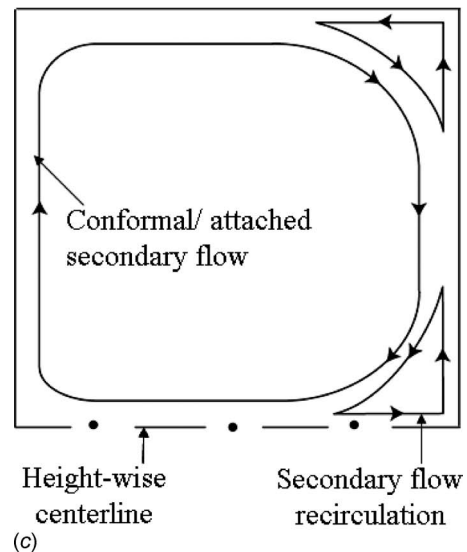
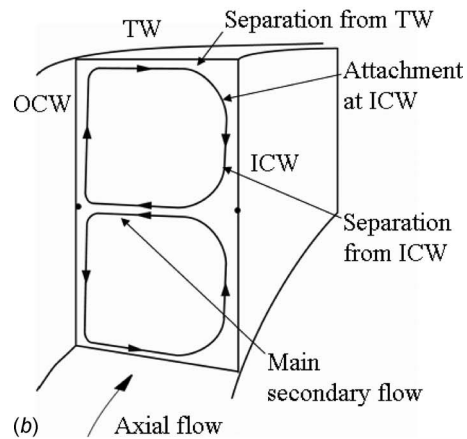
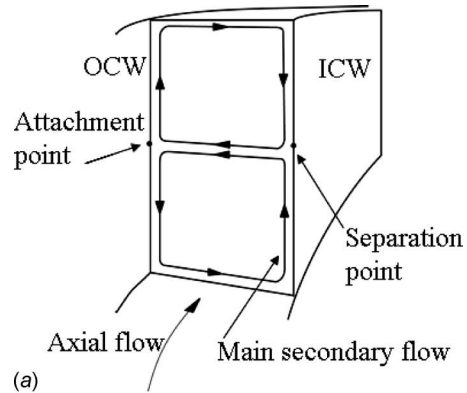


Fig. 2 Schematics of secondary flow structures in a curved channel. (a) Secondary flow conformal to all the walls occurs at low axial flow velocity (V_p), (b) secondary flow separation from multiple walls at higher V_p , and (c) main/base secondary flow and additional recirculation cells due to secondary flow separation.

mental approach, this needs detailed flow visualization at multiple cross sections, such as in Ref. [7], which is quite challenging. On the other hand, a computational model to resolve such complicated 3D flow pattern is extremely grid sensitive. Furthermore, all the curved channel flow works carried out so far consider constant c/s area only. The present work focuses on a variable c/s area curved channel, where the flow is governed by a combination of

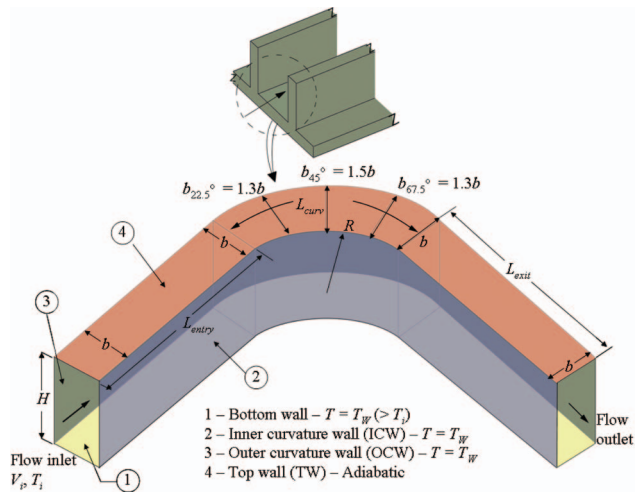


Fig. 3 Schematic of an individual flow passage between two fins, a long channel, and the numerical simulation domain

variable channel geometry and curvature effect. Motivation arises from the practical application platform shown in Fig. 1.

We developed a 3D computational model of laminar air flow through a 90 deg bend of a variable c/s area curved channel where the channel area varies along the curvature length. The channel c/s area at the curvature inlet and outlet are the same. In between, the channel width (b) first increases along the length of curvature up to the 45 deg angular position and then decreases, making it a diverging-converging curved channel. In this article we present only the flow characteristics part of the study. The primary focus is on elucidation of the flow field, i.e., understanding the interaction between the secondary flow and the axial (bulk) flow, the resulting vortices and their evolution in space. At this stage we are not conducting a parametric study of the several important geometric features, such as variable c/s area ratio, (CR), (AR), channel length, etc., that govern the flow field. Therefore, geometry is maintained constant in this study, specific to the heat sink (Fig. 1). Simulations are carried out for two configurations: (a) a diverging-converging curved channel with long, straight, constant c/s area inlet and outlet sections (entry and exit lengths); and (b) a diverging-converging curved channel with no entry or exit length, respectively, marked as the long and short channels in Fig. 1. The formation, evolution, and dynamics of multiple vortices are investigated, along with the critical Dean number and the channel pressure drop. Comparisons between the variable and constant c/s area channels are presented.

2 Physical Model

Figure 3 shows a schematic of the air flow path in the long channel. The flow passage consists of three segments: (a) a straight, constant c/s area inlet section of length L_{entry} ; (b) a 90 deg bend, a variable c/s area curved section of length L_{curv} (along the middle of the cross section); and (c) another straight, constant c/s area exit section of length L_{exit} . For a short channel there are no entry and exit lengths ($L_{entry}=L_{exit}=0$). Flow directly enters the variable c/s area curved section and leaves to the ambient at the end of the channel. For both the long and short channels, the channel height (H) remains constant. In the curved section, the channel width first increases along the length of curvature, up to an angular position of 45 deg and then decreases between the 45 deg and 90 deg position, making it a diverging-converging curved channel. Width at the channel inlet and the inlet to the curved section are b , which increases to $1.3b$ at the 22.5 deg angular position, to a maximum of $1.5b$ at the 45 deg angular position, and then back to b at the exit of the curved section. Channel width at

the inlet section (b) is used for calculating all the geometric parameters such as hydraulic diameter (D_h), (AR), and (CR).

For both the long and short channels, air at temperature T_i enters the channel at a uniform flow velocity of V_i . Ambient pressure boundary condition is specified at the channel exit. The channel bottom and the side walls are maintained at a constant temperature of T_w ($T_w > T_i$). The isothermal side wall assumption essentially means that the fins of the heat sink (shown in Fig. 1) are 100% efficient. Indeed a computational model of the entire heat sink (made of aluminum) shows that the fins are close to 99% efficient. In a practical avionics application, often the top of the fins is covered by a plate to avoid flow bypass. To simulate this condition the top channel wall is assumed adiabatic.

The two critical dimensionless flow parameters are the Reynolds number $Re=V_i D_h/\nu$ and the Dean number $De=Re\sqrt{D_h/R}$. V_i values are chosen on the basis of a practical range of air flow rates used in the heat sink. Air properties at average temperature $[T_{av}=(T_i+T_w)/2]$ are used to report these numbers. Re and De vary between the range of 183 to 1017 and 92 to 1008, respectively. The last air flow passage, having a length ($L_{av}/D_h=L_{curv}/D_h$) of 6.8, represents one asymptotic condition where uniform flow directly enters the curved section. Therefore, it is picked as the “short channel” in this study. However, the other asymptotic condition of fully developed flow entering the curved section does not occur for any of the channels of this heat sink. The dimensionless entry length (L_{fd}/D_h) for fully developed flow in a constant c/s area straight channel of AR close to 2 is $\sim 0.02 Re$ [13]. At the highest velocity condition of $Re=2017$, L_{fd}/D_h is ≈ 40 . Not even the longest air flow passage of the heat sink, shown in Fig. 1, has this much entry length. In other words for $Re=2017$, $L_{entry} < L_{fd}$ for all channels. Instead of focusing on the ideal asymptotic condition, we use the current heat sink geometry and arbitrarily pick a “long channel” having an overall average length of $L_{av}/D_h=39.1$ ($L_{av}=L_{entry}+L_{curv}+L_{exit}$), with $L_{entry}/D_h=16.1$ and $L_{exit}/D_h=16.1$. Flow entering the curved section of the chosen long channel is fully developed for $Re \leq 805$. Above this value, the flow enters the curved section in partially developed state. Clearly if a different channel were chosen as the “long channel,” magnitudes of the flow and thermal parameters would be different. However, since this study is not intended to be a parametric study of the geometric features, such as L_{entry}/D_h , L_{curv}/D_h , L_{exit}/D_h , CR , AR , etc., the specific values are not so important. The primary objective here is to understand the complex flow field for a given geometry. Therefore, for both the long and short channels, the channel geometry is kept constant, with $D_h=0.007$ m, $b_{max}/b=1.5$, $AR=2.3$, and $CR=5.6$; and the L_{entry}/D_h , L_{curv}/D_h , and L_{exit}/D_h values discussed above.

3 Numerical Simulation

Steady, laminar air flow through the passages are computationally simulated using the commercial computational fluid dynamics (CFD) code FLUENT. The continuity, momentum, and energy equations are solved. These equations are coupled due to the use of temperature dependent air properties. Some of the underlying assumptions and observations are as follows.

- (1) Even though all the features of solving compressible flow are considered, the flow is essentially incompressible. The Mach number (Ma) based on the highest inlet velocity (V_i) is 0.015.
- (2) The value of Gr/Re^2 is $\sim 9 \times 10^{-7}$ for the lowest flow velocity condition, where Gr is the Grashof number. Therefore, buoyancy effects are neglected. It may be argued that the local velocity at any point in the channel could be significantly lower than V_i . Therefore, if the above ratio is calculated with Re value based on the local velocity, the Gr/Re^2 ratio can actually become orders of magnitude higher. To address this concern, we carried out a calculation

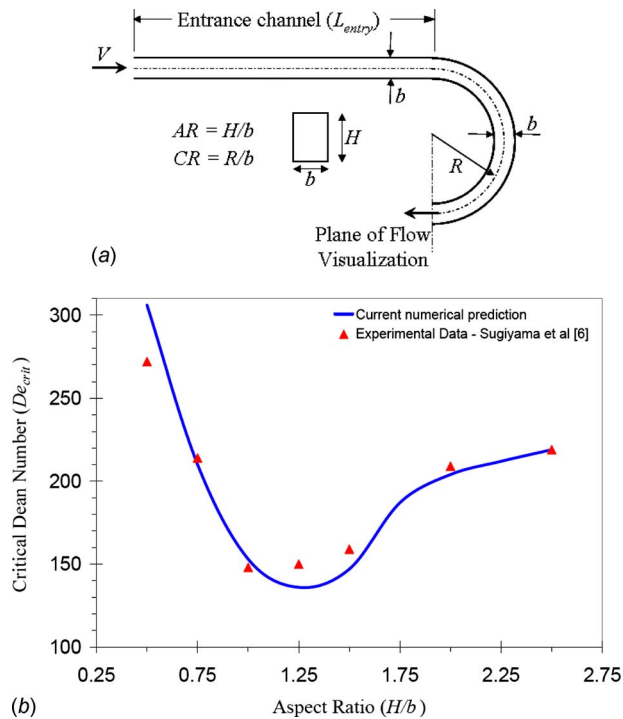


Fig. 4 Validation of the numerical model against the experimental data of Sugiyama et al. [6]. (a) Schematic of the experimental channel geometry—constant cross-sectional area curved channel with a 180 deg bend. $L_{\text{entry}}=1000$ mm, $b=20$ mm, $CR=R/b=5$, and H and $AR=H/b$ variable; (b) comparison of numerical prediction of the critical Dean number (De_{crit}) with the experimental data [6].

at the lowest velocity condition, with the buoyancy effect on. The results showed no significant difference with or without buoyancy.

- (3) The viscous dissipation term is neglected in the energy equation as the Brinkman number ($Br = \mu V_i^2 / k_f [T_w - T_i]$) is $\sim 3 \times 10^{-4}$.
- (4) Temperature dependent air properties are used. For example, (a) density (ρ)—a linear function, (b) thermal conductivity (k_f)—a linear function, and (c) viscosity (μ)—Power law— $\mu/\mu_o = (T/T_o)^{2/3}$, where μ_o and T_o are 1.716×10^{-5} kg/m s and 273 K, respectively.

A coupled pressure velocity solver algorithm is used for a robust and efficient solution. The first few iterations are run using SIMPLE algorithm, results of which are used as the initial guess for the coupled solver. A Courant number value between 10 and 20 is used to stabilize the convergence behavior. The convection terms in the momentum and energy equations are discretized using a second order UPWIND scheme. For the pressure term, the PRESTO scheme is used, recommended for flow with strongly curved domains. Further details on the numerical scheme are available in the FLUENT manual [14].

4 Validation of the Numerical Methodology

The accuracy of the numerical procedure is ascertained by validating the model against existing experimental data from literature. For this purpose, a computational model is developed with channel geometry replicating the experimental set up of Sugiyama et al. [6]. Isothermal air flow through a constant c/s area 180 deg bend, as shown in Fig. 4(a), is considered. In the model, a uniform velocity is prescribed at the inlet of the straight entry section (L_{entry}), whereas an ambient pressure outlet boundary condition is specified at the end of the 180 deg bend. Sugiyama et al. [6]

carried out a flow visualization study at the end of the bend and reported the critical Dean numbers (De_{crit}) for the onset of Dean vortices for various channel aspect ratio ($AR=H/b$) and curvature ratio ($CR=R/b$) values. Figure 4(b) shows a comparison of the predicted values from our computational model with the experimental data, for a constant CR value of 5. Note that this CR value is very close to the variable c/s area curved channel geometry investigated in this article ($CR=5.6$). This experimental paper calculated De based on channel width (b), i.e., $De=Re \sqrt{(b/R)}$, even though Re is calculated based on D_h ($Re=V_i D_h / \nu$). We report De based on D_h , i.e., $De=Re \sqrt{(D_h/R)}$. However, for the sake of the present comparison, just for this section (Fig. 4(b)), we follow their procedure. An excellent agreement between the prediction and experimental data in Fig. 4(b), for the entire range of AR values, lends significant confidence about the present computational model.

5 Results and Discussion

Prior to discussing the specific results, we start with outlining a few basic conceptual points. There are only two fundamental flow mechanisms in a curved channel: (a) the *axial or bulk flow*, i.e., the original flow component, and (b) the *secondary flow*, i.e., the created component at the curved section. The secondary flow may perfectly follow all the channel wall contours as shown in the schematic of Fig. 2(a). Or it may separate from the channel walls at multiple locations, creating a main/base secondary flow and additional recirculation cells (Fig. 2(c)). Similarly, depending on the channel geometry and flow condition, the axial flow may also separate from a channel wall, causing local axial flow reversal. Between these two basic mechanisms, a total of four different combinations are possible toward the evolution of multiple complex 3D flow structures:

- (A) forward moving axial flow and conformal secondary flow following the channel walls (fully conformal or over a certain portion of a channel wall)
- (B) axial flow reversal and conformal secondary flow
- (C) forward moving axial flow, and secondary flow separation
- (D) both axial and secondary flow separation and reversal

The following acronyms will be used for sake of convenience: (a) constant c/s area straight channel (CASC), (b) constant c/s area curved channel (CACC), and (c) variable c/s area curved channel (VACC).

6 Grid Independence Study

A grid independent numerical solution has to resolve the flow-thermal characteristics of the overall channel as well as all the secondary recirculation cells, at the highest flow rate condition. The following parameters are used to quantify the secondary flow structures at two angular positions, 45 deg and 90 deg: (a) the total number of cells (N_{cells}) at that c/s area, (b) minimum helicity (H_{min}), and (c) the dimensionless maximum velocity at that c/s (e.g., cross-sectional $V_{\text{max}} \text{ at } 45/V_i$). In addition, two points A and B are chosen, respectively, at the 45 deg and 90 deg angular positions located at the core of the recirculating flow region. The local dimensionless velocity (such as V_A/V_i), and temperature (such as $\theta_A = [T_A - T_i] / [T_w - T_i]$) are investigated at these points. Four other dimensionless parameters are used to characterize the overall channel transport fields. They are: the maximum velocity at the exit ($V_{\text{max, outlet}}/V_i$) of the long channel, the overall channel pressure drop ($2\Delta P / \rho V_i^2$), the average fluid exit temperature ($\theta_{\text{exit}} = [T_{\text{av, exit}} - T_i] / [T_w - T_i]$), and the Nusselt number ($Nu_o = h_o D_h / k_f$), characterizing the total heat transfer from the channel. Values of these local and global parameters, obtained from computational simulations with four different grid sizes, are presented in Table 1. Based on the comparison, a 351,000 cell grid is chosen

Table 1 Grid independence study for a long VACC for the highest flow velocity condition. $Re=2017$ and $De=1008$ based on uniform flow velocity (V_i) and hydraulic diameter (D_h) at channel inlet and properties at average temperature [$T_{av}=(T_i+T_w)/2$]. $AR=2.3$, $CR=5.6$, $L_{av}/D_h=39.1$, $L_{entry}/D_h=16.1$, and $L_{exit}/D_h=16.1$. Location of point A: axial location—on the 45 deg angular position from the start of the curvature, height—at $H/2$, and lateral—at $b_{45 \text{ deg}}/4$ closer to the ICW. Location of point B: axial location—on the 90 deg angular position; height and lateral location—at the geometric center of the curvature outlet plane.

Flow-thermal characteristics	Grid size (No. of cells)			
	126,720	230,400	351,000	620,880
At 45 deg angular position				
No. of recirculation cells (N_{cells})	2	2	6	6
Min. helicity (H_{min}) in m/s^2	44,027	51,280	51,686	52,079
Max. dimensionless velocity (V_{max}/V_i)	1.42	1.45	1.45	1.45
Dimensionless velocity at A (V_A/V_i)	0.17	0.08	0.10	0.09
Dimensionless temperature at A (θ_A)	0.78	0.79	0.88	0.82
At 90 deg angular position				
No. of recirculation cells (N_{cells})	6	6	6	6
Min. helicity (H_{min}) in m/s^2	24,775	28,313	28,610	28,776
Max. dimensionless velocity (V_{max}/V_i)	1.62	1.64	1.64	1.65
Dimensionless velocity at B (V_B/V_i)	1.30	1.35	1.35	1.37
Dimensionless temperature at B (θ_B)	0.31	0.32	0.32	0.31
At channel outlet				
Max. dimensionless velocity (V_{max}/V_i)	1.77	1.82	1.85	1.85
Av. dimensionless temperature θ_{av}	0.61	0.62	0.62	0.62
Dimensionless overall channel pressure drop= $2\Delta P/\rho V_i^2$	2.97	2.99	3.03	3.04
Dimensionless heat transfer coefficient (Nu_c) based on total heat transfer from the channel	5.90	6.03	6.09	6.10

for all calculations on the long VACC. Similar grid independence studies are carried out for other geometries. The optimal grid size for a long CACC is also 351,000. For short channels (both CACC and VACC) a 65,600 cell grid is used.

7 Long CACC: Flow in the Curved Section

As the channel geometry plays a pivotal role in the flow dynamics, it is useful to decouple the effect of variable c/s area first. Therefore, we start with investigating flow through a 90 deg bend of a long CACC (with entry and exit lengths). The channel geometry matches the schematic in Fig. 3, except for the fact that channel width (b) remains constant through the curved section. These results serve as the baseline case for comparison with those of variable c/s area curved channel. Even though flow through CACC has been widely investigated in the past, studies focusing on the space evolution of the flow structures remain scarce.

To follow the complex 3D secondary flow pattern, we investigate the cross-sectional view of the secondary flow, i.e., the in-plane velocity vectors, at various angular positions (Figs. 5(a)–5(e)), in conjunction with the oil flow path lines on the ICW, OCW, and TW (Figs. 6(a)–6(c), respectively). The in-plane velocity vector plots are color coded by dimensionless local velocity magnitude (=local velocity (V)/uniform channel inlet velocity (V_i)). Since the flow is symmetric (heightwise), in Fig. 5 the computational results are shown in only half the c/s , while the other half is used for explanatory schematics. The oil flow lines are plotted by releasing particles from the same curved section walls (ICW, OCW, or TW) on which the flow is visualized. The lines are color coded with particle ID. Thus the color codes do not have any physical significance as such. To retain the clarity of the oil flow line plots, various markings are shown on a separate, identical plot below each figure.

The secondary flow sets in immediately after the fluid elements enter the curved section. This secondary flow along with the forward moving axial flow, i.e., combination A, creates a pair of *base vortices*, at the top and bottom portion of the channel. The traces of base vortices in the oil flow lines plot (Fig. 6) indicate that they travel through the entire length of the curved section (0–90 deg angular position), although their shape and size change along the path. At the early portion of the curved section, the secondary flow is fully conformal to the channel walls, as in Fig. 2(a). There-

fore a pair of base vortices covers the entire c/s area of the channel, as seen in Fig. 5(a) for an angular position of 11 deg. Flow from the upper and lower base vortices collide and separate from the ICW and attach to the OCW, both around midheight, respectively, forming separation line S_1 in Fig. 6(a), and attachment line A_1 in Fig. 6(b).

Further downstream, the secondary flow starts to separate from the walls, in the corner regions between ICW, and the top and bottom walls. As the inset of Fig. 5(b) shows, the secondary flow separates from the TW and attaches to the ICW, forming a local recirculation similar to that shown in the schematic of Fig. 2(c). The oil flow lines in Fig. 6(c) indicate that the separation from TW starts at an angular position P_1 , just before the 22.5 deg location. This local, corner region, secondary flow recirculation can be traced along separation line S_2 on TW (Fig. 6(c)) and attachment line A_2 on ICW (Fig. 6(a)), both continuing all the way to the end of the curved section. This secondary flow reversal, along with the forward moving axial flow (combination B) leads to the formation of another local vortex. Since this is in addition to the base vortex, following the traditional definition, it is categorized as a Dean vortex. We name it the *corner region Dean vortex*.

The oil flow lines in the inset of Fig. 6(a) show another interesting aspect of the corner region flow. Between the angular positions P_2 and P_3 , the oil flow lines are backward and upwards. The backward axial flow can also be seen from the insets B and C of Fig. 6(c). This indicates an axial as well as secondary flow separation in the region, or combination D, that leads to the formation of a closed separation bubble. Figure 7(a) shows a schematic of this corner region axial and secondary flow separation, and the formation of the separation bubble. The corner region Dean vortex bypasses this separation region by detaching from the ICW, squeezing toward the separation line S_2 , and then coming back to the ICW beyond the separation region.

After attaching to the ICW along attachment line A_2 , the secondary flow follows the wall contour for a while, flowing toward the centerline (heightwise). However, before reaching the centerline it bounces off the ICW, causing another local secondary flow separation and flow reversal, as sketched in Fig. 2(b). The trace of this separation line S_3 in Fig. 6(a), and Fig. 5(c) indicates that this flow separation starts just upstream of the 34 deg position and increases in size along the curved path (follow Figs. 5(c)–5(e)).

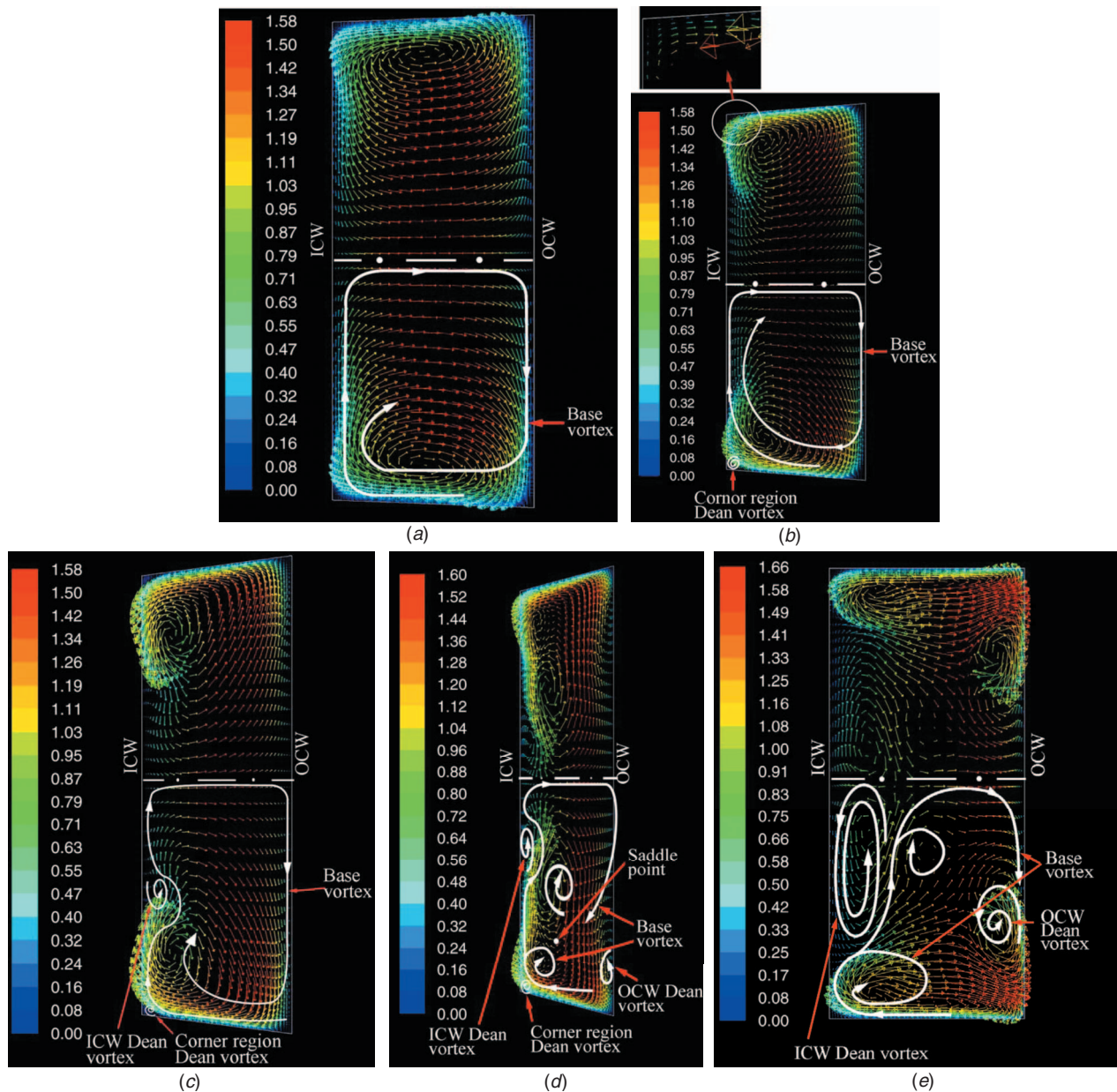


Fig. 5 Formation of secondary flow at various angular positions along a 90 deg bend of a long CACC. $Re=2017$ and $De=1008$ based on uniform flow velocity (V_i) and hydraulic diameter (D_h) at channel inlet, and properties at average temperature [$T_{av} = (T_i + T_w)/2$]. $L_{av}/D_h=39.1$, $L_{entry}/D_h=16.1$, $L_{exit}/D_h=16.1$, $AR=2.3$, and $CR=5.6$. Views: (a) angular position 11 deg, (b) 22.5 deg, (c) 37 deg, (d) 56 deg, and (e) 90 deg (outlet from the curved portion of the channel or beginning of the straight constant c/s area exit channel).

The angular position where this separation started cannot be precisely located from the current data. We tentatively identify an angular position P_4 . Coupled with the forward moving axial flow this secondary flow separation (Combination B) leads to the formation of another Dean vortex, which we term as the *ICW Dean vortex*. Flow from the top and bottom ICW Dean vortices meet at the heightwise centerline of ICW. Thus, beyond the angular position P_4 , the ICW centerline becomes an attachment line A_3 (Fig. 6(a)).

A comparison of Figs. 5(a)–5(e) shows that as the flow moves downstream, the return secondary flow (from ICW back toward OCW) gets stronger. As a result the location of the highest velocity in the channel shifts toward the OCW and the velocity boundary layer there gets thinner. An abrupt drop in the centrifugal force occurs across this thin boundary layer near the OCW. At some location between the 45 deg and 56 deg angular position, it causes

another separation of the secondary flow, this time from the OCW. A local flow reversal follows, as seen in Figs. 5(d) and 5(e). This along with the forward moving axial flow (combination B) creates the third pair of Dean vortices in the channel, now termed as the *OCW Dean vortex*. It is bounded by the separation line S_4 and attachment line A_4 in the oil flow lines of Fig. 6(b).

Figures 5(d) and 5(e) show an additional pair of recirculation cells inside the c/s , adjacent to the base vortex. Following the conventional definition, this should be another Dean vortex. The origin of this vortex is not clear. It is possible that this vortex arises from a local split of the base vortex, somewhere downstream of the 45 deg angular position. This Dean vortex weakens (shrinks in size) and gradually shifts toward the center of the channel in the downstream direction.

To summarize, Fig. 7(b) shows a schematic of the base vortex and all the Dean vortices in the top half of the channel, close to

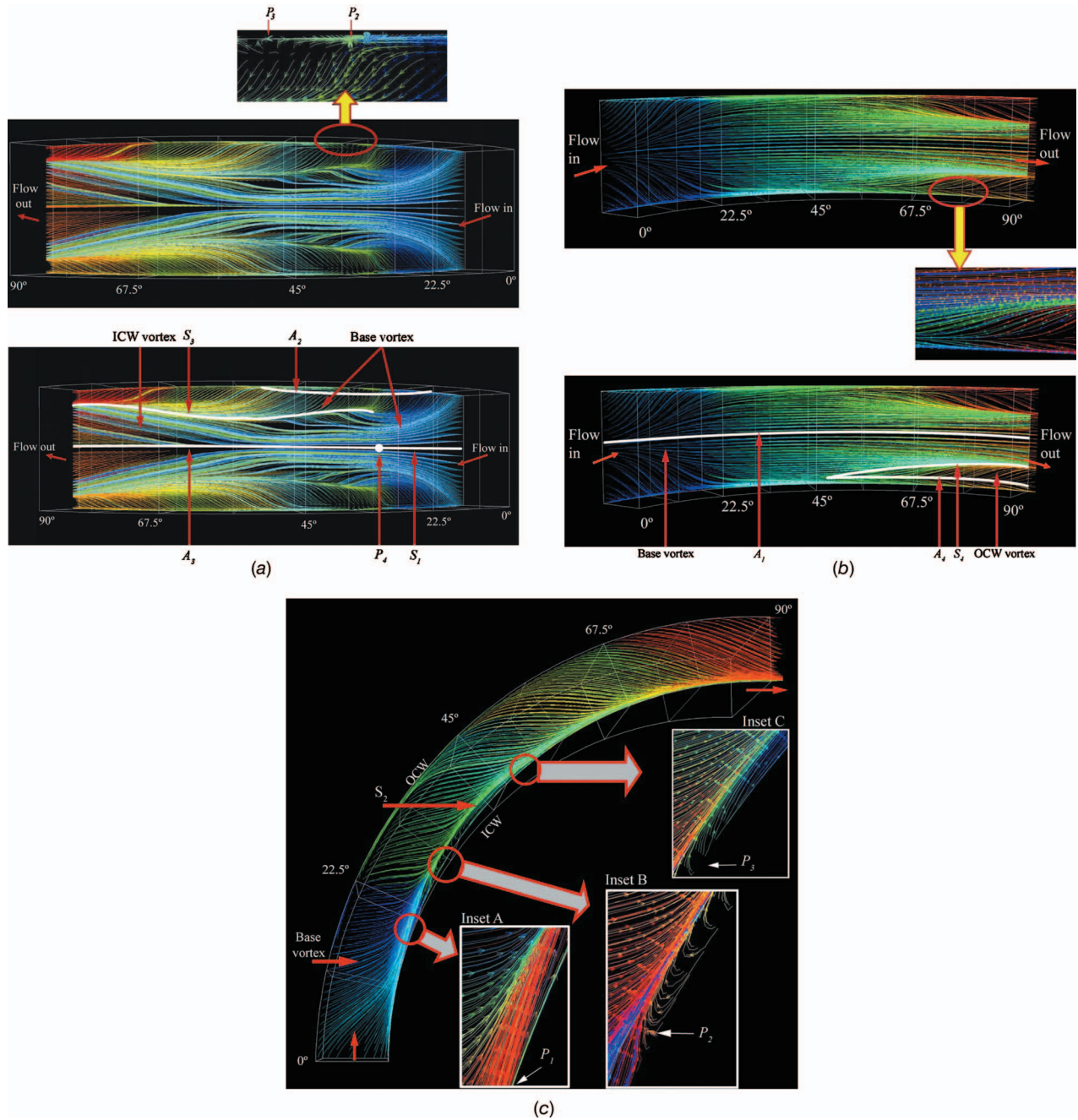


Fig. 6 Oil flow lines on the walls of the curved section (90 deg bend) of a long CACC. $Re=2017$ and $De=1008$, $L_{av}/D_h=39.1$, $L_{entry}/D_h=16.1$, $L_{exit}/D_h=16.1$, $AR=2.3$, and $CR=5.6$. (a) ICW or concave wall, (b) OCW or convex wall, and (c) TW. All views are looking into the wall from front.

the curvature exit. The origin of the multiple vortices and their evolution in space are also summarized in Table 2.

8 Long VACC: Flow in the Curved Section

With a basic understanding of the flow dynamics in the CACC, we now investigate the effect of the variable c/s area. Once again we consider the in-plane velocity vector plots at various angular positions (Fig. 8) in conjunction with the oil flow lines on the ICW, OCW, and TW (Figs. 9(a)–9(c), respectively). A slight asymmetry between the top and bottom of the channel arises due to the difference in thermal boundary conditions. The top wall is insulated while the bottom is isothermal, ($T_w > T_i$), and temperature-dependent properties are used. It is interesting to note that even though the exact same set of boundary conditions was

used for the CACC, there was no asymmetry. Clearly the temperature dependent property effect is more pronounced for the decelerating flow in the diverging section. Since our focus is on understanding the overall flow field, for all practical purposes we will ignore the slight asymmetry in the subsequent discussions.

The main/base secondary flow at the early part of the channel (close to the curvature entry) is very similar as before. Fully conformal secondary flow, in conjunction with the forward moving axial flow (combination A), creates a pair of *base vortices* at the top and bottom half of the channel (Fig. 8(a)). They meet at separation line S_1 on ICW (Fig. 9(a)) and attachment line A_1 on OCW (Fig. 9(b)). As before, the secondary flow separates from the corner regions between the ICW and the top and bottom walls somewhere between the 11 deg and 22.5 deg angular position (Point P_1

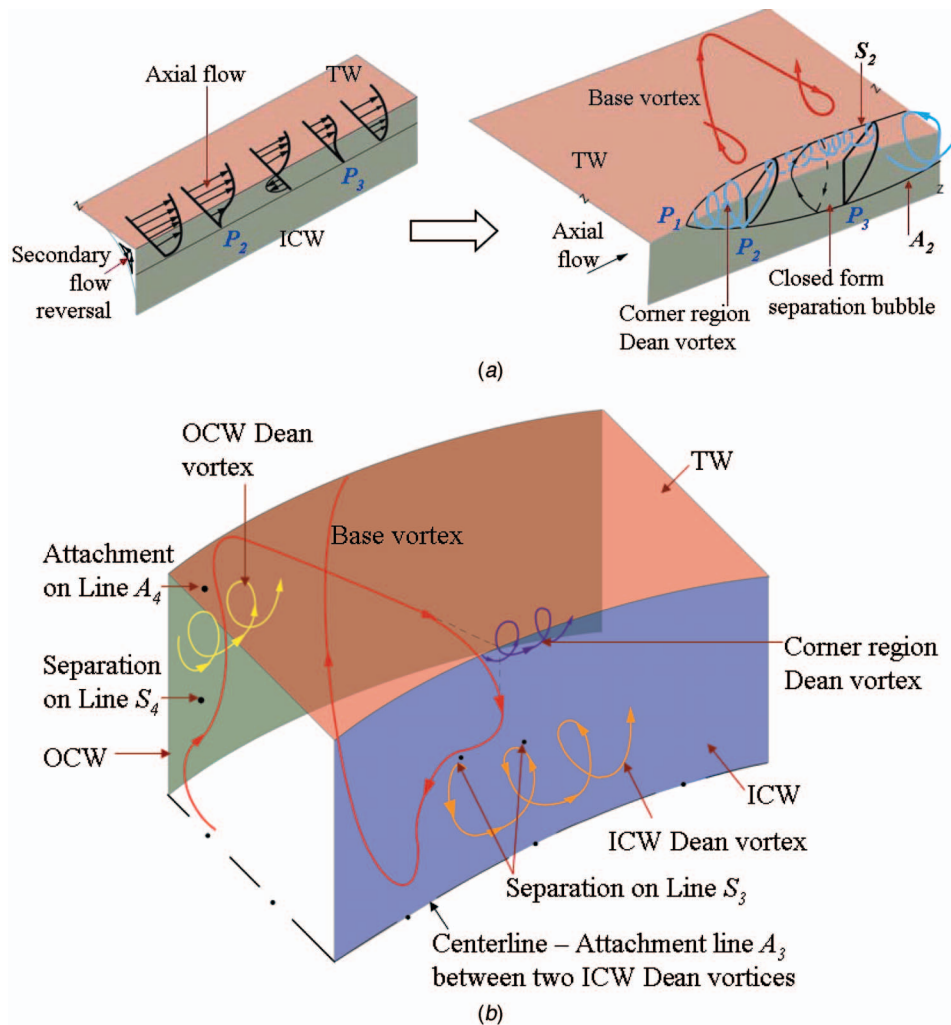


Fig. 7 Schematics of various 3D flow patterns in the curved section (90 deg bend) of a long CACC. $Re=2017$ and $De=1008$, $L_{av}/D_h=39.1$, $L_{entry}/D_h=16.1$, $L_{exit}/D_h=16.1$, $AR=2.3$, and $CR=5.6$. (a) Axial flow separation from ICW near the corner region and formation of a separation bubble, and (b) base vortex and other Dean vortices, such as corner region Dean vortex, ICW Dean vortex, and OCW Dean vortex.

in Fig. 9(c)) and follows separation line S_2 all the way to the end of the curved section. Between positions P_2 and P_3 (inset A of Figs. 9(a) and 9(c)), the axial flow also separates. The overall flow field in the corner region consists of the corner region Dean vortex and a *separation bubble*, similar to that sketched in Fig. 7(a).

Flow in the diverging section of the VACC, i.e., between the angular positions 0–45 deg, is significantly different from that of the CACC. The first noticeable effect of the variable c/s area is near the OCW, just after the flow enters the curved section. The inset of Fig. 9(b) shows that at the top half of the channel some of the oil flow lines are upwards and backward. The upward flow is indicative of conformal secondary flow at OCW, while the backward flow is due to axial flow separation. The separated axial flow and the conformal secondary flow lead to combination C, which leads to the formation of a *base vortex*, but of a different structure. Figure 10(a) shows a sketch of this base vortex structure. Figure 9(b) shows that the axial flow separation initially starts near the top and bottom walls, and gradually expands toward the center (angular position P_4), along the separation line S_3 . From the angular position of P_5 on the centerline, the axial flow starts to reattach to the wall along attachment line A_2 . The reattachment is triggered by separation of the axial flow from the ICW (discussed later), which pushes the fluid back toward the OCW.

In Fig. 9(a), two angular positions P_6 and P_7 are identified on the ICW. Between these two points, a series of oil flow lines originate from the centerline and flow backward and toward the top and bottom of the channel. This is a result of both the secondary and axial flow separation from ICW, along separation line S_4 . The axial and secondary flow separation, or combination D, leads to the formation of a *closed separation bubble near ICW* that extends from just before the 22.5 deg position to angular position P_7 , just after the 45 deg location. Figures 8(b) shows the presence of this separation bubble near ICW. The separation bubbles at the top and bottom of the channel are not symmetric heightwise. This is due to asymmetry in the boundary condition, discussed earlier. Flow from the two separation bubbles at the top and bottom of the channel forms attachment line A_3 on ICW (Fig. 9(a)), which significantly deviates from the midheight centerline. The oil flow lines in Fig. 9(a) show that the flow structure within this separation bubble is extremely complicated. Apparently there are multiple recirculation cells within the separation bubble. Figure 10(b) shows a schematic of the separation, based on the preliminary interpretation of these oil flow lines.

Another noticeable difference between the CACC and VACC is the pattern of secondary flow near OCW, particularly in the converging section (45–90 deg). In the CACC, the secondary flow

Table 2 Summary of flow pattern along the 90 deg bend of two long curved channels, (a) CACC and (b) VACC. $Re=2017$ and $De=1008$, $AR=2.3$, $CR=5.6$, $L_{av}/D_h=39.1$, $L_{entry}/D_h=16.1$, and $L_{exit}/D_h=16.1$.

	Angular Positions			
	0° – 22.5°	22.5° – 45°	45° – 67.5°	67.5° – 90°
Long, constant c/s area curved channel (CACC)	Base vortex			
	Corner region Dean vortex			
		Corner region separation bubble near ICW		Additional Dean vortex at the middle of c/s
		ICW Dean vortex		
				OCW Dean vortex
Long, variable c/s area curved channel (VACC)	Base vortex			
	Corner region Dean vortex			
		Axial flow separation at OCW		
		Corner region separation bubble near ICW		
		ICW separation bubble		
			Split base vortex	
		ICW Dean vortex		
			OCW Dean vortex	

from OCW to ICW was triggered by an imbalance in the radial pressure gradient ($\partial P/\partial r$) within the boundary layers near the top and bottom of the channel. As a result, the secondary flow from OCW to ICW occurred predominantly within this boundary layer and the flow returned to OCW over rest or most of the c/s area. On the other hand for a VACC, the continually changing geometry along the length introduces an inherent radial velocity component toward ICW. As a result, the secondary flow from OCW to ICW occurs over the entire channel height (see Figs. 8(c)–8(e) and compare with Figs. 5(d) and 5(e)). An additional pressure gradient from the top and bottom of the channel toward the center is also formed near OCW ($\partial P/\partial z$). The combined effect of these two pressure gradients is a split of the secondary flow into two streams, shown in Figs. 8(c)–8(e). One remains confined close to the top or bottom wall, similar to the traditional base vortex discussed for CACC. The other branch flows over the rest of the c/s area toward ICW. This part of the secondary flow leads to the formation of another vortex shown in the schematic of Fig. 10(c). Since this vortex arises from a conformal secondary flow, it is not a Dean vortex. We name it *split base vortex*. The branch-off starts somewhere between the 45 deg and the 56 deg location, generating a separation line S_5 on OCW (Fig. 9(b)). Therefore the mid-height centerline of OCW must transition from an attachment line A_1 in the diverging section to a separation line S_6 in the converging section. Although the position of this transition cannot be precisely located from the current data, we tentatively mark a point P_8 in Fig. 9(b), the angular position of which is coincident with the inception of S_5 .

The axial flow encounters a favorable pressure gradient in the converging section and reattaches to the ICW at angular position P_7 , just after the 45 deg location. The split base vortex starts to form around the same location. The split base vortices from the top and bottom of the channel meet at attachment line A_3 , around the midheight centerline. The structure of the *ICW and OCW Dean vortices* appear very similar to those in the CACC, with a few exceptions. Unlike CACC where the ICW Dean vortices form early in the curved channel, in VACC they appear only near 56 deg angular position. It is sandwiched between the split base vor-

tex and the base vortex, within the boundaries of attachment line A_4 and separation line S_7 . The onset of the OCW vortex is also delayed (beyond 79 deg) due to the existence of split base vortex, unlike CACC where the OCW vortex appears just after the 45 deg angular position. Along the outer curvature wall, since the flow direction of OCW vortex is similar to that of split base vortex, there is no additional attachment or separation line on OCW (other than S_5) due to this Dean vortex. This is another noticeable difference with CACC (compare Fig. 9(b) with Fig. 6(b)).

The evolution of the complex flow structures in a VACC and its difference with CACC are summarized in Table 2. Before closing this discussion, it is important to re-emphasize that some features of the complex flow structures is not yet well understood. Further studies are much needed to shed light on those aspects.

9 Long VACC: Effect of Flow Velocity

The in-plane velocity vector plots in Figs. 11(a)–11(c), and Fig. 8(e) show the secondary flow structures at the outlet of the curved section (90 deg angular position) of a VACC, for various inlet flow velocity (V_i) conditions. As before, these vector plots are color coded by the dimensionless velocity (local velocity V/V_i). At the lowest inlet velocity condition of $Re=183$ and $De=91.5$ (Fig. 11(a)), only the base vortex appears, characterized by a pair of counter-rotating, recirculating cells covering the entire c/s area of the channel. With increasing axial flow rate (thus Re and De) as the boundary layer thickness decreases, the secondary flow from OCW to ICW, and thus the base vortex, gets confined toward the top and bottom walls, as seen in Figs. 11(b) and 11(c). The thinner boundary layer also progressively lowers the maximum dimensionless velocity in that cross section. At $Re=366$ and $De=183$ in Fig. 11(b), two additional pairs of vortices are observed, which are Dean vortices by definition. They are identified as the ICW Dean vortex and the corner region Dean vortex. Further calculations show that the critical Dean number (De_{crit}) marking the onset of the Dean vortices is 129. At the onset condition, the first Dean vortex appears near the ICW. Since this is the first study of a VACC, these results cannot be directly compared with any of the

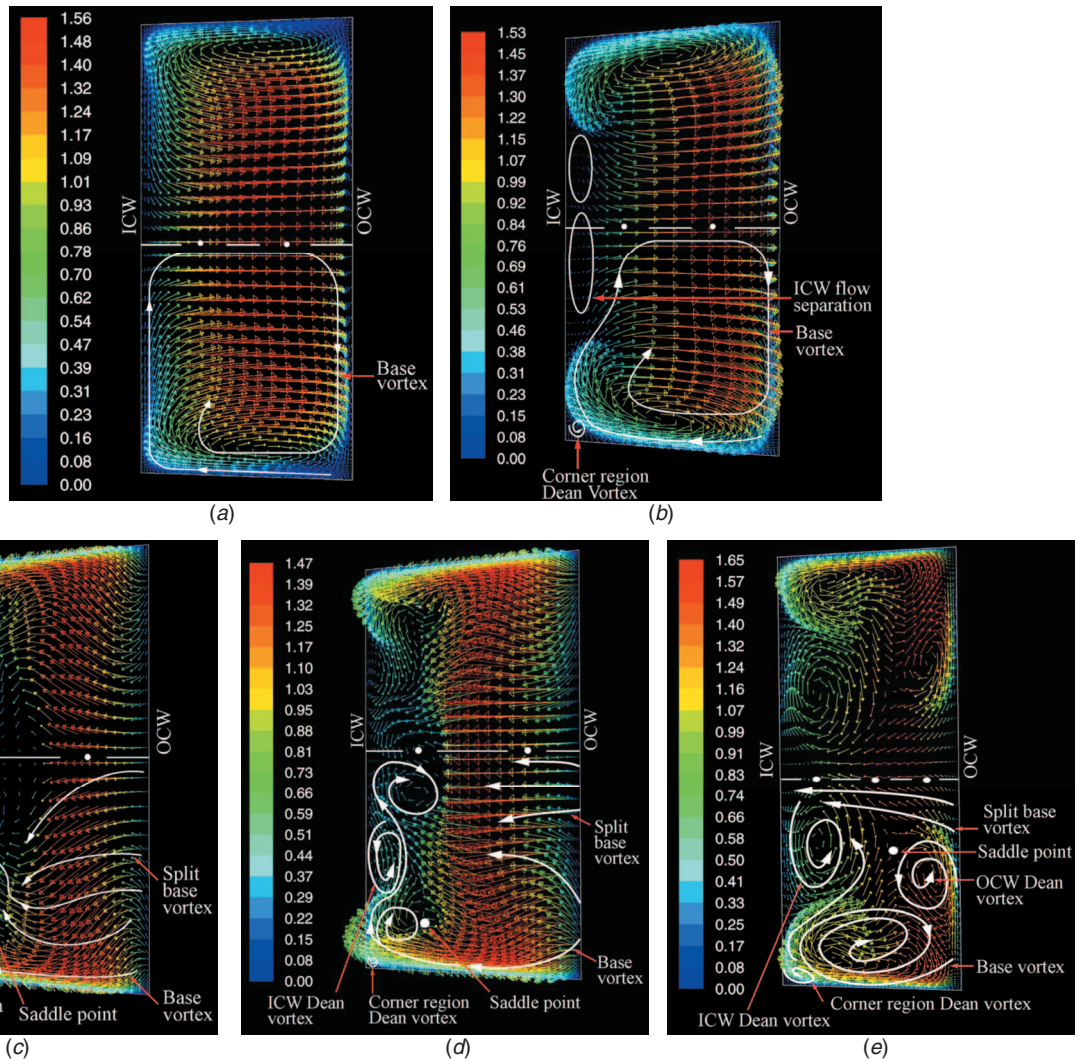


Fig. 8 Formation of secondary flow at various angular positions along a 90 deg bend of a long (diverging-converging) VACC. $Re=2017$ and $De=1008$ based on uniform flow velocity (V_i) and hydraulic diameter (D_h) at channel inlet, and properties at average temperature [$T_{av}=(T_i+T_w)/2$]. $L_{av}/D_h=39.1$, $L_{entry}/D_h=16.1$, and $L_{exit}/D_h=16.1$. $AR=2.3$, $CR=5.6$. Views: (a) angular position 11 deg, (b) 22.5 deg, (c) 56 deg, (d) 67.5 deg, and (e) 90 deg outlet from the curved portion of the channel or beginning of the straight constant c/s area exit channel.

existing literature. Therefore, we also calculated the De_{crit} value for a long CACC, which is 165. This is in the same ballpark range of results shown in Fig. 4 and the experimental literature [6]. In Fig. 4, we reported the De_{crit} values for a long CACC at the end of a 180 deg bend. For $AR=2.5$ and $CR=5$, the calculated De_{crit} value was 212. The difference in the calculated De_{crit} value between Fig. 4 and the present case (212 and 165, respectively) can be attributed to multiple factors, such as: (a) the flow entering the curved section in Fig. 4 and in Ref. [6] is fully developed, while the present case is not; (b) the AR and CR values used in the validation case of Fig. 4 and the present problem are close but different; and (c) the validation calculations are isothermal, whereas temperature dependent properties are used here.

A comparison of the CACC and VACC results reveals that the later has a lower De_{crit} value. This is due to the accelerating flow in the converging section of the VACC that leads to a stronger secondary flow compared with that in the CACC. The De_{crit} value of 129 also marks the onset condition of split base vortex. The radial pressure gradient ($\partial P/\partial r$) remains unbalanced over the entire channel depth. As a result, secondary flow from the OCW to the ICW occurs over the entire channel height and the flow splits into two streams. At low axial velocity, e.g., $De=183$ in Fig.

11(b), the split in base vortex occurs very close to the centerline (heightwise). With increasing axial flow velocity, the location of the split shifts away from the centerline and the split base vortex covers a wider area of the channel. At $De=366$ in Fig. 11(c), an early sign of formation of another pair of Dean vortex at the OCW is also observed. The OCW Dean vortex grows in size with increasing De , as seen in Fig. 8(e), ($De=1008$).

10 Short VACC: Flow Pattern

In a short channel that has no entry and exit lengths, uniform flow enters the curved section at 0 deg angular position and leaves the channel at the 90 deg position to an ambient pressure outlet boundary condition. It is important to emphasize at this point that the secondary flow structure and pressure drop (discussed later) in a short channel is highly dependent on the inlet boundary condition. In reality, the flow entering the short channel of the heat sink (Fig. 1) is neither uniform nor fully developed. Therefore, the present results for short channel geometry should be treated in a qualitative sense that underscores the role of curvature and variable c/s area by comparing various geometric configurations, such

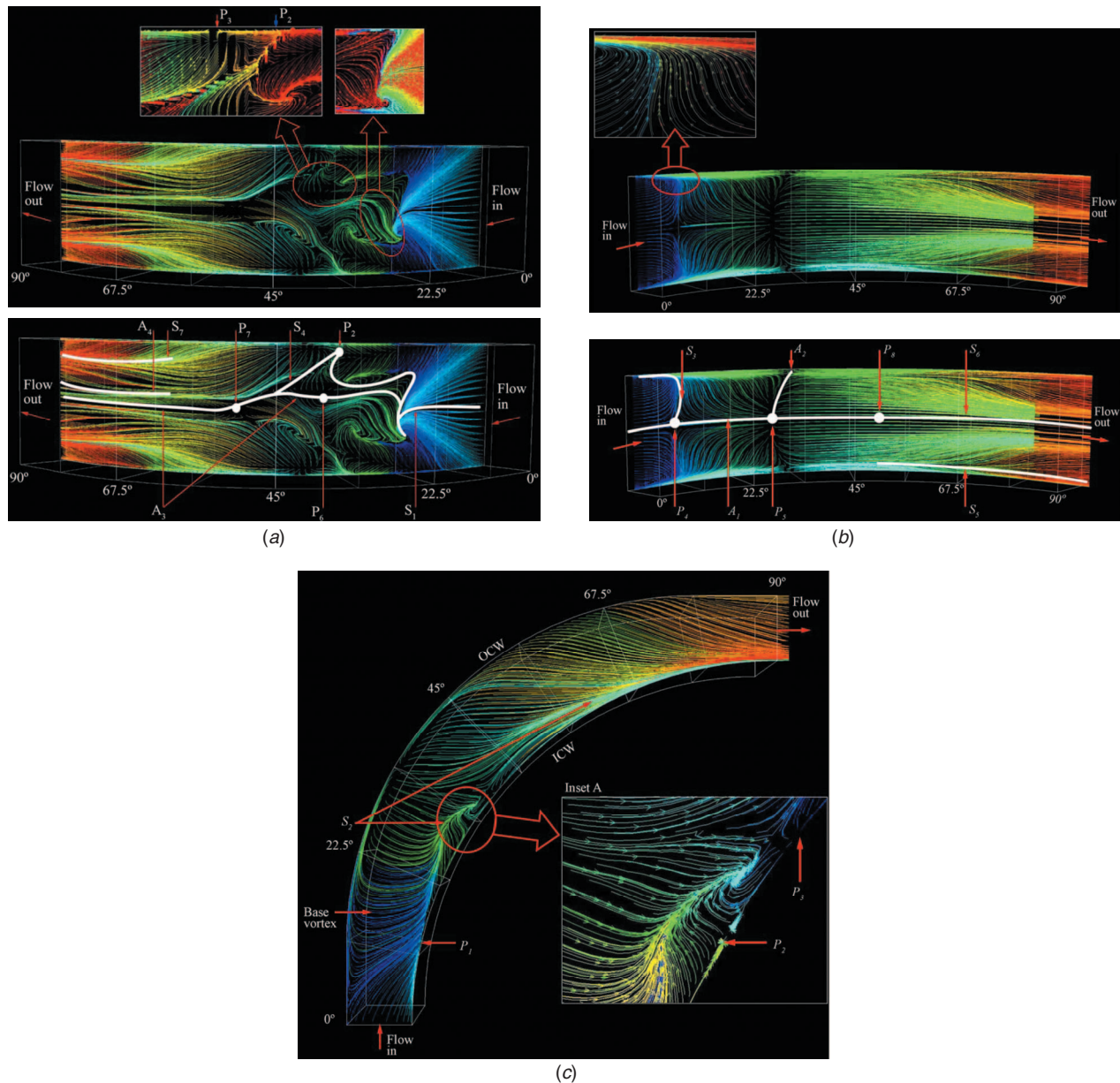


Fig. 9 Oil flow lines on the curved section (90 deg bend) of a long VACC. $Re=2017$ and $De=1008$, $L_{av}/D_h=39.1$, $L_{entry}/D_h=16.1$, $L_{exit}/D_h=16.1$, $AR=2.3$, and $CR=5.6$. (a) ICW or concave wall, (b) OCW or convex wall, and (c) TW. All views are looking into the wall from front.

as CACC, VACC, and CASC. The specific quantitative values shown here may not quite represent the real condition.

Figure 12 shows the nondimensional, in-plane velocity vector plots of secondary flow at various angular positions. Since the flow outlet is at 90 deg, we show the secondary flow at a plane just upstream, at the 89 deg position. Even though the geometry of the short channel is exactly same as that of the curved portion of the long channel, the flow pattern is significantly different (compare Fig. 12 with Fig. 8). This is mainly due to the boundary layer thickness. Uniform flow entering the short, curved channel forms a much thinner boundary layer compared with the long channel with an entry length (L_{entry}/D_h) of 16.1, discussed earlier. As a result, the main secondary flow from the OCW to ICW, that forms the *base vortex*, remains confined close to the top and bottom walls.

In addition to the base vortex, a few other flow features are similar to those for the long channel. For example, (a) The corner region Dean vortex in the ICW and top/bottom wall corner is

formed here too, although it is much smaller in size and appears further downstream (near 45 deg position as observed in Fig. 12(c)). (b) The oil flow lines (not shown here) indicate that the *axial flow separation from OCW* is observed here also, although only over a short length along the curved wall, between the 22.5 deg and 34 deg angular positions (Fig. 12(b)). (c) Splitting of *secondary flow from OCW to ICW in two streams*, one toward the top/bottom walls, and another toward the centerline. However, in the present case the splitting starts before the 45 deg angular position. (d) Formation of a pair of OCW Dean vortex near the centerline (Fig. 12(e)), just before the flow exit.

There are two noticeable differences between the flow pattern of the long and short channels. For example, (a) Formation of the additional recirculation cell near OCW at the 45 deg angular position (Fig. 12(c)). An investigation of the oil flow lines indicate that this is an OCW Dean vortex that originates just downstream of the 34 deg position and terminates on the wall between the 56 deg and 67.5 deg positions. (b) For the short channel, there is no

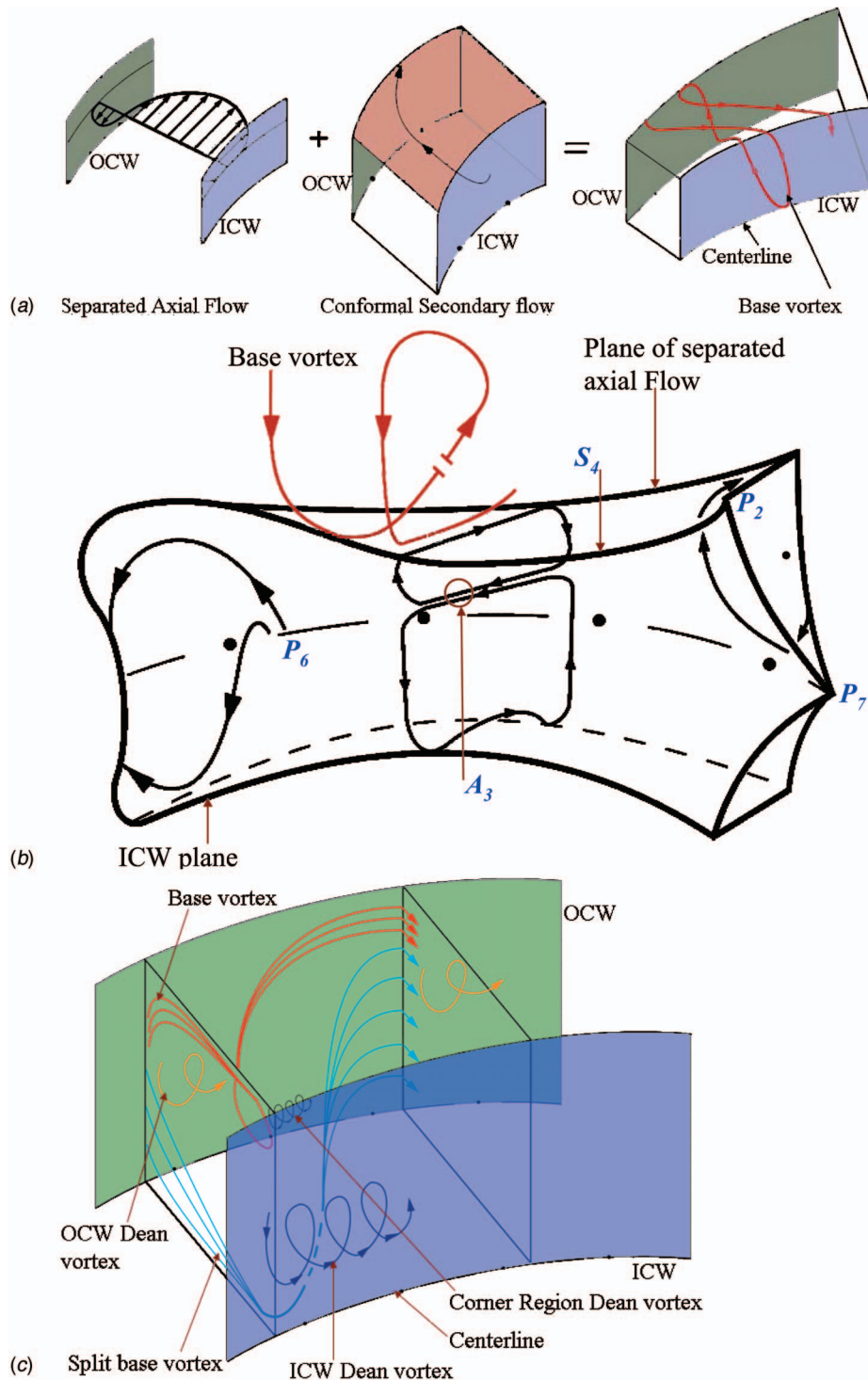


Fig. 10 Schematics of various 3D flow patterns in the curved section (90 deg bend) of a long VACC. $Re=2017$ and $De=1008$, $L_{av}/D_h=39.1$, $L_{entry}/D_h=16.1$, $L_{exit}/D_h=16.1$. $AR=2.3$, and $CR=5.6$. (a) Axial flow separation near OCW and the resulting base vortex structure at the early part of the curved channel, (b) axial and secondary flow separation from ICW, and formation of closed separation bubble, and (c) base vortex, split base vortex, and multiple Dean vortices at the converging section of the channel.

axial flow separation from ICW in the diverging section, or secondary flow separation from ICW in the converging section. As a result, Fig. 12 does not show an ICW Dean vortex and separation bubble which were observed in Fig. 8.

The effect of flow velocity (De) on the formation of secondary flow has also been investigated. The generic conclusions are very similar to that of a long channel. At the lowest velocity condition

of $De=92$, only the base vortex appeared in the channel. The onset of additional secondary vortices occurs at $De_{crit}=129$, same as that of the long channel. However, here the onset occurs in the corner region.

To summarize, the secondary flow in the short, variable c/s area, curved channel is predominantly characterized by the base vortex and the split base vortex. The Dean vortices are smaller in

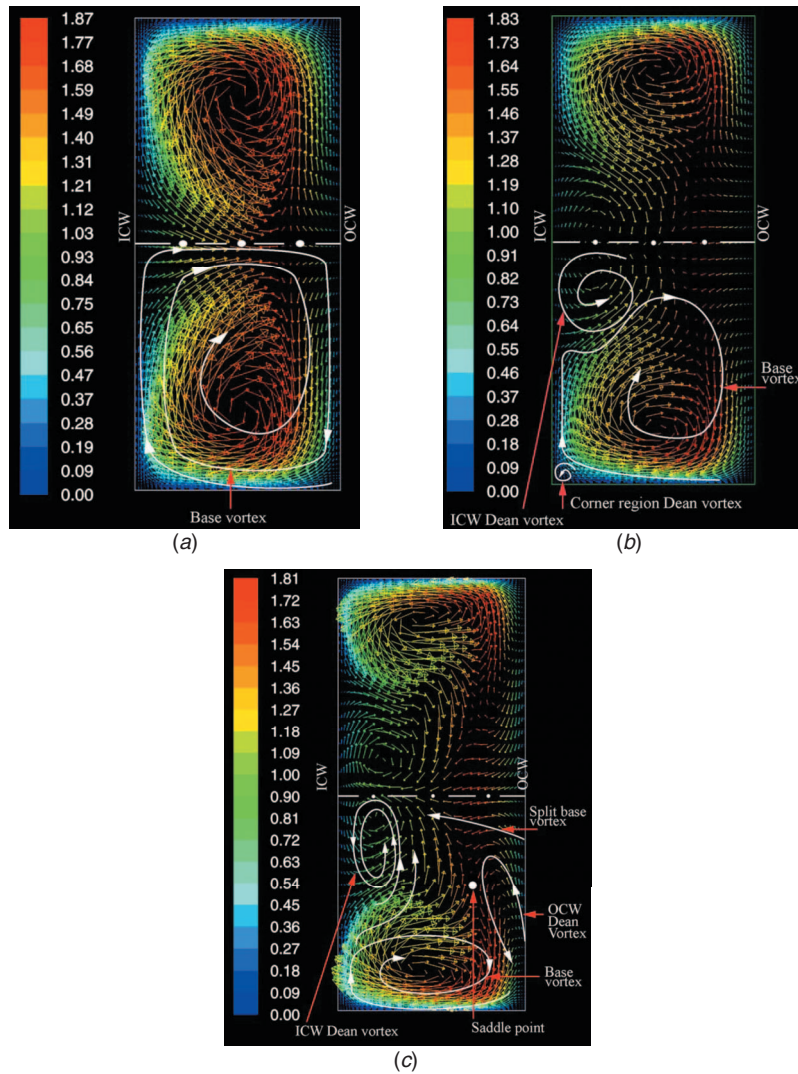


Fig. 11 Effect of axial flow velocity (Re and De) on the growth of secondary flow at the curvature outlet (at the 90 deg bend) of a long VACC. $L_{av}/D_h = 39.1$, $L_{entry}/D_h = 16.1$, $L_{exit}/D_h = 16.1$. $AR = 2.3$, and $CR = 5.6$. (a) $Re = 183$, $De = 92$; (b) $Re = 366$, $De = 183$; and (c) $Re = 732$, $De = 366$. Re and De are based on uniform inlet flow velocity (V_i), hydraulic diameter (D_h) at channel inlet, and properties at average temperature [$T_{av} = (T_i + T_w)/2$].

size and often localized, i.e., they do not cover the entire length of the curved section.

11 Pressure Drop and Friction Factor

Pressure drop between the channel inlet and exit (ΔP) is represented in a dimensionless form of friction factor f , defined as

$$f = \frac{\Delta P}{\frac{1}{2} \rho V_i^2} \frac{D_h}{4L} \quad (1)$$

The effects of flow velocity (V_i) and channel geometry (curvature and variable c/s area effect) on f are investigated. For the long channel ΔP includes pressure drop over the entire length (L_{entry} , L_{curv} , and L_{exit}), while for the short channel it is over L_{curv} only. For both the long and short channels, three different geometric configurations are investigated: the CASC, the CACC, and the VACC. Traditionally for developing flow, the product of friction factor and Reynolds number ($f Re$) is plotted against the axial location x , expressed in dimensionless form as $x^+ = x/(D_h Re)$.

Figures 13(a) and 13(b) show the variation of ($f Re$) as a function of the dimensionless total channel length ($L^+ = L/[D_h Re]$), respectively, for the long and short channel. Since D_h and L are constant, L^+ essentially represents the effect of Re or inlet flow velocity (V_i). The ($f Re$) curves for CASC in Fig. 13 closely follow the standard results of the well established literature, such as [15]. The slight difference of actual ($f Re$) values are possibly due to the use of temperature dependent properties in the present calculation.

It is well known (e.g., review in Ref. [16]) that the formation of secondary flow in a curved channel creates higher ΔP (and thus f), compared with that in a straight channel of the same length. Consistent with the prior literature, Figs. 13(a) and 13(b) show that ($f Re$) for CACC is always higher than that for CASC. In case of VACC, the velocity boundary layer thickness increases in the diverging section (0–45 deg), the axial flow slows down, and pressure increases in the downstream direction (pressure recovery). In the converging section (45–90 deg) as the flow accelerates, velocity boundary layer starts to decrease in the downstream direction and ΔP increases. On the whole it can be argued that

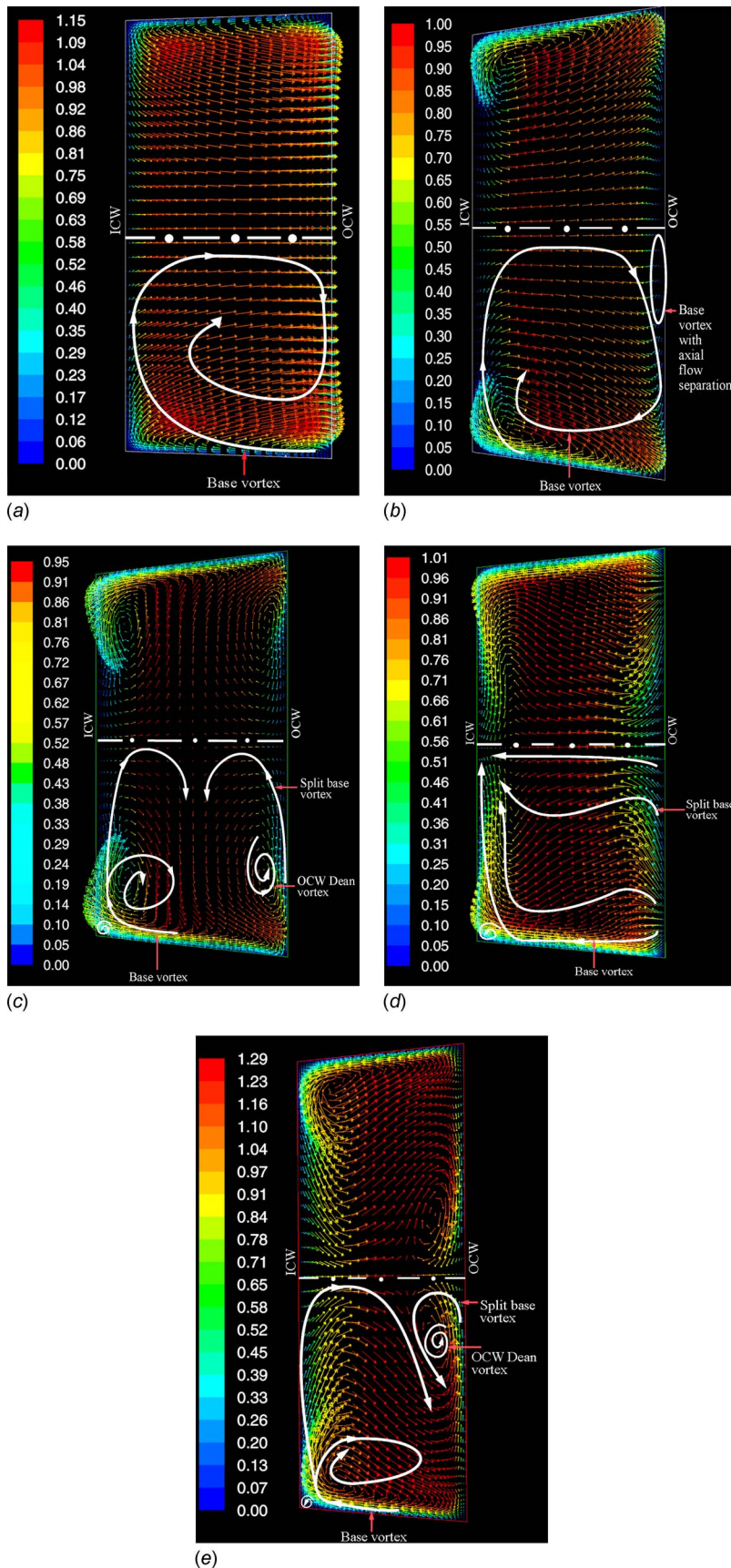


Fig. 12 Formation of secondary flow at various angular positions along a 90 deg bend of a short VACC. $Re=2017$, and $De=1008$, $L_{av}/D_h=6.8$, $L_{entry}/D_h=L_{exit}/D_h=0$, $AR=2.3$, and $CR=5.6$. View (a) angular position 11 deg, (b) 37 deg, (c) 45 deg, (d) 67.5 deg, and (e) 89 deg, just prior to the channel and curvature outlet.

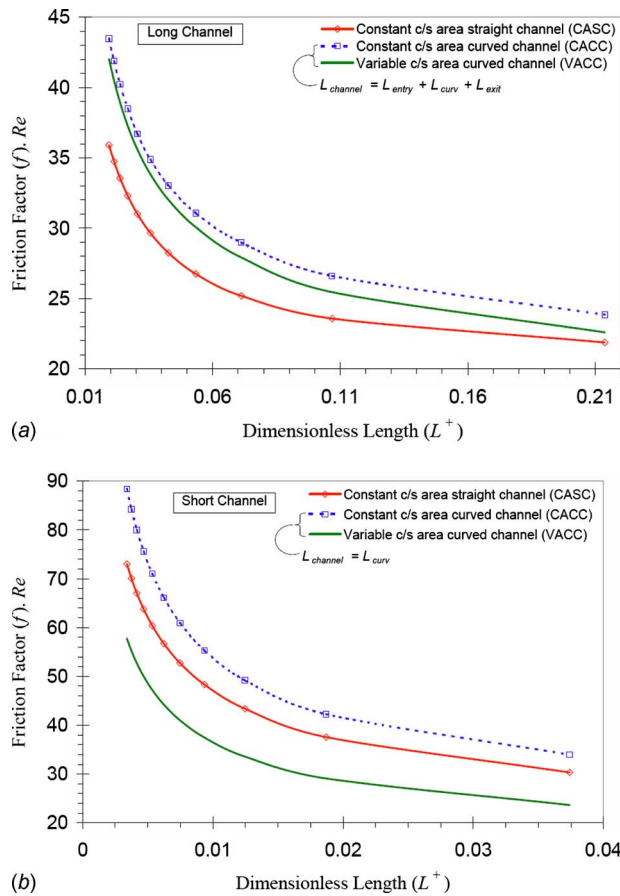


Fig. 13 The effects of flow velocity and channel geometry on the pressure drop (ΔP) between the channel inlet and outlet. Pressure drop expressed in dimensionless form as product of friction factor and Reynolds number ($f Re$), and velocity as L^+ . (a) Long channel and (b) short channel.

over the curved length (L_{curv}), the average flow area for VACC is greater than that of the CACC. Therefore, the ΔP for the former is expected to be lower than its constant area counterpart, as observed in Fig. 13.

Comparison of the short length VACC with CASC in Fig. 13(b) is quite striking. ΔP or ($f Re$) for VACC is even less than that for CASC. This is quite counter intuitive considering the presence of secondary flow in the curved geometry. At the highest flow rate condition of $Re=2017$ (corresponding $L^+ \sim 0.004$), ($f Re$) for VACC is $\sim 25\%$ lower than that of CASC. Evidently, the results suggest that the area expansion effect overwhelms the secondary flow effect. An order of magnitude, scaling analysis of ΔP can provide a reasonable explanation of this phenomenon. The in-plane velocity vector plots in Fig. 12 show that even though the secondary flow takes place over the entire channel c/s area, the velocity boundary layer of the axial (bulk) flow is very thin. As a result, the axial flow is uniform over most of the channel c/s area. Short CACC and CASC also show a similar pattern. Therefore for a short channel, ΔP should scale with the pressure drop in the core (uniform) flow area, or the difference in kinetic energy between the channel inlet and exit, i.e., $\Delta P \sim (V_{max}^2 - V_i^2)$, where V_{max} is the maximum velocity at the channel exit. For the three geometric cases shown in Fig. 13(b), at $Re=2017$, V_{max}/V_i values are 1.43, 1.39, and 1.30, respectively, for CACC, CASC, and VACC. Figure 13(b) shows that at any Re , ($f Re$) follows the decreasing trend in the same order. Based on the above V_{max} val-

ues, the ratio of $\Delta P_{VACC}/\Delta P_{CASC}$ should be ~ 0.74 . The scaling analysis estimate is strikingly close to the actual ratio shown in Fig. 13(b) for $Re=2017$.

A similar scaling analysis cannot be applied to the long channel, though. Figures 5 and 8 show that the boundary layer thickness at various angular positions of the curved section can be as high as $b/2$, or more. This indicates that the viscous effect is dominant in such flow and ΔP should scale with the viscous stress, i.e., $\Delta P/L \sim \mu U_{max}/\delta^2$, where δ is the velocity boundary layer thickness. However, since the flow is developing throughout the channel length, (U_{max}/δ^2) is a variable parameter, and thus hard to estimate from a simple scaling analysis. A better insight into the results of Fig. 13(a) is obtained by looking into the pressure drop at individual length segments (L_{entry} , L_{curv} , and L_{exit}). It turns out that for all the three geometric configurations, nearly 50% or more of the total channel ΔP occurs in the inlet section, over the length L_{entry} . Only 12–15% of the total pressure drop takes place over L_{curv} . The difference in overall ΔP is created over the exit length (L_{exit}). Since the secondary flow generated in the curved section continues into the exit length, ΔP over L_{exit} is significantly higher for both the curved channels (CACC and VACC), compared with that for the straight channel (CASC). This explains why ($f Re$) for CACC and VACC are both higher than that of CASC, unlike the results for short channel.

For the short channel, we concluded that the area expansion effect in a VACC is the dominant factor that dictates the ΔP , which is even lower than that in a CASC. To judge how much of this conclusion is affected by the uniform velocity inlet boundary condition, we investigated the ΔP over the length of the curved section (L_{curv}) only, in the long channel. Here the flow entering the curved section is partially developed. We observed a similar trend, i.e., $\Delta P_{VACC} < \Delta P_{CASC} < \Delta P_{CACC}$. However the ratio is different. For example, for the highest flow rate condition of $Re = 2017$, $\Delta P_{VACC}/\Delta P_{CASC}$, and $\Delta P_{CASC}/\Delta P_{CACC}$ over the length L_{curv} of a long channel are 0.96 and 0.79, respectively, compared with 0.75 and 0.87 for a short channel. Thus, the conclusion is valid irrespective of the inlet boundary condition, but the relative magnitude changes.

In closing, it is important to re-emphasize that the flow and pressure drop characteristics presented in this article are for a specific channel geometry picked for this study. The geometric features, such as channel lengths (L_{entry}/D_h , L_{curv}/D_h , and L_{exit}/D_h), curvature ratio (CR), aspect ratio (AR), variable c/s area ratio (b_{max}/b), etc., all play important roles in governing these characteristics. Therefore, a further parametric study illustrating the role of these geometric features is much needed.

12 Conclusion

Variable cross-sectional area curved flow passages are formed between two fin walls of curved fin heat sinks used in avionics electronics cooling. This article presents a 3D computational model of developing laminar air flow through such a flow passage with a 90 deg bend. The c/s area at the curvature inlet and outlet are the same. In between, the channel width first increases and then decreases along the length of curvature, making it a diverging-converging curved channel. The area expansion ratio is 1.5, while the channel aspect ratio, based on the constant channel height and width at the flow inlet, is 2.3. Simulations are carried out for two geometric configurations: (a) a curved channel with long, straight, constant c/s area inlet and outlet sections (entry and exit lengths), identified as a long channel; and (b) a curved channel with no entry or exit length, termed as a short channel. The computational flow visualization at various c/s areas and different flow rates reveals the formation of secondary flow, the separation and attachment of the axial and secondary flow from/to various channel walls, and the resulting growth of multiple vortices. The roles of the channel inlet flow velocity and channel geometry,

specifically the area expansion and contraction effect, on flow pattern and pressure drop are investigated. Some of the specific conclusions are as follows.

- For a constant c/s area curved channel, flow in the curved section consists of a pair of base vortices, and three sets of Dean vortices, at the inner curvature (concave) wall, the outer curvature (convex) wall, and at the corner of top/bottom wall and the concave wall.
- The flow pattern is significantly more complex in case of a variable c/s area (diverging-converging) curved channel. The secondary flow splits in two streams, creating a split base vortex, in addition to the traditional base vortex. Similar to the constant c/s area curved channel, three sets of Dean vortices are also observed here. The expanding geometry at the diverging section of the curved channel also leads to axial flow separation both from the inner and outer curvature walls, and formation of local separation bubbles.
- For both the long and short channels, only the base vortices appear at low flow velocity. There exists a critical velocity, or a critical Dean number in the dimensionless form, above which additional vortices (Dean vortices) appear in the channel. The critical Dean number is geometry dependent. For example, for a long, variable c/s area curved channel the value is 129, compared with 165 for a constant c/s area curved channel of the same length.
- Pressure drop for the variable c/s area curved channel is always lower than that of its constant c/s area counterpart, for both the long and short channels. The pressure drop characteristics in a short channel is quite counterintuitive. In spite of the presence of secondary flow in a variable c/s area curved channel, its pressure drop is lower than even that of a straight channel.

Acknowledgment

We gratefully acknowledge the support from Rockwell Collins and the technical interaction with Mr. Matthew Wells and Mr. Perry Baker. We also thank Mr. Travis Sidebotham and Mr. Benjamin Liu for their help in preparing the sketches and the data analysis.

Nomenclature

- A_{cs} = cross-sectional area of the flow channel at any location (variable in the curved section)
 AR = channel aspect ratio= H/b
 b = channel width; variable, maximum at the 45 deg angular position from the start of the curvature, and for all calculations b value at the channel inlet is used
 CR = channel curvature ratio= R/b
 De = Dean number= $Re \sqrt{(D_h/R)}$
 De_{crit} = critical Dean number for the onset of Dean vortices= $(V_{i,crit} D_h / \nu) \sqrt{(D_h/R)}$
 D_h = channel hydraulic diameter at the flow inlet = $2bH/(b+H)$
 f = friction factor= $(2\Delta P / \rho V_i^2) \times (D_h/4L)$
 H = channel height
 h_o = overall channel heat transfer coefficient=total heat dissipated/[total channel wall surface area $\times(T_w - T_i)$]
 H_{min} = magnitude of minimum helicity at a c/s area.
 k_f = thermal conductivity of air (temperature dependent)
 L_{av} = total channel length along the middle of the cross section= $L_{entry} + L_{curv} + L_{exit}$
 L^+ = dimensionless channel length= $L_{av}/(D_h Re)$
 L_{curv} = average length of the curved section, along the middle of the cross section

- L_{entry} = length of the constant c/s area entrance section in a long channel
 L_{exit} = length of the constant c/s area exit section in a long channel
 L_{fd} = channel entry length for the flow to be fully developed
 N_{cell} = total number of recirculation cells at any c/s area
 Nu_o = overall channel Nusselt number= $h_o D_h / k_f$
 P = pressure
 R = radius of curvature of the inner curved (convex) wall
 Re = Reynolds number= $V_i D_h / \nu$
 T = local temperature at any location
 $T_{av,exit}$ = area averaged temperature at the exit of the flow channel
 T_i = ambient temperature of the air entering the channel
 T_w = temperature of the channel bottom and side walls
 V = velocity magnitude at any location
 V_i = uniform flow velocity at the inlet of a channel
 $V_{i,crit}$ = critical velocity at channel inlet for the onset of Dean vortices
 ΔP = pressure drop over the entire channel length L
 μ = dynamic viscosity of air
 ν = kinematic viscosity of air
 θ = dimensionless temperature at any location= $(T - T_i)/(T_w - T_i)$

References

- [1] Garimella, S. V., 1996, "Enhanced Air Cooling for Electronic Equipment," *Air Cooling Technology for Electronic Equipment*, S. J. Kim and S. W. Lee, eds., CRC, Boca Raton, FL, Chap. 5, pp. 173–202.
- [2] Carter, D. P., Crocker, M. T., Broili, B. M., Byquist, T. A., and Llapitan, D. J., 2003, "Electronics Assemblies With High Capacity Curved Fin Heat Sinks," U.S. Patent No. 6,671,172.
- [3] McCormack, P. D., Welker, H., and Kelleher, M., 1970, "Taylor Goertler Vortices and Their Effect on Heat Transfer," *ASME J. Heat Transfer*, **92**, pp. 101–112.
- [4] Dean, W. R., 1928, "Fluid Motion in a Curved Channel," *Proc. R. Soc. London, Ser. A*, **121**, pp. 402–420.
- [5] Cheng, K. C., Nakayama, J., and Akiyama, M., 1977, "Effect of Finite and Infinite Aspect Ratios on Flow Patterns in Curved Rectangular Channels," *Proceedings of the International Symposium of Flow Visualization*, Tokyo, Japan, pp. 181–186.
- [6] Sugiyama, S., Hayashi, T., and Yamazaki, K., 1983, "Flow Characteristics in the Curved Rectangular Channels (Visualization of Secondary Flow)," *Bull. JSME*, **26**(216), pp. 961–969.
- [7] Ligrani, P. M., and Niver, R. D., 1988, "Flow Visualization of Dean Vortices in a Curved Channel With 40 to 1 Aspect Ratio," *Phys. Fluids*, **31**(12), pp. 3605–3617.
- [8] Cheng, K. C., and Akiyama, M., 1970, "Laminar Forced Convection Heat Transfer in Curved Rectangular Channels," *Int. J. Heat Mass Transfer*, **13**, pp. 471–490.
- [9] Ghia, K. N., and Sohkey, J. S., 1977, "Laminar Incompressible Viscous Flow in Curved Ducts of Rectangular Cross-Section," *ASME J. Fluids Eng.*, **99**, pp. 640–648.
- [10] Humphrey, J. A. C., Taylor, A. M. K., and Whitelaw, J. H., 1977, "Laminar Flow in a Square Duct of Strong Curvature," *J. Fluid Mech.*, **83**(3), pp. 509–527.
- [11] Hwang, G. J., and Chao, C.-H., 1991, "Forced Laminar Convection in a Curved Isothermal Square Duct," *ASME J. Heat Transfer*, **113**, pp. 48–55.
- [12] Chandratilleke, T. T., and Nursubyakto, 2003, "Numerical Prediction of Secondary Flow and Convective Heat Transfer in Externally Heated Curved Rectangular Ducts," *Int. J. Therm. Sci.*, **42**, pp. 187–198.
- [13] Beavers, G. S., Sparrow, E. M., and Magnuson, R. A., 1970, "Experiments on Hydrodynamically Developing Flow in Rectangular Ducts of Arbitrary Aspect Ratio," *Int. J. Heat Mass Transfer*, **13**, pp. 689–702.
- [14] 2006, *FLUENT 6.3 User's Guide*, Lebanon, NH.
- [15] Curt, R. M., Sharma, D., and Tatchell, D. G., 1972, "Numerical Prediction of Some Three-Dimensional Boundary Layers in Ducts," *Comput. Methods Appl. Mech. Eng.*, **1**, pp. 143–158.
- [16] Ebadin, M. A., and Dong, Z. F., 1998, "Forced Convection, Internal Flow in Ducts," *Handbook of Heat Transfer*, 3rd ed., W. M. Rohsenow, J. P. Hartnett, and Y. I. Cho, eds., McGraw-Hill, New York, Chap. 5.

Measurements of a Wall Jet Impinging Onto a Forward Facing Step

D. C. Langer

B. A. Fleck

e-mail: brian.fleck@ualberta.ca

D. J. Wilson

Department of Mechanical Engineering,
University of Alberta,
Edmonton, AB T6G 2G8, Canada

This study examines a horizontal wall jet impinging onto a forward facing vertical step in a cross-flow. Planar laser induced fluorescence (PLIF) experiments in a 68×40 mm² water channel indicate how the wall-jet flow after impinging onto the step becomes a vertical jet with an elliptical cross section. This study proposes predictive empirical correlations for the aspect ratio and perimeter of the jet's elliptical cross section based on the step geometry and the inlet flow conditions. A numerical model is also presented, which was produced from a commercial Reynolds averaged Navier–Stokes computational fluid dynamics (CFD) code with the k - ϵ closure model. The experimental results were well represented by correlations for the perimeter P and aspect ratio S using the parameters H (the step height), L_0 (the distance from the jet represented as a point source to the step), and R (the velocity ratio). The CFD simulation was able to predict the trends in the perimeter (under different conditions), aspect ratio, and the shape of the concentration profile, but overpredicted the jet's perimeter by approximately 50%. The results of these tests are required as input parameters when modeling jet trajectories.

[DOI: 10.1115/1.3203201]

1 Introduction

This study examines the flow field, which occurs when a wall jet impinges normally onto a forward facing step and is then deflected into a cross-flow. This geometry has not been examined in the literature and later may be found to have applications for other mixing or dispersion studies. The preliminary motivation for studying this geometry was given by Wilson [1], who examined the dispersion of gases released from pipeline ruptures. Underground pipelines can carry high concentrations of dangerous fluids such as sour gas or natural gas. Occasionally these pipes fail, leading to the release of significant quantities of toxic or flammable gasses. The rupture of a buried pipe produces a crater, where the gas is released at high velocities and impinges onto the crater wall. The interactions between the jet and the crater lead to significant spreading and momentum losses in the jet, which can drastically change the rate of dilution of the released gases in the surrounding air. These ruptures can produce significant ill-effects to the environment and danger for the populous surrounding the rupture area. The ability to model the concentration distributions of the pollutant within the atmosphere allows for safe placement of toxic gas pipelines and proper emergency response in the event of a poisonous gas release [1]. Through better understanding the shape and size of the jet entering into the cross-flowing fluid, better predictions of the jet's behavior can be made. The results of this study could be used with Wilson's model [1] and be incorporated into hazard assessment models to more accurately determine the dispersion of hazardous pollutants after a pipeline rupture.

Planar laser induced fluorescence (PLIF) measurements were used for both flow visualization and to measure the concentration profiles within the jet [2]. The vertically deflected jet above the step was studied to determine the shape of the jet entering into the cross-flow. In preliminary experiments it was found that the jet exiting the step was elliptical in nature, and the aspect ratio was dependent on the jet velocity (V_{jet}), cross-flow velocity (V_∞), step height H , and the distance from the step to the jet L . This study

aims to determine how these parameters influence the shape and behavior of the jet as it is deflected into the cross-flow. Future work will study the elliptical jet as it enters the cross-flow to predict the jet's trajectory based on the shape of the ellipse and other parameters.

CFD simulations were also undertaken to determine the feasibility of using numerical methods to predict the behavior of the flow. These simulations were modeled using ANSYS-CFX (which solves the Reynolds averaged Navier–Stokes (RANS) equations) with a standard k - ϵ turbulence model. The k - ϵ model has been used by several researchers to simulate the flow of free jets [3] and impinging jets [4]. It is also a model, which is computationally inexpensive and robust, allowing for a variety of parameters to be tested. This combination of experimental and CFD results provides insight into the study of this novel geometry under several different flow conditions.

2 Experimental Method

Experiments were performed in the recirculating water channel facility at the University of Alberta [5–7]. The facility consists of a 5.24 m long rectangular channel with a cross section measuring 47×68 cm² with a water depth of 40 cm. A centrifugal pump with a variable outlet diameter was used to control the velocity of the cross-flow, which was varied from 0.041 m/s to 0.081 m/s, producing Reynolds numbers (based on hydraulic diameter) ranging from 2×10^4 to 4×10^4 . A turbulent boundary layer shear flow was developed in the channel using a grid composed of square aluminum tubes, a sawtooth trip fence, and roughness elements composed of a 1.27 mm diamond shaped steel mesh attached to acrylic panels on the bottom of the water channel. The shear flow used in this experiment was measured [5] and was found to produce conditions similar to the atmospheric boundary layer.

The experimental test section consisted of the jet tube and step shown in Fig. 1 and was located 3 m from the channel inlet. The jet consisted of a 1.11 m ($126d$) long brass tube with an inner diameter of 8.75 mm, which was made from the jet tube and turbulence generator used by Johnston and Wilson [7] with a 1 m extension tube attached to the end. This ensured that the vertical inlet tube did not significantly effect the cross-flow, and that there was fully developed turbulent flow within the pipe at the exit. The

Contributed by the Fluids Engineering Division of ASME for publication in the JOURNAL OF FLUIDS ENGINEERING. Manuscript received September 9, 2008; final manuscript received June 29, 2009; published online August 18, 2009. Assoc. Editor: Juergen Kompenhans.

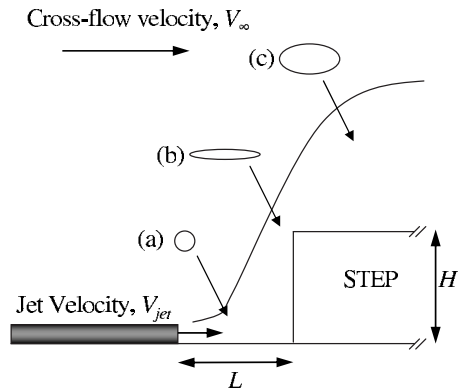


Fig. 1 Schematic of the test section. The step height (H), the effective distance (L), and the velocity ratio ($R = V_{jet}/V_{\infty}$) were varied for the parametric study. The shape of the cross section perpendicular to the direction of the jet is shown at three locations: the pipe exit (a), the top of the step (b), and downstream of the step (c). The round jet flattens at the step (b) and forms a high aspect ratio ellipse which then “rolls-up” to become more circular.

pipe was mounted flush with the grid on the bottom of the channel, producing a wall jet, which was centered midway across the water channel. Based on the logarithmic fit to the velocity profile performed by Hilderman and Wilson [5], the boundary layer thickness of the cross-flow at the jet exit location was calculated to be approximately 15 mm (2d). A more detailed explanation of the cross-flow is provided by Hilderman and Wilson [5]. Dyed water for the jet was stored in a 75 l tank, which was maintained at 2.1 bars, and was connected to the pipe using flexible tubing. Water from the jet and channel were of equal temperature, preventing any buoyancy effects. The velocity of the jet was controlled using a needle valve and a rotameter giving average jet velocities of 0.47 m/s, 0.78 m/s, and 1.10 m/s. This corresponded to pipe Reynolds numbers based on diameter of 4.1×10^3 , 7.0×10^3 , and 9.6×10^3 . The step was constructed from a 1.2 m long sheet of black acrylic, which covered the entire width of the water channel. The height of the step was adjusted by adding strips of 1.27 cm thick acrylic (which ensured that the step remained of uniform height) and was set at 2.54 cm, 3.81 cm, and 5.08 cm. The front surface was perpendicular to the floor of the water channel and parallel to the face of the jet tube outlet. The jet outlet was located $5d$, $9d$, and $15d$ from the step (43.75 mm, 78.75 mm, and 131.25 mm).

Measurements were taken to determine the shape of the jet leaving the step (with illumination in planes parallel to the water channel floor). The system was composed of a 4 W Coherent Innova 70 argon-ion laser, steering optics, a Powell lens, and a 12-bit Cooke SensiCam CCD camera. The laser was run in single line mode, producing a single beam at 488 nm, with a rated power of 2.1 W. The beam was passed through a focusing lens, decreasing the thickness of the laser sheet at the center of the water channel to approximately 1 mm. It was then steered by two mirrors into a 30 deg Powell lens [8]. The laser sheet was used to illuminate fluorescein sodium salt ($C_{20}H_{10}Na_2O_5$), which was pre-mixed in the jet tank at a concentration of 0.20 ± 0.02 mg/l. The absorption peak for this dye is approximately 488 nm, and the emission peak is at 515 nm [2]. A number 12 Kodak *wratten* gelatin filter was placed in front of the camera to effectively attenuate the diffracted and reflected laser light from the recorded images. The filter was rated to have zero transmittance at 488 nm and approximately 25% transmittance at 515 nm (the wavelength of peak fluorescence emission). The camera was oriented (effectively) perpendicular to the laser sheet and focused using a 75 mm Cosmicar TV zoom lens. The resolution of the images was found to be 0.25 mm/pixel. The experimental signal to noise ratio was

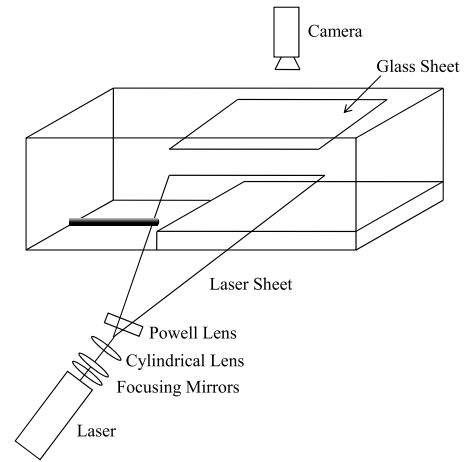


Fig. 2 Schematic of the experimental apparatus. The laser beam is steered into a cylindrical focusing lens through the use of two focusing mirrors. The beam then travels into a Powell lens forming a laser sheet. The camera is oriented perpendicularly to the laser sheet and located above the water channel. A sheet of glass is used at the top of the water surface to remove the distortions caused by waves within the channel.

approximately 50 in the areas of high concentration, and 15 in the areas of lower concentrations. A schematic of the experimental optics and measurement apparatus is shown in Fig. 2. More detailed information regarding the optical setup is given by Torres [9].

Calibration was required to remove the effects of the nonuniformity of the laser sheet's light intensity, which were caused by the spreading of the laser, the profile produced by the Powell lens, the operating mode of the laser, and the heterogeneous CCD sensitivity. The nonuniformities in the light sheet and camera array sensitivity were factored into the daily calibration using a method similar to that of [5] but assuming a linear concentration-fluorescence relationship [2]. For each inlet condition, 500 images were acquired at a rate of 7.6 frames per second (FPS) with an exposure time of 10 ms. These conditions produced measurement times of 65.8 s. Background measurements were taken before and after the jet measurements to determine the buildup of dye in the water channel. In all cases this buildup was found to be less than 1% of the peak concentration. For each experiment, jet images were processed and converted to an average concentration image.

The laser sheet was positioned parallel to the floor of the water channel, with its center 2 mm above the top of the step. Images were taken with the camera perpendicular to the laser sheet to show the cross section of the jet. An example of a single image is shown in Fig. 3. Images were processed to produce an average image, as shown in Figs. 4, parts a and b. As can be seen in the figures, the jet at this location resembles a high aspect ratio elliptic jet. As such, the size and shape of the jet were characterized by two measurements, the jet's depth (along the original jet axis) and the jet's width (perpendicular to the original jet axis). The ellipse was defined as the contour line, which encompassed 70% of the maximum measured concentration within the measurement plane. This 70% contour was determined based on experimental results, as it was the contour, which gave the best representation of the shape of the vertical jet entering the cross-flow for all of the flow conditions tested. It was found that for concentrations less than 70%, the size of the contour varied significantly due to the fluid entrainment at the boundaries of the jet. At concentrations greater than 70%, the shape of the contours was found to be dominated by local maxima and did not have a repeatable shape. To minimize the effects of noise in the measurement of the maximum concentration, the 30 pixels with the highest concentration were averaged to determine the maximum. These points typically had a standard

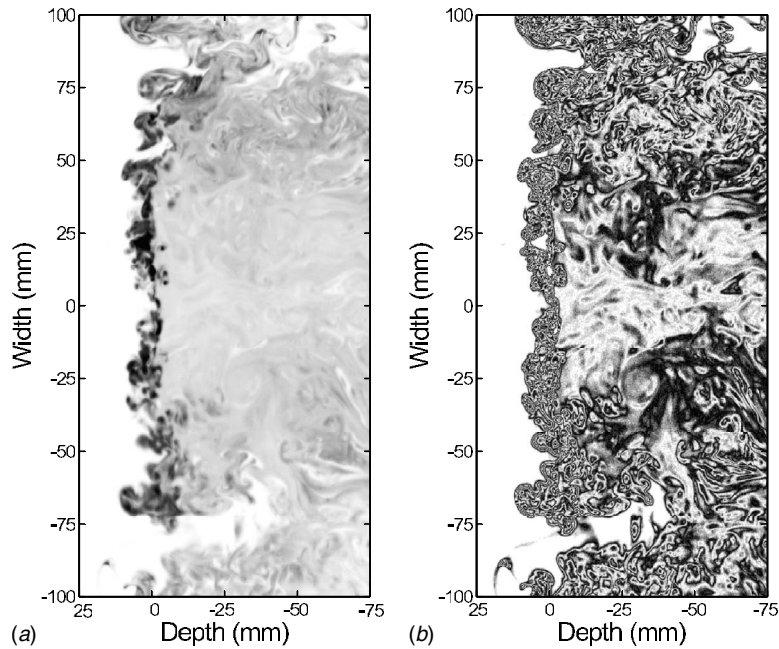


Fig. 3 Single experimental image of the concentration profile within the jet. A linear concentration scale is shown in (a) and a sawtooth scale used to emphasize the structures apparent in the jet is shown in (b). The cross-flow moves from left to right, with the jet fluid moving out of the page. The step is located at 0 mm.

deviation of less than 1% of their mean. Once the maximum value was determined, a Gaussian fit was used along each row and column, with a threshold value of 60% of the peak. The two intersections of each Gaussian curve with the 70% concentration value were used to determine the depth and width of each row and column. An example of the Gaussian fits used for jet widths and jet depths is shown in Fig. 5. This fit produced a series of depth and width measurements, from which the maximum width and depth were defined as the major and minor axis of the elliptical jet. The jet aspect ratio was then found by dividing the maximum width (a) by the maximum depth (b), and the perimeter was approximated by Eq. (1). The jet aspect ratio is defined in Eq. (2)

$$P = \pi \left[2(a^2 + b^2) - \frac{(a-b)^2}{2} \right]^{1/2} \quad (1)$$

$$S = \frac{a}{b} \quad (2)$$

3 CFD Constraints

3.1 Geometry. The geometry used for the simulations was identical to that used in the water channel experiments. The cross-flow was allowed to develop for 1 m before and after the step to minimize the effects of the inlet and outlet conditions. A symmetry argument along the center of the channel was used to decrease the computational effort and time required for each test. This argument is justified because the wall jet, impinging jet, and jet in cross-flow possess symmetry along the jet centerline. The depth of the channel in the model was identical to that of the experimental system to help mimic both the cross-flow boundary layer and the penetration of the jet into the cross-flow. A dimensioned diagram of the model is shown in Fig. 6(a). The two dimensions, which are given by letters (L and H), were varied in different simulations. The length, L , was set at $5d$, $10d$, and $15d$ (43.75 mm, 87.5 mm, and 131.25 mm), and the height, H , was set at 25.4 mm, 38.1 mm, and 50.8 mm. These lengths were chosen to compare the CFD results with the experimental results. Lengths of 5 diameters and

15 diameters were chosen to be compared directly with the experimental measurements at the same locations. The intermediate length was chosen to be ten diameters for the CFD results to provide a central value for curve fitting. The experimental length of nine diameters differs from the ten diameters used for the CFD only because of experimental limitations.

3.1.1 Boundary Conditions. The locations of the boundary conditions are shown in Fig. 6(b). The inlet condition for the cross-flow had three initial normal speeds: 0.041 m/s, 0.061 m/s, and 0.081 m/s, all with an initial turbulence intensity of 1%. The inlet was defined as a subsonic flow with a scalar concentration of 0 mg/l. The jet inlet was also a subsonic flow, with an initial concentration of 0.7 kg/m³. The jet velocity was set at three different normal speeds: 0.47 m/s, 0.78 m/s, and 1.10 m/s, with a turbulence intensity of 5%. An average static pressure condition was used at the outlet, which was set at 0 Pa relative to the flow. The bottom of the channel, the step, and the side wall were all set as smooth walls with the no-slip condition. The top of the channel was set as a wall with free slip to best simulate the free surface at the top of the channel.

3.1.2 Meshing. Three computational grids were used to determine the effect of grid dependence: the grids were designated as coarse, medium, and fine. The grid used for all of the simulations (except the grid convergence study) is shown in Fig. 6(c). Due to computer limitations, the coarse grid was used for the parametric study, and only one simulation was run using each the medium and fine grids. Since the purpose of the CFD study was to determine the feasibility of using computer simulations to predict the perimeter of the jet, the usage of the coarse grid was justified. It was further justified by the parametric study that was analyzed, which required several different simulations, limiting the available computer time. An analysis of the effects of using the coarse grid on the accuracy due to grid dependence is discussed in Sec. 3.1.4.

The three grids used had spacings of 2.5 cm, 2 cm, and 1.5 cm between nodes in the free stream region. Along the floor of the channel and on the step, inflation was used to increase the number of elements near to the walls. In all cases the inflated layer had a

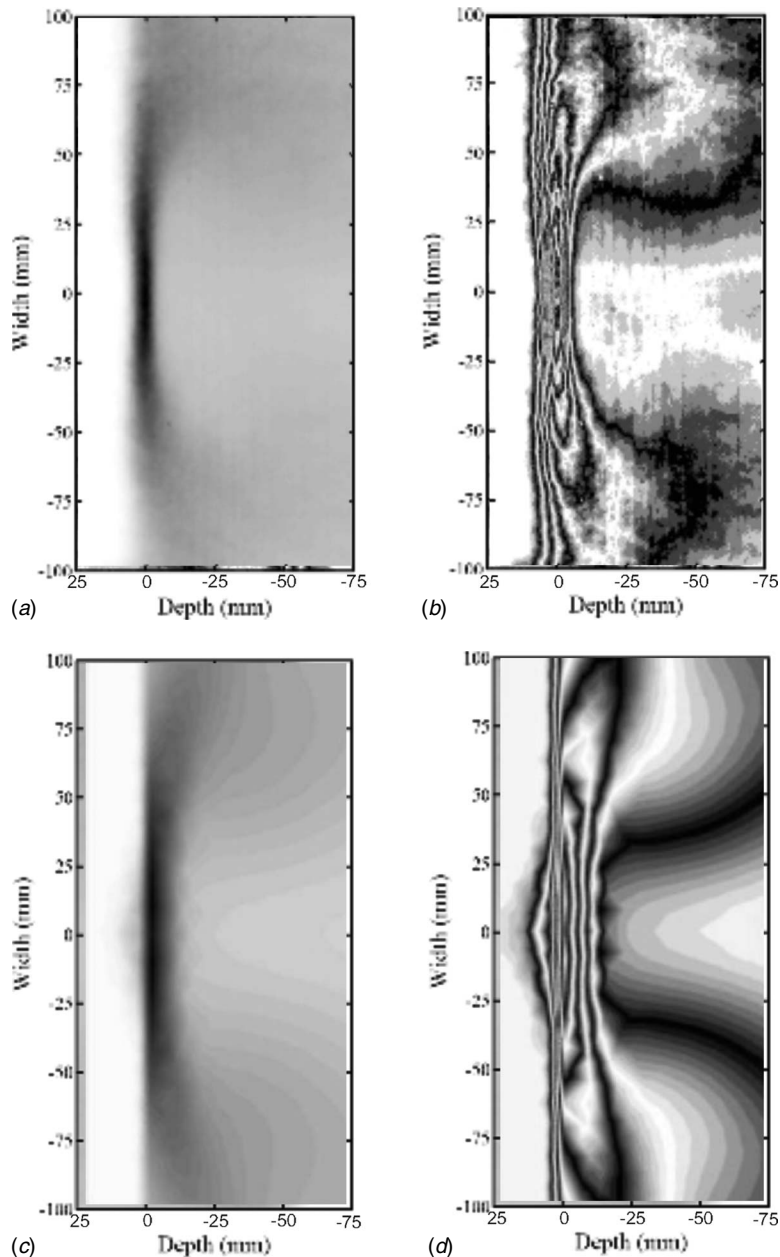


Fig. 4 Experimental ((a) and (b)) and CFD ((c) and (d)) concentration profiles. Linear and sawtooth concentration scales are shown so flow structures can be compared. The cross-flow moves from left to right with the jet fluid moving out of the page. The step is located at 0 mm.

maximum thickness of 10 cm, and the expansion factors used were 1.1 for the coarse and medium grids and 1.08 for the fine grid. There were 15 inflated layers in the coarse grid, 20 in the medium, and 30 in the fine grid. Each grid also had a region of refinement around the step because this was the region with the largest flow gradient and also the area of greatest interest. Two cylindrical regions located along the two corners of the step with a radius of 8 cm were used for grid refinement. In these regions the spacing between nodes was 0.8 cm, 0.6 cm, and 0.5 cm, respectively, for the coarse, medium, and fine grids. The expansion factor in these regions was 1.1 for the coarse and medium grids and 1.07 for the fine grid. With these characteristics, the number of nodes for each grid were 99,646, 198,341, and 397,942. This led to a grid refinement factor, r , of 2.0.

3.1.3 Solver Parameters. The software used a “coupled multigrid solver” to solve the linear system of discretized equations.

The advection scheme selected in the CFX software was the “high resolution advection scheme.” For this, CFX defines a blending factor, which will be referred to as ϕ (but is β in the CFX manual), which represents the order of the numerical scheme, with $\phi=0$ representing an upwind differencing scheme and $\phi=1$ representing a second order accurate scheme. The high resolution advection scheme set ϕ as close to 1 as possible without introducing oscillations into the flow. This resulted in ϕ being variable throughout the flow with a solution, which was greater than first order accurate throughout the domain though not fully second order. Values of ϕ for a line along the jet centerline for the vertical velocity component is shown as an example in Fig. 7.

The standard $k-\epsilon$ model with a scalable wall function was used for the turbulence within the flow. The coefficients for this model were $C_{\mu}=0.09$, $C_{\epsilon 1}=1.44$, $C_{\epsilon 2}=1.92$, $\sigma_k=1.0$, and $\sigma_{\epsilon}=1.3$. The scalable wall function [10] limits the value of y^* (to be greater

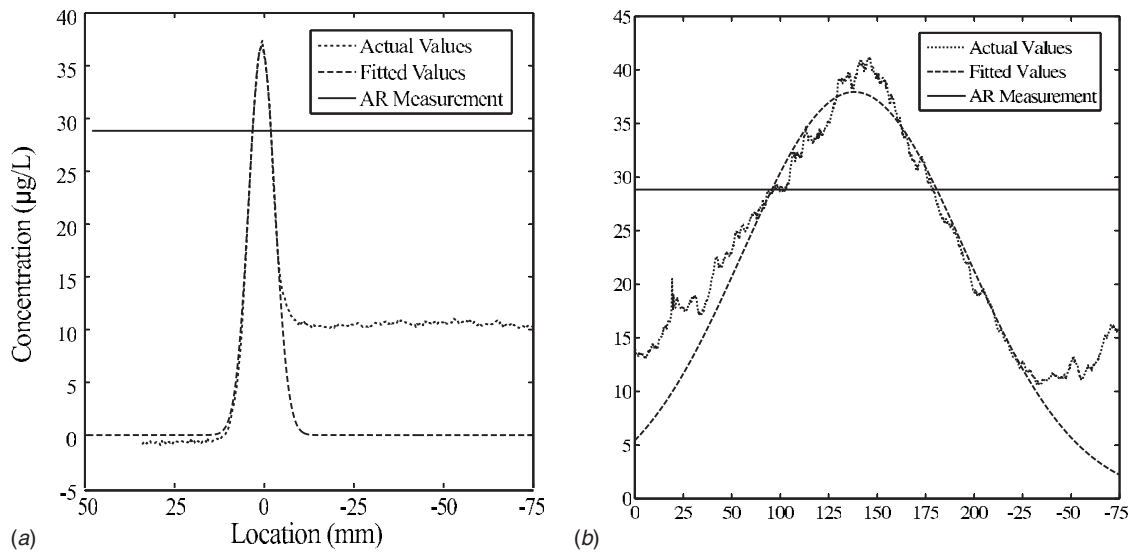


Fig. 5 Measured concentrations along the maximum depth line (a) and the maximum width line (b). The horizontal line shows the 70% value where the depth and width are measured. A threshold value of 60% of the maximum concentration was used to determine the Gaussian fit.

than 11.06) to avoid placing mesh points within the viscous sub-layer (which produces the inconsistencies outlined by Grotjans and Menter [11]). Although the $k-\epsilon$ method has been shown to overpredict turbulent spreading in round jets and can “fail profoundly” for three-dimensional flows [12], it provided fast convergence and was sufficiently robust for all of the flow conditions. Other methods, such as the shear stress transport model and two

Reynolds stress models (Baseline Wilcox Model and Speziale-Sarkar-Gatski Model), were tested but produced oscillatory results for the conditions used and would not converge.

A stationary solution was found for the simulation in order to minimize its computational cost. Since the experiments were performed to determine averaged concentration intensities, a steady state approximation was all that was required. The timescale and length scale used in the solution used the default settings: automatic and conservative, respectively. The required convergence level was set to an average residual of 10^{-6} . The effect of the residual on the jet perimeter is shown in Table 1. This shows that the choice of residual causes less than a 1% variation in the perimeter. The passive scalar transport equation was used to determine the movement of the scalar throughout the flow. It was assumed the concentration variable was a volumetric scalar. The remainder of the tuning parameters present in the software remained at their default settings.

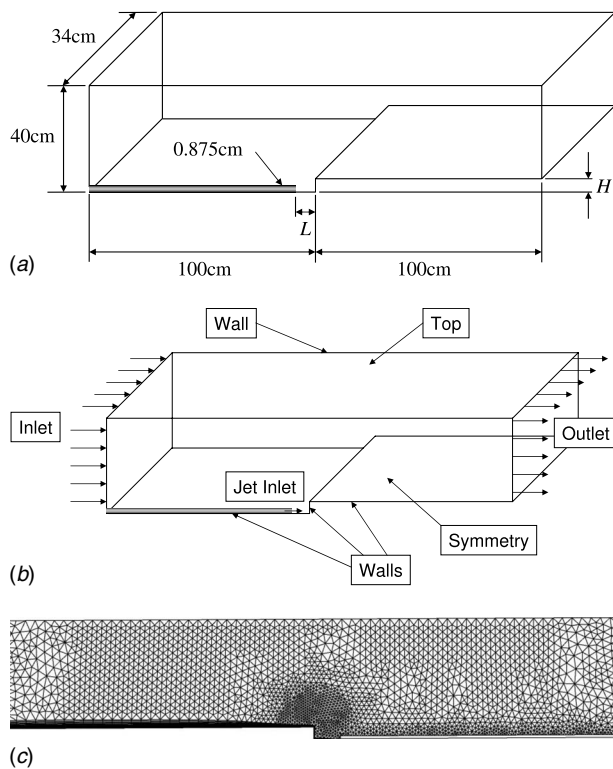


Fig. 6 Physical definitions in the CFD code. Dimensions were chosen to match the water channel facility used for the experiments (a). The type and locations of the boundary conditions are given in (b). The coarse mesh, which was used for the simulations (with the exception of the grid refinement study), is given viewed along the symmetry plane in (c).

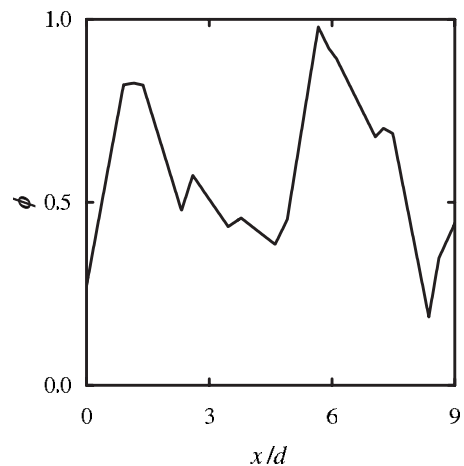


Fig. 7 Variation in ϕ , the blending factor used in the CFD code, where $\phi=0$ represents a first order method and $\phi=1$ represents a second order method. Values are for the vertical velocity along the major axis of the elliptical cross section in the measurement plane. The global order of the solution was found to be 1.2, which corresponds to a ϕ value of approximately 0.2.

Table 1 Effect of the average maximum residual used for convergence on perimeter measurement. To save computational time, a residual of 10^{-6} was used for the simulations.

Residual	Perimeter (mm)
1×10^{-05}	220.6
1×10^{-06}	222.9
1×10^{-07}	220.9
1×10^{-08}	220.9

3.1.4 Grid Independence and Uncertainty. The uncertainty in the results produced by this simulation was determined primarily through the methods outlined by Roache [13]. The validation method defines a grid convergence factor (*GCI*) which is given in Eq. (3). The *GCI* is meant to be used as both an estimate of the error bars, which surround the simulation data and a method of reporting grid convergence. The error is approximated for the coarse grid using the fine grid as a reference [13]

$$GCI_2^{\text{coarse}} = F_s |E_2| \quad (3)$$

where F_s is a safety factor, for which a value of 3.0 is recommended for conservative estimates of the errors [13]. E_2 is defined in Eq. (4)

$$E_2^{\text{coarse}} = \frac{r^p \varepsilon}{1 - r^p} \quad (4)$$

where $\varepsilon = f_2 - f_1$ gives the variation in the parameter of interest (perimeter for this case) between the coarser grid (2) and the finer grid (1). r is the refinement factor, which is the ratio between the size of the control volumes between the coarse and fine case. p is the formal order of accuracy of the algorithm, which is defined in Eq. (5).

The order of accuracy of the simulation algorithm (p) can be calculated through the use of a three grid refinement study, providing the grid refinement ratio is constant [14]. The equation defining the order [14] was used in the formulation of the *GCI*, so Roache's [13] notation is used, shown in Eq. (5). In this study, the parameter of interest is the perimeter of the vertical jet issuing from the step, denoted by f in the general form [13]

$$p = \ln\left(\frac{f_3 - f_2}{f_2 - f_1}\right) / \ln(r) \quad (5)$$

where f is the parameter of interest in the three grids being tested, with the subscripts 1, 2, and 3 representing the finest, medium, and coarsest grids studied.

For the study presented here, the order, p was found to be 1.2. From this, the coarse *GCI* (relating the medium grid to the coarse grid) was calculated for the jet's perimeter and found to have a value of 28 mm, and represents the approximate error bars for the system (due to the discretization error). If more computing resources were available, the fine grid could be used, which had a *GCI* (when compared with the medium grid) of 12.2 mm. It was found that the grids were all within the range asymptotic convergence, and the solution was found to be 1.2 orders accurate [13]. Truncation errors for low order systems (like this simulation) have been shown by researchers [15] to cause significant effects on the modeled flow behavior. The truncation errors from the scheme used here (1.2 orders accurate) cause an artificial viscosity to be incorporated into the flow, leading to the overprediction of diffusion within the flow. Thus, it is expected that this model will overpredict the spreading rate of the jet.

The third primary source of uncertainty in this study is caused by the assumptions implicit in the $k-\varepsilon$ model. The $k-\varepsilon$ model, though commonly used in flow studies, was designed primarily for two dimensional shear flow problems. The model assumes that

“zero velocity gradient is accompanied by zero shear stress” [16]. In cases with large streamline curvatures and large pressure gradients, such as impinging jets, the $k-\varepsilon$ model can be inaccurate [12]. Cusworth [3] found that the $k-\varepsilon$ model significantly overpredicted (on the order of 30%) the turbulent kinetic energy and thus the spreading rate of a free round jet. The model can also highly overpredict the rate of heat (or scalar) transfer within flows [4]. From this, it can be assumed that the use of the $k-\varepsilon$ model will lead to the overprediction of diffusion and the spreading of the jet in the study presented here. Modifications of the coefficient in the eddy viscosity C_μ term can minimize this overprediction [17] and could be used later to improve the accuracy of this model.

It has been shown that there are large uncertainties in the solution method used for this study due to modeling, truncation, and discretization. It should be expected that the CFD results significantly overpredict the spreading rate of the jet. This simulation is, however, computationally inexpensive; predictions of the trends in the jet perimeter for parametric studies could be very valuable. Further improvements on the computational model could be made to improve the predictions of the jet perimeter in the future. However, the purpose of this study was to determine the feasibility of using CFD to predict experimental data.

3.2 Perimeter Measurement Method. CFD results were analyzed to determine the perimeter and aspect ratio of the ellipse encircling the 70% of the maximum concentration contour lines of the flow. This was measured by analyzing the contour lines along a horizontal plane located at the top of the step ($z=0$ mm). Contours on this plane are shown in Fig. 4 (parts c and d) for a standard case. From this, the 70% contour was isolated and measured to determine the width and depth of the contour using the tools available in CFX. The perimeter and aspect ratio were then calculated for the CFD results in the same manner as the experimental results.

4 Experimental Results

Experiments were done to determine the effects of three parameters: L , H , and R . The results of this parametric study are shown in Fig. 8. The data plotted here show the average of all of the tests taken at each flow condition (typically two runs). The error bars were determined by taking two times the standard deviation of one condition where five tests were run. Figure 8(a) shows the relation between perimeter and length is nearly linear for all of the step heights. Figure 8(b) shows the effect of the step height, which is also possesses linearity. Figure 8(c) shows the perimeter compared with the logarithm of the velocity ratio for a constant step height ($H=38.1$ mm) and a constant length ($L=9d$). It can be seen in these figures that the data is dependent on L , H , and R . These data were used to create the universal scaling law for this geometry proposed in Sec. 5.

5 Discussion

5.1 Empirical Perimeter Correlation. An empirical correlation predicting the perimeter of the jet based on R , L , and H was determined using the data presented above. In order to better fit the model, the length L was altered to the distance from a point momentum source to the step (L_c), located five diameters behind the jet outlet. This produced the empirical correlation given in Eq. (6), and shown in Fig. 9. From the fit, it can be seen that this model predicts the perimeter within 13% error for all of the data points. This correlation provides allows for the perimeter of the jet entering the cross-flow to be predicted for any H , L_c , and R within the range tested

$$\frac{P}{d} = 1.84R^{0.2} \left(\frac{HL_c}{d^2} \right)^{1/2} - 5.79 \quad (6)$$

Both Eq. (6) and Fig. 9 normalize the perimeter by the inlet jet diameter. This scaling is not fully justified by the experiments, as

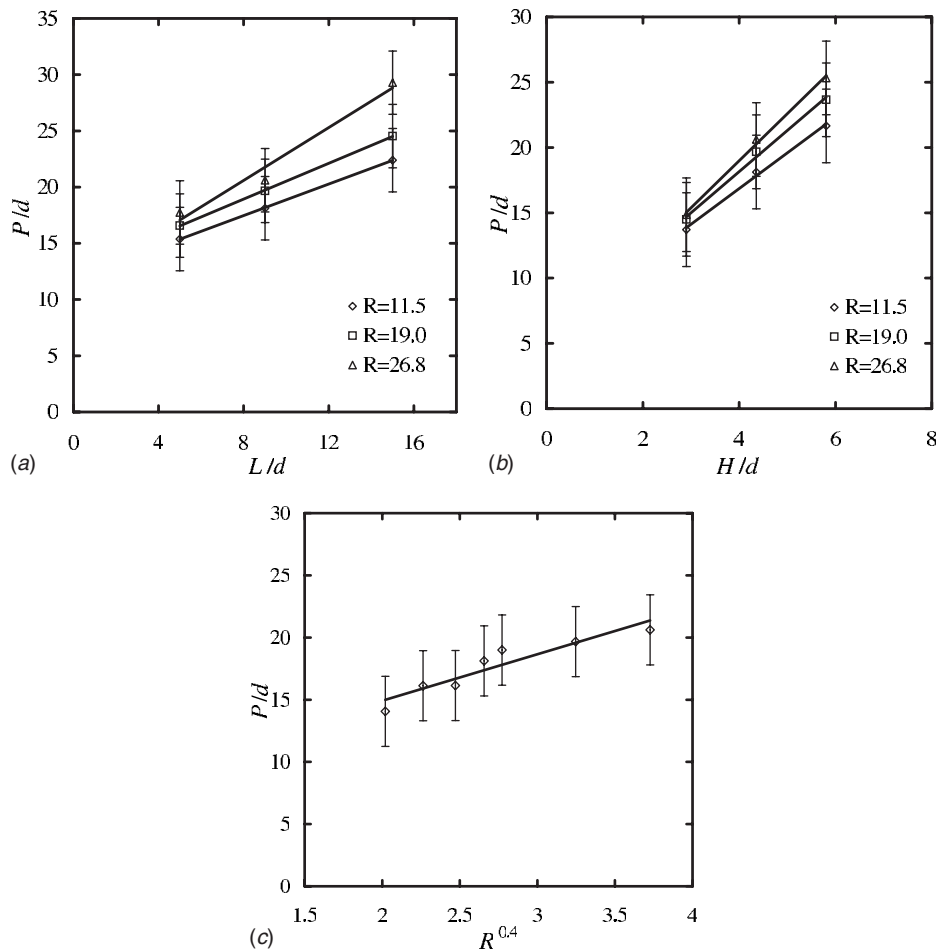


Fig. 8 Measured values of perimeter compared with the different inlet conditions, normalized with the jet diameter d . The effect of the step position (L) with different velocity ratios and a constant step height is shown in (a). The effect of the step height (H) at different velocity ratios is shown in (b). The effect of velocity ratio R for a single step height and length is shown in (c).

only one diameter was tested. The diameter is a convenient factor, which is used frequently in the literature for nondimensionalizing length units. Further experiments are required to fully justify this scaling. Attempts at finding a different length scale to produce

nondimensional groups were unsuccessful, however, it may be found that a turbulence or friction length scale could be used instead of the jet diameter.

5.2 Experimental Aspect Ratio Correlation. To fully define the shape of the ellipse representing the vertical jet entering the cross-flow, the perimeter, and aspect ratio (S) are required. The experimental correlation for S related to the inlet conditions is given in Eq. (7) and shown in Fig. 10. In this correlation it is apparent that the ratio of H and L_0 is used instead of their product (as used in Eq. (6)). As L_0 increases, the wall jet grows vertically, which upon impingement leads to increased depth in the ellipse. It was found that the rate of growth of the depth is significantly larger with L_0 than H when compared with the growth of the width. This leads to a decrease in S with increasing L_0 .

$$S = 8.38 \left(\frac{H}{L_0} \right)^{0.3} R^{0.4} \quad (7)$$

5.3 Comparison of CFD to Experimental Data. A comparison of the concentration profiles along the measurement plane is shown in Fig. 4. Parts (a) and (c) show the concentration profile on a linear scale, which appears to have similar shapes for both the actual and modeled jets. Parts (b) and (d) used a sawtooth concentration profile, which emphasized the structures in the flow. From this, it can be seen that the simulation accurately predicted

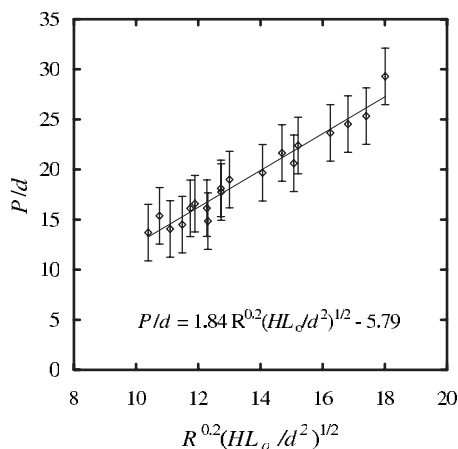


Fig. 9 Measured perimeters compared with the experimental fit outlined in Eq. (6). The error bars represent twice the standard deviation of the condition where five tests were taken.

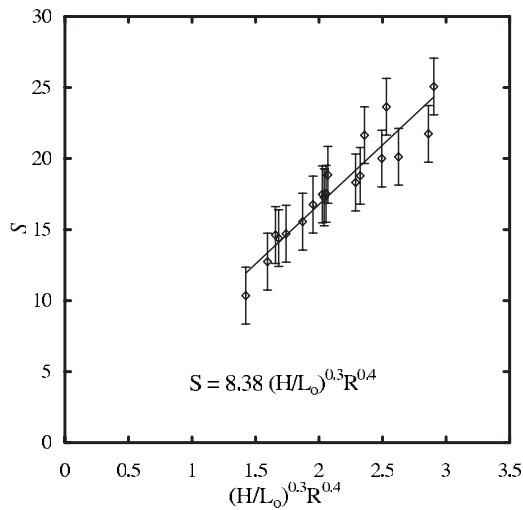


Fig. 10 Experimental correlation for the jet aspect ratio S (defined in Eq. (7)) based on the step height H , effective distance to the step L_0 , and velocity ratio R

the elliptical shape of the vertical jet, though with slightly larger depth than the experimental case. The location of the counter-rotating vortex pair downstream of the jet is also accurately predicted by the simulation. The comparison of the flow visualization images shows that the CFD code can clearly predict mean characteristics of this flow.

The perimeters of the ellipses formed by the 70% contours for all of the experiments and simulations are shown in Fig. 11. A comparison of the aspect ratios is shown in Fig. 12. This figure shows significant overlap between the CFD and experimental results. It can be seen that the perimeters predicted by the simulation do not match those determined experimentally within error. As can be seen in Fig. 11, the jet perimeter predicted through the numerical model is significantly larger than the measured values. According to Pope [12], “a well-known deficiency of the k -epsilon model is that it significantly overpredicts the rate of spreading for the round jet.” This increased spreading would lead to an increase in the jet’s perimeter. Since the overprediction of the spreading is equal in all directions, it has little effect on the

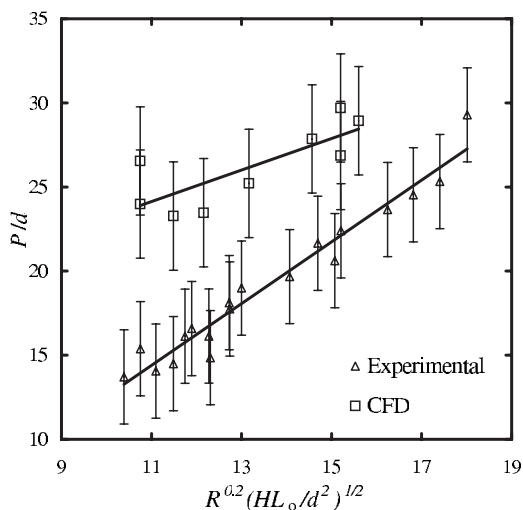


Fig. 11 Comparison of CFD results to experimental results using the scaling relation given in Eq. (6). CFD results slightly overpredict the perimeter due to the artificial viscosity introduced into the flow by the k - ϵ turbulence model and the low order of the simulation.

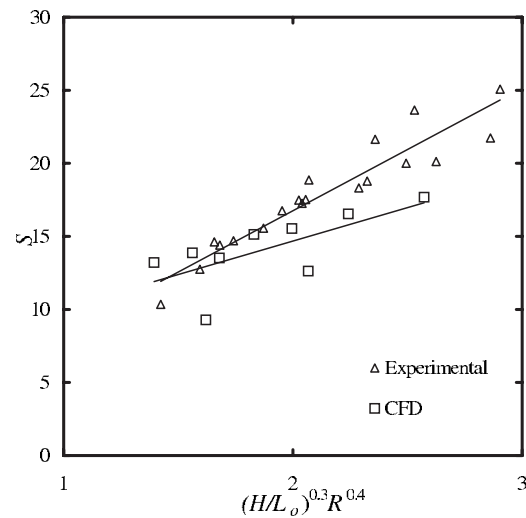


Fig. 12 Comparison of aspect ratio measurements S for CFD results and experimental results in terms of the step height H , effective distance to the step (L_0), and velocity ratio R

jet’s aspect ratio, as shown in Fig. 11. They do however predict a similar trend and could be used to provide a reasonable prediction for the perimeter based on the inlet conditions if the constant overprediction caused by the artificial viscosity introduced into the flow is taken into account. The error bars shown here are those recommended by Roache [13] and equal to the GCI outlined in Eq. (3). Despite the prediction of the trend, the error bars are significant and it should be noted that a horizontal line with a value of approximately $P/d=25$ can be drawn through the error bars.

Through comparing the CFD data to the experimental data, it can be seen that the CFD model can give a reasonable estimate of the actual value of the perimeter. The trend in the data is predicted to within 30%, with a constant overprediction of about 50%. This gives a reasonable order of magnitude prediction and can also be used to perform further parametric studies on the effects of different flow conditions.

6 Conclusions

The findings of a study on a jet impinging onto a forward facing step in a uniform cross-flow have been presented. It has been shown that after the initial impingement, the jet leaves the step as a high aspect ratio elliptical jet and enters into the cross-flow. The perimeter and aspect ratio of the jet were found to be dependent on H , L , and R and can be predicted with the relations given in Eqs. (6) and (7). CFD measurements were found to accurately predict the structures within the flow and provided a reasonable estimate of the jet perimeter. The trends of the parametric study predicted by the CFD model were found to follow those measured experimentally.

This paper presents predictive correlations for the size and shape of the jet issuing into the cross-flow after impingement. A study is in progress, which uses these measurements to predict the trajectory of the jet in cross-flow. Through that study and the use of the experimentally measured predictive model developed here, the trajectory of the mean plume can be predicted using only the initial conditions of the flow.

Acknowledgment

The work presented here was made possible by NSERC research grants to B.A.F. and D.J.W., and an NSERC graduate scholarship to D.C.L.

Nomenclature

- ϕ = blending factor in CFD code
 a = width of elliptical cross section
 b = depth of elliptical cross section
 d = jet diameter, m
 F_s = safety factor in GCI calculation
 H = step height, m
 L = distance from jet inlet to step, m
 L_o = distance from point source to step, m
 p = order of accuracy of CFD code
 P = perimeter of vertical jet, mm
 r = grid refinement ratio
 R = jet to cross-flow velocity ratio
 S = jet aspect ratio
 V_∞ = cross-flow velocity, m/s
 V_{jet} = jet velocity, m/s
 z = height above the step

References

- [1] Wilson, D. J., 1979, "The Release and Dispersion of Gas From Pipeline Ruptures," Alberta Environment, Contract No. 790686.
- [2] Walker, D. A., 1987, "A Fluorescence Technique for Measurement of Concentration in Mixing Liquids," *J. Phys. E*, **20**, pp. 217–224.
- [3] Cusworth, R. A., and Sislian, J. P., 1987, "Computation of Turbulent Free Isothermal Swirling Jets," University of Toronto Institute for Aerospace Studies, Technical Report No. 315.
- [4] Behnia, M., Parneix, S., and Durbin, P. A., 1998, "Prediction of Heat Transfer in an Axisymmetric Turbulent Jet Impinging on a Flat Plate," *Int. J. Heat Mass Transfer*, **41**(12), pp. 1845–1855.
- [5] Hilderman, T. L., and Wilson, D. J., 2007, "Predicting Plume Meandering and Averaging Time Effects on Mean and Fluctuating Concentrations in Atmospheric Dispersion Simulated in a Water Channel," *Boundary-Layer Meteorol.*, **122**, pp. 535–575.
- [6] Shahzad, K., Fleck, B. A., and Wilson, D. J., 2007, "Small Scale Modeling of Vertical Surface Jets in Cross-Flow: Reynolds Number and Downwash Effects," *ASME J. Fluids Eng.*, **129**, pp. 311–318.
- [7] Johnston, C. R., and Wilson, D. J., 1997, "A Vortex Pair Model for Plume Downwash Into Stack Wakes," *Atmos. Environ.*, **31**(1), pp. 13–20.
- [8] Powell, I., 1987, "Design of a Laser Beam Line Expander," *Appl. Opt.*, **26**(17), pp. 3705–3709.
- [9] Torres, L. A., 2008, "Turbulent Round Jet in a Counter Flow: Effects of Small Inlet Yaw Angle," MS thesis, University of Alberta, Edmonton, Alberta, Canada.
- [10] Launder, B. E., and Spalding, D. B., 1974, "Numerical Computation of Turbulent Flows," *Comput. Methods Appl. Mech. Eng.*, **3**, pp. 269–289.
- [11] Grotjans, H., and Menter, F., 1998, "Wall Functions for General Application CFD Codes," *Proceedings of the Fourth European Computational Fluid Dynamics Conference*, Wiley, New York, Vol. 1, pp. 1112–1117.
- [12] Pope, S. B., 2000, *Turbulent Flows*, Cambridge University Press, New York.
- [13] Roache, P. J., 1997, "Quantification of Uncertainty in Computational Fluid Dynamics," *Annu. Rev. Fluid Mech.*, **29**, pp. 123–160.
- [14] de Vahl Davis, G., 1983, "Natural Convection of Air in a Square Cavity: A Bench Mark Numerical Solution," *Int. J. Numer. Methods Fluids*, **3**, pp. 249–264.
- [15] Fletcher, C. A. J., 1991, *Computational Techniques for Fluid Dynamics*, 2nd ed., Springer-Verlag, Berlin, Vol. 1.
- [16] Andreasson, P., and Svensson, U., 1992, "A Note on a Generalized Eddy-Viscosity Hypothesis," *ASME J. Fluids Eng.*, **114**, pp. 463–466.
- [17] Hanjalić, K., 1994, "Advanced Turbulence Closure Models: A View of Current Status and Future Prospects," *Int. J. Heat Fluid Flow*, **15**(3), pp. 178–203.

Large-Eddy Simulation of Wake and Boundary Layer Interactions Behind a Circular Cylinder

S. Sarkar¹

e-mail: subra@iitk.ac.in

Sudipto Sarkar

Department of Mechanical Engineering,
Indian Institute of Technology Kanpur,
Kanpur-208016, India

*Large-eddy simulations (LESs) of flow past a circular cylinder in the vicinity of a flat plate have been carried out for three different gap-to-diameter (G/D) ratios of 0.25, 0.5, and 1.0 (where G signifies the gap between the flat plate and the cylinder, and D signifies the cylinder diameter) following the experiment of Price et al. (2002, "Flow Visualization Around a Circular Cylinder Near to a Plane Wall," *J. Fluids Struct.*, **16**, pp. 175–191). The flow visualization along with turbulent statistics are presented for a Reynolds number of $Re = 1440$ (based on D and the inlet free-stream velocity U_∞). The three-dimensional time-dependent, incompressible Navier–Stokes equations are solved using a symmetry-preserving finite-difference scheme of second-order spatial and temporal accuracy. The immersed-boundary method is employed to impose the no-slip boundary condition at the cylinder surface. An attempt is made to understand the physics of flow involving interactions of shear layers shed from the cylinder and the wall boundary layer. Present LES reveals the shear layer instability and formation of small-scale eddies apart from their mutual interactions with the boundary layer. It has been observed that G/D ratio has a large influence on the modification of wake dynamics and evolution of the wall boundary layer. For a low gap ratio, it is difficult to identify the boundary layer because of its strong interactions with the shear layers; however, a rapid transition to turbulence of the boundary layer, which is similar to bypass transition, is observed for a large gap ratio. [DOI: 10.1115/1.3176982]*

Keywords: wake-boundary layer interactions, shear layer transition, LES, IB method

1 Introduction

The vortex shedding and the aerodynamic forces of flow past a circular cylinder near a plane wall have been the subject of many studies for academic interests and for practical applications. This kind of study can directly be related to many engineering problems, such as flow past a suspension bridge, pipelines near the ground, flow through heat exchanger tubes near the wall, forced air-cooling of board-mounted electronic components, etc. The most attractive feature of flow over a circular cylinder, when the Reynolds number (Re) is close to around 50, is the instability of symmetric wake and the onset of a time-periodic alternate vortex shedding (two-dimensional (2D)), known as the Kármán vortex street. The formation of this vortex street is generally considered to be the result of the Kelvin–Helmholtz instability with separated shear layers. By further increasing the Re , a transition to three-dimensional flow occurs when the Re is close to 180; however, the vortex shedding phenomenon retains the dominant large-scale structure at a higher Re in the turbulent wake [2,3]. This alternate shedding of vortices in the near wake leads to large fluctuating pressure forces in a direction transverse to the flow that may cause structural vibration, acoustic noise, or resonance.

The presence of a wall close to the cylinder changes the dynamics of vortex shedding as compared with the unbounded condition. The impermeability of the wall offers an irrotational constraint to the cylinder wake that cannot spread without limit resulting in a finite mean force directed away from the wall. The boundary layer presents a nonuniform velocity in front of the cylinder, which causes asymmetry in the strength of vortex shed-

ding. Furthermore, the vorticity shed from the cylinder interacts with the vorticity of the boundary layer downstream resulting in an excited wake-induced boundary layer with complex flow structures. If the gap between the cylinder and the wall is relatively low, this interaction is strong, provoking the separation of the boundary layer apart from a drastic change in the entire wake. Thus, the dynamics of vortex shedding in presence of a wall are influenced by the approaching boundary layer thickness, Reynolds number, and gap between the cylinder and the wall. These factors also control the evolution of boundary layer, its transition under excitation of migrating wake. In brief, the major modifications of flow dynamics past a cylinder in the vicinity of a wall can be identified as (1) deflection of the boundary layer away from the flat plate, (2) suppression of vortex shedding from the lower half of the cylinder, (3) presence of separation bubble both upstream and downstream of the cylinder, and (4) a significant change in flow parameters, such as lift, drag coefficients, and Strouhal number.

One of the very early experiments in this area was performed by Taneda [4]. A circular cylinder close to a wall was towed through the stagnant water at a low Reynolds number $Re=170$, where there was no effect of boundary layer. He observed a single vortex row behind the cylinder for a small gap ratio $G/D=0.1$ with re-establishment of a regular double row of vortices as the gap ratio was increased to $G/D=0.6$; the row of vortices became unstable and broke down downstream. Several experiments were conducted for flow around a cylinder in the presence of the boundary layer at moderately high Reynolds number, from $Re = 2 \times 10^4$ to 10^5 [5–8]. In most of these cases, the approaching boundary layer was turbulent. It was reported that the aerodynamic forces on the cylinder were modified with a slight variation in shedding frequency. The suppression of vortex shedding was observed when the body was closer than a critical distance from the wall such that G/D ratio becomes 0.3–0.4 [5,9]. At smaller

¹Corresponding author.

Contributed by the Fluids Engineering Division of ASME for publication in the *JOURNAL OF FLUIDS ENGINEERING*. Manuscript received October 23, 2008; final manuscript received June 16, 2009; published online August 14, 2009. Assoc. Editor: Paul Durbin.

distances, the wake is almost steady and the periodic shedding is strongly inhibited with separation bubbles on the wall. Later, Lei et al. [8] reported that the suppression of vortex shedding occurs at a gap ratio of about 0.2–0.3; the value depends on the thickness of the turbulent boundary layer (δ). This critical gap ratio decreases as the thickness of the boundary layer increases and it appears relatively independent of Reynolds number.

When the cylinder is placed close to a wall, the frontal stagnation point moves toward the wall producing an upward lift (C_L) on the cylinder with a consequence of deviation of the wake away from the wall. This increases the base pressure resulting in a low mean value of coefficient of drag, C_D , although its value depends on the boundary layer, its character and thickness. Furthermore, the rms values of both C_L and C_D decrease as the wall is approached. This may be attributed to the diffusion of velocity fluctuations because of the boundary layer [7,8]. Angrilli et al. [10] conducted the experiment of cylinder wake and boundary layer interactions at $Re=2.8 \times 10^3$ to 7.6×10^3 and found an influence of G/D ratio on vortex shedding frequency if the gap ratio is less than 5.0, whereas others observed that the shedding frequency was almost independent of gap ratio [5–8,11]. A possible reason of this difference is the different range of Re used in the previous experiments.

The flow around a circular cylinder near a wall was demonstrated in Ref. [1] with the help of particle image velocimetry (PIV) and hot-film anemometry for Re in the range of 1200–4960 and G/D ratio of 0–2. It was concluded that G/D was a major factor for the change in flow characteristics. The flow interactions between the cylinder wake and the boundary layer were divided in four regimes based on G/D ratio. For $G/D < 0.125$, the flow beneath the cylinder was suppressed, and separation of boundary layer occurred both upstream and downstream of the cylinder. Although there was no regular vortex shedding, a periodicity associated with the outer shear layer was found. For $0.125 < G/D < 0.5$, the separation region decreased, but the flow characteristics were the same as that of the previous regime. A strong coupling between the inner-shear layer shed from the cylinder and the wall boundary layer was observed because of opposite sign of vorticity. For $0.5 < G/D < 0.75$, the vortex shedding was first observed and for $G/D > 1.0$, there was no separation of the wall boundary layer either upstream or downstream of the cylinder. The paper presented the flow structures and modification of wake dynamics in low subcritical range of Reynolds number, where the variation in Strouhal frequency (St) with gap ratio was mainly dependent on Re . For $Re < 2600$, the Strouhal number for $G/D < 2$ was significantly greater than that of an isolated cylinder. But as Re increased ($Re > 4000$), St became insensitive to the G/D ratio. However, the aerodynamic forces, the mean velocity field and turbulence characteristics were not discussed.

As compared with the experiments, there are a few numerical simulations of flow past a circular cylinder in the vicinity of flat plate. Vada et al. [12] were the first to perform a 2D simulation using vortex in cell method at a transcritical Reynolds number, $Re=3.6 \times 10^6$ and $G/D=0.4, 0.8, \text{ and } 1.5$. The simulation suffered from overprediction of drag coefficient and underprediction of lift coefficient as compared with the experiment [11]. Liou et al. [13] performed a large-eddy simulation (LES) of the turbulent wake behind a square cylinder for a $Re=2.2 \times 10^4$, and the discussion was focused on the phase-averaged vortex dynamics. The celerity of the positive vortex shed from the lower side of the cylinder was smaller than that of the upper side shed vortex due to the interaction with the boundary layer. Recently in Ref. [14], a 2D simulation of cylinder-boundary layer interaction with $\psi-\omega$ formulation was presented, and the flow features were explained by vortex dynamics comparing with the experiment [1] for $Re=1200$ and $G/D=0.5$ and 1.5 . The computation illustrated larger vortical structures as compared with the experiment with rollout of vortices closer to the cylinder. This was attributed to the fact that the

absence of spanwise direction in 2D simulation failed to redistribute the energy in the third direction developing unrealistic large structures [15].

There are number of experiments illustrating flow around a circular cylinder in the vicinity of a wall, but the discussions were largely focused on vortex shedding process and modification of aerodynamic forces on the cylinder. Most of the numerical simulations made so far on this flow configuration are in two-dimensional framework and elucidate the flow characteristics with limited success particularly for high Reynolds numbers. Thus, the objective of the present paper is to characterize the vortex shedding, either qualitatively or quantitatively, illustrating the flow physics in terms of vortex stretching, breakdown and turbulence generation. Here, we try to explain the mutual interactions, i.e., modification of wake dynamics due to the presence of the boundary layer and the excitation of boundary layer because of the wake. It should be noted that the eddy motions and their interactions are expected to be resolved to understand the dynamical process in turbulent flows for the concerned problem. A direct numerical simulation (DNS) would have been ideal for the problem, but it is extremely costly and Reynolds-averaged Navier–Stokes calculations will not provide the answer. Hence, LES can be pursued as an alternative means with the benefit being a considerably lower computational effort. In the present study, a 3-D LES with a dynamic subgrid-scale model has been used to investigate the flow around a cylinder in proximity to a wall boundary layer at $Re=1440$ and for G/D of 0.25, 0.5 and 1.0. The Reynolds number considered here is in the range of shear layer transition [3].

2 Numerical Methods

2.1 Governing Equations. In the present study, we perform LES of incompressible flow. The filtered mass and momentum equations can be expressed as,

$$\frac{\partial \bar{u}_j}{\partial x_j} = 0 \quad (1)$$

$$\frac{\partial \bar{u}_i}{\partial t} + \frac{\partial}{\partial x_j} (\bar{u}_j \bar{u}_i) = -\frac{1}{\rho} \frac{\partial \bar{P}}{\partial x_i} + \frac{1}{Re} \nabla^2 \bar{u}_i - \frac{\partial \tau_{ij}}{\partial x_j} + \bar{f}_i \quad (2)$$

where, \bar{u}_i denotes the filtered velocity field and $\tau_{ij} = \overline{u_i u_j} - \bar{u}_i \bar{u}_j$ is the residual stress tensor (also known as subgrid-scale stress, SGS). The presence of the body forces \bar{f}_i is due to the immersed-boundary (IB) method, which will be discussed later. The above equations have been made dimensionless using the inlet free-stream velocity U_∞ and the cylinder diameter D . The resulting Reynolds number is defined as $Re = U_\infty D / \nu$, ν being the kinematic viscosity. The model proposed by Germano et al. [16] and modified by Lilly [17] is used here to include the effect of subgrid motions in the resolved LES, where the model coefficient is dynamically calculated instead of input a priori. The momentum advancement is explicit using the second-order Adams-Bashforth scheme, except for the pressure term, which is solved by a standard projection method [18]. The pressure equation is discrete Fourier transformed in the spanwise direction (an infinite cylinder is assumed neglecting end effects and hence the flow can be considered homogeneous allowing periodicity of flow to be imposed) and is solved by the BI-CG algorithm [19] in the other two directions. The spatial discretization is second-order accurate on a staggered mesh arrangement using a symmetry-preserving central-difference scheme, which is widely used in LES owing to its nondissipative and conservative property [20,21].

Here, the simulations of flow past a cylinder in proximity to a wall have been performed in the Cartesian grid considering the origin of axes lies on the flat plate and at a distance of $10D$ from the leading edge. The coordinates x, y, z denote the streamwise, wall-normal and spanwise directions respectively and the corre-

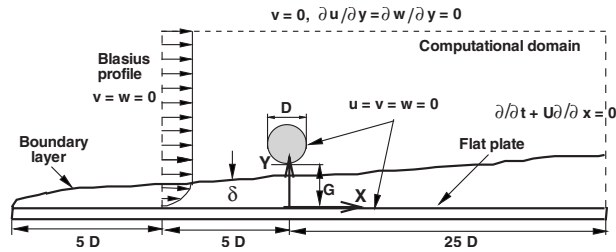


Fig. 1 Computational configuration and boundary conditions

sponding velocities are denoted by u , v and w . The computational domain and boundary conditions used here are illustrated in Fig. 1. The domain extends from $-5D$ at the inflow to $25D$ at the outflow with a spanwise length of $3D$. It should be noted that the same span was used in Refs. [20,22,23], while simulating the flow around a circular cylinder in unbounded condition for the shear layer transition region. It was also reported that doubling the domain in the spanwise direction did not affect the results significantly [23]. In the wall-normal direction, the domain is extended up to $9D$ for $G/D=1.0$ and $8.5D$ for $G/D=0.25, 0.5$.

A Blasius profile is imposed at the inlet considering the computational domain begins at $5D$ distance downstream from the leading edge of the flat plate, where the boundary layer thickness is considered as $0.295D$ (calculated from boundary layer theory). A nonreflecting boundary condition [24] is applied at the exit. The no-slip boundary condition ($u=v=w=0$) is applied on the flat plate and on the cylinder surface. A free-slip velocity ($v=0$, $\partial u/\partial y = \partial w/\partial y = 0$) is imposed along the upper surface of the domain, which does not allow outflow through the top surface. This causes the flow to accelerate above the boundary layer in order to compensate for the growth of boundary layer. In our simulations, the maximum value of the acceleration parameter $K \equiv (\nu/U_\infty^2) \times (dU_\infty/dx)$ due to this effect was 1×10^{-6} and 5×10^{-7} for $G/D=0.25$ and 1.0 , respectively. The value of K at which a turbulent boundary layer is expected to relaminarize is around 3×10^{-6} [25]. Thus in the present case, the values of K assure that the acceleration of the free-stream would not alter the flow physics of wake and boundary layer interactions. In the spanwise direction, the periodic boundary condition is used.

The IB method helps to impose boundary conditions on a given surface not coinciding with the computational grid as in the present case. Thus, to satisfy the no-slip boundary conditions at the cylinder surface, the immersed-boundary technique is employed following Ref. [26], which belongs to the class of "direct forcing method." The velocity field near the boundary of the body is modified at each step in such a way that the no-slip boundary condition is satisfied on the surface. This is done using some interpolations, which is equivalent to include a body force f_i in the momentum equation. In this paper, a quadratic unidirectional interpolation by Muldoon and Acharya [27] is used. The flow solver has been extensively validated for a variety of transitional and turbulent flows [28–30], including simulation of vortex dynamics behind a circular cylinder for a wide range of Reynolds numbers [31,32].

2.2 Computational Details. In the streamwise direction, a uniform and refined mesh is used near the cylinder to get adequate immersed-boundary points on the cylinder surface. In the flow-normal direction, a refined and uniform mesh is employed near the wall (up to $y/D=2$ for $G/D=0.25, 0.5$ and $y/D=2.5$ for $G/D=1.0$) to resolve the wake behind the cylinder and its interaction with the boundary layer. Away from the cylinder, the mesh is slowly stretched out. A uniform mesh is used in the spanwise direction owing to the symmetry of the body.

In order to ensure the accuracy of calculations, a grid resolution test has been carried out for a gap ratio of $G/D=0.25$. The grid

requirements for the simulation of fully turbulent boundary layer using a second-order accurate LES solver are well known ($\Delta x^+ \approx 50$, $\Delta y_{\min}^+ < 1.0$ and $\Delta z^+ \approx 20$). However, the grid requirements to resolve the transitional flow or the boundary layer excited by external disturbances are less well established. Jacobs and Durbin [33] indicated that the prediction of boundary layer transition induced by free-stream turbulence (fst) is sensitive to streamwise resolution. Furthermore, Ovchinnikov et al. [34] illustrated that an under-resolved calculation predicts a premature and abrupt transition. In the case of bluff-bodies, two types of interactions of wakes with the boundary layer can be identified [35]: (i) a strong interaction, where the wake retains coherent eddies in the region of interaction, and (ii) a weak interaction, which takes place sufficiently far downstream of the cylinder when the spanwise rolls have decayed. The instant study falls in the first category, where the interactions occur on relatively larger scales, and it is anticipated that the grid requirements would be less restrictive as compared with the grid employed in the boundary layer transition by fst [33]. In the present computation, four levels of mesh, such as $288 \times 192 \times 32$, $384 \times 160 \times 32$, $384 \times 192 \times 32$, and $384 \times 192 \times 64$ (designated as grid 1, grid 2, grid 3, and grid 4) in the streamwise, wall-normal, and spanwise directions, respectively, are used. For grid 1, among 288 streamwise grid points, 32 points are distributed upstream of the cylinder ($-5D$ to $-D$), 96 points surrounding the cylinder ($-D$ to $+D$), 108 points near wake region ($+D$ to $+10D$) and rest are distributed in the far field downstream ($+10D$ to $+25D$), where as for other three mesh levels (384 points), the distribution is 40, 96, 160, and 88 in the respective regions. In the wall-normal direction, a total of 128 grid points with equal spacing are used between 0 and $2D$, and the remaining 64 points are slowly stretched away from the cylinder ($+2D$ to $+8.5D$) for grid levels 1, 3, and 4. For grid 2, the distribution is 96 and 64 in the respective regions. A total of 146 IB-points for u -velocity along the cylinder surface are obtained for grid level 3, as compared with 140 surface points used in Ref. [20] for a LES of flow past a circular cylinder at $Re=3900$. It should be noted that the boundary layer thickness assuming a laminar flow at the location of cylinder without its presence is $0.42D$, and approximately 27 grid points are employed within the boundary layer for grid 3.

The mean streamwise velocity (u/U_∞) and turbulent kinetic energy (TKE) profiles at $x/D=2, 3, 5, 7, 10$, and 15 are depicted in Fig. 2 for all four grid levels. The data are normalized by the free-stream velocity and the cylinder diameter. A maximum change of 1% in the mean velocity profiles is observed between grid 1 and grid 4 except at $x/D=3$ (Fig. 2(a)). However, appreciable changes in TKE profiles are seen between grid levels 1 and 4, Fig. 2(b). This indicates that there is a need for a large number of grid points in the near wake region and inside the boundary layer. For the subsequent analysis, grid 3 is chosen, considering the fact that there were no appreciable changes in both the mean velocity and TKE profiles by further increasing the grid points. In the near wake ($x/D=3$ to 15) region, nondimensional mesh spacing for grid 3 varies as $\Delta x^+=0.15-15$, $\Delta y^+=0.07-1.5$, and $\Delta z^+=0.1-7.5$. For $G/D=0.5$, the same computational domain and grid distribution are used as considered in $G/D=0.25$. The computational domain is extended by $0.5D$ in the wall-normal direction for $G/D=1$, keeping the streamwise domain unchanged. Here, a total of 160 grid points with equal spacing are used between 0 and $2.5D$, and 64 grid points are distributed in the remaining ($+2.5D$ to $+9D$) normal direction. Few parameters, such as the domain, grid distributions, and the values of Δx^+ , Δy^+ , and Δz^+ , averaged between $x/D=3$ to 15 and are summarized in Table 1 for different cases.

The time step was about $\Delta t = 1.125 \times 10^{-3} (D/U_\infty)$ in the nondimensional unit. This kept the Courant number below 0.2 for the entire simulation, and the viscous stability number was much less. The flow field was allowed to evolve for 15 vortex shedding

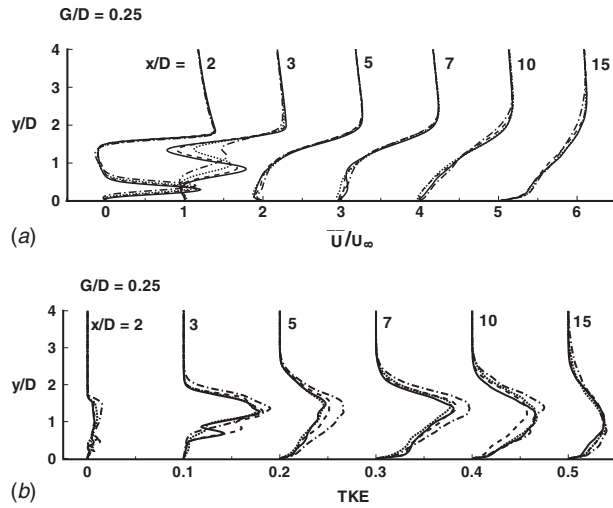


Fig. 2 Grid independent test for $G=0.25D$ and $Re=1440$ considering (a) mean streamline velocity (\bar{U}/U_∞) and (b) turbulent kinetic energy profiles at different streamwise locations: --- $288 \times 192 \times 32$ (grid 1), - - - $384 \times 160 \times 32$ (grid 2), — $384 \times 192 \times 32$ (grid 3), and $384 \times 192 \times 64$ (grid 4)

cycles to get a dynamically steady state solution. Then the data were collected for statistics for a period of 15 cycles that were found sufficient to ensure statistically converged results.

3 Results and Discussion

Before discussing in detail, a few results of flow past a cylinder in proximity to a wall from the present LES are compared with the corresponding experiment [1] for validation. Figure 3 shows the isocontours of spanwise vorticity (ω_z) illustrating the flow over the cylinder for $G/D=0.25$ and 0.5 . The wake-boundary layer interactions, formation of separation bubbles both upstream and downstream of the cylinder, stretching of shear layers shed from the cylinder, rollup, and then breaking down to smaller eddies are well represented. The lower half of the shear layer is suppressed by the boundary layer. The deflection of the boundary layer away from the wall downstream of the cylinder creates a separation bubble. The numerical visualization of instantaneous flow field illustrates a close resemblance with the experimental observations in terms of vortex dynamics and flow structures.

From the flow visualization, it is difficult to appreciate the vortex shedding particularly for a low gap ratio. However, there exists a strong periodicity component to the predicted velocity signal in the cylinder wake; almost certainly, this is associated with the shear layer shed from the outer surface of the cylinder. A spectral analysis of streamwise velocity component at $x/D=3.3$ and $y/D=1.5$ from the cylinder center for $G/D=0.25$ is shown in Fig. 4 and is compared with the experimental data [1]. This reveals that the dominant wake frequency occurs at $St=0.4$; however, there is a secondary peak at $St=0.25$. The comparison of the power spectra density with the experiment [1] demonstrates a good agree-

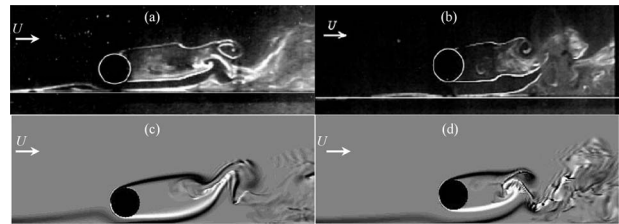


Fig. 3 Instantaneous spanwise vorticity (ω_z): (a) and (b) experiment at $Re=1900$ [1]; (c) and (d) present LES at $Re=1440$. (a) and (c) $G/D=0.25$ and (b) and (d) $G/D=0.5$.

ment. As G/D ratio increases, the effect of the wall boundary layer reduces and the two peaks that appeared in the power spectra density merge into one peak, the value of which approaches 0.2. In the present simulation, St becomes 0.29 and 0.25 for $G/D=0.5$ and 1.0 , respectively, whereas the corresponding values in the experiment [1] are 0.27 and 0.255. The validation illustrates that the present LES can be used to describe the evolution of shear layers shed from the cylinder under the influence of wall boundary layer.

3.1 Instantaneous Flow Structure. To visualize the vortex dynamics in proximity to a wall during the shedding cycle, the snapshots of isocontours of spanwise vorticity (ω_z) are presented in Figs. 5–7 for different gap ratios. These figures are drawn between a time-period (T) of vortex shedding that has been calculated assuming the Strouhal frequency as 0.2 and following the experiment of Price et al. [1]. However, it should not be interpreted as $St=0.2$ for all cases; indeed there is no such periodicity of the wake at all for a low gap ratio, $G/D=0.25$ at $Re=1440$. The Strouhal number as 0.2 represents an approximate average value over a range of G/D . Instantaneous vorticity is span-averaged that removes the small-scale fluctuations and tends to identify the coherent structures. A brief description of the vortex formation, its downstream convection, interaction with the boundary layer and breaking down to smaller eddies are presented in this section.

Figure 5 depicts the instantaneous span-averaged vorticity between $t/T=0.0$ to 0.8 for a small gap ratio $G/D=0.25$, which corresponds to $G/\delta=0.6$ (δ being the boundary layer thickness at the location of cylinder without its presence). For $t/T=0.0$, the outer shear layer shed from the cylinder is seen to curl up forming a vortex (denoted by A) over the inner-shear layer, which is deflected away from the wall. The inner-shear layer from the cylinder remains frozen for a long period of time, and there is no apparent rollup. A strong pairing between the inner-shear layer and the boundary layer is observed being of opposite signs that suppresses the shedding of the inner-shear layer. This coupling is also attributed to the lift-off of boundary layer forming a large separation bubble downstream of the cylinder. The boundary layer appears to rollup (denoted by B) beneath the inner-shear layer. For the next few steps ($t/T=0.2-0.6$), the inner-shear layer is stretched further, developing a Kármán vortex sheetlike structure (denoted by C): one end of it remains attached to the cylinder to form a quasisteady attached wake, while the other end engulfs the

Table 1 Computational grid and box size

G/D	Dimension of Box ($L_x \times L_y \times L_z$)	Grid ($n_x \times n_y \times n_z$)	Δx^+	Δy^+	Δz^+	Comments
0.25	$30D \times 8.5D \times 3D$	$288 \times 192 \times 32$ (grid 1)	7.96	0.68	4.11	Test case
		$384 \times 160 \times 32$ (grid 2)	3.82	0.86	3.85	Test case
		$384 \times 192 \times 32$ (grid 3)	4.35	0.71	4.41	Useful
		$384 \times 192 \times 64$ (grid 4)	4.23	0.74	2.25	Test case
0.5	$30D \times 8.5D \times 3D$	$384 \times 192 \times 32$	4.07	0.68	4.12	Useful
1.0	$30D \times 9D \times 3D$	$384 \times 224 \times 32$	4.87	0.8	4.93	Useful

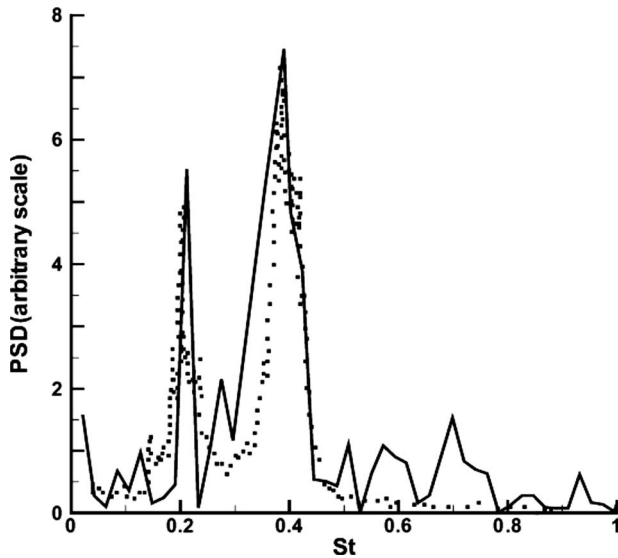


Fig. 4 Power spectra density of streamwise velocity at $x/D = 3.3$, $y/D = 1.5$ for $Re = 1440$, and $G/D = 0.25$: — present LES, ... experiment [1]

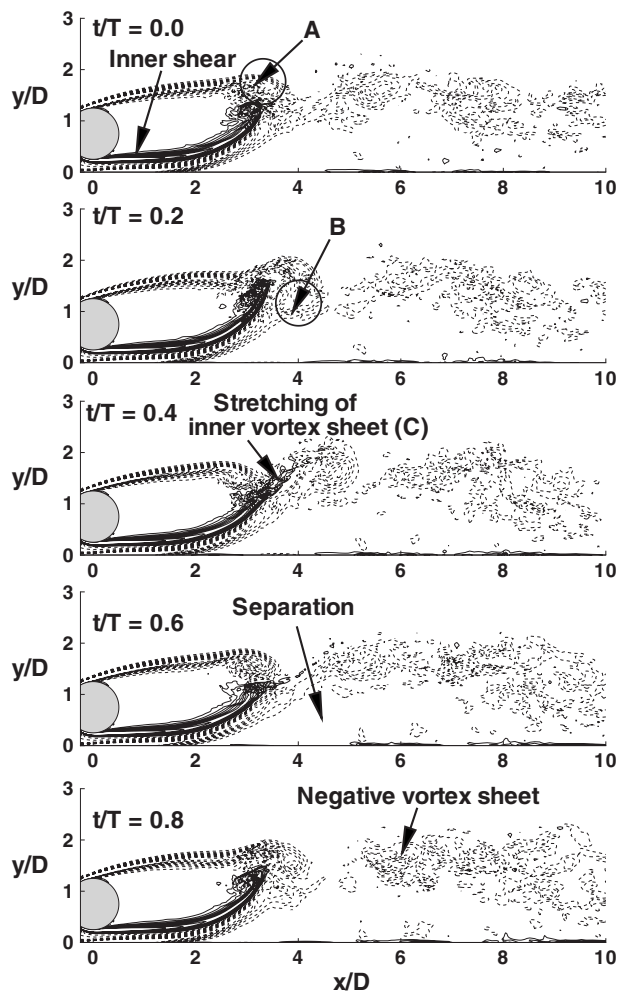


Fig. 5 Span averaged vorticity contours for $G/D = 0.25$. A total of 20 nondimensional contours are considered in between -5 and $+5$. The negative vorticity is represented by dotted line.

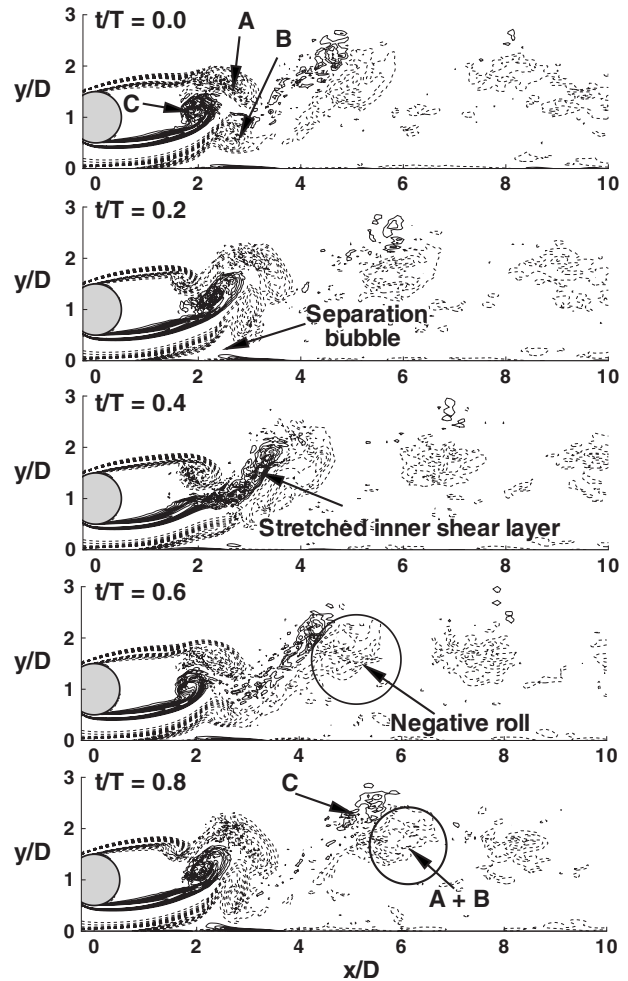


Fig. 6 Span averaged vorticity contours for $G/D = 0.5$. For details refer Fig. 5.

outer roll A, resulting in a cross over of trajectories of the shed vortices. Thus, the roll of negative vortices from the upper shear layer merges with the boundary layer vortices and convects downstream before breakdown to form the final wake sheet of the same-sign vorticity. At $t/T = 0.8$, neither the vortex A nor the vortex B is identified downstream, but a negative free-shear sheet appears that convects with a speed slower than the free-stream.

For $G/D = 0.5$ that corresponds to $G/\delta = 1.2$, both the inner and outer shear layers shed from the cylinder curl up in an alternating fashion producing two rolls (denoted by A and C), although lack of symmetry is evident, as shown in Fig. 6, at $t/T = 0$. The lift-off of wall boundary layer occurs with a tongue-like vortex sheet that forms a roll denoted by B. However, this deflection of the boundary layer decreases that, in turn, reduces the size of the downstream separation bubble as compared with the earlier. The curling of the shear layers also appears to form closer to the cylinder. As the time progresses ($t/T = 0.2 - 0.6$), a rapid stretching of the inner-shear layer is observed forming an elongated vortex sheet, and its coupling with the wall boundary layer lead to form a large negative roll as before. The mutual interaction of the wall vortices with the shed vortices creates a remarkable difference in the wake dynamics: The trajectories of shed vortices cross each other, and the final vertical position is opposite with respect to the unbounded case. Thus, the negative vortices shed from the upper side of the cylinder occupy the lower position, while the positive vortices shed from the inner-side of the cylinder occupy the upper position in the sheet; a similar trend is reported by Zovato and Pedrizzetti

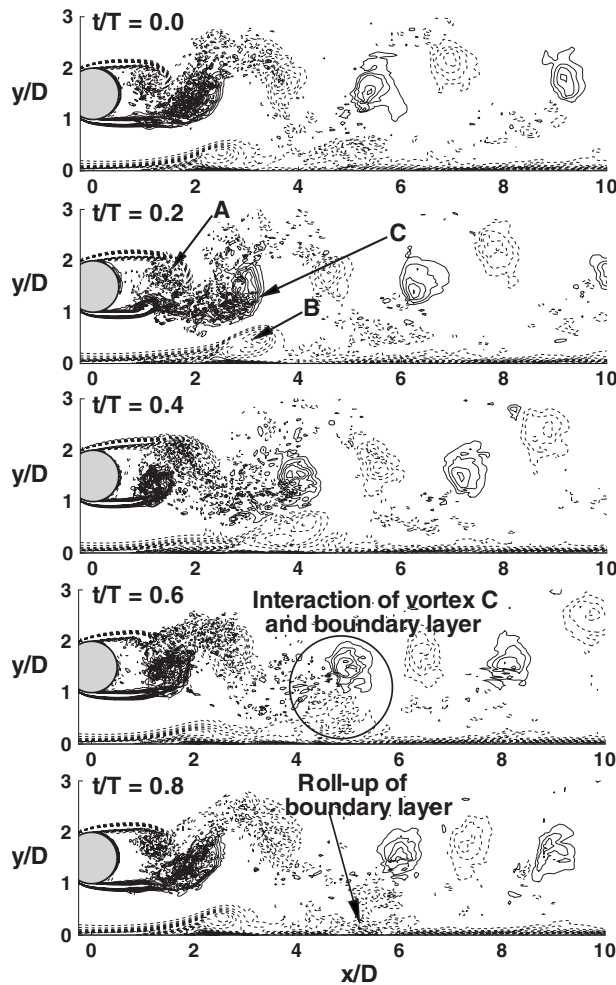


Fig. 7 Span averaged vorticity contours for $G/D=1.0$. For details refer Fig. 5.

[36]. The celerity of positive roll and negative vortex sheet is marginally different. This stretching process decays the circulation of the wake vortex because of dissipation.

As the gap ratio increases to $G/D=1$ that corresponds to $G/\delta=2.4$ (when the cylinder remains well outside the boundary layer), Fig. 7 illustrates that the cylinder behaves more closely to an isolated cylinder with an alternate vortex shedding. However, this shedding of the Kármán vortex, particularly the inner-shear layer and the associated positive vortex rolls (denoted by C), influences the wall boundary layer in a different fashion. The excitation of the boundary layer downstream appears to be substantial by these positive migrating rolls. In detail, downstream of the cylinder a negative vortex from the wall boundary layer eventually elongates (denoted by B) forming a vortex sheet that is seen to be engulfed by the positive convective vortex roll ($t/T=0.6$). This creates an unsteady bubble beneath the negative vortex sheet; the periodicity of which appears to be same as that of the vortex shedding. The rollup of boundary layer forming small-scale eddies are apparent downstream of $x/D=5$ (marked in Fig. 7) because of the convective coherent vortices imparting momentum to the boundary layer. The flow dynamics demonstrated in the present LES supports the experimental observations [1].

Figures 8 and 9 illustrate the overall trajectory of vortex peaks and the variation in vortex peak values along the streamwise direction for $G/D=0.25$ and 1.0 . The location of the vorticity peak can be identified as the vortex center. Three vortices emanating from the outer shear layer, the inner-shear layer, and the wall boundary layer are traced to reveal the vortex motion. For G/D

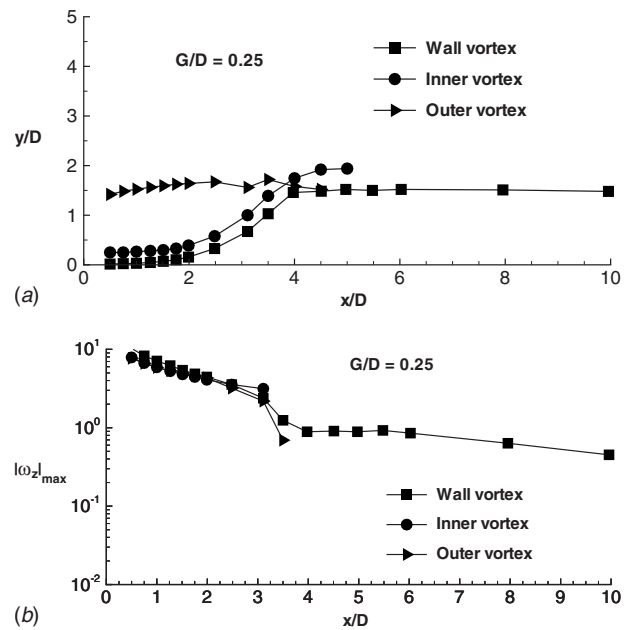


Fig. 8 (a) Trajectory of vortex peak and (b) variation in ω_z peak for $G/D=0.25$ and $Re=1440$

$=0.25$, vortices from the inner-shear layer and the wall boundary layer travel in a parallel trajectory owing to the strong pairing between them (Fig. 8(a)) and move in the wall-normal direction immediately behind the cylinder ($x/D < 3.5$). The outer shear layer vortices move almost parallel to the wall. Near $x/D=4$, a strong mutual interaction between vortices is reflected by the cross over of trajectories of the shed vortices emerging a single negative vortex sheet that travels downstream and remains almost parallel to the wall. It is difficult to identify whether this negative vortex is produced by the upper shear layer or by the wall vortices as explained before. Figure 8(b) indicates that the peak values of all vortices decay in same pace with increasing streamwise coordinate; they decay rapidly in the vicinity of the cylinder and at a slower rate downstream of $x/D=4$. This is attributed to the break-

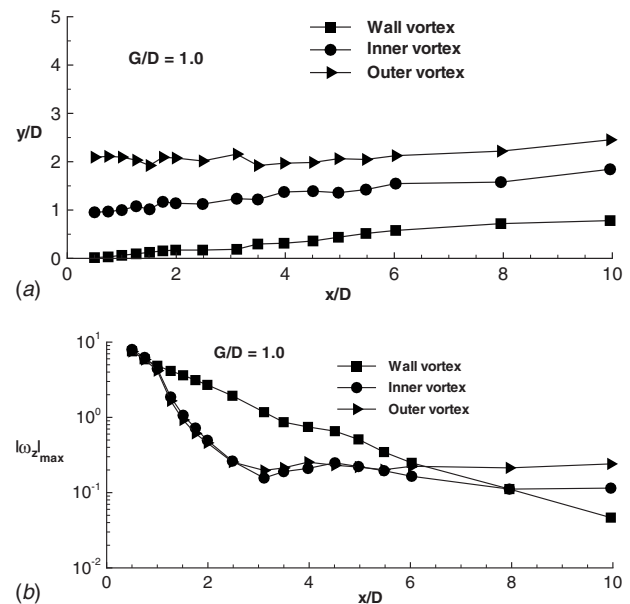


Fig. 9 (a) Trajectory of vortex peak and (b) variation in ω_z peak for $G/D=1.0$ and $Re=1440$

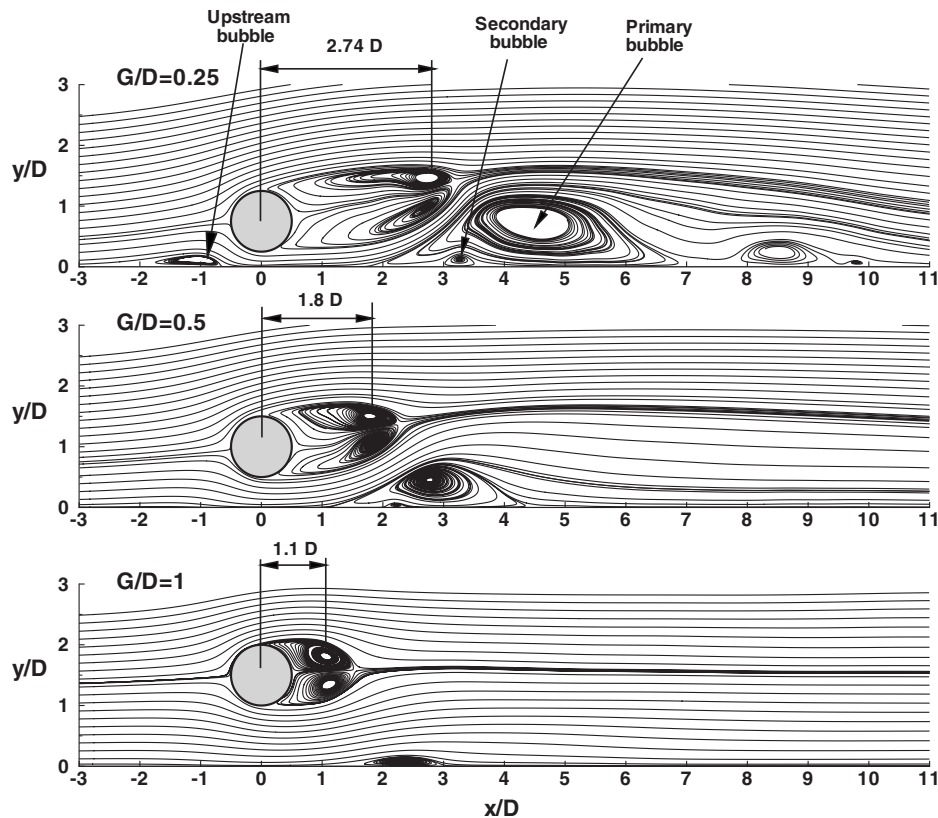


Fig. 10 Mean streamlines for $G/D=0.25$, 0.5 , and 1.0

down of the larger-scale vortex to the random small-scale eddies resulting in a decrease in the magnitudes of lower frequency and the increase in higher frequency energy-content eddies. It should be further noted that the inner-shear layer and the wall boundary layer do not cancel each other behind the cylinder, although of different signs of vorticity. This supports the experimental observation of Price et al. [1], while contradicts to the suggestion of Grass et al. [6] and Taniguchi and Miyakoshi [7].

For $G/D=0.5$, trends of the trajectory of the shed and the wall vortices remain almost the same as before, but the lift-off of the boundary layer is relatively less severe in this case (figures are not presented). Here, the decay rate of shed vortices is higher than that of the wall vortices in the vicinity of the cylinder. As the cylinder is moved farther away from the wall ($G/D=1$), the outer- and inner-side shed vortices along with the wall vortex can be separately identified far downstream of the cylinder, Fig. 9. The trajectories of vortex peak illustrate that the vortices migrate parallel to each other. In this case, the effect of the boundary layer is minimum and so both the outer- and inner-shear layers rollup to produce almost identical vortices. Further, the outer and inner vortices have the same decay profile (rapidly in the vicinity of the cylinder and at a slower pace downstream of $x/D=4$), which means that the interaction between them is a mutual process. The wall vortex appears to decay continuously, but at a slower rate behind the cylinder.

3.2 Time-Averaged Flow Features. This section presents the time-averaged results describing the mean effect of interactions of wakes with the boundary layer behind a circular cylinder. The mean streamlines depict the formation of separation bubbles both at upstream and downstream of the cylinder for a low gap ratio, $G/D=0.25$, Fig. 10. An elongated separation region is observed downstream, which is designated as the primary bubble rotating in the clockwise direction. A secondary bubble rotating in the opposite direction is formed beneath the primary bubble. This large

separation region can be attributed to the strong coupling between the inner-shear layer and the wall boundary layer, which deflects the boundary layer away from the wall. Figure 10 also indicates that when the cylinder is very close to the wall, the shear layers remain frozen for a considerable time before they curl up to form the Kármán rolls (the center of the outer roll is marked). These rolls also lost the symmetry because of suppression of the shear layers by the boundary layer. The downstream separation bubble rapidly reduces, and the upstream separation bubble disappears as the gap ratio increases. Furthermore, for a relatively large gap ratio ($G/D=1.0$), the inner and outer shear layer appear symmetrical and they roll close to the cylinder.

The isocontours of time-averaged streamwise (u_m) and wall-normal velocity (v_m) along with the mean pressure coefficient [$C_p=(P-P_\infty)/0.5\rho U_\infty^2$] are presented in Fig. 11. The contour with zero value of u_m is drawn with the white line to separate the zones of positive and negative velocity apart from to mark the stagnation points. The front stagnation point moves toward the wall from the centerline of the cylinder. Furthermore, the inner separation point shifts downstream along the shoulder of the lower half of the cylinder, while the outer separation point moves upstream along the shoulder of the upper half as the wall is approached. These movements of stagnation and separation points change the wake size behind the cylinder and vary the base pressure: The pressure distribution becomes quite asymmetrical for $G/D=0.25$. The maximum value of C_p is attained at the front stagnation point, whereas the lowest pressure occurs on the top and bottom of the cylinder near the point of separation of the shear layers, and these positions depend on the gap ratio. The center of the core of recirculation region coincides with the negative pressure zone downstream that shifts closer to the cylinder as gap ratio decreases. The stagnation point determined from the present LES was approximately at $\theta_s=-10.6^\circ$, -9.0° , and -4.9° for $G/D=0.25$, 0.5 , and 1.0 , respectively. These values moderately agree with the experi-

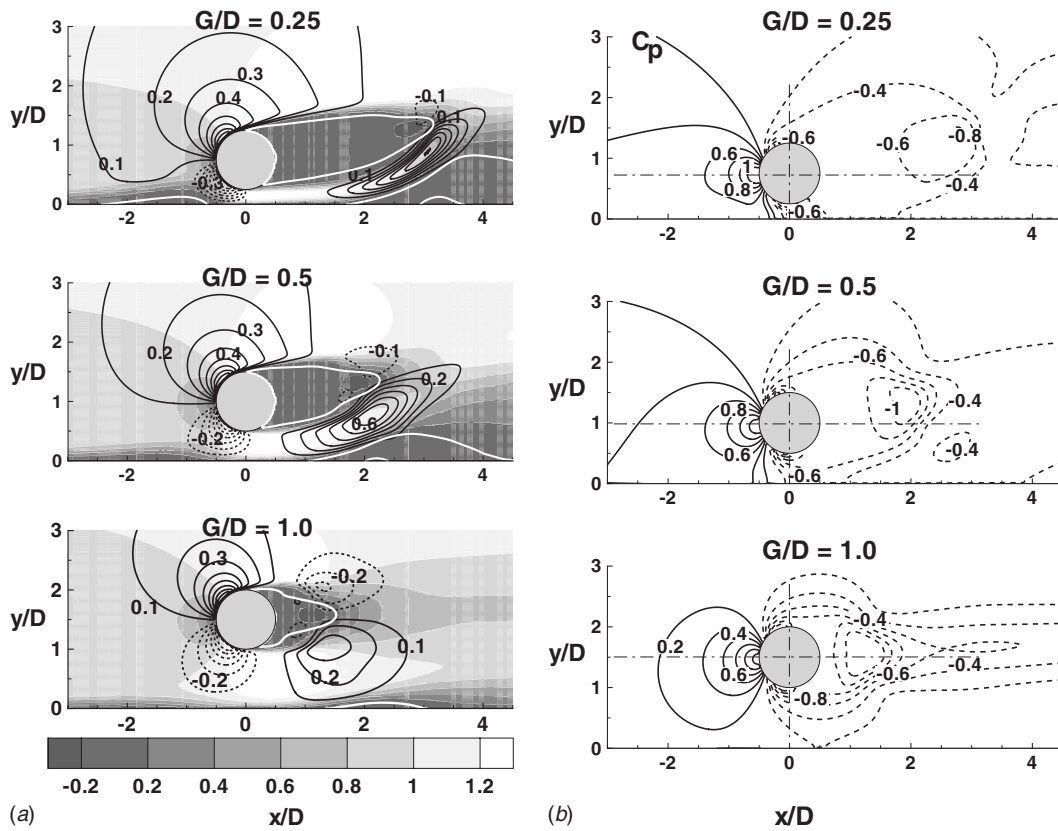


Fig. 11 The mean (a) streamwise and wall-normal velocity contours and (b) coefficient of pressure distributions for different G/D . Streamwise velocity contours are drawn by flood and wall-normal velocity contours are drawn by line (black color) diagrams. The thick white line indicates zero contour level for mean streamwise velocity.

ment [8] even at $Re = 1.45 \times 10^4$ and $\delta/D = 0.48$, where $\theta_s = -9.6^\circ$, -6.8° , and -3.3° for $G/D = 0.3, 0.5$, and 1.0 , respectively. Here, θ_s is measured from the front point on the horizontal axis of the cylinder and in the clockwise direction. The movement of stagnation point will be associated with the generation of lift; an effect of the boundary layer that has already been reported in Refs. [8,36]. The deflection of the wake and its departure from the symmetry due to the wall proximity can be understood by the isocontours of streamwise velocity. Negative u_m values upstream and downstream of the cylinder depict the flow separations that diminish as the cylinder is moved away from the wall. Asymmetry in the wake shape and lift-off of the boundary layer are well reflected in v_m values. As the gap ratio increases ($G/D = 1.0$), distribution of v_m approaches a symmetric look, although the effect of the boundary layer is evident.

The streamwise evolutions of mean skin friction ($\overline{C_f} = \overline{\tau_w} / 0.5\rho U_\infty^2$, where $\overline{\tau_w} = \mu \partial u / \partial y|_{y=0}$ being the wall shear stress) for the three gap ratios are shown in Fig. 12. The separation and reattachment points along with the length of bubbles both upstream and downstream of the cylinder are summarized in Table 2. For $G/D = 0.25$, C_f becomes negative at $x/D = -2.58$ to -0.71 indicating an upstream separation, which is absent in the other two cases. The drop followed by a sharp rise in $\overline{C_f}$ upstream of $x/D = 0$ is due to the combination of wall proximity and flow acceleration beneath the cylinder. The peak value of C_f becomes maximum for this gap because the flow beneath the cylinder is under the maximum negative pressure. Downstream of the cylinder, $\overline{C_f}$ becomes negative for all the cases indicating the separation region. The appearance of a secondary bubble downstream is also reflected in the streamwise evolution of $\overline{C_f}$ for a low gap ratio. When compared with the skin friction values evaluated from the correlation

of turbulent flow, Fig. 12 illustrates the relaxation of flow near the wall. For $G/D = 1$, an overshoot of C_f is observed after reattachment of flow, and it approaches the level of turbulent C_f downstream. For other two cases, large regions of negative $\overline{C_f}$ are seen

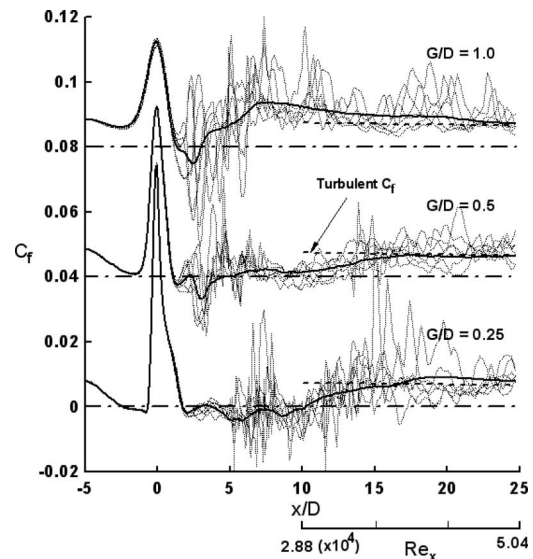


Fig. 12 Profiles of C_f for $G/D = 0.25, 0.5$, and 1.0 . The solid lines indicate $\overline{C_f}$ and the dotted lines are corresponding instantaneous C_f , separated by $0.2T$. Turbulent C_f profile is obtained from the correlation $C_f = 0.058/Re_x^{1/5}$.

Table 2 The onset of separation and reattachment

G/D	Upstream separation (x/D)			Downstream separation (x/D)					
	Start	End	Length	Primary bubble			Secondary bubble		
				Start	End	Length	Start	End	Length
0.25	-2.58	-0.71	1.87	1.69	10.06	8.37	2.89	3.64	0.75
0.5	-	-	-	1.06	4.57	3.51	1.95	2.52	0.57
1.0	-	-	-	1.34	3.04	2.7	-	-	-

that slowly attain the level of turbulent C_f far downstream. To highlight the near-wall flow, the skin friction distributions at six instants within a shedding period are superimposed. Large amplitude oscillations with low and high frequencies are observed behind the cylinder illustrating the unsteady bubble dynamics and its breakdown. The oscillations in instantaneous C_f also start earlier for a large gap ratio as compared with a low gap. This is attributed to the delayed instability of shear layers for a low gap ratio that will be explained in Sec. 3.3.

3.3 Development of 3D Motion and Breakdown to Turbulence. The isosurface of the spanwise component of instantaneous vorticity for different gap ratios is depicted in Fig. 13 to visualize the internal growth mechanism of shear layers in proximity to a wall and the 3D flow structures. For a low gap ratio ($G/D=0.25$), the outer shear layer shed from the cylinder appears to remain laminar up to $x/D=2.5$ and then the shear layer instability sets in that quickly breaks down to turbulent flow down-

stream. As stated earlier, the boundary layer cannot be identified separately because of its strong coupling with the inner-shear layer and a large separation region is observed. The flow is turbulent away from the wall with the appearance of small-scale eddies and loss of coherent structures leaving a relatively calm near-wall.

With increase of G/D ratio, the effect of wall proximity is decreased, and the breakdown of both the outer- and the inner-shear layer occurs relatively closer to the cylinder. The shear layers tend to retain their coherent structures with appearance of small-scale eddies. Further to note that the deflection of the boundary layer is inhibited. For $G/D=1$, the boundary layer preserves its identity with formation of a thin separation bubble. In this case, the perturbations created by the turbulent shear layers are amplified near the wall with appearance of longitudinal streaky structures, which are the features of flow transition. A sectional view of instantaneous velocity fluctuations (u' and v' that are obtained by subtracting the mean part from the instantaneous value) along with streamwise velocity (u) contours in the x - y plane is presented in Fig. 14(a) for a large gap ratio ($G/D=1$). The flow is characterized by alternating Kármán vortices behind the cylinder, and these have not been suppressed. From a zoomed view it is clear that the Kármán vortices interact with the outer part of the boundary layer resulting in local eddies, which convect and breakdown downstream. Thus, the formation of these eddies in the outer part of the boundary through a Kelvin-Helmholtz-like instability is the root to transition under the convective wake. A similar view of boundary layer transition under

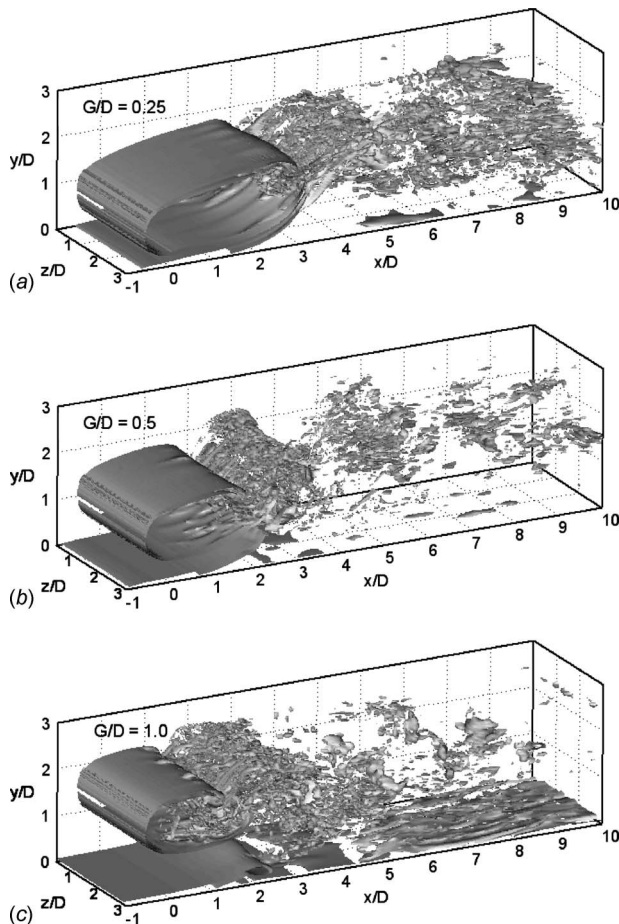


Fig. 13 Isosurfaces of spanwise vorticity ($\omega_z = \pm 2.0$) for $G/D = 0.25, 0.5, \text{ and } 1.0$

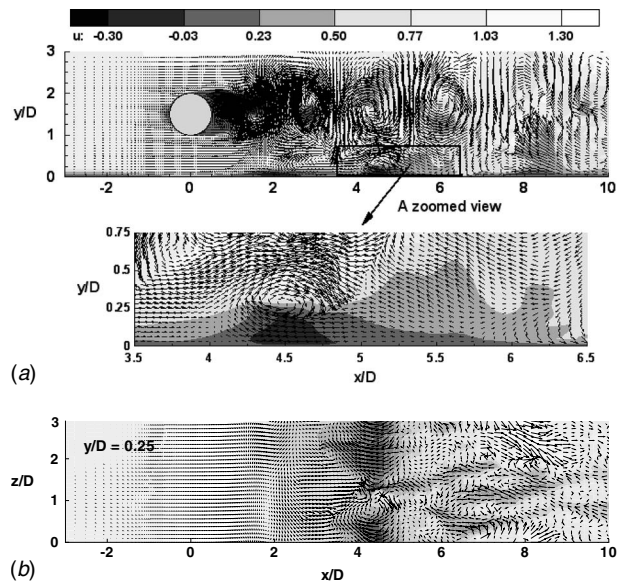


Fig. 14 Streamwise velocity contour and vector plot of velocity fluctuations (u', v') for (a) front view (x - y plane) along with a zoomed section, (b) top view (x - z plane) considering a gap ratio of $G/D=1.0$. For better visualization, two vectors are skipped in the x -direction and four vectors in the y -direction, respectively.

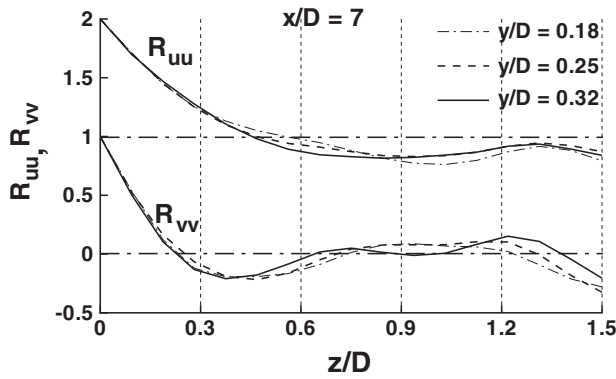


Fig. 15 Spanwise correlation functions of the streamwise and the wall-normal velocity fluctuations

passing wakes is described in Ref. [37]. The top view along a section near the wall ($y/D=0.25$) shows the development of low-speed streaks because of boundary layer excitation by these migrating coherent vortices, Fig. 14(b). These near-wall structures are visible up to $x/D=8.5$.

The average spacing between the streamwise streaks, which are the features of transition under free-stream turbulence can be determined from the spanwise correlation functions of streamwise (R_{uu}) and wall-normal velocity fluctuations (R_{vv}). For a large gap ratio ($G/D=1$), where the boundary layer retains its identity and appears to approach a canonical layer, the variation in R_{uu} and R_{vv} at a streamwise location of $x/D=7.0$, and three wall-normal positions are shown in Fig. 15. Both R_{uu} and R_{vv} predict an average streak spacing of $1.6D$ (twice the distance to the first R_{uu} minimum, or four times the distance to the first R_{vv} minimum). In terms of boundary layer thickness (δ), the streak spacing becomes 1.33δ , being $\delta=1.2D$ at the location. Here, δ is calculated from the location of maximum mean velocity in between the plate and the wake. The experiments and simulations on boundary layer transition due to moderate to strong levels of fst [33,38] illustrate streamwise streaks with mean separation of the order of boundary layer thickness. Thus, the present study indicates that the transition mechanism of the boundary layer for a large gap ratio is similar to the bypass transition by fst, although here the excitation is caused by the Kármán vortices: the observation is consistent with Ref. [34].

To characterize the boundary layer further under the excitation of wake for $G/D=1$, the profiles of u_{rms} are presented in Fig. 16, where the wall-normal coordinate is scaled with the local displacement thickness (δ^*) and u_{rms} with its maximum inside the boundary layer. Here $\delta^* = \int_0^y (1 - \bar{U}/U_\delta) dy$, where U_δ is the maximum mean velocity in between the plate and the wake. The experimental data of Matsubara and Alfredsson [38] are superimposed, which were obtained from a transitional boundary layer subjected to moderate free-stream turbulence. The computed profiles of u_{rms} exhibit an approximate self-similarity near the wall and within $x/D=3.5$ to 5.0 . High values attributing to the wake flow are observed in the outer region, Fig. 16(a). The agreement with the measured data [38] appears good illustrating that the mode of transition and formation of streaks in this case are similar to those of boundary layer perturbed by strong levels of fst. The location of u_{rms} peak shifts toward the wall depicting the end of transition downstream of $x/D=7.5$, Fig. 16(b). In the region of $x/D=5-7$, a large value of u_{rms} is noticed, which is attributed to interactions of large-scale eddies of the shear layers with the boundary layer.

For $G/D=0.5$, some important features of shear layer transition under the influence of boundary layer can be illustrated by instantaneous velocity fluctuations along with streamwise velocity (u)

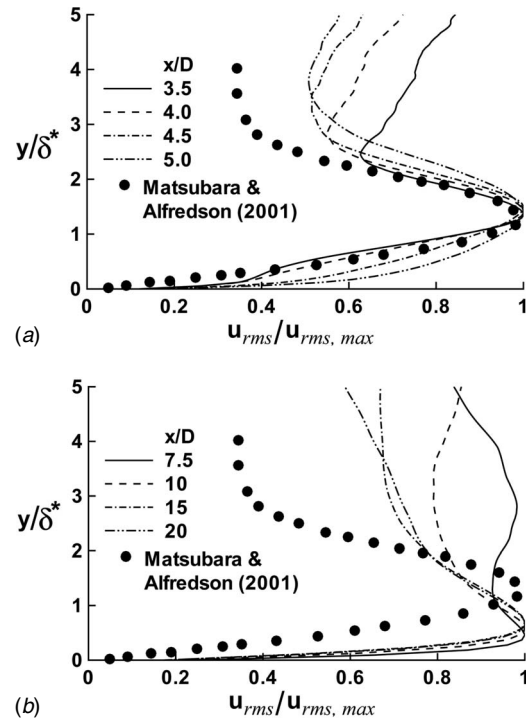


Fig. 16 Time-averaged nondimensional u_{rms} near the wall: (a) between $x/D=3.5-5.0$ and (b) after $x/D=7.5$

contours in Fig. 17(a): a sectional view along the x - y plane. The wake flow seems to be turbulent downstream of $x/D=3.0$ with appearance of large- and small-scale structures. The coherent vortices formed due to mutual interactions of shear layers suffer from

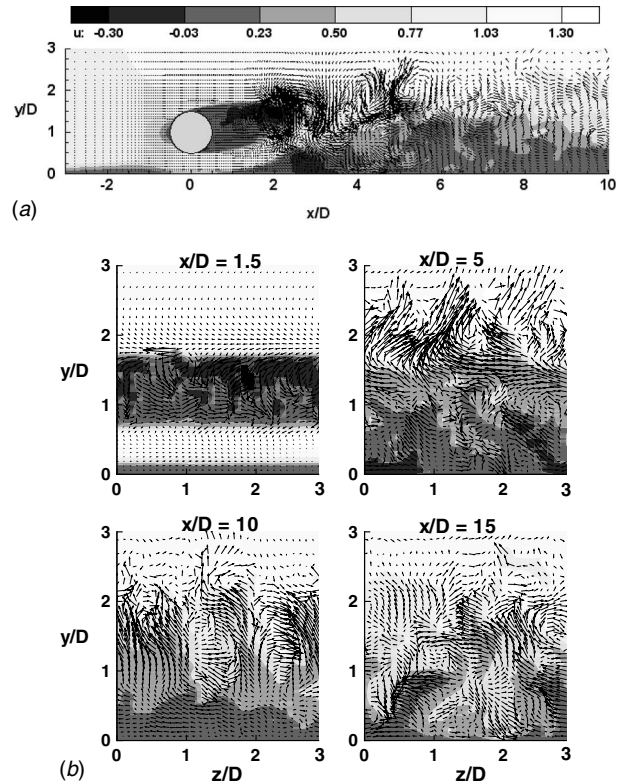


Fig. 17 Streamwise velocity contour and vector plot of velocity fluctuations (u' , v') for (a) front view (x - y plane) and (b) side views (y - z plane) considering a gap ratio of $G/D=0.5$. For details refer Fig. 14.

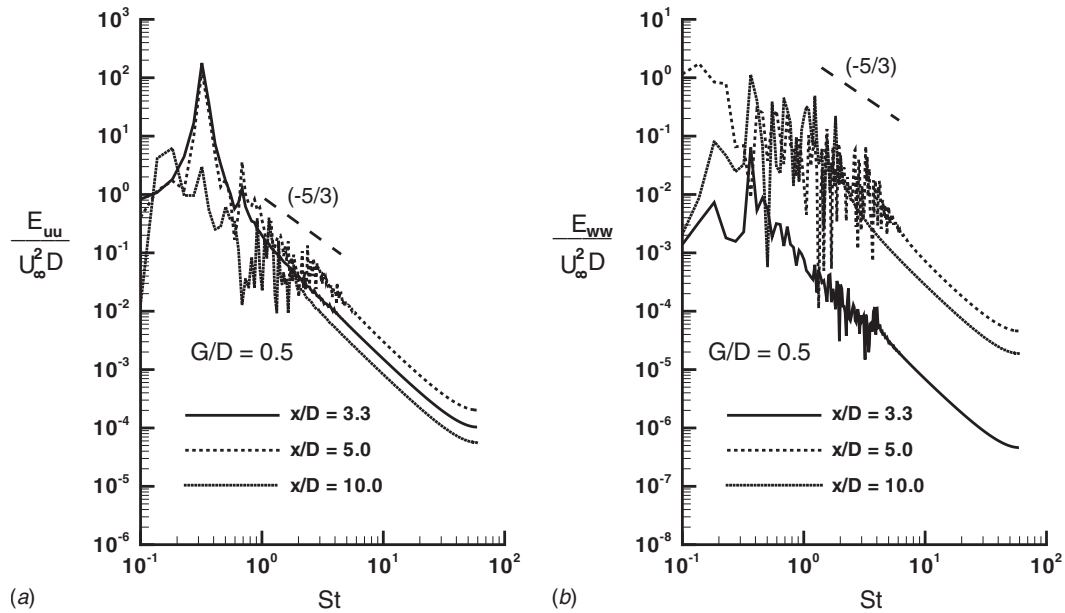


Fig. 18 The power spectra at $Re=1440$ for $G/D=0.5$: (a) streamwise velocity and (b) spanwise velocity

the intrusion of the deflected boundary layer and hence loss of symmetry. The velocity contours become negative near the wall indicating an unsteady separation bubble that breaks down and convects downstream. The cross-sectional flow at different y - z planes is presented in Fig. 17(b). At $x/D=1.5$, both the shear layers shed from the cylinder and the boundary layer can be separately identified. The shear layers at this section are laminar with small fluctuations. At $x/D=5$, the flow in the outer layer is perturbed with large spanwise vortices that are most possibly attributed to the shear layer instability. These large spanwise vortices, which constantly eject fluid from the inner layer, are visible even at $x/D=10$. At $x/D=15$, the flow field including the near-wall region is dominant with fine-scale turbulent structures.

The power spectra considering the streamwise and spanwise velocity fluctuations are depicted in Fig. 18(a) and 18(b) for $G/D=0.5$ and $Re=1440$. The velocity histories have been collected in the midspan plane at locations of $x/D=3.3, 5,$ and $10, y/D=2.0$ over a time-period of $TU_\infty/D=15$ (T being the time-period of vortex shedding). At $x/D=3.3$, a peak in the power spectra is observed at $St=0.25$ for both E_{uu} and E_{ww} , which can be considered as the vortex shedding frequency in proximity to a wall. At $x/D=5$ and 10 , a wide range of shedding frequency with more energetic high frequency harmonic are observed. This is attributed to the breakdown of primary vortices to small-scale energetic eddies downstream. The mesh used in the present LES appears good to resolve the wake and boundary layer interactions. The power spectra E_{ww} ensure the development of spanwise fluctuations.

3.4 Turbulence Statistics. The profiles of the streamwise component of mean (\bar{U}/U_∞) and fluctuating (u_{rms}/U_∞) velocities at different sections ($x/D=2, 3, 5, 7, 10,$ and 15) for the three gap ratios are shown in Fig. 19. The evolutions of velocity profile derived from the Blasius solution are also superimposed to illustrate the change in flow field due to the presence of a cylinder near the wall. For a low gap ratio, $G/D=0.25$ corresponding to $G/\delta=0.6$, the velocity profiles indicate a fairly large wake-deficit behind the cylinder ($x/D=2$ and 3) apart from an accelerated flow beneath it and a large downstream separation. This large wake-deficit is attributed to the frozen shear layers for a relatively longer period when the cylinder is submerged within the boundary

layer. The presence of the velocity deficit is visible far downstream even up to $x/D=10$ and is almost parallel to the wall. As explained earlier, the strong coupling between the inner-shear layer and the boundary layer in this case causes the deflection of

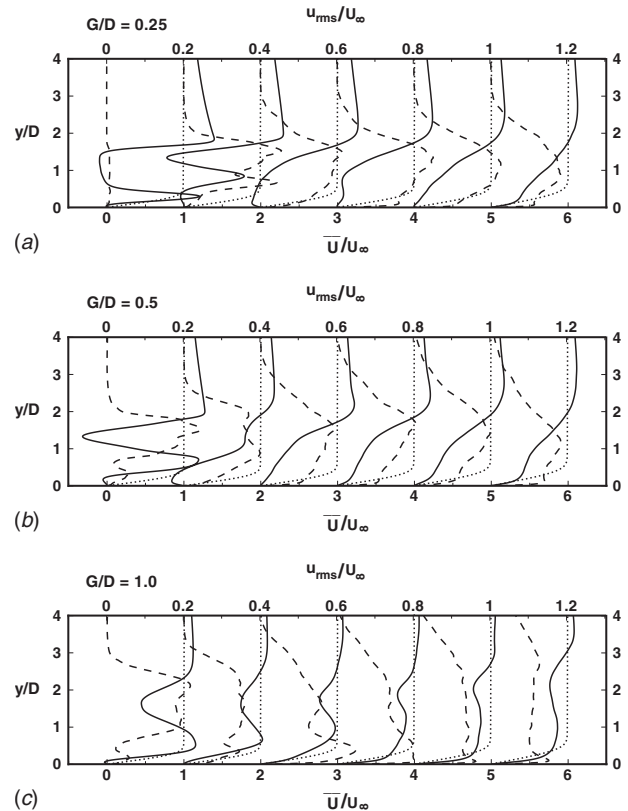


Fig. 19 Profiles of streamwise mean and rms velocity along with the Blasius solution for $G/D=0.25, 0.5,$ and 1.0 at $x/D=2, 3, 5, 7, 10,$ and 15 ; — \bar{U}/U_∞ , - - - u_{rms}/U_∞ , Blasius solution

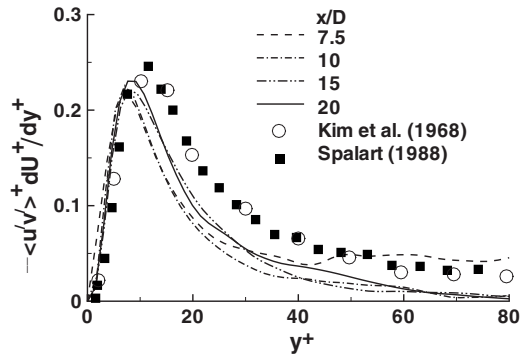


Fig. 20 Time-averaged nondimensional turbulent kinetic energy productions near the wall and after $x/D=7.5$

the boundary layer, and they convect in a parallel trajectory. When the turbulent fluctuations are compared with the corresponding velocity profiles, it illustrates that the turbulence generation occurs along the trajectory of the shear layer, which remains away from the wall. Thus, the mutual interactions between the shed vortices and the boundary layer originate turbulence. For $G/D=0.5$ or $G/\delta=1.2$, the mechanism of turbulence generation remains the same as before with considerably large wake deficit, although lift-off of the boundary layer is less severe with appearance of a relatively smaller downstream separation.

For $G/D=1$ that corresponds to $G/\delta=2.4$, the cylinder remains well outside the boundary layer. Thus, the wake deficit and the growth of boundary layer can be separately identified in velocity profiles except in the near wake, where the shear layers govern the turbulence. The peak values in velocity fluctuation shift toward the wall downstream illustrating the interactions of large coherent vortices in the wake with the boundary layer. When compared with the Blasius solution, the velocity profiles become inflexional between $x/D=2$ and 3, and the boundary layer appears turbulent downstream of $x/D=7$. To characterize the state of boundary layer after being excited by the coherent vortices in this case, profiles of the time-averaged turbulent kinetic energy production $P^+ = -u'v'(\partial u^+ / \partial y^+)$ (normalized by wall parameters) at four streamwise stations are compared with the DNS of Spalart [39] and the experimental data of Kim et al. [40] in Fig. 20. The study of Spalart on the turbulent boundary layer revealed that profiles of P^+ at three different momentum thickness Reynolds numbers ($Re_\theta=300, 670, \text{ and } 1410$) are self-similar. P^+ evaluated from the resolved part of the present LES almost reproduces this feature as evident in the self-similarity of the profiles downstream of $x/D=7.5$, although the data of Spalart and Kim et al. are under predicted by about 8%. It should be noted that the value of Re_θ calculated from LES is approximately 150 at $x/D=7.5$, where the boundary layer appears turbulent. The boundary layer becoming turbulent at low range of Re_θ has also been observed in Ref. [34]: characteristics of wake-boundary layer interactions.

To understand the relative effects of G/D ratio on the wake and boundary layer interactions, the profiles of turbulent kinetic energy ($TKE = \frac{1}{2} \overline{u_i' u_i'}$) along with its production ($P_{TKE} = -\overline{u_i' u_j'} \partial \overline{u_i} / \partial x_j$) at different locations downstream of the cylinder are presented in Fig. 21. The zone of high TKE and production is approximately marked in the figure. As expected, the enhancement of turbulence occurs along the trajectories of the shear layers leaving a relatively calm near-wall region for low gap ratios (G/D up to 0.5). This is attributed to the strong coupling between the approaching boundary layer and the inner-shear layer leading to a rapid growth of disturbances with appearance of small-scale eddies in regions away from the wall: an example of mutual interactions between the boundary layer and the shear layer. The production occurs in regions of high turbulent stress and high spatial velocity gradient aligned in the same direction. Thus, the high

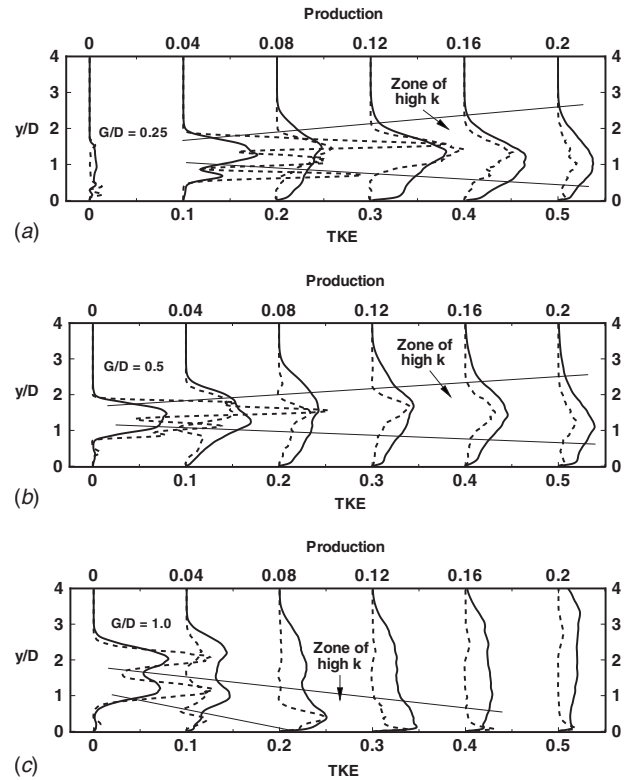


Fig. 21 Profiles of turbulent kinetic energy and production for $G/D=0.25, 0.5, \text{ and } 1.0$ at $x/D=2, 3, 5, 7, 10, \text{ and } 15$; — TKE, -- production

production along the path of the wake is due to the coexistence of turbulent stress and shear in the wake fluid. For a large gap ratio ($G/D=1.0$), the high TKE and production are not confined along the path of the shear layers, rather the augmentation is migrated toward the wall as marked. In this case, the inner-shear layer shed from the cylinder perturbs the inflexional boundary layer during its convection generating higher frequency energy-content eddies. Hence, the high production near the surface can be considered as the combined effect of a local concentration of vorticity and a growing level of turbulence in the boundary layer under excitation of the convective wake.

4 Conclusions

LES of flow past a circular cylinder in proximity to a wall has been carried out to understand the insight of flow physics involving the wake and boundary layer interactions for different gap ratios. The resolved flow field elucidates the mutual effects, i.e., modification of wake dynamics due to the presence of boundary layer and excitation of the boundary layer because of the wake flow. The Reynolds number considered here is in the range of shear layer transition.

For a low gap ratio, when the lower shear layer lies within the boundary layer ($G=0.6\delta$), a strong pairing between the inner-shear layer and the boundary layer is observed. This delays the shear layer transition from two-dimensional to three-dimensional flow in the wake and deflects the boundary layer immediately behind the cylinder with a relatively large separation. It also inhibits the creation of a vortex pair evolving a unique row of like-signed vortices after breakdown to small-scale eddies downstream of $x/D=4$. In this case, the dominant wake shedding frequency shifts to 0.4. Furthermore, the inner-shear layer and the boundary layer do not cancel each other, although of different signs of vorticity. This supports the experimental observation of Price et al. [1].

At a moderate gap ratio (when $G \approx \delta$), the inner- and the outer-layer shed from the cylinder tends to curl up in an alternate fashion, although lack of symmetry is strongly evident. Here also the boundary layer is stretched because of the attraction of the inner-shear layer evolving an unsteady bubble, the periodicity of which appears to be same of vortex shedding. The mutual interactions of the wall vortices and that with the shed vortices create a remarkable difference in the wake dynamics: trajectories of shed vortices cross each other and an inversion on the position of vortices occurs with respect to the unbounded case. The presence of a wall causes movements of stagnation and separation points changing the wake size and base pressure and thus an upward lift on the cylinder is generated.

When the cylinder is far apart from the wall ($G=2.4\delta$), the vortex shedding is similar to the Kármán sheet and the Strouhal frequency becomes close to 0.2, but asymmetry in wake shape is still evident. The Kármán vortices excite the boundary layer in an alternate fashion that triggers its transition.

An attempt is made to describe the transition mechanism of the shear layers and that of the boundary layer with respect to the gap ratio. For a relatively low gap ratio ($G=0.6\delta-1.2\delta$), the shear layer instability sets in with appearance of a spanwise wavelength that becomes three-dimensional and breakdowns to turbulent flow downstream. Here, the coherent vortices of the shear layers suffer from the intrusion of the deflected boundary layer. The boundary layer loses its identity downstream because of its strong coupling with the shear layers. Thus, the generation of turbulence and production in this case is mainly due to shear in the wake fluid illustrating a high active outer region along the wake trajectory and a relatively calm near-wall. On the other hand, when the cylinder is well outside the boundary layer ($G=2.4\delta$), the shear layers and the boundary layer can be separately identified. The breakdown of both the outer- and inner-shear layer occurs relatively closer to the cylinder and the wake tends to retain its coherent structures with appearance of small-scale eddies. These coherent structures inject momentum to the boundary layer during their convection that in turn evolves streaks leading to transition to turbulence of the boundary layer, an example of receptivity to external disturbances. Thus, the transition mechanism of the boundary layer for a large gap ratio is somewhat similar to the bypass transition by fst, although here the excitation is caused by the Kármán vortices. Downstream of $x/D=7.5$, the boundary layer approaches a canonical turbulent layer. This is noteworthy in terms of differences in response of the boundary layer close to a migrating wake as gap ratio changes.

Acknowledgment

The authors wish to express their gratitude to the reviewers for their valuable comments and suggestions.

References

- [1] Price, S. J., Sumner, D., Smith, J. G., Leong, K., and Paidoussis, M. P., 2002, "Flow Visualization Around a Circular Cylinder Near to a Plane Wall," *J. Fluids Struct.*, **16**, pp. 175–191.
- [2] Norberg, C., 1994, "An Experimental Investigation of the Flow Around a Circular Cylinder: Influence of Aspect Ratio," *J. Fluid Mech.*, **258**, pp. 287–316.
- [3] Williamson, C. H. K., 1996, "Vortex Dynamics in the Cylinder Wake," *Annu. Rev. Fluid Mech.*, **28**, pp. 477–539.
- [4] Taneda, S., 1965, "Experimental Investigation of Vortex Streets," *J. Phys. Soc. Jpn.*, **20**, pp. 1714–1721.
- [5] Bearman, P. W., and Zdravkovich, M. M., 1978, "Flow Around a Circular Cylinder Near a Plane Boundary," *J. Fluid Mech.*, **89**, pp. 33–47.
- [6] Grass, A. J., Raven, P. W. J., Stuart, R. J., and Bray, J. A., 1984, "The Influence of Boundary Layer Velocity Gradients and Bed Proximity on Vortex Shedding From Free Spanning Pipelines," *ASME J. Energy Resour. Technol.*, **106**, pp. 70–78.
- [7] Taniguchi, S., and Miyakoshi, K., 1990, "Fluctuating Fluid Forces Acting on a Circular Cylinder and Interference With a Plane Wall," *Exp. Fluids*, **9**, pp. 197–204.

- [8] Lei, C., Cheng, L., and Kavanagh, K., 1999, "Re-Examination of the Effect of a Plane Boundary on Force and Vortex Shedding of a Circular Cylinder," *J. Wind. Eng. Ind. Aerodyn.*, **80**, pp. 263–286.
- [9] Buresti, G., and Lanciotti, A., 1979, "Vortex Shedding From Smooth and Roughened Cylinders in Cross-Flow Near a Plane Surface," *Aeronaut. Q.*, **30**, pp. 305–321.
- [10] Angrilli, F., Bergamaschi, S., and Cossalter, V., 1982, "Investigation of Wall Induced Modifications to Vortex Shedding From a Circular Cylinder," *ASME J. Fluids Eng.*, **104**, pp. 518–522.
- [11] Zdravkovich, M. M., 1985, "Forces on a Circular Cylinder Near a Plane Wall," *Appl. Ocean Res.*, **7**, pp. 197–201.
- [12] Vada, T., Nestegard, A., and Skomedal, N., 1989, "Simulation of Viscous Flow Around a Circular Cylinder in the Boundary Layer Near a Wall," *J. Fluids Struct.*, **3**, pp. 579–594.
- [13] Liou, T. M., Chen, S. H., and Hwang, P. W., 2002, "Large Eddy Simulation of Turbulent Wake Behind a Square Cylinder With a Nearby Wall," *ASME J. Fluids Eng.*, **124**, pp. 81–90.
- [14] Dipankar, A., and Sengupta, T. K., 2005, "Flow Past a Circular Cylinder in the Vicinity of a Plane Wall," *J. Fluids Struct.*, **20**, pp. 403–423.
- [15] Mittal, R., and Balachandar, S., 1995, "Effect of Three-Dimensionality on the Lift and Drag of Nominally Two-Dimensional Cylinders," *Phys. Fluids*, **7**, pp. 1841–1865.
- [16] Germano, M., Piomelli, U., Moin, P., and Cabot, W. H., 1991, "A Dynamic Subgrid-Scale Eddy Viscosity Model," *Phys. Fluids A*, **3**, pp. 1760–1765.
- [17] Lilly, D. K., 1992, "A Proposed Modification of the Germano Subgrid-Scale Closure Method," *Phys. Fluids A*, **4**, pp. 633–635.
- [18] Chorin, A. J., 1968, "Numerical Solution of the Navier–Stokes Equations," *Math. Comput.*, **22**, pp. 745–762.
- [19] Zhang, S. L., 1997, "GPBi-CG: Generalized Product-Type Methods Based on Bi-CG for Solving Nonsymmetric Linear Systems," *SIAM J. Sci. Comput. (USA)*, **18**, pp. 537–551.
- [20] Mittal, R., and Moin, P., 1997, "Suitability of Upwind-Biased Finite-Difference Schemes for Large-Eddy Simulation of Turbulent Flows," *AIAA J.*, **35**, pp. 1415–1417.
- [21] Morinishi, Y., Lund, T. S., Vasilyev, O. V., and Moin, P., 1998, "Fully Conservative Higher Order Finite Difference Schemes for Incompressible Flow," *J. Comput. Phys.*, **143**, pp. 90–124.
- [22] Beaudan, P., and Moin, P., 1994, "Numerical Experiments on the Flow Past a Circular Cylinder at Sub-Critical Reynolds Number," Department Mechanical Engineering, Stanford University, Report No. TF-62.
- [23] Kravchenko, A. G., and Moin, P., 2000, "Numerical Studies of Flow Over a Circular Cylinder at $Re_D=3900$," *Phys. Fluids*, **12**, pp. 403–417.
- [24] Orlanski, I., 1976, "Simple Boundary Condition for Unbounded Hyperbolic Flows," *J. Comput. Phys.*, **21**, pp. 251–269.
- [25] Spalart, P. R., 1986, "Numerical Study of Sink Flow Boundary Layers," *J. Fluid Mech.*, **172**, pp. 307–328.
- [26] Fadlun, E. A., Verzicco, R., Orlandi, P., and Mohd-Yusof, J., 2000, "Combined Immersed Boundary Finite Difference Methods for Three Dimensional Complex Flow Simulations," *J. Comput. Phys.*, **161**, pp. 35–60.
- [27] Muldoon, F., and Acharya, S., 2005, "Mass Conservation in Immersed Boundary Method," *Proceedings of the FEDSM*, pp. 1–9, Paper No. FEDSM-77301.
- [28] Sarkar, S., 2008, "Identification of Flow Structures on a LP Turbine Blade Due to Periodic Passing Wakes," *ASME J. Fluids Eng.*, **130**, p. 061103.
- [29] Sarkar, S., 2007, "The Effects of Passing Wakes on a Separating Boundary Layer Along a Low-Pressure Turbine Blade Through Large-Eddy Simulation," *Proc. Inst. Mech. Eng., Part A*, **221**, pp. 551–564.
- [30] Sarkar, S., and Voke, P. R., 2006, "Large-Eddy Simulation of Unsteady Surface Pressure on a LP Turbine Blade Due to Interactions of Passing Wakes and Inflectional Boundary Layer," *ASME J. Turbomach.*, **128**, pp. 221–231.
- [31] Sarkar, S., and Sarkar, S., 2007, "Large-Eddy Simulations of Cylinder Boundary Layer Interactions," *Proceedings of the ACFD7*, pp. 1349–1360.
- [32] Sarkar, S., and Sarkar, S., 2007, "Immersed Boundary Method for Simulating Complex Flows," *Proceedings of the ICFD'07*, University of Reading, UK.
- [33] Jacobs, R. G., and Durbin, P. A., 2001, "Simulations of Bypass Transition," *J. Fluid Mech.*, **428**, pp. 185–212.
- [34] Ovchinnikov, V., Piomelli, U., and Choudhari, M. M., 2006, "Numerical Simulations of Boundary-Layer Transition Induced by a Cylinder Wake," *J. Fluid Mech.*, **547**, pp. 413–441.
- [35] Zhou, M. D., and Squire, L. C., 1985, "The Interaction of a Wake With a Turbulent Boundary-Layer," *J. Aeronaut. Sci.*, **89**, pp. 72–81.
- [36] Zovatto, L., and Pedrizzetti, G., 2001, "Flow About a Circular Cylinder Between Parallel Walls," *J. Fluid Mech.*, **440**, pp. 1–25.
- [37] Wu, X., Jacobs, R. G., Hunt, J. C. R., and Durbin, P. A., 1999, "Simulation of Boundary Layer Transition Induced by Periodically Passing Wakes," *J. Fluid Mech.*, **398**, pp. 109–153.
- [38] Matsubara, M., and Alfredsson, H., 2001, "Disturbance Growth in Boundary Layers Subjected to Free-Stream Turbulence," *J. Fluid Mech.*, **430**, pp. 149–168.
- [39] Spalart, P. R., 1988, "Direct Simulation of Turbulent Boundary Layer Up to $Re_\theta=1410$," *J. Fluid Mech.*, **187**, pp. 61–98.
- [40] Kim, H. T., Kline, S. J., and Reynolds, W. C., 1968, "An Experimental Study of Turbulence Production Near a Smooth Wall in a Turbulent Boundary Layer With Zero Pressure Gradient," Stanford University, CA, Report No. MD-20.

On the Pulsed and Transitional Behavior of an Electrified Fluid Interface

Paul R. Chiarot

Sergey I. Gubarenko

Ridha Ben Mrad

Pierre E. Sullivan

e-mail: sullivan@mie.utoronto.ca

Department of Mechanical and Industrial
Engineering,
University of Toronto,
5 King's College Road,
Toronto, ON M5S 3G8, Canada

Transient modes of an electrified fluid interface are investigated, specifically, (a) intermittent or pulsed cone-jet mode and (b) smooth and abrupt transitions of the interface in response to a step voltage. These modes were studied experimentally by capturing the motion of the interface and measuring the emitted ion current (via electrospray) as they occur. The observed phenomena are described using an analytical model for the equilibrium of an electrified fluid interface, and the effect of operational parameters on the transient modes is discussed. Pressure, which is related to the supplied flow rate, significantly influences the behavior of the transient modes. It is useful to understand transient modes so they can be avoided in applications that require a stable electrospray. However, with improved knowledge, the modes studied here can assist in the development of specialized applications. [DOI: 10.1115/1.3203203]

1 Introduction

An electrospray will form from an air-fluid interface subject to a large electric field. The interface deforms into a conical shape, and the spray, consisting of highly charged droplets, emits from the apex of the cone. This mechanism is used in electrospray ionization, where compounds are transferred from solution into the gas phase. Electrospray is of great importance for mass spectrometry [1], material deposition [2], and sample synthesis [3].

The shape of an electrified interface, the conditions that lead to the onset of jetting, and the properties of the emitted jet have been studied for decades. Taylor [4] first reported an analytical model for the formation and structure of the electrified cone. Basaran and Scriven [5] and Pantano et al. [6] investigated the shape and stability of droplets in an electric field, and Stone et al. [7] used slender body theory to study drops with conical ends. The “modes” or “regimes” that an electrified interface can exhibit were reported by Cloupeau and Prunet-Foch [8]. Fernandez de la Mora [9] accounted for the effect of space charge in the emitted jet on the cone shape to explain differences in observed cone angles from that predicted by Taylor [4]. Fernandez de la Mora and Loscertales [10] and Ganan-Calvo et al. [11] studied the spray current and emitted droplet size of a conical electrified interface, and introduced scaling laws to predict these two quantities. Cherny [12] used perturbation methods to investigate the structure of the Taylor cone and the emitted jet. For a complete review on the subject of Taylor cones, see Ref. [13].

More recently the dynamic and transient behavior of an electrified interface has received greater attention. Collins et al. [14] reported a simulation of cone and jet formation and droplet breakup. Notz and Basaran [15] investigated drop formation in an electric field, and Reznik et al. [16] investigated the shape evolution of an electrified interface over time, examining isolated droplets and the impact of electrical Bond number on interface evolution.

In this study, two transient modes are examined: (a) intermittent or pulsed cone-jet mode, and (b) smooth and abrupt transitions of the interface in response to a step voltage. These modes are studied by capturing the motion of the interface and measuring the emitted ion current. The observed phenomena are then accounted

for using a recently developed equilibrium model by Gubarenko et al. [17]. The model simplifies the treatment of the complex modes by assuming that the operating point of the interface parameters moves within an operational space and transitions between equilibrium and quasi-equilibrium states. This allows for these phenomena to be understood and predicted, and the impact of operational parameters on the transient behavior is determined.

Several experimental techniques have been used to probe the dynamic behavior of electrified interfaces. Zhang and Basaran [18] used fast imaging to characterize the dynamics of drop formation from a nozzle under electric fields of weak to moderate strengths. Marginean et al. [19] used a combination of fast imaging and current measurements to study the same problem under weak, moderate, and large electric fields. Others used Phase Doppler Anemometry to measure the size and velocity of droplets produced by an electrospray [20,21]. Here, we follow Marginean et al. [19], and use a two pronged approach based on imaging and current measurements.

Typically, a steady cone-jet is of primary importance, especially in applications such as mass spectrometry. Knowledge of the transient modes considered in this study, and the operational parameters that cause them, is useful to avoid the negative aspects of these modes. However, if better understood, the transient modes considered here can assist in the further development of useful applications, such as e-jet printing [22] and material deposition [23].

2 The Equilibrium Model

A full description of the equilibrium model is given by Gubarenko et al. [17], and the details are briefly summarized here. The model describes the impact of the three dominant stresses—surface tension, electric (Maxwell) stress, and pressure difference—on the equilibrium of an electrified interface (note that the impact of the viscous stress is small and can be neglected). A three dimensional space of the operating parameters is described, and regions or subdomains are defined where equilibrium, quasi-equilibrium, and nonequilibrium conditions exist. These subdomains are explicitly defined below. The surfaces dividing the subdomains are referred to as “critical surfaces,” and represent the boundary of equilibrium (or quasi-equilibrium) and nonequilibrium states. It is convenient to work in a two dimensional operational space, so the electrode separation distance is typically fixed, and the impact of the applied voltage and pressure difference is focused on. In this case, the critical surface is re-

Contributed by the Fluids Engineering Division of ASME for publication in the JOURNAL OF FLUIDS ENGINEERING. Manuscript received October 17, 2008; final manuscript received June 11, 2009; published online August 17, 2009. Assoc. Editor: Steven T. Wereley.

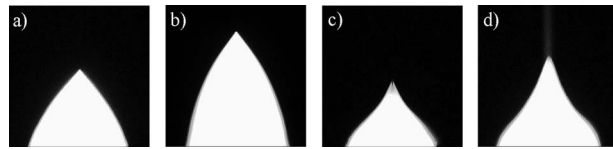


Fig. 1 Quasi-equilibrium states for the interface. In all cases, the interface emits a spray.

duced to a “critical curve.” The model reveals that the angle at the center of the interface, the apex angle (θ), dramatically affects the location of the critical surface in the operational space.

“Equilibrium” means all forces are balanced on the interface, the apex angle is 0 deg, and the interface does not emit a spray. In “quasi-equilibrium,” all forces are balanced on the interface; however, the apex angle is nonzero and the interface emits a spray (see Fig. 1 for examples of an interface in quasi-equilibrium). Fluids of high conductivity have a small jet formation region located almost entirely at the apex of the cone [8]. This means that an interface in quasi-equilibrium can accurately be described as a continuous function after specifying an apex angle (i.e., the jet formation region can be omitted in the model). Highly conductive fluids are the focus of both this study and the analytical model [17].

An electrified interface has an operating point that is a function of the applied voltage, electrode separation, and pressure difference residing inside the operational space. The location of the operating point defines the important characteristics of the interface. By using the equilibrium model, properties of the interface can be predicted or selected, including the equilibrium status of the interface, the presence of an electro-spray, and the shape of the meniscus. The operating point can also move within the operational space and transfer between equilibrium subdomains.

To use the equilibrium model, it is necessary to specify the value of the apex angle and calculate the pressure difference across the interface. The sine of the apex angle defines the location of the critical surface, and the pressure difference dictates (along with the applied voltage and electrode separation distance) the location of the interface operating point in the operational domain. The apex angle term is calculated from the experimental data by fitting a linear function to several points (on the order of 10–20) to a portion of the interface in the vicinity of the apex. It is important to note that the apex angle used here and the classic Taylor angle θ_T [4] are related as $\theta + \theta_T = 90$ deg.

For an interface under pressure, surface tension, and electric stress, the pressure term is found by solving a stress balance for the interface, knowing the curvature of the interface and surface tension coefficient (giving the stress from the surface tension), and the applied voltage and counterelectrode separation (giving the electric stress). Note that the pressure term is the excess internal pressure at the interface that balances the surface tension and electric stress. The position of the interface as a function of pressure difference can be expressed using the stress balance, and compared with the position of the interface at experimentally found points. By minimizing the difference between the measured and calculated points, the pressure difference across the interface can be found [24]. The pressure difference for interfaces not under electric stress can be determined by solving the Young–Laplace equation. Pressure values are gauge pressures.

The equilibrium model accounts for the observed transient phenomena of an electrified interface. The phenomena considered in this study are intermittent or pulsed cone-jet mode and smooth and abrupt transitions of the interface in response to a step voltage. The equilibrium model accounts for these phenomena as movement of the operating point of the interface within the operational domain and the transition between equilibrium and quasi-equilibrium states. This approach simplifies the treatment of these transient phenomena while still accurately describing the observed behavior.

Most applications require transient phenomena to be avoided all together. In mass spectrometry or material deposition, stable cone-jets emitting a steady stream of material are essential. However, other more specialized applications find transient phenomena to be useful. For example, it is possible to use pulsed cone-jet mode to emit discrete packets of droplets through the electro-spray mechanism. Rather than having a continuous spray, droplets are emitted intermediately using this mode, and it was proposed to use pulsed cone-jets in printing [22] and material deposition [23] applications. It might also be possible to use this mechanism to mimic the function of an ion gate or shutter. A theoretical understanding of intermittent or pulsed cone-jet mode using the analytical model reported in Ref. [17], combined with the results of this study, will assist in the further development of specialized applications. Application of the equilibrium model to transient phenomena is discussed in Sec. 3.

3 Experimental Investigation of Transient Phenomena

3.1 Materials and Experimental Setup. Testing was performed using metal tubing with a radius of 150 μm . The electrified interface was located at the edge of the metal tubing that was positioned directly in front of the counterelectrode. For the imaging of the interface, the bulk fluid used in this study was a 100 μM solution of Rhodamine B in 70:30 MeOH:H₂O. The surface tension values were determined using Ref. [25]. Rhodamine B is a fluorescent dye and was used to improve the recording, analysis, and display of the interface. For the experiments that involved measuring the emitted ion current, the bulk fluid is a 100 μM solution of sodium iodide (NaI) in 90:10 MeOH:H₂O. For some experiments, the bulk fluid is modified by adding 1% AcOH.

The flow rate was controlled using a syringe pump (Cole Parmer, Montreal, QC, Canada), and the interface was observed and recorded using an inverted fluorescent microscope (Leica, Wetzlar, Germany) and charge-coupled device (CCD) camera (Sony, Tokyo, Japan). Using optical filters and a dichromatic mirror (a filter cube), the microscope can illuminate the interface with light at a wavelength of 515–560 nm, and pass light at a wavelength exceeding 590 nm to the CCD camera. These wavelengths are ideal for the excitation/emission spectrum of Rhodamine B. Voltage is applied to the metal tubing using a high voltage source (Labsmith HVS448) with an operating range 0–3000 V. The radius of the interface in all of the captured images is 150 μm , which is the same as the outer radius of the metal tubing. Images of the interface are captured at a resolution of 640 \times 480 in PNG format and processed using MATLAB [26].

The use of Rhodamine B allows for the interface to be more easily visualized and processed. However, it was typically found that the emitted jet could not be visualized when illuminated by filtered light. This is likely because of the narrow bandwidth applied and the small volume of the jet. The jet was visualized when the full spectrum (bandwidth) of light is applied. All frames are aligned so that the bottom of the image is aligned with the end of the metal tubing. This was confirmed visually and simplifies image processing.

Emitted ion current measurements are made using a current amplifier (Keithley, Cleveland, OH), and the output is monitored using a digital oscilloscope (Agilent, Santa Clara, CA). Ions are emitted from the apex of the Taylor cone and neutralized on the counterelectrode. This current was measured, converted to a voltage, and then amplified for measurement.

3.2 Intermittent or Pulsed Cone-Jet Mode. The intermittent or pulsed cone-jet mode was identified by Cloupeau and Prunet-Foch [8] who reported that this occurs when “the voltage is slightly lower than for which a single permanent jet is obtained,” and this mode is one focus of this study. Marginean et al. [19] studied transitions between the operating regimes of an electro-spray in experimental studies, and Li [27] investigated meniscus

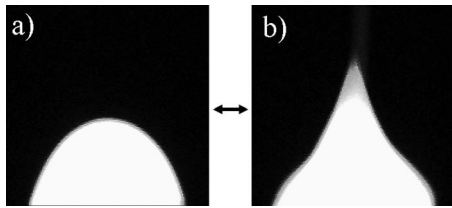


Fig. 2 Two images of an electrified interface in “intermittent or pulse cone-jet mode.” The shape of the interface cycles back and forth between (a) and (b) at a frequency of 6 Hz. The apex angle in (b) is 63 deg.

deformation under the influence of a pulsed voltage—in contrast to this work where intermittent or pulsed cone-jet mode is observed for constant voltages.

An example of pulsed cone-jet mode is shown in Fig. 2. The applied voltage was held constant at 3000 V and the flow rate was $0.1 \mu\text{l}/\text{min}$. The time difference between Figs. 2(a) and 2(b) is 165 ms. These two interface shapes repeated cyclically at a constant frequency of 6 Hz, transforming from a rounded apex (slope at the middle equal to zero) to a typical cone-jet configuration, and back again. During the brief cone-jet period, the interface emits a spray, resulting in a pulsed spray being emitted at the same frequency as the interface transition.

As shown in the operational domain in Fig. 3, this pulsed cone-jet transition will straddle two critical curves—one corresponding to $\theta=0$ deg and the other corresponding to $\theta=63$ deg (the apex angle in Fig. 2(b)). The operating point of the interface in Fig. 2(a) sits left of the critical curve in equilibrium. As the pressure increases, the operating point moves to the right and crosses the critical curve (to the point marked “●”). The movement is in a straight horizontal line as the voltage is held constant. As the operating point crosses the critical curve to the point marked ●, it smoothly and immediately relocates into the quasi-equilibrium region, left of the critical curve for $\theta=63$ deg, as shown by the broken arrow in Fig. 3. Once in the quasi-equilibrium region, the interface appears as seen in Fig. 2(b).

Once in the quasi-equilibrium region, the pressure increases for a short amount of time until it crosses the critical curve for $\theta=63$ deg to the point marked with a ●. Once it crosses this curve, the interface is in nonequilibrium, and it adjusts to find an equi-

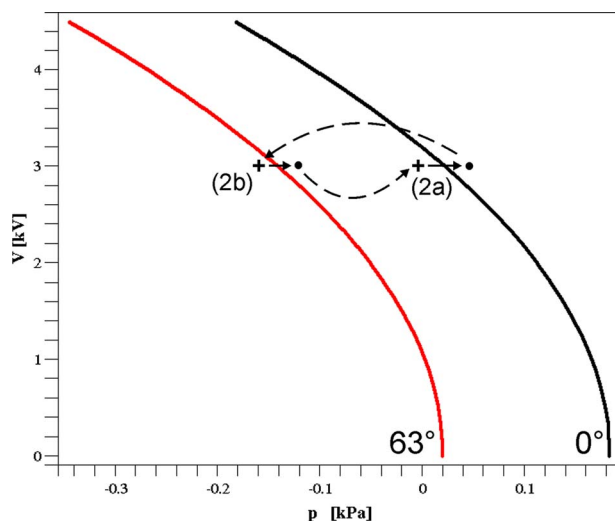


Fig. 3 Operational domain for an electrode separation distance of 7 mm and surface tension coefficient of 27.48 mN/m. The operating point moves left and right in the domain across the critical curves between equilibrium and quasi-equilibrium.

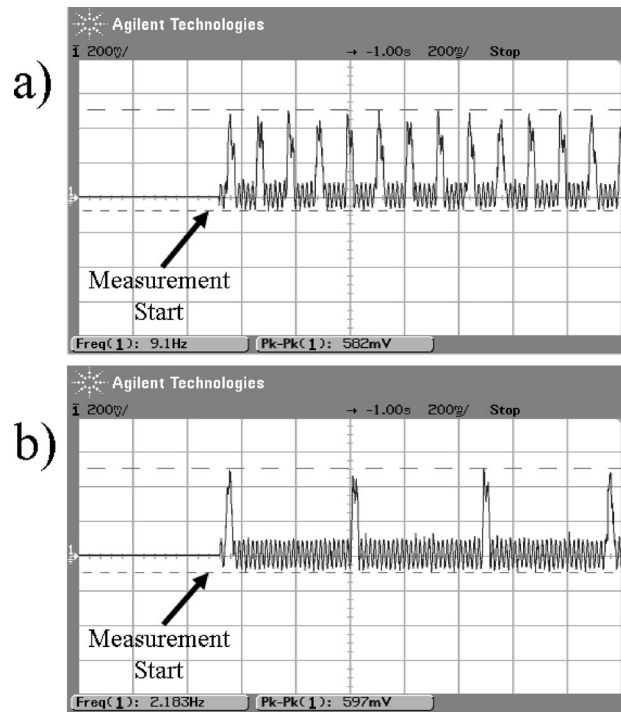


Fig. 4 Current measurements of emitted ion current. The ion current is collected at the counterelectrode and converted to a voltage. The bulk fluid is a $100 \mu\text{M}$ solution of NaI in 90:10 MeOH:H₂O. The flow rate in (a) is $2 \mu\text{l}/\text{min}$ and in (b) is $0.5 \mu\text{l}/\text{min}$. The current peaks represent the quasi-equilibrium state of the interface.

librium state. Due to the low applied flow rate, the interface collapses and returns to the equilibrium state (shown by the broken arrow). Once back in equilibrium, the pressure builds again and the process repeats itself. This cyclic process is observed to occur at a very regular frequency of approximately 6 Hz.

The question remains as to why the interface in Fig. 2(b), after moving out of the quasi-equilibrium region, collapses to an equilibrium state rather than moving to a second quasi-equilibrium state (as seen for the smooth transition below). This is because of the supplied flow rate. For similar operating conditions at higher flow rates, a stable cone-jet can form [17]. Experimentally, it was found that higher flow rates create larger pressure differences (in the negative direction) across the interface. A similar finding was reported in other electro spray studies [28]. At low flow rates, the pressure difference across the interface remains small, and the operating point of the interface is limited by the amount it can move in the negative pressure direction (to the left in Fig. 3). As a result, the operating point—after crossing into nonequilibrium—must move to the right, back to the equilibrium region. Thus, the contention of Cloupeau and Prunet-Foch [8] that pulsed cone-jet mode occurs at voltages slightly below those required for a stable cone-jet should also include the importance of sufficient pressure (related to flow rate) as well. Fernandez de la Mora and Loscertales [10] and Chen and Pui [29] also reported a required minimum flow rate to achieve a stable electro spray. In their work, scaling laws for the minimum flow rate (Q_{min}) are expressed as a function of the bulk fluid parameters, but they do not specifically address the relationship of flow rate and pulsed mode.

Ion current measurements confirm the regularity of pulsed cone-jet mode and the impact of flow rate (pressure) on the pulse frequency. Figure 4 shows the measured ion current emitted by an interface in pulse cone-jet mode for two different flow rate conditions. Figure 4(a) shows a flow rate of $2 \mu\text{l}/\text{min}$ and Fig. 4(b) shows a flow rate of $0.5 \mu\text{l}/\text{min}$. In both cases, the bulk fluid is a

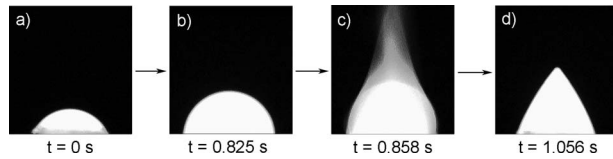


Fig. 5 Time lapsed images of an interface undergoing an abrupt transition. The pressure difference is smoothly increased in (a) and (b), and a step voltage is discontinuously (abruptly) applied in (c). A loss of mass from the interface can be seen when the voltage is applied. (d) The stable final cone-jet.

100 μM solution of NaI in 90:10 MeOH:H₂O. The current between pulses is primarily attributed to external electrical noise. In Fig. 4, the current peaks correspond to a quasi-equilibrium state of the interface (i.e., Fig. 2(b)), and the zero current condition corresponds to the equilibrium state (i.e., Fig. 2(a)). The pulsed mode seen in Fig. 4 is the low frequency component of what Juraschek and Rollgen [28] identified as “axial spray mode I.” The low frequency oscillation of the spraying jet corresponds to the jumping (i.e., movement) of the operating point in the parameter space between equilibrium and quasi-equilibrium subdomains. This measurement shows that the magnitude of the emitted current remains constant despite changes in the pulse frequency, and that the pulse frequency (the emitted ions) can be controlled via the pressure difference across the interface (i.e., the supplied flow rate).

3.3 Smooth and Abrupt Transitions in Response to a Step Voltage.

Experimental evidence reveals that it is possible to have both smooth and abrupt transitions from equilibrium to final quasi-equilibrium state. The type of transition (for fixed electrode separation) depends on how smoothly the pressure difference and voltage are applied to the interface. Smoothly applying an increasing pressure difference across the interface is done by operating the syringe pump at a constant flow rate. Smoothly applying the voltage is more difficult, as most high voltage supplies (including the unit used in the study) do not allow gradual transitions over a wide operating range, instead, allowing only finite steps. Nevertheless, the impact of varying the spray voltage, as well as the resultant response of the interface, was previously addressed by Marginean et al. [19].

Examples of transitions are shown in Figs. 5 and 6. Figure 5 represents an abrupt transition where pressure is smoothly applied, and the voltage is abruptly applied (a voltage step) from 0 V up to 3000 V. Figure 6 represents a smooth transition where the voltage is applied before any fluid is present (at 3000 V), and then pressure is smoothly applied. The time delay between each frame is shown in each figure.

The transition of the interface in Figs. 5 and 6 can be tracked using the operational domains shown in Figs. 7 and 8, respectively. The solid and dashed arrows represent smooth transitions

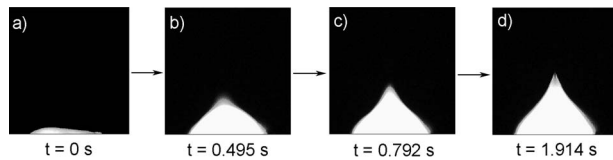


Fig. 6 Time lapsed images of an interface undergoing a smooth transition. The voltage is applied in (a) before any fluid is present. The pressure difference smoothly changes from (b) to (d). The interface in (d) has been steady for hundreds of milliseconds. No abrupt loss of mass is seen for this smooth transition compared with the abrupt transition.

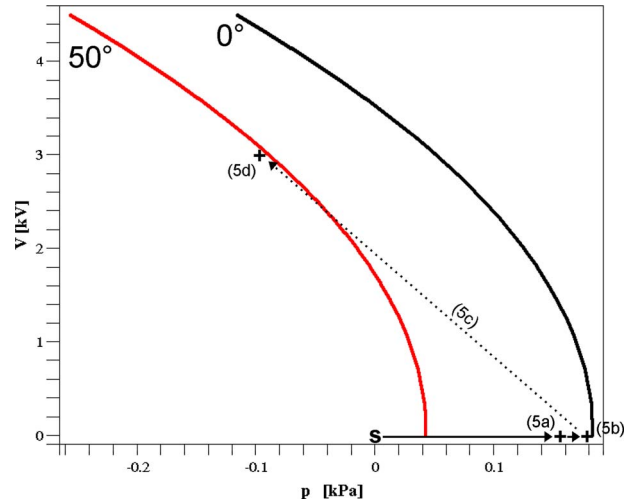


Fig. 7 Operational domain for an electrode separation distance of 10 mm and surface tension coefficient of 27.48 mN/m. The solid arrow represents the smoothly increasing pressure difference, and the dotted arrow represents a discontinuous or abrupt increase in voltage. The application of voltage is discontinuous and not smooth. The pressures at (a), (b), and (d) are known exactly. There is no pressure to report for (c) since the interface has ruptured.

and the dotted arrow represents an abrupt change in voltage. For both cases, the electrode separation is fixed.

The operating point of the interface shown in Fig. 5 on the domain shown in Fig. 7 starts with a zero pressure difference and zero applied voltage (S in Fig. 7). As fluid is infused with the syringe pump, the operating point moves smoothly to the right (increasing positive pressure), up to the point shown in Fig. 5(a). The pressure difference across the interface in Fig. 5(a) can be found by measuring the height of the interface [17]. Mass is continually infused until nearly the boundary of equilibrium shown in Fig. 5(b). At this point, a step voltage of 3000 V is applied, and an image was taken (Fig. 5(c)) showing the interface undergoing an abrupt transition. As the interface completely ruptures, a substan-

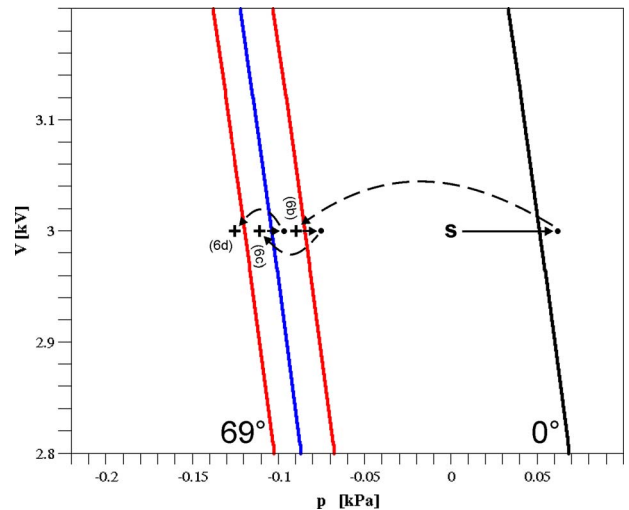


Fig. 8 Operational domain for an electrode separation distance of 10 mm and surface tension coefficient of 27.48 mN/m. The solid arrow represents smoothly increasing pressure difference, and the dashed arrow represents smooth relocations of the operating points. The transition is smooth; therefore there is no abrupt loss of mass, as seen in Fig. 5.

tial mass of fluid is ejected. Since the interface loses mass, the pressure difference across the interface moves in the negative direction. The operating point after transition (Fig. 5(d)) is to the left of the critical curve for $\theta=50$ deg in a quasi-equilibrium state, since the interface emits a spray after the voltage is applied.

Reznik et al. [16] also found a total rupturing of the interface, as in Fig. 5(c) (they defined this as droplets “jumping off”), but only for large contact angles in excess of 0.8π . Here, rupturing occurs at much smaller angles. Reznik et al. [16] dealt with isolated droplets—while here droplets are infused with mass from the syringe pump.

Qualitatively, it has been observed that when the pressure difference across the interface is large before an abrupt transition, the sudden loss of mass from the interface in transition is large. As seen in Fig. 5, when the applied pressure before transition is near the equilibrium limit, the mass lost when the voltage is applied was large. For smaller pressure differences before abrupt transition, the amount of mass lost from the interface was observed to be comparatively less.

For the smoothly transitioning interface in Fig. 6, the operating point starts at zero pressure difference but at an applied voltage of 3000 V (the step voltage is applied before any fluid is present). Mass is continually infused with the syringe pump, and the pressure difference smoothly increases in the positive direction, causing the operating point on the domain in Fig. 8 to start at *S* and move to the right. After crossing the critical curve for $\theta=0$ deg, the operating point immediately relocates to the quasi-equilibrium region, where the pressure increases again. Here the operating point moves to the right, crossing into nonequilibrium, and adjusts to find equilibrium. The flow rate in this case is sufficiently high; therefore the operating point can move to the left (for decreasing pressure, as also noted in Ref. [28]), and the interface moves into a second quasi-equilibrium state. This process repeats until the interface reaches a final steady operating location.

For the operating domain in Fig. 8, only three discrete transitions into three different quasi-equilibrium regions are shown and correspond to the three time delays of the interface shown in Fig. 6. It is possible to take more intermediate images of the interface and plot additional operating points. This would show a series of transitions between quasi-equilibrium states until reaching the steady configuration shown in Fig. 6(d), and would mean that the transitional operating points and critical curves would get increasingly closer together.

Overall, the interface in Fig. 6 smoothly transitions to a final quasi-equilibrium state: cone-jet mode. On the operating domain, the operating point moves in a smooth manner. Most notably, there is no dramatic rupture of the interface that is found for the abrupt transition found in Fig. 5, just a smooth transition to an interface in cone-jet mode.

The smooth transition can be compared with the pulsed cone-jet configuration considered in Sec. 3.2. In this case, the interface does not collapse and is able to return to a quasi-equilibrium state after a critical curve is crossed. The most notable difference in operating conditions is the supplied flow rate, where the smooth transition in Fig. 6 is an order of magnitude larger than the conditions in Fig. 2. With adequate flow rate, the pressure difference can decrease sufficiently, such that the operating point can move to the left. The operating point will relocate in a smooth manner between quasi-equilibrium regions, until a steady value for pressure difference is reached.

4 Summary

Two transient modes of operation for an electrified interface, intermittent or pulsed cone-jet mode and the smooth and abrupt transitions of the interface in response to a step voltage, have been investigated. Using an analytical model [17], the behavior was simplified by assuming that the operating point of the interface parameters moves within an operational domain and transitions between equilibrium and quasi-equilibrium states. The experimen-

tally measured interface motion and emitted ion current confirmed this and revealed the impact of the operational parameters on the transient modes. It was found that pulsed cone-jet mode is not only influenced by the applied voltage—pressure (related to the supplied flow rate) also plays a role in its formation and behavior.

When applying a step voltage, it is important to avoid an abrupt transition in most applications. When forming an electrospray for use in mass spectrometry, a dramatic loss of mass, as the voltage is first applied, could result in significant sample loss (contained in the solvent). For material deposition, an abrupt emission of mass affects the uniformity of the film being applied. The amount of mass ejected during the abrupt transition is unpredictable, and a good way to avoid abrupt transitions is to smoothly vary the pressure difference (from zero) after the step voltage is applied.

Acknowledgment

The authors gratefully acknowledge the financial support of the Natural Sciences and Engineering Research Council of Canada (NSERC) and Engineering Services Inc. (ESI).

References

- [1] Fenn, J. B., Mann, M., Meng, C. K., Wong, S. F., and Whitehouse, C. M., 1989, “Electrospray Ionization for Mass Spectrometry of Large Biomolecules,” *Science*, **246**(4926), pp. 64–71.
- [2] Satterley, C., Perdigao, L., Saywell, A., Magnano, G., Rienzo, A., Mayor, L., Dhanak, V., Beton, P., and O’Shea, J., 2007, “Electrospray Deposition of Fullerenes in Ultra-High Vacuum: In Situ Scanning Tunneling Microscopy and Photoemission Spectroscopy,” *Nanotechnology*, **18**, p. 455304.
- [3] Barrero, A., and Loscertales, I. G., 2007, “Micro- and Nanoparticles Via Capillary Flows,” *Annu. Rev. Fluid Mech.*, **39**, pp. 89–106.
- [4] Taylor, G. I., 1964, “Disintegration of Water Drops in Electric Field,” *Proc. R. Soc. London*, **280**(1382), pp. 383–397.
- [5] Basaran, O., and Scriven, L. E., 1990, “Axisymmetric Shapes and Stability of Pendant and Sessile Drops in an Electric Field,” *J. Colloid Interface Sci.*, **140**(1), pp. 10–30.
- [6] Pantano, C., Ganan-Calvo, A. M., and Barrero, A., 1994, “Zeroth-Order, Electrohydrostatic Solution for Electro spraying in Cone-Jet Mode,” *J. Aerosol Sci.*, **25**, pp. 1065–1077.
- [7] Stone, H., Lister, J., and Brenner, M., 1999, “Drops With Conical Ends in Electric and Magnetic Fields,” *Proc. R. Soc. London, Ser. A*, **455**, pp. 329–347.
- [8] Cloupeau, M., and Prunet-Foch, B., 1994, “Electrohydrodynamic Spaying Functioning Modes: A Critical Review,” *J. Aerosol Sci.*, **25**(6), pp. 1021–1036.
- [9] Fernández de la Mora, J., 1992, “The Effect of Charge Emission From Electrified Liquid Cones,” *J. Fluid Mech.*, **243**, pp. 561–574.
- [10] Fernández de la Mora, J., and Loscertales, I. G., 1994, “The Current Emitted by Highly Conducting Taylor Cones,” *J. Fluid Mech.*, **260**, pp. 155–184.
- [11] Ganan-Calvo, A. M., Davila, J., and Barrero, A., 1997, “Current and Droplet Size in the Electro spraying of Liquids. Scaling Laws,” *J. Aerosol Sci.*, **28**(2), pp. 249–275.
- [12] Cherney, L., 1999, “Structure of Taylor Cone-Jets: Limit of Low Flow Rates,” *J. Fluid Mech.*, **378**, pp. 167–196.
- [13] Fernandez de la Mora, J., 2007, “The Fluid Dynamics of Taylor Cones,” *Annu. Rev. Fluid Mech.*, **39**, pp. 217–243.
- [14] Collins, R. T., Jones, J. J., Harris, M. T., and Basaran, O., 2008, “Electrohydrodynamic Tip Streaming and Emission of Charged Drops From Liquid Cones,” *Nat. Phys.*, **4**, pp. 149–154.
- [15] Notz, P. K., and Basaran, O., 1999, “Dynamics of Drop Formation in an Electric Field,” *J. Colloid Interface Sci.*, **213**, pp. 218–237.
- [16] Reznik, S., Yarin, A., Theron, A., and Zussman, E., 2004, “Transient and Steady Shapes of Droplets Attached to a Surface in a Strong Electric Field,” *J. Fluid Mech.*, **516**, pp. 349–377.
- [17] Gubarenko, S., Chiarot, P., Ben Mrad, R., and Sullivan, P., 2008, “Plane Model of Fluid Interface Rupture in an Electric Field,” *Phys. Fluids*, **20**(4), p. 043601.
- [18] Zhang, X., and Basaran, O., 1996, “Dynamics of Drop Formation From a Capillary in the Presence of an Electric Field,” *J. Fluid Mech.*, **326**, pp. 239–263.
- [19] Marginean, I., Nemes, P., and Vertes, A., 2007, “A Stable Regime in Electro sprays,” *Phys. Rev. E*, **76**, p. 026320.
- [20] Gomez, A., and Tang, K., 1994, “Charge and Fission of Droplets in Electrostatic Sprays,” *Phys. Fluids*, **6**(1), pp. 404–414.
- [21] Venter, A., Sojka, P., and Cooks, R., 2006, “Droplet Dynamics and Ionization Mechanisms in Desorption Electrospray Ionization Mass Spectrometry,” *Anal. Chem.*, **78**, pp. 8549–8555.
- [22] Choi, H., Park, J., Park, O., Ferreira, P., Georgiadis, J., and Rogers, J., 2008, “Scaling Laws for Jet Pulsations Associated With High-Resolution Electrohydrodynamic Printing,” *Appl. Phys. Lett.*, **92**, p. 123109.

- [23] Paine, M., Alexander, M., Smith, K., Wang, M., and Stark, J., 2007, "Controlled Electrospray Pulsation for Deposition of Femtoliter Fluid Droplets onto Surfaces," *J. Aerosol Sci.*, **38**, pp. 315–324.
- [24] Chiarot, P., Gubarenko, S., Ben Mrad, R., and Sullivan, P., 2008, "Application of an Equilibrium Model for an Electrified Fluid Interface—Electrospray Using a PDMS Microfluidic Device," *J. Microelectromech. Syst.*, **17**(6), pp. 1362–1375.
- [25] Lide, D., ed., 2006, *CRC Handbook of Chemistry and Physics*, 87th ed., Taylor and Francis, New York.
- [26] The Mathworks Inc., 2002, *MATLAB* Version 6.5.
- [27] Li, J. L., 2006, "On the Meniscus Deformation When the Pulsed Voltage Is Applied," *J. Electrostat.*, **64**, pp. 44–52.
- [28] Juraschek, R., and Rollgen, F., 1998, "Pulsation Phenomena During Electrospray Ionization," *Int. J. Mass Spectrom.*, **177**, pp. 1–15.
- [29] Chen, D., and Pui, D., 1997, "Experimental Investigation of Scaling Laws for Electrospraying: Dielectric Constant Effect," *Aerosol Sci. Technol.*, **27**, pp. 367–380.

Curved Non-Newtonian Liquid Jets With Surfactants

Jamal Uddin¹

e-mail: uddinj@maths.bham.ac.uk

Stephen P. Decent

School of Mathematics Edgbaston,
University of Birmingham,
Birmingham, B15 2TT, United Kingdom

Applications of the breakup of a liquid jet into droplets are common in a variety of different industrial and engineering processes. One such process is industrial prilling, where small spherical pellets and beads are generated from the rupture of a liquid thread. In such a process, curved liquid jets produced by rotating a perforated cylindrical drum are utilized to control drop sizes and breakup lengths. In general, smaller droplets are observed as the rotation rate is increased. The addition of surfactants along the free surface of the liquid jet as it emerges from the orifice provides a possibility of further manipulating breakup lengths and droplet sizes. In this paper, we build on the work of Uddin et al. (2006, "The Instability of Shear Thinning and Shear Thickening Liquid Jets: Linear Theory," ASME J. Fluids Eng., 128, pp. 968–975) and investigate the instability of a rotating liquid jet (having a power law rheology) with a layer of surfactants along its free surface. Using a long wavelength approximation we reduce the governing equations into a set of one-dimensional equations. We use an asymptotic theory to find steady solutions and then carry out a linear instability analysis on these solutions.

[DOI: 10.1115/1.3203202]

1 Introduction

The manufacture of small spherical pellets can be achieved through the industrial prilling process. In such a process a specially perforated large cylindrical drum is made to rotate about its axis. Molten liquid is pumped into the drum, and long curved jets are produced from the holes in the surface of the drum, which break up due to centrifugal and capillary instabilities. Break up leads to the production of droplets, which subsequently solidify and form pellets. This process is widely used in industry for the manufacture of fertilizers, magnesium, and aluminium pellets (see Refs. [1,2]).

Previous studies to investigate the prilling process for Newtonian liquids have been investigated by Wallwork et al. [3,4] and Decent et al. [5]. Nonlinear effects have also been considered by Părau et al. [6,7] and Wong et al. [8]. The linear and nonlinear instability of rotating power law jets were investigated by Uddin et al. [9–11]. Experimental studies to model the prilling process for Newtonian jets were performed by Wong et al. [8] with a similar investigation for shear thinning jets by Hawkins et al. [12].

Previous studies on the effect of surfactants along straight liquid threads or bridges have been carried out by Whitaker [13], who considered the instability of a liquid thread encased in an inviscid environment and Hansen et al. [14] who investigated the linear instability of a liquid thread (containing soluble surfactants) with a viscous surrounding fluid. They found, as expected, that surfactants slow the growth of disturbances and that as the importance of surfactant activity increases that the dominant, or most unstable, the wavenumber decreases. Timmermans and Lister [15] considered nonlinear approximations to the governing equations of a surfactant laden thread in an inviscid surrounding. They formulated a one-dimensional nonlinear model to investigate instability of the thread to changes in surface tension gradients. Using a scaling argument they showed that surfactants are swept away from pinching regions and thus have little effect on any dynamics in those regions. An extension of these situations involving coaxial jets have been considered by Kwak and Pozrikidis [16] and Blyth et al. [17], and a fully nonlinear one-dimensional approxi-

mation to the governing equations for liquid bridges has been performed by Abravaneswaran and Basaran [18]. The effects of surfactants on the deformation of droplets have also been extensively studied (see Ref. [19]). The stability of a two-layer channel flow and flow down an inclined plane with insoluble surfactants has been investigated by Blyth and Pozrikidis [20,21]. A review of the surfactant transport equation for an elongating thread and a stretched interface is provided by Blyth and Pozrikidis [22].

2 Problem Formulation

We assume that a large cylindrical container having radius s_0 is made to rotate with angular velocity Ω along its axis of symmetry. A small orifice is placed at the side of the container having radius a , which is considered small in relation to the radius of the container. We assume that the emerging liquid jet has a thin layer of insoluble surfactant (of fixed concentration Γ) along its free surface (see for example Ref. [23]). Furthermore, the liquid is assumed incompressible.

We examine the problem by considering a coordinate system (x, y, z) , which rotates with the container, having an origin at the axis of the container and with the position of the center of the orifice at $(s_0, 0, 0)$. The effects of gravity on the jet can be neglected if the centripetal acceleration of the jet $s_0\Omega^2$ is much greater than the acceleration due to gravity g , as is the case with industrial prilling. Then the jet moves solely in the x - z -plane and thus we can describe the centerline of the jet by coordinates $(X(s, t), 0, Z(s, t))$, where s is the arclength along the centerline of the jet, measured from the orifice, and t is time.

The rotation of the container causes the jet to curve on leaving the orifice and any analysis of the jet in the rotating (x, y, z) coordinate system becomes cumbersome. We therefore introduce a coordinate system previously used by Wallwork [4], which is similar to the approach adopted by Ribe [24] and Entov and Yarin [25], where we have one coordinate lying along the centerline of the jet corresponding to the arc length s of the jet, with the remaining coordinates as the plane polar coordinates n, ϕ (radial and azimuthal) in any cross section of the jet. The associated unit vectors are represented by $\mathbf{e}_s, \mathbf{e}_n,$ and \mathbf{e}_ϕ , respectively, and their derivation is explained further in Ref. [4].

To describe the flow we use the velocity vector $\mathbf{u} = u\mathbf{e}_s + v\mathbf{e}_n + w\mathbf{e}_\phi$ to arrive at the familiar equations of motion (including the continuity equation) given by

¹Corresponding author.

Contributed by the Fluids Engineering Division of ASME for publication in the JOURNAL OF FLUIDS ENGINEERING. Manuscript received October 15, 2008; final manuscript received July 2, 2009; published online August 18, 2009. Assoc. Editor: Neelesh A. Patankar.

$$\nabla \cdot \mathbf{u} = 0 \quad (1)$$

$$\mathbf{u}_t + \mathbf{u} \cdot \nabla \mathbf{u} = -\frac{1}{\rho} \nabla p + \frac{1}{\rho} \nabla \cdot (\eta \boldsymbol{\xi}) - 2\boldsymbol{\omega} \times \mathbf{u} - \boldsymbol{\omega} \times (\boldsymbol{\omega} \times \mathbf{r}) \quad (2)$$

where ρ and p are the density and pressure, t is time, and η is the apparent viscosity such that

$$\eta = m \left(\frac{\boldsymbol{\xi} : \boldsymbol{\xi}}{2} \right)^{(\alpha-1)/2} \quad (3)$$

where m is the flow consistency number, α is a dimensionless number referred to as the flow index number, and $\boldsymbol{\xi} = \nabla \mathbf{u} + (\nabla \mathbf{u})^T$ is the rate of strain tensor. Fluids with α less than or greater than unity are termed shear thinning and shear thickening, respectively. The angular velocity vector of the container is given by $\boldsymbol{\omega} = (0, \Omega, 0)$. The position vector of a particle on the free surface is given by $\mathbf{r} = \int \mathbf{e}_s ds + n \mathbf{e}_n$.

The free surface of the liquid jet can be described by the function $n = R(s, \phi, t)$ hence we have the unit normal vector \mathbf{n} to the free surface as

$$\mathbf{n} = \frac{\nabla(n - R(s, t, \phi))}{|\nabla(n - R(s, t, \phi))|}$$

The concentration of surfactant along the free surface of the jet is governed by (see Ref. [22])

$$\Gamma_t + \nabla_s \cdot (\Gamma \mathbf{u}_s) + \Gamma (\nabla_s \cdot \mathbf{n}) (\mathbf{u} \cdot \mathbf{n}) = S(\Gamma, B_s) + D_s \nabla_s^2 \Gamma \quad (4)$$

where $\nabla_s = (\mathbf{I} - \mathbf{n}\mathbf{n}) \cdot \nabla$ is the surface gradient operator, D_s is the surface diffusivity of surfactant, and $\nabla_s \cdot \mathbf{n} = \kappa$, where κ is the mean curvature of the free surface. S is the surfactant source term, which takes into account absorption from the free surface and is a function of the surfactant concentration on the surface Γ and surfactant concentration in the bulk B_s . In this paper we consider insoluble surfactants (so S is taken as zero) and assume that the diffusivity of surfactant is small and negligible (i.e., $D_s = 0$). Under these assumptions, and after using the properties of the surface gradient operator, we have

$$\Gamma_t + \mathbf{u} \cdot \nabla \Gamma - \Gamma \mathbf{n} \cdot ((\mathbf{n} \cdot \nabla) \mathbf{u}) = 0 \quad (5)$$

The boundary conditions, which apply on the free surface of the jet, are identical to those found in Ref. [9], except here the presence of a variable surface tension (which is a consequence of the addition of surfactants) leads to nonzero tangential stresses. Thus, we have the normal and tangential stress conditions as

$$\mathbf{n} \cdot \boldsymbol{\Pi} \cdot \mathbf{n} = \sigma \kappa \quad \text{and} \quad \mathbf{t}_i \cdot \boldsymbol{\Pi} \cdot \mathbf{n} = \mathbf{t}_i \cdot \nabla \sigma$$

where $\boldsymbol{\Pi}$ is the total stress tensor given by $\boldsymbol{\Pi} = \rho \mathbf{I} + \eta \boldsymbol{\xi}$, κ is the curvature such that $\kappa = \nabla_s \cdot \mathbf{n}$, and \mathbf{t}_i are the two tangent vectors to the normal at the free surface. The kinematic condition is given by

$$\frac{D}{Dt} (R(s, t, \phi) - n) = 0 \quad \text{for} \quad n = R(s, \phi, t)$$

The equation of state relating the surfactant concentration Γ to the surface tension of the liquid-gas interface is given by the nonlinear Szyskowsky equation

$$\sigma = \tilde{\sigma} + \Gamma_m R_g T \log \left(\frac{\Gamma_m - \Gamma}{\Gamma_m} \right) \quad (6)$$

where $\tilde{\sigma}$ is the surface tension of the liquid in the absence ($\Gamma = 0$) of any surfactant, Γ_m is the maximum packing concentration of surfactant, R_g is the universal gas constant, and T is the temperature.

We make our equations dimensionless using the transformations

$$\{\bar{u}, \bar{v}, \bar{w}\} = \frac{1}{U} \{u, v, w\}, \quad \{\bar{s}, \bar{X}, \bar{Z}, \bar{t}, \boldsymbol{\epsilon}\} = \frac{1}{s_0} \{s, X, Z, Ut, a\}$$

$$\bar{p} = \frac{p}{\rho U^2}, \quad \{\bar{n}, \bar{R}\} = \frac{1}{a} \{n, R\}, \quad \bar{\Gamma} = \frac{\Gamma}{\Gamma_m}, \quad \text{and} \quad \bar{\sigma} = \frac{\sigma}{\tilde{\sigma}}$$

where U is the exit speed of the jet in the rotating frame, $\boldsymbol{\epsilon}$ is the aspect ratio of the jet, and u , v , and w are the tangential, radial, and azimuthal velocity components relative to the centerline of the jet, respectively.

We exploit the fact that the radius of the orifice is small when compared to the radius of the cylinder by expanding u , v , w , and p in Taylor series in $\boldsymbol{\epsilon} n$ (see Refs. [26,27]), and R , X , and Z in asymptotic series in $\boldsymbol{\epsilon}$. We assume that the leading order axial component of the velocity is independent of ϕ and that the centerline of the jet is unaffected by small perturbations to leading order. Thus we have

$$u = u_0(s, t) + (\boldsymbol{\epsilon} n) u_1(s, \phi, t) + (\boldsymbol{\epsilon} n)^2 u_2(s, \phi, t) + \dots$$

$$v = (\boldsymbol{\epsilon} n) v_1(s, \phi, t) + (\boldsymbol{\epsilon} n)^2 v_2(s, \phi, t) + \dots$$

$$w = (\boldsymbol{\epsilon} n)^2 w_2(s, \phi, t) + \dots$$

$$p = p_0(s, \phi, t) + (\boldsymbol{\epsilon} n) p_1(s, \phi, t) + \dots$$

$$R = R_0(s, t) + \boldsymbol{\epsilon} R_1(s, \phi, t) + \dots$$

$$X = X_0(s) + \boldsymbol{\epsilon} X_1(s, t) + \dots \quad Z = Z_0(s) + \boldsymbol{\epsilon} Z_1(s, t) + \dots$$

In addition we have the following expansions for the surfactant concentration Γ and variable surface tension σ as

$$\Gamma = \Gamma_0(s, t) + \boldsymbol{\epsilon} \Gamma_1(s, t) + O(\boldsymbol{\epsilon}^2)$$

$$\sigma = \sigma_0(s, t) + \boldsymbol{\epsilon} \sigma_1(s, t) + O(\boldsymbol{\epsilon}^2) \quad (8)$$

where both these quantities are assumed to vary on the free surface of the jet and only along the jet.

The resulting equations contain a group of nondimensional parameters, which include the Reynolds number $\text{Re}_\alpha = (\rho/m) s_0^\alpha U^{2-\alpha}$, the Rossby number $\text{Rb} = U/(s_0 \Omega)$, and the Weber number $\text{We} = \rho U^2 a / \tilde{\sigma}$.

The continuity equation at leading order gives $v_1 = -u_{0s}/2$ and at order $\boldsymbol{\epsilon} n$ we obtain

$$u_{1s} + 3v_2 + w_{2\phi} + 3v_1 S \cos \phi = 0 \quad (9)$$

where $S = (X_{0s} Z_{0ss} - X_{0ss} Z_{0s})$. The second tangential stress condition is automatically satisfied at leading order and at order $\boldsymbol{\epsilon}^2$ we have

$$3R_0^2 R_1 v_{1\phi} + R_0^4 (w_2 + v_{2\phi}) = 0 \quad (10)$$

Since v_1 is a function of s only we therefore have

$$w_2 + v_{2\phi} = 0 \quad (11)$$

From the first tangential stress condition at leading order we have

$$u_1 = u_0 S \cos \phi \quad (12)$$

After differentiating Eq. (11) with respect to ϕ we obtain

$$w_{2\phi} = -v_{2\phi\phi} \quad (13)$$

Therefore,

$$v_{2\phi\phi} - 3v_2 = u_{1s} + 3v_1 S \cos \phi \quad (14)$$

and using the expressions for u_1 and v_1 we see that

$$v_{2\phi\phi} - 3v_2 = \left(u_0 S_s - \frac{u_{0s}}{2} S \right) \cos \phi \quad (15)$$

Periodic solutions for v_2 and w_2 are

$$v_2 = \frac{1}{4} \left(\frac{u_{0s}}{2} \mathcal{S} - u_{0s} \mathcal{S}_s \right) \cos \phi \quad (16)$$

$$w_2 = \frac{1}{4} \left(\frac{u_{0s}}{2} \mathcal{S} - u_{0s} \mathcal{S}_s \right) \sin \phi \quad (17)$$

The dimensionless apparent viscosity can be expressed as

$$\eta = \hat{\eta} + O(\epsilon n) \quad (18)$$

where the leading order apparent viscosity is given by $\hat{\eta} = |\sqrt{3}u_{0s}|^{\alpha-1}$. The first tangential stress condition at order ϵ^2 is given by

$$u_2 = \frac{3}{2} u_{0s} \frac{R_{0s}}{R_0} + \frac{u_{0ss}}{4} + \hat{\eta} \left(\frac{\text{Re}_\alpha}{\text{We}} \right) \frac{\sigma_{0s}}{2R_0} \quad (19)$$

From the second Navier–Stokes equation, we have at leading order $p_{0n}=0$, which is automatically satisfied. At order ϵ we get

$$p_1 = \left(u_0^2 \mathcal{S} - \frac{2}{\text{Rb}} u_0 + \frac{(X+1)Z_s - ZX_s}{\text{Rb}^2} \right) \cos \phi - \frac{\hat{\eta}}{\text{Re}_\alpha} \left(\frac{6-\alpha}{2} u_{0s} \mathcal{S} + \alpha u_{0s} \mathcal{S}_s \right) \cos \phi \quad (20)$$

For simplicity of notation we will relabel X_0 and Z_0 with X and Z , respectively.

The Navier–Stokes equation in the azimuthal direction gives at leading order $p_{0\phi}=0$, which is automatically satisfied. At order ϵ we get the above equation differentiated with respect to ϕ . From the normal stress condition we obtain at leading order and order ϵ

$$p_0 = -\frac{\hat{\eta}u_{0s}}{\text{Re}_\alpha} + \frac{\sigma_0}{R_0 \text{We}}, \quad p_1 = \frac{\sigma_0}{R_0 \text{We}} \left(-\frac{R_1 \phi_\phi + R_1}{R_0^2} + \mathcal{S} \cos \phi \right) + \frac{4\hat{\eta}}{\text{Re}_\alpha} v_2 + \frac{\sigma_1}{R_0 \text{We}} \quad (21)$$

By substituting the expression for $p_{1\phi}$ (using Eq. (21)) into the expression formed by differentiating Eq. (20) with respect to ϕ , and noting that R is periodic in ϕ , we get

$$(X_s Z_{ss} - X_{ss} Z_s) \left(\frac{(7-\alpha)\hat{\eta}u_{0s}}{2 \text{Re}_\alpha} + \frac{1}{R_0 \text{We}} - u_0^2 \right) + \frac{2}{\text{Rb}} u_0 = \frac{(X+1)Z_s - ZX_s}{\text{Rb}^2} + \frac{(\alpha-1)\hat{\eta}}{\text{Re}_\alpha} u_0 (X_s Z_{sss} - X_{sss} Z_s) \quad (22)$$

This equation is valid only if the leading order terms in the expansion of X and Z are independent of t . If we had retained leading order translational velocity terms v_0 and w_0 in our expansions for v and w , and had $X_{0t} \neq 0$ and $Z_{0t} \neq 0$, then the right hand side of Eq. (22) would contain some additional unsteady terms in $E = Z_s X_t - Z_t X_s$. However $E \approx 0$ has already been found in Ref. [6] to be a very accurate approximation between the orifice and the break up point of the jet. In particular Părău et al. [7] considered an expansion of the form $X(s,t) = X_0(s) + \hat{X}(s,t)$ and $Z(s,t) = Z_0(s) + \hat{Z}(s,t)$ and then solved the linearized version of the resulting equations. Perturbations of the steady centerline were found to be within a maximum deviation of order 10^{-2} and thus are relatively small when compared to $O(1)$ values of $X_0(s)$ and $Z_0(s)$ (effectively making the trajectory steady). This is backed up by the experimental observations of Wong et al. [8], which show that the centerline of the jet is steady (in the rotating frame), giving $X_t \approx 0$, $Z_t \approx 0$ and $E \approx 0$ for experimental observations.

The Navier–Stokes equation in the axial direction at order ϵ is

$$u_{0t} + u_0 u_{0s} = -p_{0s} + \frac{(X+1)X_s + ZZ_s}{\text{Rb}^2} + \frac{\hat{\eta}}{\text{Re}_\alpha} (u_{0ss} + 4u_2 + u_{2\phi\phi}) + \frac{2}{\text{Re}_\alpha} \hat{\eta}_s u_{0s} \quad (23)$$

which after using the expressions for u_2 and p_0 becomes

$$u_{0t} + uu_{0s} = -\frac{1}{\text{We}} \left(\frac{\sigma_0}{R_0} \right)_s + \frac{(X+1)X_{0s} + Z_0 Z_{0s}}{\text{Rb}^2} + \frac{3\hat{\eta}}{\text{Re}_\alpha} \left(\alpha u_{0ss} + 2u_{0s} \frac{R_{0s}}{R} \right) + \frac{2\sigma_{0s}}{\text{We}R_0} \quad (24)$$

From the kinematic condition, we obtain at order ϵ

$$R_{0t} + \frac{u_{0s}}{2} R_0 + u_0 R_{0s} = 0 \quad (25)$$

The arclength equation at leading order gives

$$X_s^2 + Z_s^2 = 1 \quad (26)$$

And finally the last equation to be found is the convection-diffusion equation, which at leading order is

$$\Gamma_{0t} + u_0 \Gamma_{0s} + \frac{u_{0s}}{2} \Gamma = 0 \quad (27)$$

We see that we have now five equations (22) and (24)–(27) for the five unknowns u_0 , R_0 , Γ_0 , X , and Z . The dimensionless equation of state relating the surfactant concentration Γ to the surface tension of the liquid-gas interface is given by the nonlinear Szyskowsky equation

$$\sigma = 1 + \beta \log(1 - \Gamma) \quad (28)$$

where the parameter $\beta = \Gamma_\infty R_g T / \bar{\sigma}$ determines how “effective” or important surfactants are.

3 Steady-State Solutions

We search for steady-state solutions by considering all the variables to be functions of s . In this case we have

$$uu_{0s} = -\frac{1}{\text{We}} \left(\frac{\sigma_0}{R_0} \right)_s + \frac{(X_0+1)X_{0s} + Z_0 Z_{0s}}{\text{Rb}^2} + \frac{3\hat{\eta}}{\text{Re}_\alpha} \left(\alpha u_{0ss} + 2u_{0s} \frac{R_{0s}}{R} \right) + \frac{2\sigma_{0s}}{\text{We}R_0} \quad (29)$$

$$(X_{0s} Z_{0ss} - X_{0ss} Z_{0s}) \left(\frac{(7-\alpha)\hat{\eta}u_{0s}}{2 \text{Re}_\alpha} + \frac{1}{R_0 \text{We}} - u_0^2 \right) + \frac{2}{\text{Rb}} u_0 = \frac{(X_0+1)Z_{0s} - Z_0 X_{0s}}{\text{Rb}^2} + \frac{(\alpha-1)\hat{\eta}}{\text{Re}_\alpha} u_0 (X_{0s} Z_{0sss} - X_{0sss} Z_{0s}) \quad (30)$$

$$\frac{u_{0s}}{2} R_0 + u_0 R_{0s} = 0 \quad (31)$$

and

$$u_0 \Gamma_{0s} + \frac{u_{0s}}{2} \Gamma = 0 \quad (32)$$

From Eqs. (31) and (32) we observe that $R_0^2 u_0$ and $\Gamma_0^2 u_0$ are constant and by using $R_0(0)=1$, $\Gamma_0(0)=\zeta$ (where ζ is the initial surfactant concentration at the nozzle) and $u_0(0)=1$, we have $R_0^2 u_0 = 1$ and $\Gamma_0^2 u_0 = \zeta^2$ so that we can substitute R_0 and u_0 in the previous equations, which now become

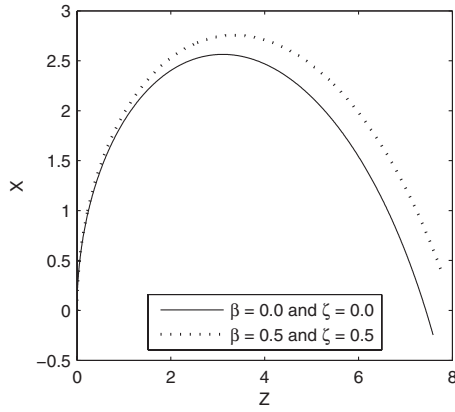


Fig. 1 The steady centerline of a rotating Newtonian ($\alpha=1.0$) liquid jet with and without surfactants. Here we have $Rb=5.0$, $We=6.0$, $\beta=0.5$, and $\zeta=0.5$. The presence of surfactants leads to the jet curving less.

$$u_0 u_{0s} = -\frac{(1 + \beta \log(1 - \zeta u_0^{-1/2}))}{We} \frac{u_{0s}}{2\sqrt{u_0}} + \frac{\beta \zeta}{2Weu_0(1 - \zeta u_0^{-1/2})} u_{0s} + \frac{(X+1)X_s + ZZ_s}{Rb^2} + \frac{3\hat{\eta}}{Re_\alpha} \left(\alpha u_{0ss} - \frac{u_{0s}^2}{u_0} \right) \quad (33)$$

$$(X_{0s}Z_{0ss} - X_{0ss}Z_{0s}) \left(u_0^2 - \frac{(7-\alpha)\hat{\eta}u_{0s}}{2Re_\alpha} - \frac{1}{We}(1 + \beta \log(1 - \zeta u_0^{-1/2}))\sqrt{u_0} \right) = \frac{2u_0}{Rb} - \frac{(X_0+1)Z_{0s} - Z_0X_{0s}}{Rb^2} + \frac{(\alpha-1)\hat{\eta}}{Re_\alpha} u_0(X_{0s}Z_{0sss} - X_{0sss}Z_{0s}) \quad (34)$$

and finally

$$X_{0s}^2 + Z_{0s}^2 = 1 \quad (35)$$

The unknowns in Eqs. (33)–(35) are X_0 , Z_0 , and u_0 . This nonlinear system of ordinary differential equations could be solved using a centered finite difference method (as in Ref. [7] for the case where $\hat{\eta}=1$), however, since it can be shown that viscosity has a negligible influence (see Refs. [7,9,28]) on the steady-state solutions for X , Z , and u_0 except in the case of highly viscous fluids (which we do not consider here), we will solve Eqs. (33)–(35) in the simpler inviscid limit (i.e., as $Re_\alpha \rightarrow \infty$). In this inviscid limit the resulting nonlinear equations are similar to those found in Ref. [9] except here there are some extra terms due to variable surface tension. We solve this system using a Runge–Kutta method with initial conditions $R_0=u_0=X_{0s}=1$ and $X_0=Z_0=Z_{0s}=0$ for $s=0$. The effect of changing the initial surfactant concentration ζ on the steady centerline of the jet is shown in Fig. 1. The trajectory is seen to curve less when surfactants are present.

4 Temporal Instability

In this section we consider the linear stability of disturbances about our leading order steady-state solution obtained in Sec. 3. In this linear analysis it is sufficient to consider a linearized version of the surface tension equation of state. By expanding Eq. (28) in a Taylor series about the initial surfactant concentration ζ we have

$$\sigma = (1 + \beta \log(1 - \zeta)) + \sigma'(\zeta)(\Gamma - \zeta) = (1 + \beta \log(1 - \zeta)) - \frac{\beta}{(1 - \zeta)}(\Gamma - \zeta) = \sigma_e - E\Gamma \quad (36)$$

where $\sigma_e = (1 + \beta \log(1 - \zeta)) + \beta \zeta / (1 - \zeta)$ is the surface tension of the undisturbed liquid jet corresponding to a uniform surfactant concentration ζ , and $E = \beta / (1 - \zeta)$ is the Gibbs elasticity.

If the centerline of the rotating jet is assumed to curve over a lengthscale of $s=O(1)$ and perturbations along the jet are of order a (which is comparable to ϵ when $s=O(1)$) then travelling wave modes of the form $\exp(ik\bar{s} + \lambda\bar{t})$ must be considered, where $\bar{s} = s/\epsilon$ and $\bar{t} = t/\epsilon$, in order to have $k=k(s)=O(1)$ and $\lambda=\lambda(s)=O(1)$. We begin by expressing our disturbances about our steady state (obtained from Sec. 3) as

$$\begin{bmatrix} u \\ R \\ \Gamma \end{bmatrix} = \begin{bmatrix} u_0 \\ R_0 \\ \Gamma_0 \end{bmatrix} + \delta \begin{bmatrix} \hat{u} \\ \hat{R} \\ \hat{\Gamma} \end{bmatrix} e^{ik\bar{s}} e^{\lambda\bar{t}} \quad (37)$$

where δ is some dimensionless small constant. In this case the symbols with subscripts denote steady state solutions, and k is a real wavenumber with λ being complex, so that $\lambda = \lambda_r + i\lambda_i$ where λ_r is the growth rate of disturbances and λ_i is the wavenumber of disturbances along the jet. In order to prevent instability to wave-modes with zero wavelength we replace the leading order pressure term in Eq. (24) with the full curvature expression (this ad-hoc approach is discussed in detail in the review on liquid jets by Eggers [26]). We thus have

$$u_{0t} + u_0 u_{0s} = -\frac{1}{We} \left[\sigma_0 \left[\frac{1}{R_0(1 + R_{0s}^2)^{1/2}} - \frac{\epsilon^2 R_{0ss}}{(1 + R_{0s}^2)^{3/2}} \right] \right]_s + \frac{(X_0+1)X_{0s} + Z_0Z_{0s}}{Rb^2} + \frac{3\hat{\eta}}{Re_\alpha} \left[\alpha u_{0ss} + 2u_{0s} \frac{R_{0s}}{R_0} \right] + \frac{2\sigma_{0s}}{WeR_0} \quad (38)$$

We substitute Eq. (37) into our governing equations (25), (27), and (38), and drop the subscript zero from our variables. We get at leading order the eigenvalue relation

$$\left[\frac{3\alpha\hat{\eta}}{Re_\alpha} k^2 + (\lambda + iku) \right] (\lambda + iku)^2 - \frac{k^2\sigma R}{2We} \left[\frac{1}{R^2} - k^2 \right] (\lambda + iku) + \frac{Ek^2\Gamma}{2RWe} (\lambda + iku) = 0 \quad (39)$$

where we have rescaled the Reynolds number (and based it on the orifice radius a) so that $\bar{Re}_\alpha = \epsilon Re_\alpha$ to bring in viscous terms and obtain a distinguished limit. By choosing $\lambda_r = -ku$ so that disturbances are convected along the jet we find that

$$\lambda_r^2 + \frac{3\alpha\hat{\eta}}{Re_\alpha} k^2 \lambda_r - \frac{k^2}{2We} \left[\sigma R \left(\frac{1}{R^2} - k^2 \right) - \frac{E\Gamma}{R} \right] = 0 \quad (40)$$

which has solution

$$\lambda_r = -\frac{3\alpha\hat{\eta}}{2Re_\alpha} k^2 + \frac{k}{2} \left[\left(\frac{3\alpha\hat{\eta}k}{Re_\alpha} \right)^2 + \frac{2}{We} \left(\frac{1}{R^2} - k^2 \right) \sigma R - \frac{2E\Gamma}{RWe} \right]^{1/2} \quad (41)$$

Differentiating the above equation to find the wavenumber for which λ_r is a maximum (which we shall henceforth refer to as k^*) we find

$$k^* = \frac{1}{(2R^3)^{1/4}} \left[\frac{(\sigma - E\Gamma)}{\sigma \sqrt{2R + 3\alpha Oh \hat{\eta} \sqrt{\sigma}}} \right]^{1/2} \quad (42)$$

where $Oh = \sqrt{We}/\bar{Re}_\alpha$ is the Ohnesorge number. In the limiting case of zero rotation $\Omega=0$, the steady-state solution for the radius of the jet R_0 is simply a constant so that $R_0=1$. With this value of the steady state for R_0 the eigenvalue relation (40) reduces to the long-wave limit eigenvalue relation obtained by Timmermans and Lister [15] for the case of a straight surfactant laden liquid thread.

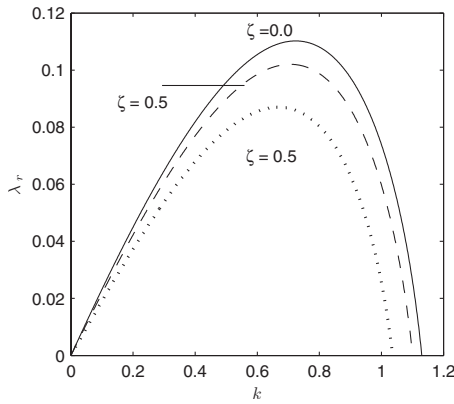


Fig. 2 The growth rate of disturbances of a rotating shear thinning liquid jet subject to arbitrary disturbance wavenumbers k at a short distance away from the orifice. The effect of increasing the initial surfactant concentration ζ is seen to lower growth rates and also to lower the most unstable wavenumber (where λ_r attains a minimum). Here the parameters are $We = 10$, $Rb = 1.0$, $Re = 24$, $\beta = 0.2$, and $\alpha = 0.8$.

When there is no surfactant present (i.e., $\Gamma_0 = 0$), we have $\sigma = 1$ and the above expression reduces to the most unstable wavenumber of a viscous power law liquid jet (see Ref. [9])

$$k^* = \frac{1}{(2R_0^3)^{1/4}} \frac{1}{\sqrt{3Oh\hat{\eta} + \sqrt{2R_0}}} \quad (43)$$

5 Results and Discussion

As with previous works (see Ref. [9]) we find that due to variations in the steady-state variables R and u , both the most unstable wavenumber and its associated growth rate vary along the jet. In Fig. 2 we plot the growth rate of disturbances λ_r (as given by Eq. (41)) at a distance $s = 0.3$ from the orifice for a shear thinning rotating liquid jet as the initial surfactant concentration ζ is altered. We find that the effect of adding surfactants is to reduce the growth rate of disturbances (to all unstable wavenumbers), as well as reducing the wavenumber k at which the growth rates attain a maximum. Furthermore, the effect of increasing the initial surfactant concentration is to reduce the range of instability. In Fig. 3 we plot the growth rate of disturbances to arbitrary k for a surfactant laden shear thickening and shear thinning rotating liquid jet. For these parameter values we find the shear thinning fluid to have

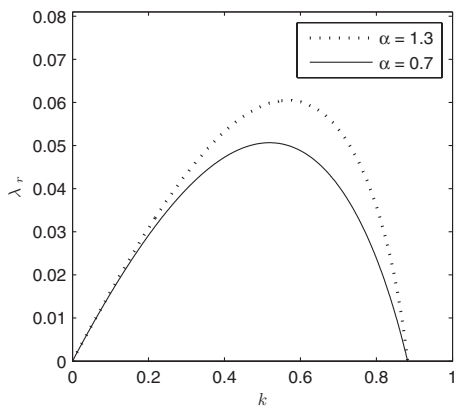


Fig. 3 The growth rate of disturbances of a rotating liquid jet subject to arbitrary disturbance wavenumbers k at the orifice at low rotation rates. Shear thinning jets are more stable and the most unstable wavenumber increases with the flow index number. $We = 12$, $Rb = 4.0$, $Re = 24$, $\beta = 0.2$, and $\zeta = 0.5$.

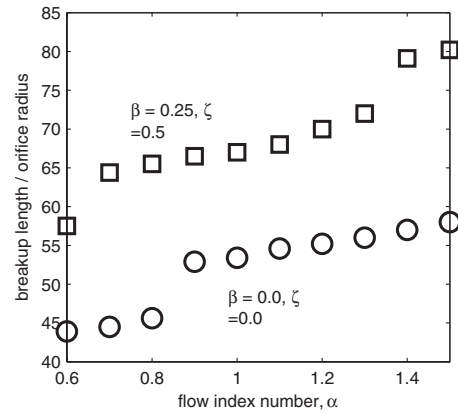


Fig. 4 The breakup length of a rotating liquid jet against the flow index number as calculated using the linear theory in Sec. 4. The case where surfactants are present along the interface and the case without is shown. Here the parameters are $We = 10$, $Rb = 1.0$, $Re = 24$, $\delta = 0.01$, $\epsilon = 0.01$, $\alpha = 1.5$, $\beta = 0.25$, and $\zeta = 0.5$.

larger growth rates at all wavenumbers and a relatively smaller value for the most unstable wavenumber. In the classical theory of Rayleigh [29] the resonant or “Rayleigh” wavenumber is the wavenumber $k = k^*$ at which perturbations grow most rapidly and lead to the shortest distance between the orifice and first droplet. Droplet sizes can be estimated by determining the wavelength associated with this wavenumber $\lambda^* = 2\pi/k^*$ and then equating the volume contained within this wavelength into a sphere. Since in the present case, both the most unstable wavenumber and its associated growth rate vary as we move along the jet, it is necessary to determine the location at which breakup occurs (and then calculate the value of the most unstable wavenumber there) in order to provide a good estimate of the size of droplets produced. In order to achieve this we substitute the expression for the most unstable wavenumber and its associated growth rate (see Eqs. (42) and (41)) into the equation that describes the evolution of small unsteady perturbations about the steady-state solution (see Eq. (37)). Although the variable \bar{t} does not appear explicitly in our steady-state analysis in Sec. 3, it does appear implicitly as a function of s and u (more specifically $\bar{t} = \int (1/u(s)) ds$). After choosing a suitable value of the dimensionless parameter δ we can then determine the location at which $R = R_0(s) + \delta e^{iks} e^{\lambda \bar{t}} = 0$. We take this value of s , at which $R = 0$, to be the “breakup point” of the jet. In Fig. 4 we plot the breakup lengths, as determined by the method outlined above for rotating liquid jets with different flow index numbers. It can be seen that surfactants impede the growth of disturbances (and thus produce longer jets). The solutions obtained can be put on the physical x - z plane by first determining the steady centerline solution; this allows us to calculate $X(s)$, $Z(s)$, $X'(s)$, and $Z'(s)$ for each $s \geq 0$. We then use Eqs. (41) and (42) in Eq. (37) to determine $R(s, t)$. Subsequently the equation of the free surface of the jet on the x - z plane is given by $(X'(s) \pm R(s, t)Z'(s), Z(s) \mp R(s, t)X'(s))$ for each s . Profiles of the jets are shown in Fig. 5 for different flow index numbers and in Fig. 6 for different Rossby numbers. The resonant wavenumber or most unstable wavenumber at the breakup point $k = k_{br}^*$ is shown in Fig. 7 for a rotating liquid jet at moderately high rotation rates when the initial surfactant concentration on the free surface is varied. While k_{br}^* is seen to decrease as ζ is increased for both shear thinning and shear thickening jets, we see that irrespective of the value of ζ shear thinning jets have larger values of k_{br}^* and that the difference between them decreases as the initial surfactant concentration is increased. When the jet eventually ruptures it is to be expected (in the context of linear theory) that the volume of

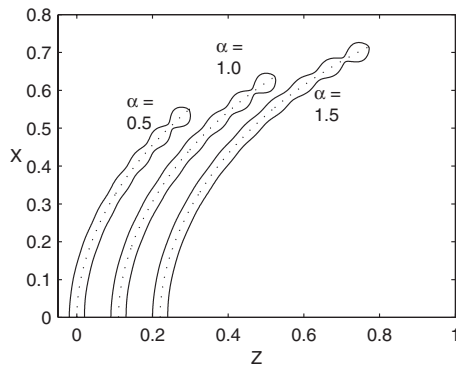


Fig. 5 The profile of a rotating liquid jet with surfactants for different flow index numbers as calculated using the linear theory. Here the parameters are $We=12$, $Rb=1.0$, $Re=15$, $\delta=0.01$, $\epsilon=0.01$, $\beta=0.2$, and $\zeta=0.5$. The dotted lines represent the steady centerline of the jet.

fluid containing one wavelength of the disturbance at breakup will separate and form a droplet (in reality the jet will breakup into main and satellite droplets). In Fig. 8 we estimate the size of droplets produced by a rotating shear thickening liquid jet with surfactants as the rotation rate is varied. Larger droplets are pro-

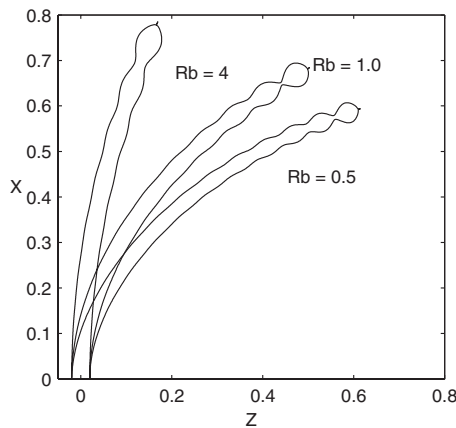


Fig. 6 The profile of a rotating shear thickening liquid jet on the x - z plane for different Rossby numbers. Here the parameters are $We=10$, $Re=20$, $\alpha=1.5$, $\delta=0.005$, $\epsilon=0.01$, $\beta=0.2$, and $\zeta=0.2$.

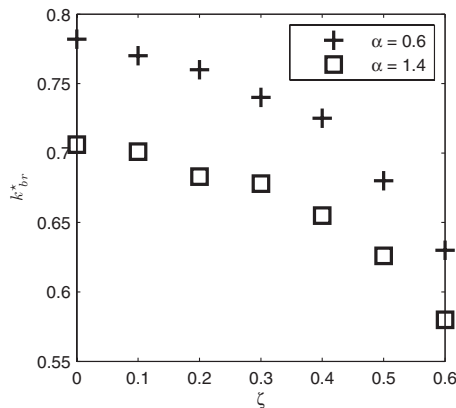


Fig. 7 The most unstable wavenumber at breakup for a shear thinning and shear thickening rotating liquid jet for different initial surfactant concentrations ζ . Here the parameters are $We=10$, $Re=20$, $Rb=1.0$, $\delta=0.0025$, $\epsilon=0.01$, and $\beta=0.4$.

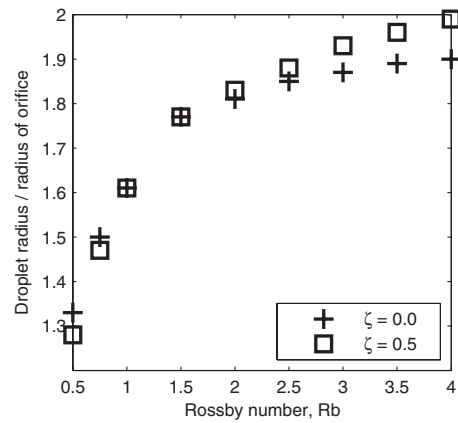


Fig. 8 Predicted droplet sizes for a rotating shear thickening ($\alpha=1.3$) liquid jet when the Rossby number is varied. Here the parameters are $We=10$, $Re=24$, $\delta=0.005$, $\epsilon=0.01$, and $\beta=0.25$.

duced as the rotation rate is decreased (in agreement with Newtonian results obtained by Părău et al. [7]). Moreover, it can be seen that there exists a nonmonotonic behavior with regard to the size of droplets as Rb is changed; in particular, we have that surfactant free jets produce larger droplets for large rotation rates as compared with jets with surfactants, however, for smaller rotation rates (i.e., larger values of Rb) this result is vice versa. A similar qualitative picture is obtained in Fig. 9 for a shear thinning liquid jet. Finally, in Fig. 10 we show the effect of changing the Weber number on droplet sizes. Droplets become smaller as the Weber number is increased (i.e., the effects of surface tension are reduced).

6 Conclusions

The linear stability of a slender rotating liquid jet having a layer of surfactants along its free surface has been investigated. The most unstable wavenumber along with the corresponding growth rate has been examined for different flow index numbers and different initial surfactant concentrations.

Liquid jet rupture commonly leads to the production of parasitic satellite droplets. The use of linear theory cannot predict the occurrence of such droplets and a nonlinear analysis is needed to examine this phenomenon in greater detail. The results within this work can be used to aid in optimizing the parameter space when using a fully nonlinear method to determine breakup lengths and droplet sizes (in particular, the disturbance wavenumber k at the

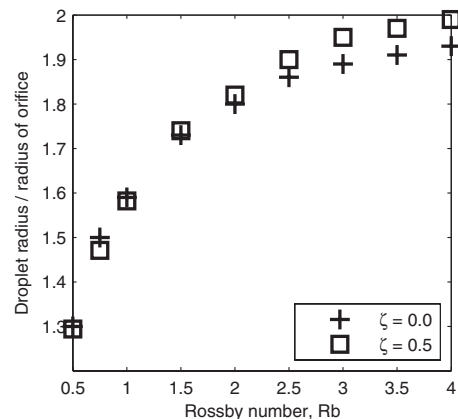


Fig. 9 Predicted droplet sizes for a rotating shear thinning ($\alpha=0.7$) liquid jet when the Rossby number is varied. Here the parameters are $We=10$, $Re=24$, $\delta=0.005$, $\epsilon=0.01$, and $\beta=0.25$.

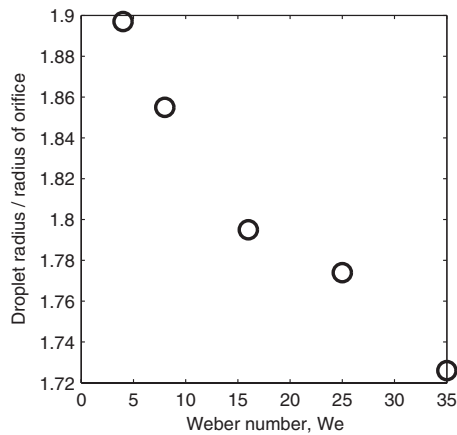


Fig. 10 Predicted droplet sizes for a rotating shear thinning ($\alpha=0.5$) liquid jet when the Weber number is varied. Here the parameters are $Rb=2.0$, $Re=24$, $\delta=0.005$, $\epsilon=0.01$, $\beta=0.25$, and $\zeta=0.5$.

orifice which results in the shortest jet is of practical importance and is usually determined by examining jets subject to a range of k (as in Refs. [7,12]). Investigating the nonlinear effects of surfactant transport and diffusion along shear thinning rotating liquid jets is the focus of current work.

Acknowledgment

J.U. would like to thank EPSRC-GB for their financial support.

References

[1] Andersen, K. G. and Yttri, G., 1997, Porso vert, Universitets for laget Oslo.
 [2] Ornek, D., Gurkan, T., and Oztin, C., 2000, "Prilling of Aluminium Sulphate," *J. Chem. Technol. Biotechnol.*, **75**(8), pp. 689–694.
 [3] Wallwork, I. M., Decent, S. P., King, A. C., and Schulkes, R. M. S., 2002, "The Trajectory and Stability of a Spiralling Liquid Jet. Part 1, Inviscid Theory," *J. Fluid Mech.*, **459**, pp. 43–65.
 [4] Wallwork, I. M., 2002, "The Trajectory and Stability of a Spiralling Liquid Jet," Ph.D. thesis, University of Birmingham, Birmingham.
 [5] Decent, S. P., King, A. C., and Walwork, I. M., 2002, "Free Jets Spun From a Prilling Tower," *J. Eng. Math.*, **42**, pp. 265–282.
 [6] Päräü, E. I., Decent, S. P., King, A. C., Simmons, M. J. H., and Wong, D. C. Y., 2006, "Nonlinear Travelling Waves on a Spiralling Liquid Jet," *Wave Motion*, **43**, pp. 599–618.
 [7] Päräü, E. I., Decent, S. P., Simmons, M. J. H., Wong, D. C. Y., and King, A. C., 2007, "Nonlinear Viscous Liquid Jets From a Rotating Orifice," *J. Eng. Math.*, **57**, pp. 159–179.

[8] Wong, D. C. Y., Simmons, M. J. H., Decent, S. P., Päräü, E. I., and King, A. C., 2004, "Break-Up Dynamics and Drop Sizes Distributions Created From Spiralling Liquid Jets," *Int. J. Multiphase Flow*, **30**(5), pp. 499–520.
 [9] Uddin, J., Decent, S. P., and Simmons, M. H., 2006, "The Instability of Shear Thinning and Shear Thickening Liquid Jets: Linear Theory," *ASME J. Fluids Eng.*, **128**, pp. 968–975.
 [10] Uddin, J., Decent, S. P., and Simmons, M. H., 2008, "Nonlinear Waves Along Rotating Non-Newtonian Liquid Jets," *Int. J. Eng. Sci.*, **46**, pp. 1253–1265.
 [11] Uddin, J., Decent, S. P., and Simmons, M. H., 2008, "The Effect of Surfactants on the Instability of a Rotating Liquid Jet," *Fluid Dyn. Res.*, **40**, pp. 827–851.
 [12] Hawkins, V. L., Simmons, M. J. H., Brisbane, C. J., Uddin, J., and Decent, S. P., 2007, "Break-Up of Spiralling Non-Newtonian Liquid Jets," Sixth International Conference on Multiphase Flow, Leipzig, Germany.
 [13] Whitaker, S., 1976, "Studies of Drop-Weight Method for Surfactant Solutions III," *J. Colloid Interface Sci.*, **54**, pp. 231–248.
 [14] Hansen, S., Peters, G. W. M., and Meijer, H. E. H., 1999, "The Effect of Surfactant on the Stability of a Fluid Filament Embedded in a Viscous Fluid," *J. Fluid Mech.*, **382**, pp. 331–349.
 [15] Timmermans, M.-L. E., and Lister, J. R., 2002, "The Effect of Surfactant on the Stability of a Liquid Thread," *J. Fluid Mech.*, **459**, pp. 289–306.
 [16] Kwak, S., and Pozrikidis, C., 2001, "Effect of Surfactants on the Instability of a Liquid Thread or Annular Layer. Part I: Quiescent Fluids," *Int. J. Multiphase Flow*, **17**, pp. 1–37.
 [17] Blyth, M. G., Luo, H., and Pozrikidis, C., 2006, "Stability of Axisymmetric Core-Annular Flow in the Presence of an Insoluble Surfactant," *J. Fluid Mech.*, **548**, pp. 207–235.
 [18] Ambraveswaran, B., and Basaran, O. A., 1999, "Effects of Insoluble Surfactants on the Nonlinear Deformation and Breakup of Stretching Liquid Bridges," *Phys. Fluids*, **11**(5), pp. 997–1015.
 [19] Stone, H. A., and Leal, L. G., 1990, "The Effect of Surfactant on Drop Formation and Breakup," *J. Fluid Mech.*, **220**, pp. 161–186.
 [20] Blyth, M. G., and Pozrikidis, C., 2004b, "The Stability of Two-Layer Channel Flow With Surfactants," *J. Fluid Mech.*, **505**, pp. 59–86.
 [21] Blyth, M. G., and Pozrikidis, C., 2004c, "The Effect of Surfactant on the Stability of Film Flow Down an Inclined Plane," *J. Fluid Mech.*, **521**, pp. 241–250.
 [22] Blyth, M. G., and Pozrikidis, C., 2004a, "Evolution Equations for the Surface Concentration of an Insoluble Surfactant; Applications to the Stability of an Elongating Thread and a Stretched Interface," *Theor. Comput. Fluid Dyn.*, **17**, pp. 147–164.
 [23] Xue, Z., Corvalan, C. M., Draavid, V., and Sojka, P. E., 2008, "Breakup of Shear Thinning Liquid Jets With Surfactants," *Chem. Eng. Sci.*, **63**, pp. 1842–1849.
 [24] Ribe, N. M., 2004, "Coiling of Viscous Jets," *Proc. R. Soc. London, Ser. A*, **460**, pp. 3223–3239.
 [25] Entov, V. M., and Yarin, A. L., 1984, "The Dynamics of Thin Liquid Jets in Air," *J. Fluid Mech.*, **140**, pp. 91–113.
 [26] Eggers, J., 1997, "Nonlinear Dynamics and Breakup of Free Surface Flows," *Rev. Mod. Phys.*, **69**(3), pp. 865–929.
 [27] Hohman, M. M., Shin, M., Rutledge, G., and Brenner, M. P., 2001, "Electrospinning and Electrically Forced Jets. II. Applications," *Phys. Fluids*, **13**(8), pp. 2221–2236.
 [28] Uddin, J., 2007, "An Investigation Into Methods to Control Breakup and Droplet Formation in Single and Compound Liquid Jets," Ph.D. thesis, University of Birmingham, Birmingham, UK.
 [29] Rayleigh, L., 1878, "On the Instability of Jets," *Proc. London Math. Soc.*, **s1-10**, pp. 4–13.

Circulation Generation and Vortex Ring Formation by Conic Nozzles

Moshe Rosenfeld

School of Mechanical Engineering,
Tel Aviv University,
Tel Aviv 69978, Israel

Kakani Katija

John O. Dabiri

Graduate Aeronautical Laboratories and
Bioengineering,
California Institute of Technology,
Pasadena, CA 91125

Vortex rings are one of the fundamental flow structures in nature. In this paper, the generation of circulation and vortex rings by a vortex generator with a static converging conic nozzle exit is studied numerically. Conic nozzles can manipulate circulation and other flow invariants by accelerating the flow, increasing the Reynolds number, and by establishing a two-dimensional flow at the exit. The increase in the circulation efflux is accompanied by an increase in the vortex circulation. A novel normalization method is suggested to differentiate between two contributions to the circulation generation: a one-dimensional slug-type flow contribution and an inherently two-dimensional flow contribution. The one-dimensional contribution to the circulation increases with the square of the centerline exit velocity, while the two-dimensional contribution increases linearly with the decrease in the exit diameter. The two-dimensional flow contribution to the circulation production is not limited to the impulsive initiation of the flow only (as in straight tube vortex generators), but it persists during the entire ejection. The two-dimensional contribution can reach as much as 44% of the total circulation (in the case of an orifice). The present study offers evidences on the importance of the vortex generator geometry, and in particular, the exit configuration on the emerging flow, circulation generation, and vortex ring formation. It is shown that both total and vortex ring circulations can be controlled to some extent by the shape of the exit nozzle.

[DOI: 10.1115/1.3203207]

Keywords: vortex ring, circulation, nozzle, laminar flow, CFD

1 Introduction

The present paper studies the generation of circulation and vortex rings using conic converging static nozzles in an attempt to control or manipulate the emerging flow field. The kinematics and dynamics of vortices formed by starting the flow through parallel-walled tubes were studied extensively in experiments over the past 70 years [1–8]. Theories and numerical simulations were implemented to reproduce many of the salient features of the vortex formation process, such as initial vortex sheet rollup [9] and vortex pinch-off [10–14].

A common way of generating vortex rings is by pushing a piston in a tube [1,3–5]. Two main vortex generator configurations have been considered: either a tube with an exit protruding into the flow field, referred to as a *nozzle*, or a tube with an exit flushed with a vertical plate, referred to as an *orifice*. Rosenfeld et al. [10] did not observe significant differences in the maximal total circulation between the two configurations (<2%), but the formation number (see definition in Gharib et al. [5]) was slightly lower for the orifice (3.83 versus 3.97) due to vorticity cancellation of the forming vortex with the side walls. Gharib et al. [5] found experimentally larger differences in the formation number (3.6 and 4.2 for the orifice and nozzle cases, respectively). Mohseni et al. [13] generated numerically vortex rings by applying a nonconservative force rather than conventional piston/tube arrangements. Nevertheless, the properties of the formed vortex rings were similar to those generated by a piston in a tube, and they were also affected by the generation characteristics, such as the amplitude and duration of the forcing.

In addition to these vortex generator types, one can envision employing nozzles with an axially varying cross section to decrease the exit area, and thus, to control the exit flow conditions, such as the mean velocity and the velocity profile. Such exit con-

figurations can be found in numerous biological systems. Intracardiac blood flow and aquatic propulsion are two areas of active research in which the dynamics of the starting flow through conic-like nozzle geometries is known to govern the overall system performance [15,16]. The shape of the vortex generator, and in particular, the exit geometry, may have a significant influence on the vortex ring formation and pinch-off since the rate of generation of the motion invariants (circulation, impulse, and kinetic energy) depend on the details of the flow in the vortex generator. Indeed, Allen and Naitoh [17] and Dabiri and Gharib [18] manipulated the circulation production rate, vortex circulation, and energy by dynamically closing an orifice or opening/closing a nozzle, respectively.

The most widely used analytical tool for predicting the formation kinematics of vortex rings employing parallel wall vortex generators is the slug model approximation for the vorticity flux generated by the starting flow [1,4]. By assuming the vorticity in the flow to be confined into a very thin layer near the wall, one can derive a simple expression relating the circulation flux to the spatially averaged axial velocity U_e of the jet efflux $d\Gamma/dt = (1/2)U_e^2(t)$, where t is the time, and Γ is the accumulated circulation. The slug model has had reasonable success in matching theoretical predictions with empirical measurements of vortex formation from parallel-walled tubes, as long as the discharge duration is short, and the Reynolds number is large [4]. However, its prominent role in current modeling efforts is more closely related to its ease of use rather than accuracy.

The case of the starting flow through conic nozzle geometries is inherently beyond the purview of the slug model, due to the existence of nonzero transverse velocity components in the ejected jet, resulting from the two-dimensional nature of the flow at the exit. These components are also present during the early stages of vortex formation from parallel-walled tubes [1,19]. However, in the latter case, their contribution represents a nearly constant shift in the circulation production, and thus, can be resolved by the addition of an empirical constant. By contrast, in conic nozzle

Contributed by the Fluids Engineering Division of ASME for publication in the JOURNAL OF FLUIDS ENGINEERING. Manuscript received April 14, 2009; final manuscript received July 8, 2009; published online August 18, 2009. Assoc. Editor: Mark Stremmer.

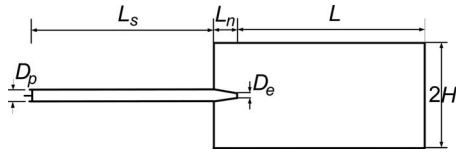


Fig. 1 Sketch of the domain of computation

geometries, the relationship between the vorticity flux and the transverse velocity component is nonlinear and time dependent.

The present study is limited to vortex generators employing static rigid and conic nozzles. The goal is to study circulation generation and vortex ring formation for this simple, yet unexplored geometry, as a starting point for the full comprehension of the dynamically varying nozzles. The present Navier–Stokes numerical simulations demonstrate the ability to control and manipulate the emerging flow.

2 Methods

2.1 Numerical Model. A sketch of the axisymmetric computational domain is given in Fig. 1. The vortex generator has two sections: a straight tube of length $L_s=40$ cm and a constant diameter of $D_p=2.5$ cm, and a conic nozzle of length $L_n=5.1$ cm (the dimensions are chosen to match the experimental setup) and exit diameter D_e of $D_e/D_p=0.2, 0.4, 0.6, 0.8,$ or 1 . The computational domain downstream of the nozzle exit has a length of $L/D_p=32$, and the outer boundary is at a radial distance of $H/D_p=4$. Numerical experiments have verified that the downstream and outer boundaries are placed far enough from the region of interest.

The moving piston is modeled as a uniform velocity inlet. Undocumented simulations performed in the course of the present study proved that this model produces results that are very similar to a moving piston, as long as the maximal stroke length is smaller than the length of the vortex generator. An impulsive velocity program of the piston is used with a constant piston velocity of $U_p=2$ cm/s in all the cases of the present study. Two velocity programs are used: (i) a continuous inflow velocity (velocity program no. 1) and (ii) the constant inflow is stopped at a given dimensionless time (velocity program no. 2). On the outer and downstream boundaries, zero gauge pressure is specified. On all the other boundaries, wall conditions are given, except on the axis of symmetry.

The axisymmetric, incompressible, time dependent, and laminar Navier–Stokes equations have been solved using the finite-volume package of FLUENT 6.23, ANSYS, Inc. Second-order accurate temporal and spatial schemes have been used with pressure-implicit with splitting of operators (PISO) pressure-velocity coupling. Mesh-size and time-step independence tests have been performed, resulting in a mesh of 180,000 nodes with clustering in the shear layer and near the walls, and a maximal dimensionless time step of $\Delta t_e^*=(U_e \Delta t/D_e)0.02$, where Δt is the uniform time step. The difference in the circulation of the selected mesh relative to a finer mesh with 685,000 nodes is less than 1%, and relative to a time step, twice as fine, is less than 0.1%.

2.2 Dimensionless Parameters. The choice of nondimensional parameters is not obvious in the present case since two velocity scales exist—one is the piston velocity (that remains constant in all the cases) and the other is the spatial average exit velocity U_e (that depends on the diameter of the nozzle exit). The corresponding length scales are the piston diameter and the nozzle-exit diameter, respectively. Gharib et al. [5] suggested for a straight tube vortex generator a dimensionless formation time defined by

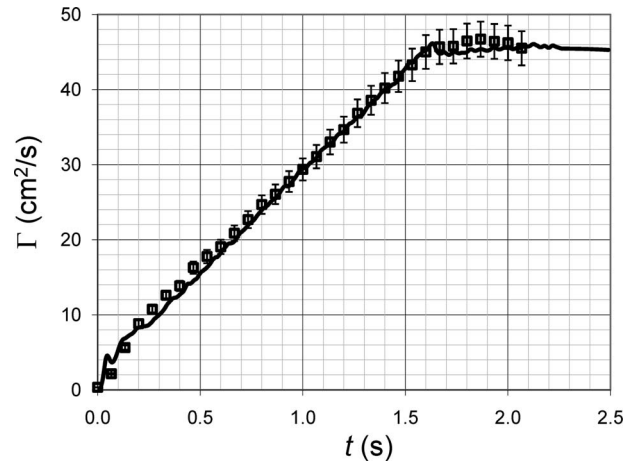


Fig. 2 Comparison of the circulation evolution of the numerical (solid line) and experimental (symbols) results ($D_e/D_p=0.6$)

$$t^* = \frac{U_p t}{D_p} \quad (1a)$$

This formation time is equivalent to the dimensionless piston stroke divided by the piston diameter $t^*=L_p/D_p$. A nondimensional circulation can be defined by

$$\Gamma^* = \frac{\Gamma}{U_p D_p} \quad (1b)$$

although other alternatives were suggested [3,13], while Gharib et al. [5] preferred using the dimensional form of the circulation. In a similar way, a nondimensional formation time and circulation, based on the nozzle-exit parameters, can be defined as

$$t_e^* = \frac{U_e t}{D_e} \quad \text{and} \quad \Gamma_e^* = \frac{\Gamma}{U_e D_e} \quad (2)$$

where the spatial average velocity is $U_e=U_p(D_p/D_e)^2$. The relationship between the two formation time definitions is $t_e^*=t^*/(D_e/D_p)^3$. As D_e/D_p decreases, the inflow duration to reach a given t_e^* is shorter. For example, to reach a formation time of $t_e^*=4$ requires a piston stroke of $t^*=L_p/D_p=4, 2.1, 0.85, 0.25,$ and 0.03 for a nozzle with $D_e/D_p=1, 0.8, 0.6, 0.4,$ and 0.2 , respectively.

The Reynolds number, based on nozzle-exit parameters, is $Re=2500, 1250, 830, 625,$ and 500 for the nozzles with $D_e/D_p=0.2, 0.4, 0.6, 0.8,$ and 1.0 , respectively. Consequently, in all the simulations, a laminar flow is assumed, although the case with $Re=2500$ might be transitional [2,20].

2.3 Validation With Experiments. A set of digital particle image velocimetry (DPIV) experiments with a nozzle of $D_e/D_p=0.6$ have been performed for validating the numerical simulations. The experimental setup is described in Ref. [7]. A nearly impulsive velocity program, as recorded in the experiments (with a mean velocity of $U_p \cong 5.7$ cm/s), was imposed in the simulations. The circulation is a major quantity of interest in the present study, and therefore, the measured and calculated evolution of the circulation are compared in Fig. 2. Excellent agreement is obtained.

3 The Flow Inside the Vortex Generator

The efflux of circulation and other motion invariants, and the vortex ring formation are determined by the velocity profile at the exit of the vortex generator, e.g., Refs. [10,12,21]. This emerging

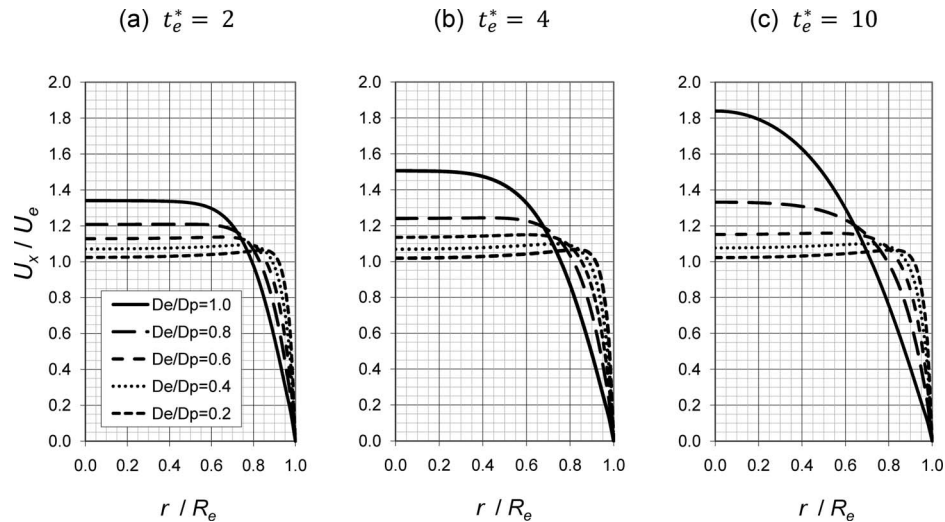


Fig. 3 The evolution of the axial velocity profile at the nozzle exit (velocity program no. 1)

flow is affected by the dynamics of the flow inside the vortex generator. In this section, the characteristics of the nozzle-exit flow are investigated.

In the straight segment of the flow are similar to that described in Refs. [21,22]. A Stokes layer is created along the straight tube wall with the instantaneous start of the inflow. As the inflow continues, a developing flow in the upstream part is established, and it advances downstream with time. By $t^*=12$, a stationary flow is obtained along the entire straight segment of the tube with an almost parabolic velocity profile at the downstream end. Another observation is that the flow entering the conic cross section is found to be independent of the nozzle geometry.

The converging shape of the nozzle accelerates the mean flow, influencing the boundary layer thickness, and consequently, the efflux of circulation, impulse, and kinetic energy. It also changes the Reynolds number of the emerging flow. The favorable pressure gradient decreases the thickness of the boundary layer. As the exit diameter decreases, the boundary layer thinning is more pronounced, resulting in a more uniform exit velocity profile and a thinner shear layer.

To examine more closely the nozzle-exit flow, Fig. 3 plots the axial velocity profile for formation times of $t_e^*=2, 4$, and 10, and for the different exit diameter nozzles in the case of velocity program no. 1. The first formation time ($t_e^*=2$) is in the roll up phase of the vortex ring, the second ($t_e^*=4$) is approximately equal to the formation number of a straight tube, and in the latter instant ($t_e^*=10$), the leading vortex ring has propagated downstream, far enough to not affect the flow at the nozzle exit (see Fig. 4). The theory of Gharib et al. [5] predicts that the vortex ring properties are determined by the ejection characteristics up to a formation time of $F^*=t_e^*\approx 4$ (for the case of a straight tube vortex generator); this value is also referred to as the formation number [5]. Looking at the nozzle-exit profile reveals that for $D_e/D_p < 0.8$, the flow is (i) quasisteady in the core and (ii) a thin Stokes layer exists in an otherwise uniform velocity profile. For $D_e/D_p < 0.8$, the axial velocity profile has enough dimensional time to develop into a nearly parabolic profile for $D_e/D_p=1$.

4 Vortex Dynamics and Circulation Evolution

4.1 Vorticity Evolution. The vorticity field for $t_e^*=2, 4$, and 10 is shown in Fig. 4 for all the nozzle cases and for velocity program no. 2, with the inflow stopping at $t_e^*=8$. The vorticity is normalized by U_e/D_e , and the axial and radial coordinates by D_e . This straightforward normalization reveals the similarity in the

vorticity distribution for all the nozzle cases. In the formation phase, the more constricted nozzles exhibit a smaller and more concentrated vortex core, originating from the thinner vortex sheet. Significant differences in the vorticity distribution are noticeable only after the formation phase ($t_e^*>4$). The thicker shear layers generated at the lower Reynolds number cases (i.e., larger D_e/D_p) create a thicker core vortex ring, as was also observed by Mohseni et al. [13] for a straight tube vortex generator. The decrease in D_e/D_p has a dual effect regarding viscosity. First, the Reynolds number (based on the exit parameters) increases linearly; for $D_e/D_p=1$, it increases to $Re=500$, while for $D_e/D_p=0.2$, it increases to $Re=2500$. Second, as D_e/D_p decreases, the physical time decreases as well for a given t_e^* , and consequently, viscosity has less time to act through vorticity decay and vorticity cancellation. The combined effect of these two factors is a larger vorticity magnitude and thinner core vortex ring as D_e/D_p decreases. At the latest formation time shown ($t_e^*=10$), the vorticity decay and vorticity cancellation have a prominent effect on the vorticity distribution for $D_e/D_p \geq 0.8$. In the case of $D_e/D_p=0.2$, the vorticity accumulated in the tail is susceptible to the Kelvin-Helmholtz instability due to the large Reynolds number of the emerging flow.

4.2 Total Circulation Evolution. Normalization of the total circulation by piston parameters might be appealing since it is common to all the cases considered in the present study. However, the similarity found in the normalized vorticity field, Fig. 4, supports the normalization of the circulation with the nozzle-exit pa-

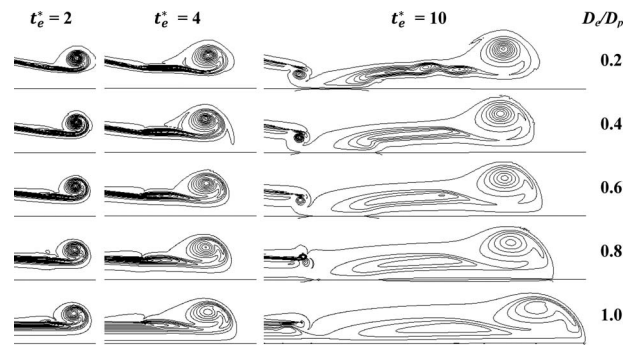


Fig. 4 The scaled vorticity (contour lines between 0 to 20 with an increment of 1) for velocity program no. 2. The spatial coordinates are scaled by D_e .

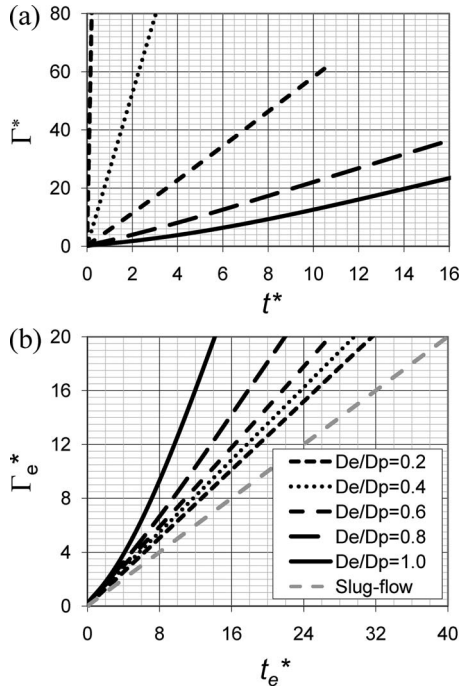


Fig. 5 The evolution of the total circulation, (a) normalization by piston parameters, and (b) normalization by exit parameters

rameters. To test these normalizations of the circulation, the evolution of the total circulation is depicted in Fig. 5 for the continuous velocity program no. 1. Normalization by the piston or the exit parameters are plotted in Figs. 5(a) and 5(b), respectively. The total circulation is calculated by integrating the vorticity field in the region outside of the straight tube vortex generator.

The circulation Γ^* (that is also proportional to the dimensional circulation) can be significantly increased by decreasing the exit diameter of the nozzle, Fig. 5(a). The dependence of Γ_e^* on D_e/D_p is smaller. In the latter normalization, the smallest D_e/D_p exhibits the lowest normalized circulation for a given t_e^* . The circulation, as predicted by the slug model, is also plotted in Fig. 5(b). In all the nozzle cases, the circulation is larger than the slug model prediction. The deviation decreases as D_e decreases due to the more uniform exit velocity profile (Fig. 3) that conforms with the slug model approximation.

None of these normalizations could collapse the evolution of the total circulation of all the nozzle cases into a single line, although the same velocity program of the piston is employed. In an attempt to alleviate this, an alternative normalization of the circulation and formation time is suggested hereof. It will also allow separating between two contributions to the ejected circulation, a slug-type one-dimensional flow contribution, and an inherently two-dimensional flow contribution.

4.3 The Two-Dimensional Contribution to Circulation.

The circulation flux ejected out of the nozzle (neglecting diffusive fluxes) can be decomposed [1,19] into

$$\frac{d\Gamma}{dt} = \int_0^{D_e/2} u\omega dr = \frac{1}{2}U_{cl}^2 + \int_0^{D_e/2} u \frac{\partial v}{\partial x} dr \quad (3)$$

where u and v are the axial (x) and radial (r) velocity components, respectively, w is the azimuthal vorticity, and U_{cl} is the exit centerline velocity. The time integration of this circulation is identical to the total circulation (except a small deviation during the early formation of the vortex due to the generation of vorticity at the outer lip of the nozzle). This form suggests the following normalization:

$$t^{**} = \frac{\tilde{U}t}{D_e} \quad (4)$$

$$\Gamma^{**} = \frac{\Gamma}{\tilde{U}D_e}$$

where the velocity scale $\tilde{U} = \sqrt{\bar{U}_{cl}^2}$ is the running mean velocity $\bar{U}_{cl}^2 = \frac{1}{t} \int_0^t U_{cl}^2 d\tau$. The integration of Eq. (3) using the normalization of Eq. (4) leads to

$$\Gamma^{**} = \frac{t^{**}}{2} + \frac{1}{\tilde{U}D_e} \int_0^t \int_0^{D_e/2} u \frac{\partial v}{\partial x} dr d\tau \quad (5)$$

The first term is the contribution related to the one-dimensional flow, while the second term originates from the inherently two-dimensional flow at the exit.

In the generalized slug model, the two-dimensional contribution is neglected, resulting in $\Gamma^{**} = t^{**}/2$, or in dimensional form $\Gamma = (1/2)\bar{U}_{cl}^2 t$, i.e., the circulation ejected out of the vortex generator depends on the centerline exit velocity rather than the mean velocity that is used in the original slug model. The generalized slug model extends the original slug model into cases with a nonuniform axial velocity profile, while keeping the assumption of a one-dimensional flow at the exit, see for example Ref. [19]. In many previous studies, short ejection time and high Reynolds number cases have been considered, leading to flows with thin boundary layers with the mean velocity almost identical to the centerline velocity. Shusser et al. [21] introduced a first-order approximation that corrected the centerline velocity as a result of the evolution of a thin Stokes layer, leading to an improved estimation of the circulation generation for intermediate ejection times. In the cases of long ejection times and/or low Reynolds number flows, as in the present study, it is necessary to employ the generalized slug model to account for the enhanced circulation generation, due to the exit parabolic-like velocity profile.

The second contribution to the circulation (Eq. (5)) is significant only when the exit flow is two-dimensional, i.e., when the integral of $u(\partial v/\partial x)$ is significant. Most existing studies ignore this inherently two-dimensional contribution. Didden [1] and Krueger [19] realized the importance of the two-dimensional contribution to circulation generation in the case of straight tube vortex generators. Krueger [19] showed that for nearly impulsive velocity programs, a noticeable two-dimensional flow is formed at a very short time during the initiation of the flow. This results in a small constant circulation offset ($\Gamma^* \approx 1/\pi$) to the (classical) slug model. Krueger [19] related this offset to the overpressure that develops during the initial phases of the flow.

In the present case of conic nozzles, a significant two-dimensional contribution is expected throughout the ejection phase due to the shape of the exit nozzle that enforces a two-dimensional flow. Figure 6 plots Γ^{**} versus t^{**} for the (continuous) velocity program no. 1. Less dependence of Γ^{**} on D_e/D_p is obtained than in the previous normalizations (Fig. 5), indicating the relatively large one-dimensional contribution. The slope, however, does depend on D_e/D_p . The smaller D_e/D_p is, the larger the slope is and the larger is the deviation of Γ^{**} from the generalized slug model, i.e., the two-dimensional contribution is more significant. To assess the relative two-dimensional contribution to the circulation flux throughout the continuous ejection, $d\Gamma^{**}/dt^{**}$ versus t^{**} is plotted in Fig. 7(a). Any deviation of $d\Gamma^{**}/dt^{**}$ from 1/2 originates from two-dimensional effects at the exit. Moreover, the magnitude of the difference is proportional to the relative two-dimensional contribution to the total circulation generation. It should be noted, however, that the *magnitude* itself of the one-dimensional contribution cannot be evaluated from the normalized Γ^{**} (since $\Gamma^{**} = 1/2$ by definition).

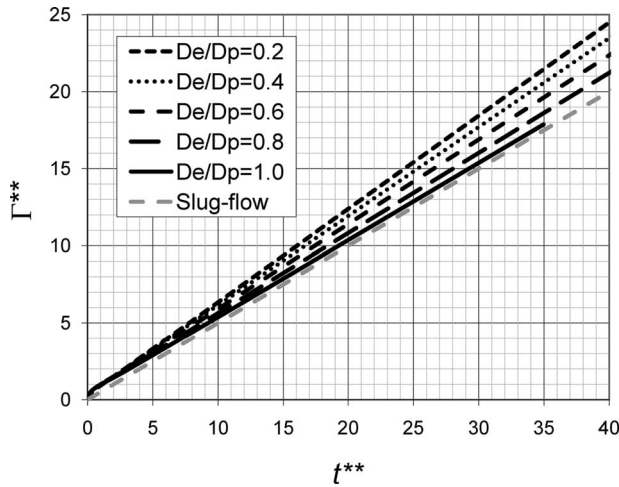


Fig. 6 The evolution of the double-star normalized circulation

With the impulsive initiation of the flow, a very large $d\Gamma^{**}/dt^{**}$ is obtained, in agreement with the analysis of Krueger [19]. These effects are significant up to $t^{**} \approx 1/2$, i.e., in the initial forming phase of the vortex ring. In contrast to the findings of Krueger [19] for a straight tube, the two-dimensional effects do not vanish after the initiation of the flow. Rather, $d\Gamma^{**}/dt^{**}$ approaches a constant asymptotic value greater than 1/2 in the converging nozzle cases. Figure 8 plots the asymptotic ratio of the two-dimensional contribution to the total circulation. It increases linearly with the decrease in D_e/D_p up to a value of 17%.

Krueger [19] used the centerline exit pressure p_{cl} to evaluate the 2D contribution to the circulation instead of the “double-star” normalization employed in the present study. He also pointed out the equivalence of p_{cl}/ρ (ρ is the density) to the two-dimensional contribution $\int_0^{D_e/2} u(\partial v/\partial x) dr$. Indeed, plotting the calculated $p_{cl}/\rho U_e^2$ versus t_e^* , Fig. 7(b), yields a very similar plot to Fig. 7(a). The persisting two-dimensional contribution of the constricted conic nozzles can be also noticed in the nonvanishing asymptotic value of p_{cl} for $D_e/D_p < 1$. One can notice for $D_e/D_p > 0.6$ that for a brief period in the formation phase ($t_e^* \approx 1$), the 2D effects contribute a *negative* circulation flux ($d\Gamma^{**}/dt^{**} < 1/2$ in Fig. 7(a), and $p_{cl}/\rho U_e^2 < 0$ in Fig. 7(b)). For larger exit diameter cases, the negative two-dimensional contribution cancels out a portion of the circulation added in the flow initiation phase. This occurs when the vortex ring is developed enough to induce a significant negative radial velocity at the exit, reversing the sign of $\partial v/\partial x$. With the translation of the vortex ring farther downstream, the

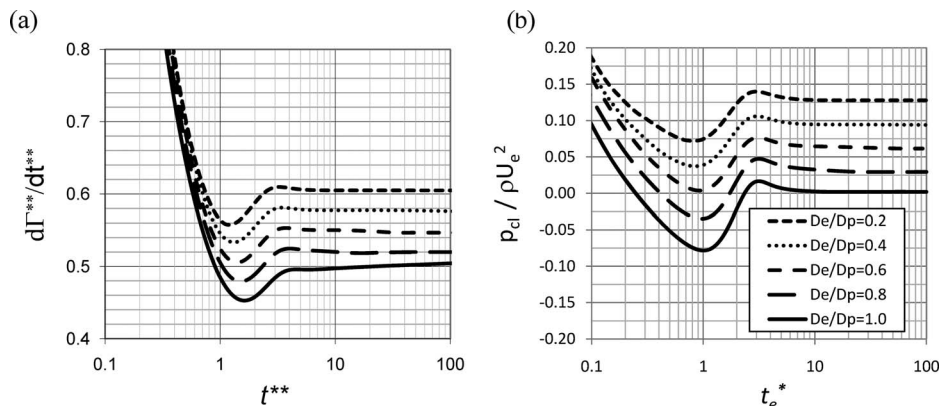


Fig. 7 The evolution of (a) the normalized circulation flux versus the formation time t^{**} , and (b) the centerline exit pressure versus t_e^*

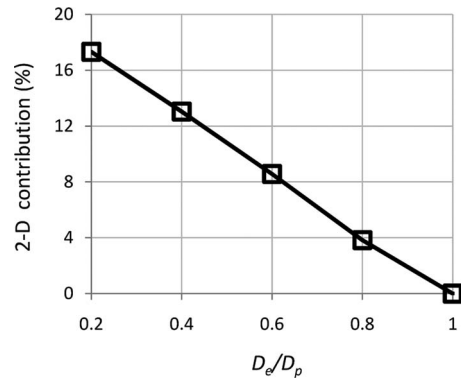


Fig. 8 The asymptotic two-dimensional contribution to the total circulation generation (%)

sign of $\partial v/\partial x$ changes back to positive (in the case of $D_e/D_p < 1$).

5 Vortex Ring Properties

The evolutions of total and vortex ring circulations (both normalized by the exit parameters) are shown in Fig. 9 for velocity program no. 2 (the inflow is stopped at $t_e^* = 8$). The maximal vortex ring circulation is given in Table 1 for the various D_e/D_p cases. For $D_e/D_p \geq 0.8$, the enhanced circulation efflux increases the normalized vortex ring circulation as well. For the straight tube case ($D_e/D_p = 1$), it is $\Gamma_{e,V}^* = 3.8$, significantly larger than the vortex circulation of $\Gamma_{e,V}^* \approx 2.7$ found by Rosenfeld et al. [10] for a uniform exit velocity profile. In the case of an imposed *parabolic* exit velocity profile, they have obtained a larger vortex circulation of $\Gamma_{e,V}^* = 3.5$, close to the value calculated in the present study for the straight tube. The relatively low Reynolds number flow in the present straight tube case ($Re = 500$) results in a parabolic-like exit velocity profile (Fig. 3), and hence, the increase in the vortex circulation. The augmented vortex circulation is accomplished by an axis-touching vortex ring that resembles a Hill’s spherical vortex, Fig. 4. For smaller exit diameter cases ($D_e/D_p < 0.6$), the vortex circulation reduces to $\Gamma_{e,V}^* = 2.7$, identical to the values obtained for a uniform exit velocity profile [10,12].

To further study the formation process, the evolution of the normalized energy ejected out of the nozzle, as well as the normalized energy of the vortex ring, are plotted in Fig. 10. Following Gharib et al. [5], the normalized energy is defined as $e = E/\sqrt{I}^3$, where E is the kinetic energy, and I is the impulse. The normalized vortex ring energy is very useful in studying the dy-

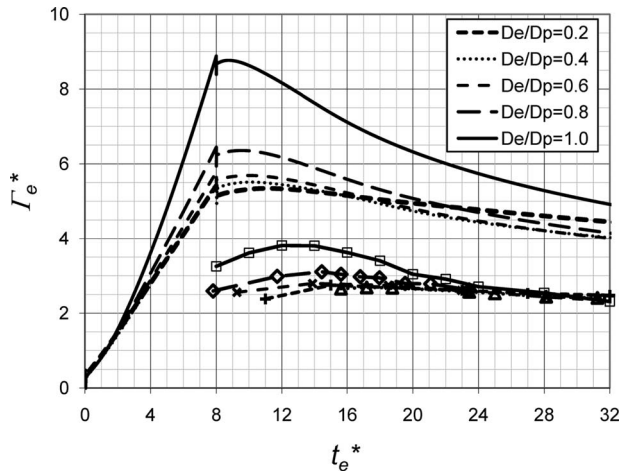


Fig. 9 The evolutions of the total (lines) and vortex ring (lines with symbols) circulations

namics of vortex rings as it invokes the three motion invariants being delivered by the vortex generator. The dependence of the maximal vortex ring energy on the nozzle-exit diameter is also given in Table 1. Unlike the normalized circulation, the normalized kinetic energy is larger for the more constricted nozzles, resulting in more energetic vortex rings for a given circulation and impulse. The decrease of e with the increase in D_e/D_p is related to the shape (vorticity distribution) of the vortex ring, as can be seen in Fig. 4. With the increase in D_e/D_p and the associated decrease in the Reynolds number, the vortex ring transforms from a thin core concentrated vortex ring into a thick core axis-touching vortex that resembles the Hill's spherical vortex. Gharib et al. [5] showed that for thin core vortex rings, $e \approx 0.33$ decreases to a value of $e \approx 0.16$ for the Hill vortex. In the present case, the larg-

Table 1 The dependence of the vortex ring parameters on the exit diameter

D_e/D_p	$\Gamma_{e,V}^*$	F^*	e
0.2	2.73	4.1	0.27
0.4	2.69	3.9	0.24
0.6	2.79	3.8	0.22
0.8	3.10	3.9	0.22
1.0	3.80	4.1	0.21

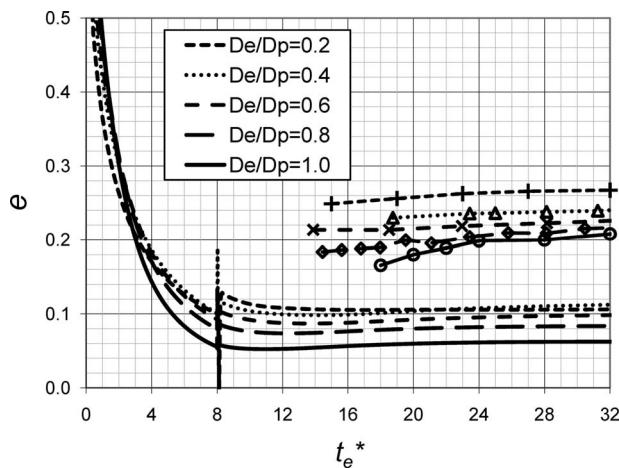


Fig. 10 The evolutions of the total (lines) and vortex ring (lines with symbols) normalized energies

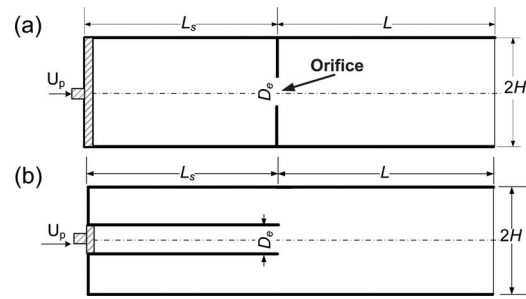


Fig. 11 Geometry of the limiting cases (a) orifice and (b) straight tube vortex generators ($D_e=1.5$ cm, $H=10$ cm, $L_s=45.1$ cm, and $L=80$ cm)

est vortex energy of $e=0.27$ is found for $D_e/D_p=0.2$, while the smallest is $e=0.21$ for $D_e/D_p=1$. The decrease in the vortex energy with the increase in the vortex circulation was also found by Mohseni et al. [13] for a straight vortex generator. Zhao et al. [12] calculated a vortex energy of $e=0.31-0.34$ for a set of imposed hyperbolic tangent exit axial velocity profiles with thin boundary layers. However, when Zhao et al. [12] imposed a parabolic exit velocity profile, the calculated vortex energy dropped to $e=0.195$. Obviously, developed velocity profiles (with thick shear layers) reduce the normalized energy of the vortex ring.

Despite the dependence of the circulation efflux and vortex ring circulation on the conic nozzle-exit diameter, the formation number, as defined by Gharib et al. [5], yields an almost constant value of $F^*=3.85 \pm 0.25$, Table 1, well within the range found in previous experimental and computational studies of straight tube vortex generators, see for example Refs. [5,10,13]. The invariance of the formation number with the exit diameter is a consequence of the finding that the increase in the ejected circulation, as D_e/D_p increases, is accompanied by an increase in the vortex ring circulation as well.

6 Effect of the Nozzle Length

So far, only one factor of the conic nozzle has been considered: the exit diameter, while the length of the nozzle was kept constant. The shortening of the nozzle is expanded to increase the two-dimensional contribution. A limiting case is a zero-length nozzle—i.e., an orifice, see Fig. 11(a). Such a case with an orifice diameter of $D_e=1.5$ cm, equal to the exit diameter of the conic nozzle $D_e/D_p=0.6$, has also been simulated. It should be noticed that in most previous vortex ring formation studies that refer to an orifice case, e.g., Refs. [5,10], the geometry is different. It consists of a flat plate, flushed with the exit of a straight tube with a small diameter (D_p rather than $2H$, as in the present case). The most significant difference is that in the latter case, the flow at the exit is mostly parallel to the wall of the tube, while in the present case, there is a large radial component of the flow, upstream of the orifice, that leads to a large axial gradient of the radial velocity component, and consequently, to a significant two-dimensional contribution to the circulation production.

Yet another limiting case that has been simulated is that of a straight tube vortex generator with a constant diameter equal to the diameter of the orifice ($D_e=D_p=1.5$ cm), Fig. 11(b). The inflow rate identical to previous conic nozzle cases is employed in these two additional simulations as well, maintaining the same exit Reynolds number as of the conic nozzle with $D_e/D_p=0.6$ ($Re=830$).

The exit centerline velocity determines the magnitude of the one-dimensional contribution, Eq. (3). The evolution of the exit centerline velocity for these three identical exit diameter cases is shown in Fig. 12. In all the cases, the initiation of the flow ($t_e^* < 1$) is accompanied by an overshoot of the exit velocity profile near the walls, leading to a centerline velocity lower than the

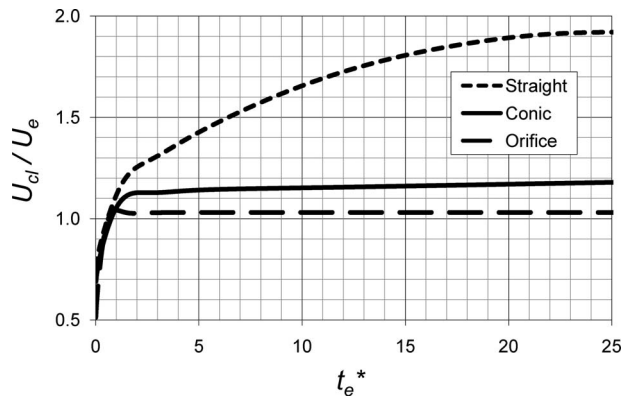


Fig. 12 The evolution of the exit centerline velocity for the cases with an equal exit diameter ($D_e=1.5$ cm)

mean exit velocity. Afterwards, the exit velocity profile of the orifice case is almost uniform and steady ($U_{cl}/U_e \approx 1.03$). The conic nozzle has a less uniform axial velocity but only by a small amount ($U_{cl}/U_e \approx 1.15$). However, it does evolve slowly in time. In the straight tube case, the velocity profile develops into a nearly parabolic flow ($U_{cl}/U_e \approx 1.92$) by $t_e^* = 20$.

The evolutions of Γ_e^* and $d\Gamma_e^*/dt_e^*$ are plotted in Fig. 13. The circulation generated by the conic nozzle and straight tube cases are almost identical during the starting phase of the flow ($t_e^* < 3$), when the exit velocity profile is almost uniform. Only later on ($t_e^* > 4$), with the increase in the centerline velocity, the straight tube generates a larger circulation (attributed to the one-dimensional contribution). The growth of the centerline velocity increases the slope $d\Gamma_e^*/dt_e^*$ as well, until $t_e^* \sim 20$, when an almost fully developed flow is attained. Subsequently, the exit flow becomes stationary, and the circulation efflux is also steady.

The two-dimensional contribution in the orifice case is larger than in the other two cases (it contributes as much as 44% of the

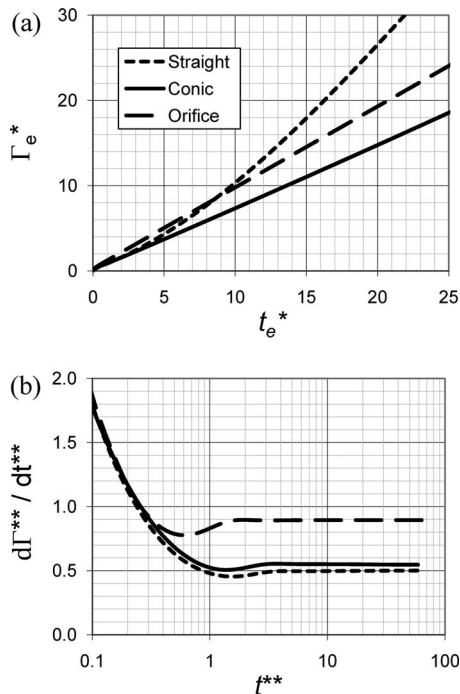


Fig. 13 Evolution of the (a) circulation and (b) circulation flux for the cases with an equal exit diameter ($D_e=1.5$ cm)

Table 2 Vortex ring parameters for three cases with identical exit diameter ($D_e=1.5$ cm)

	$\Gamma_{e,V}^*$	F^*	e
Straight tube	3.99	4.2	0.18
Conic nozzle	2.79	3.8	0.22
Orifice	3.83	3.7	0.24

total contribution), generating a larger overall circulation efflux up to $t_e^* = 8$. Afterwards, the continuous increase in the centerline exit velocity of the straight tube case generates a significantly larger circulation than the orifice case. Yet, the larger two-dimensional contribution of the orifice leads to the generation of a larger circulation than in the conic nozzle case.

The vortex circulation and normalized energy, as well as the formation number of these cases, are summarized in Table 2. The straight tube and orifice cases generate significantly larger circulation vortices: $\Gamma_{e,V}^* = 3.99$ and 3.83 , respectively, as a result of the larger circulation efflux during the vortex formation phase. The circulation production is larger either due to a larger centerline velocity (i.e., one-dimensional contribution) in the straight tube case, or due to the two-dimensional contribution in the orifice case. In the conic nozzle case that is characterized by an almost uniform exit velocity profile and relatively small ($\sim 9\%$) two-dimensional contribution, the vortex circulation is in the range reported previously for straight tubes with uniform exit velocity ($\Gamma_{e,V}^* \approx 2.8$).

The formation number is within the common range, in agreement with the previous findings of the present study. The almost uniform exit velocity profile of the orifice case yields the largest vortex energy ($e=0.24$), while the straight tube with the nonuniform exit velocity profile generates the least energetic vortex ring $e=0.18$. The lower energy of the vortex ring is consistent with the higher formation number since pinch-off occurs later (the feeding vortex sheet is disconnected only when the vortex ring energy exceeds that of the feeding flow [5]).

7 Conclusions

The present study presented evidences on the importance of the vortex generator geometry, and in particular, the exit configuration on the generation of circulation and on the vortex ring properties in the case of long ejection times. Conic nozzles allow flow manipulation by increasing the exit mean velocity and the Reynolds number, and by enforcing a two-dimensional flow at the exit. While the one-dimensional contribution is proportional to the square of the centerline exit velocity, and therefore, to approximately the fourth power of D_p/D_e (keeping the same volumetric flow rate), the two-dimensional contribution is found to be linear with D_p/D_e .

The control of the circulation ejection (as well as other motion invariants) is a target of any vortex ring optimization procedure. The one-dimensional contribution to the circulation is determined by the magnitude of the exit centerline velocity. It is a function of time and of the geometry of the vortex generator. Consequently, the control of the one-dimensional contribution is limited and indirect in nature. A more straightforward control can be obtained by manipulating the *two-dimensional* contribution through shaped nozzles, such as conic nozzles. The two-dimensional contribution persists the *entire* duration of the ejection, affecting the circulation rate as well. The double-star normalization has the advantage of allowing a quantitative assessment of the two-dimensional contribution *relative* to the one-dimensional contribution, while the alternate form of Krueger [19] cannot provide such a quantitative comparison. It has been found that the two-dimensional contribution to the circulation increases as the cone opening angle increases (i.e., the exit diameter decreases), and consequently, the

circulation generation increases as well. In the limiting case of an orifice (with an opening angle of 90 deg), the two-dimensional contribution is as large as 44% of the total circulation production. In the conic cases considered in the present study, the maximal two-dimensional contribution (17%) is obtained for the smallest exit diameter case ($D_e/D_p=0.2$).

The increase in the circulation generation rate is accompanied by an increase in the vortex ring circulation as well, keeping the formation number almost constant, $F^* \approx 4$. Thus, conic nozzles affect the magnitude of circulation or energy but not the strategy for obtaining optimal values. Thus, optimization of thrust or other quantities should employ techniques similar to previous studies of straight tube vortex generators, e.g., Refs. [6,14].

Nomenclature

D	= diameter
E	= kinetic energy ($\text{g cm}^2/\text{s}^2$)
e	= normalized kinetic energy
F^*	= formation number
H	= distance of the outer boundary (from the axis) (cm)
I	= impulse ($\text{g cm}^2/\text{s}$)
L	= length of the computational domain (from the nozzle exit) (cm)
L_p	= piston stroke (cm)
L_n	= length of the conic segment of the tube (cm)
L_s	= length of the straight segment of the tube (cm)
p	= pressure (dyn/cm^2)
Re	= Reynolds number
t	= time (s)
t_e^*	= formation time based on exit parameters (Eq. (2))
t^*	= formation time based on piston parameters (Eq. (1))
t^{**}	= double-star formation time (Eq. (4))
u, v	= the axial and radial velocity components (cm/s)
\tilde{U}	= velocity scale $\tilde{U} = \sqrt{\bar{U}_{cl}^2}$, where $\bar{U}_{cl}^2 = 1/t \int_0^t U_{cl}^2 d\tau$
U	= nozzle exit axial velocity (cm/s)
x, r	= axial and radial coordinates (cm)

Greek Symbols

ρ	= density (g/cm^3)
ω	= azimuthal vorticity (1/s)
Γ	= circulation ejected out of the tube (cm^2/s)
Γ^*	= normalized circulation based on piston parameters (Eq. (1))
Γ_e^*	= normalized circulation based on exit parameters (Eq. (2))

Γ^{**} = double-star normalized circulation (Eq. (4))

Subscripts

cl	= nozzle exit centerline
e	= nozzle exit
p	= piston

References

- [1] Didden, N., 1979, "Formation of Vortex Rings—Rolling-Up and Production of Circulation," *Z. Angew. Math. Phys.*, **30**(1), pp. 101–116.
- [2] Glezer, A., 1988, "The Formation of Vortex Rings," *Phys. Fluids*, **31**(12), pp. 3532–3542.
- [3] Glezer, A., and Coles, D., 1990, "An Experimental-Study of a Turbulent Vortex Ring," *J. Fluid Mech.*, **211**, pp. 243–283.
- [4] Shariff, K., and Leonard, A., 1992, "Vortex Rings," *Annu. Rev. Fluid Mech.*, **24**, pp. 235–279.
- [5] Gharib, M., Rambod, E., and Shariff, K., 1998, "A Universal Time Scale for Vortex Ring Formation," *J. Fluid Mech.*, **360**, pp. 121–140.
- [6] Krueger, P. S., and Gharib, M., 2003, "The Significance of Vortex Ring Formation to the Impulse and Thrust of a Starting Jet," *Phys. Fluids*, **15**(5), pp. 1271–1281.
- [7] Dabiri, J. O., and Gharib, M., 2004, "Fluid Entrainment by Isolated Vortex Rings," *J. Fluid Mech.*, **511**, pp. 311–331.
- [8] Krueger, P. S., Dabiri, J. O., and Gharib, M., 2006, "The Formation Number of Vortex Rings Formed in Uniform Background Co-Flow," *J. Fluid Mech.*, **556**, pp. 147–166.
- [9] Pullin, D. I., 1979, "Vortex Ring Formation at Tube and Orifice Openings," *Phys. Fluids*, **22**(3), pp. 401–403.
- [10] Rosenfeld, M., Rambod, E., and Gharib, M., 1998, "Circulation and Formation Number of Laminar Vortex Rings," *J. Fluid Mech.*, **376**, pp. 297–318.
- [11] Mohseni, K., and Gharib, M., 1998, "A Model for Universal Time Scale of Vortex Ring Formation," *Phys. Fluids*, **10**(10), pp. 2436–2438.
- [12] Zhao, W., Frankel, S. H., and Mongeau, L. G., 2000, "Effects of Trailing Jet Instability on Vortex Ring Formation," *Phys. Fluids*, **12**(3), pp. 589–596.
- [13] Mohseni, K., Ran, H. Y., and Colonius, T., 2001, "Numerical Experiments on Vortex Ring Formation," *J. Fluid Mech.*, **430**, pp. 267–282.
- [14] Linden, P. F., and Turner, J. S., 2001, "The Formation of "Optimal" Vortex Rings, and the Efficiency of Propulsion Devices," *J. Fluid Mech.*, **427**, pp. 61–72.
- [15] Gharib, M., Rambod, E., Kheradvar, A., Sahn, D. J., and Dabiri, J. O., 2006, "Optimal Vortex Formation as an Index of Cardiac Health," *Proc. Natl. Acad. Sci. U.S.A.*, **103**(16), pp. 6305–6308.
- [16] Dabiri, J. O., Colin, S. P., and Costello, J. H., 2006, "Fast-Swimming Hydromedusae Exploit Velar Kinematics to Form an Optimal Vortex Wake," *J. Exp. Biol.*, **209**(11), pp. 2025–2033.
- [17] Allen, J. J., and Naitoh, T., 2005, "Experimental Study of the Production of Vortex Rings Using a Variable Diameter Orifice," *Phys. Fluids*, **17**, p. 061701.
- [18] Dabiri, J. O., and Gharib, M., 2005, "Starting Flow Through Nozzles With Temporally Variable Exit Diameter," *J. Fluid Mech.*, **538**, pp. 111–136.
- [19] Krueger, P. S., 2005, "An Over-Pressure Correction to the Slug Model for Vortex Ring Circulation," *J. Fluid Mech.*, **545**, pp. 427–443.
- [20] Naitoh, T., Fukuda, N., Gotoh, T., Yamada, H., and Nakajima, K., 2002, "Experimental Study of Axial Flow in a Vortex Ring," *Phys. Fluids*, **14**(1), pp. 143–149.
- [21] Shusser, M., Gharib, M., Rosenfeld, M., and Mohseni, K., 2002, "On the Effect of Pipe Boundary Layer Growth on the Formation of a Laminar Vortex Ring Generated by a Piston/Cylinder Arrangement," *Theor. Comput. Fluid Dyn.*, **15**(5), pp. 303–316.
- [22] Heeg, R. S., and Riley, N., 1997, "Simulations of the Formation of an Axisymmetric Vortex Ring," *J. Fluid Mech.*, **339**, pp. 199–211.

Measurements of High Velocity Gradient Flow Using Bubble Tracers in a Cavitation Tunnel

Bu-Geun Paik
e-mail: ppaik@moeri.re.kr

Kyung-Youl Kim

Jong-Woo Ahn

Maritime and Ocean Engineering Research
Institute,
KORDI,
Jang-dong 171,
Yuseong-gu,
Daejeon 305-343, Korea

The objective of the present study is to investigate propeller wake using particle image velocimetry (PIV) technique with bubble type of tracers, naturally generated by the decrease in the static pressure in a cavitation tunnel. The bubble can be grown from the nuclei melted in the water tunnel and the size of bubbles is changed by varying the tunnel pressure. A series of experiments are conducted in the conditions of the uniform and high velocity gradient flows to find out the characteristics of bubble tracers and compared the measurement results using bubbles with those using solid particles. Bubbles showed good trace ability in the region of $15 < Re_S < 75$; however, some discrepancies showed at high velocity gradient region of $Re_S \approx 1000$. The fitted vorticity reduction rate would give reference for the prediction in a real flow when bubble tracers are utilized in PIV measurements of a vortical flow. In addition, the characteristics of bubble slip velocity can provide information on the vortex core center and the reduction in the Reynolds shear stress caused by bubble's deformability. [DOI: 10.1115/1.3192136]

Keywords: PIV (particle image velocimetry), bubble, slip velocity, cavitation tunnel, vorticity, turbulence

1 Introduction

The flow velocity can be measured with the PIV technique if there are tracers in the flow field, which is similar to the laser Doppler velocimetry (LDV) technique. In the case of LDV, the measurement volume is about a few mm^3 and the velocity measurement is available even though there is small number of tracers in the flow. On the other hand, the PIV technique, not a pointwise measurement but a field measurement, needs uniformly distributed tracers in the flow for the appropriate measurements since it can have the measurement range of a few μm to a few meters. In addition, the tracer has the size of a few nanometers to a few millimeters with the variation in the experimental conditions and the size of the measurement plane. As the size of the tracer is getting larger, the light intensity scattered from the tracer within the laser light sheet is also getting higher and this can provide some merits to the PIV measurement. However, larger tracers may play a role of additional nuclei in the cavitation tunnel and affect the cavitation patterns to some degree. As a result, the PIV measurements cannot be conducted together with the cavitation observation tests in a tunnel and lead to some harsh works to clean the whole cavitation tunnel after them. The Maritime and Ocean Engineering Research Institute's (MOERI's) midsize cavitation tunnel holds water of about 50 tons and the cleaning works to remove tracer particles were possible after PIV measurements. Recently, the MOERI has been constructing another cavitation tunnel, which will have a large test section of $2.8 \times 1.8 \times 12.5 \text{ m}^3$ and will contain about 2400 tons of water. In this new cavitation tunnel, the cleaning works are considered to be nearly impossible because they will require too much cost and time. Therefore, serious considerations would be necessary for the effective employment of the PIV measurements in the large cavitation tunnel as well as the midsize one.

The typical experiments carried out in the MOERI's midsize cavitation tunnel consists of the reproduction of the ship's hull

wake, propeller performance tests, rudder cavitation observation, and so on. For the realization of the hull wake, the equipment called the wake screen made of several steel meshes is used to simulate the wake flows behind the bare hull. Since this wake screen has quite fine and dense meshes, many tiny bubbles can be generated additionally. Although the large cavitation tunnel does not need the wake screen but the ship model, it would be meaningful to investigate the trace ability of the bubbles in the presence of the wake screen for the expansion of the PIV application. The tunnel pressure should be controlled to match the propeller operation condition and lots of bubbles occurred when it was decreased under the water vapor pressure.

Studies on the bubbly flow have been performed by many researchers. Brenn et al. [1] investigated the unsteady two-phase flow with small rising bubbles using phase Doppler anemometry (PDA). They revealed information about flow behaviors of the two-phase system through relative (slip) velocities. The increase in drag on bubbles due to interaction between bubbles and turbulence was introduced numerically by Lane et al. [2]. The bubble size effect was investigated on the gravity-driven pumping by injecting gas in the pipe using four-point fiber probe and laser Doppler anemometry (LDA) (see Ref. [3]).

The PIV measurements for the two-phase flow were performed to obtain velocity fields in the bubbly flows. Lindken and Merzkirch [4] did the studies to separate each velocity component of the liquid or the vapor in the bubbly flow. Although Jansen [5] investigated the breaking wave containing bubbles using the fluorescent particles and ultraviolet rays; they did not show good spatial resolution of the velocity field. Govender et al. [6] showed insufficient explanation of the PIV technique itself although he tried to get some information on the two-phase flow. It is necessary to study the details about the light source because the intensity of the scattered light from the bubbles is small in the bubbly flow with low void fraction and small-size bubbles. Ryu et al. [7] conducted successfully PIV measurements based on the silhouette technique considering the bubbles as the tracer to visualize the green water over the head deck of a ship. Recently, Paik et al. [8] measured the velocity fields using bubble tracers; however, they did not give detailed information on the bubble tracers and their characteristics.

Contributed by the Fluids Engineering Division of ASME for publication in the JOURNAL OF FLUIDS ENGINEERING. Manuscript received September 3, 2008; final manuscript received June 23, 2009; published online August 12, 2009. Assoc. Editor: Steven Ceccio.

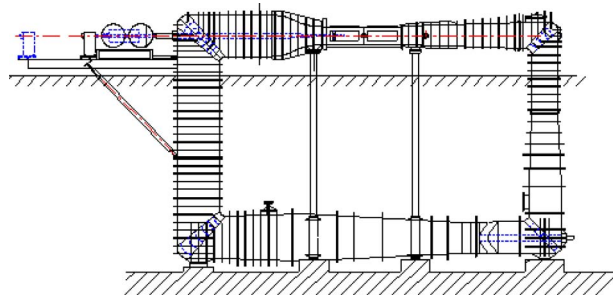


Fig. 1 Schematic diagram of a cavitation tunnel

In the present study, the propeller wake as a high velocity gradient flow was investigated using bubbles generated naturally by the decrease in tunnel pressure. In particular, velocity fields were extracted to confirm the PIV technique with bubble tracers from both the uniform flow and the propeller wake within the condition of high Reynolds number over 10^6 . In addition, the reason why some discrepancies between two tracer cases occurred was investigated in the viewpoint of the slip velocity. Reference data were also provided to correct vorticity values in the results of bubbly flow.

2 Experimental Apparatus and Method

The experiments have been conducted in the midsize cavitation tunnel of the MOERI. The rectangular test section has dimensions of $0.6^H \times 0.6^W \times 2.6^L$ m³. The maximum flow speed is 12 m/s, and the pressure can be varied from 0.1 kg_f/cm² to 2.0 kg_f/cm². A schematic diagram of the tunnel is shown in Fig. 1. The two-frame PIV system consists of a dual-head neodymium-doped yttrium aluminium garnet (Nd:YAG) laser (200 mJ/pulse), two charge-coupled device (CCD) cameras, a synchronizer, and a frame grabber, as shown in Fig. 2. The CCD cameras have a resolution of 1024×1024 pixels, and a thin laser light sheet was used to illuminate the center plane longitudinally and capture the pairs of particle images separated by short time intervals by using the frame-straddling method. Velocity fields were extracted using the PIV algorithm of a cross-correlation method based on the fast fourier transform (FFT). The field of view was 10×10 cm² in the uniform flow and the measurements were conducted to observe the behaviors of tracers with the variation in experimental conditions, as shown in Table 1. The tunnel flow speed was detected from the Pitot tube installed on the wall ahead of the test section.

In this study, together with the uniform flow, the propeller wake was also measured to find out the likelihood of bubbles as tracers in the 2D PIV technique. The propeller model for the container

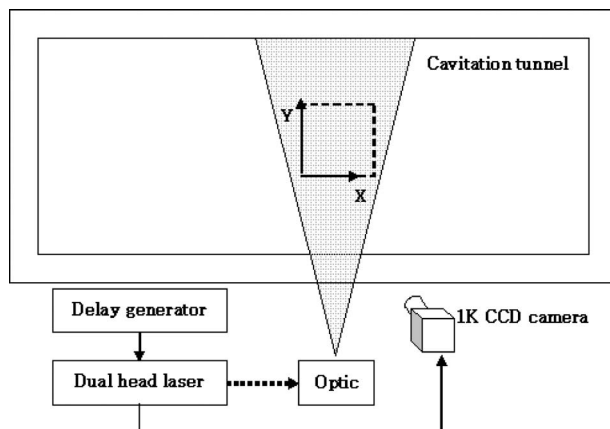


Fig. 2 Schematic diagram of a PIV experimental setup

Table 1 Test conditions for 2D PIV measurements

Flow speed (m/s)	3	5	8
Time interval (μ s)	120	100	80
Tunnel pressure (atm)	1.0	1.0	1.0
	0.8	0.8	0.8
	0.5	0.5	0.5
	0.3	0.3	0.3
	0.2	0.2	0.2

ship model has five blades, a mean pitch ratio of 0.990, and a diameter of 250 mm. The wake screen was arranged in front of the propeller model to consider the bare hull wake. The significant decrease in tunnel pressure for the sake of the generation of bubbles may result in a reduction in the thrust, mismatching the design condition of the propeller. Therefore, bubble generation has to be considered after finding appropriate revolution condition. The present study satisfied well the thrust identity.

The analysis of measurement uncertainties or precision errors was carried out for actual particle images whose flow field was known in advance. The quiescent flow was tested for the uncertainty evaluation of the present PIV system by following the procedure recommended by Raffel et al. [9] to estimate the measurement errors of PIV systems under the same condition as explained in the experimental apparatus and method. The standard errors encountered in measuring the displacement vector were calculated, and the results were summarized in Table 2. To minimize the measurement uncertainties, 150 instantaneous velocity fields were ensemble-averaged in the postprocessing. As a result, the uncertainty levels measured by PIV system were 0.038% and 0.063% for the axial and radial velocity vectors, respectively. Instantaneous velocity fields were obtained for each measurement phase. They were ensemble-averaged to obtain the time-averaged in-plane velocity, vorticity, turbulence intensity, and Reynolds shear stress in terms of tracers for PIV.

In addition, the bubble size was measured by using the shadowgraph technique with the images of bubbles as tracers. Although the shadowgraph technique may give rather less accurate sizing values than phase Doppler or global rainbow methods, we employed it because of the absence of other bubble sizing equipments. Two light bulbs were utilized to illuminate the bubbles at the bottom and side wall. The visualization system consisted of a high-speed camera (Photron, FASTCAM APX-RS), a Nikon 50 mm lens ($f=1.4$), metal lamps (Photron, HVC-SL), an image processor, and a PC. Figure 3 shows one image of the shadowgraph technique at 0.38 atm. The camera frame rate was varied from 2000 frames/s (fps) to 6000 fps, since the flow speed was changed in the range 3–8 m/s. The spatial resolution and the size of the measurement plane were 512×512 pixels and 15×15 cm², respectively. The bubble size was determined from the occupied pixels by a bubble, the measurement area, and the spatial resolution of the camera.

Table 2 Measurement uncertainties of displacement vectors measured by the PIV system used in this study

	root-mean-square (rms)	Fluctuations (μ m)	
		Min.	Max.
$\sigma_{\Delta x}$	0.050	-6.317	6.367
$\sigma_{\Delta y}$	0.082	-8.052	8.4562

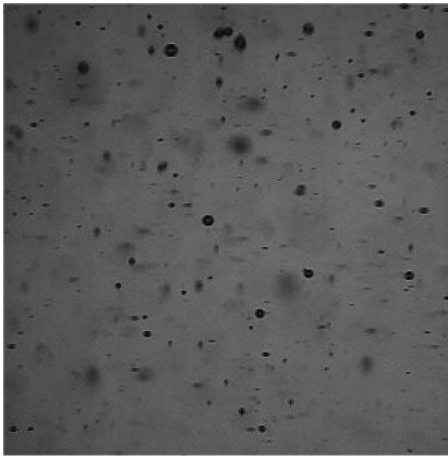


Fig. 3 One image of shadowgraph technique at 0.38 atm

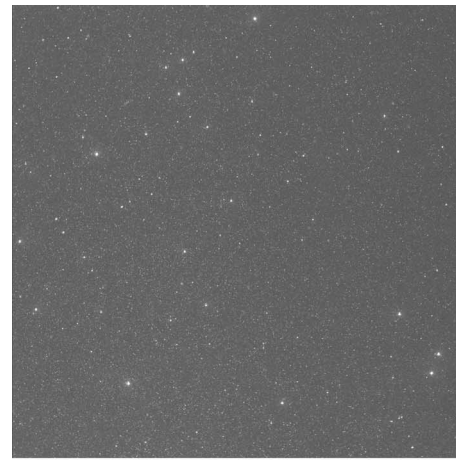
3 Results and Discussion

As the 2D PIV system uses the time interval between laser pulses and the frame-straddling method of the CCD camera, the particle images were captured according to the variation in the time interval and the tunnel flow speed. Generally, the time interval was chosen for the particle displacement of 3–5 pixels, which are efficient for the operation of the PIV algorithm, and the particle images were acquired accordingly.

Figure 4(a) shows the particle image when the flow speed (in the X direction only) and the tunnel pressure were 3 m/s and 0.2 atm, respectively. The tunnel water has no polyamide particles of 20–30 μm in diameter, which were used in the tunnel for the typical PIV measurements. These polyamide particles increased the contamination of the water and made the cavitation observation quite difficult. In addition, heavy cost and much effort are necessary to clean the remains of the particles attached to the tunnel walls and the impeller. The picture shows both large and small particles; the larger ones mean the bubbles and the small ones are titanium dioxide (TiO_2) particles of 3 μm . The TiO_2 particles do not affect the cavitation patterns on the body surfaces because they do not function as the nuclei of cavitation. The particle images are similar to each other from 1 atm to 0.3 atm in tunnel pressure. When the tunnel pressure was lowered below 0.3 atm, many bubbles appeared in the tunnel water. The bubble tracer has a mean diameter of 0.74 ± 0.24 mm as shown in Table 3, and it could be employed for the PIV measurements. However, the influences of the bubbles on the near flow field and their trace ability in the high velocity gradient flow had to be investigated minutely for the availability of bubble tracers.

Figure 4(b) shows the image of particles 5 m/s in flow speed and 0.2 atm in tunnel pressure. As the increase in the tunnel speed increasingly lowered the water pressure, the bubbles appeared from the 0.3 atm tunnel pressure. The bubbles have a mean diameter of 1.03 ± 0.13 mm at 5 m/s, without the scattering band of the bubble, and larger than that in the condition of 3 m/s. The increase of the tunnel flow speed to 8 m/s raised the number of the bubbles and increased the mean diameter to 1.60 ± 0.11 mm. Since the increase in flow speed resulted in the growth of the bubble occupied region and the number of bubbles, the buoyancy that might be caused by the increment of bubble size should be studied by using the velocity field measurements.

The interrogation window size for PIV measurements was 50% overlapped 48×48 pixels in the uniform flow. To compare the differences among velocity field results, the original vector maps were arranged without removing any error vectors or interpolations in Fig. 5. Figure 5(a) shows the small error vectors in the velocity field. They indicate that the particle images including the bubbles with a diameter of less than 1 mm would be useful for the



(a)



(b)



(c)

Fig. 4 Particle images at the tunnel pressure of 0.2 atm: (a) 3 m/s, (b) 5 m/s, and (c) 8 m/s

PIV analysis. The increment in the flow speed raised the number of the error vectors in the vector map as shown in Fig. 5(c). The empty spaces in the velocity fields mean errors caused by bubbles. The velocity field of the flow speed of 8 m/s with the tunnel pressure of 0.3 atm was similar to that of 0.2 atm and 5 m/s. As the condition of 8 m/s and 0.2 atm largely increased the error

Table 3 Results obtained from the velocity fields in the uniform flows

U_0 (m/s)	P_t (atm)	Bubble size (mm)	Error ratio (%)	U mean (pixel)	V mean (pixel)	Standard error ($\times 10^{-3}$ pixel)
3	1.0	-	0.5	3.080	-0.03	9.51
	0.2	0.74 ± 0.24	1.0	3.077	-0.02	9.98
5	1.0	-	0.8	4.210	-0.03	12.72
	0.2	1.03 ± 0.13	1.5	4.215	-0.02	10.43
8	1.0	-	2.8	5.487	-0.05	14.16
	0.2	1.60 ± 0.11	3.5	5.490	-0.03	18.25

vectors caused by the light scattered from the bubble, the appropriate bubble images should be considered in advance according to the experimental conditions.

Table 3 shows the results of the 400 velocity fields in each uniform flow case. Here, U_0 and P_t mean the free stream velocity and tunnel pressure, respectively. Only the error ratio (equal to the number of error vectors/number of total vectors) was obtained from the original velocity fields, and other parameters such as mean value and standard error were extracted after the post-processing of vector maps. The mean displacement in the vertical direction shows a nearly constant value of about -0.03 pixels, which were independent of the tunnel flow speed and the size of bubbles. In other words, the buoyancy effect did not occur in the uniform flow conditions. At the atmospheric pressure condition, the error ratio was below 2%, indicating a good uniformity in the tracer distribution. In the case of 3 m/s, the error ratio and standard error had small values regardless of the variation in the tunnel pressure. With the flow speed of 5 m/s, the error ratio and the standard error had values larger than those of 3 m/s because of the increase in the bubble tracer. However, the PIV measurement could be employed in the 5 m/s condition because the error ratio of less than 2% means the acquisition of good particle images. Although the error ratio and the standard error at 8 m/s were also larger than those of at 3 m/s, a fine control of the time interval between the two laser sheets, the laser intensity and the aperture of the CCD camera would be helpful in acquiring better images. In the case of the 8 m/s and 0.2 atm tunnel pressure, the error ratio was larger than the 1.0 atm tunnel pressure. The increase in the error ratio is attributed to the secondary effects by the light sources scattered from the rather larger bubbles, which illuminate the surrounding flow region needlessly. Most of all, it is necessary to treat the bubble tracers carefully in the case of high flow speed and low tunnel pressure so that large bubbles would not fill up the whole interrogation window area.

To measure the high velocity gradient flow trace ability of bubbles in a complicated flow by using the 2D PIV technique, the propeller wake was selected because it contains the vortical structure with a high velocity gradient. The wake screen in front of the rotating propeller provided many tiny bubbles through the small meshes on it, and this made it possible to reduce the interrogation window for PIV measurements to 50% overlapped 32×32 pixels. In the condition of 5 m/s and 0.25 atm, the mean diameter of the bubble was 1.03 mm and the size of the measurement plane was 20×10 cm². Since the propeller is working in fixed conditions of above pressure and flow speed, the variation in bubble size was not available in the propeller wake case. The propeller wake has a quite complicated flow structure that consists of hub vortices, tip vortices, and trailing vortices. The hub vortices were excluded in this study because the diffused reflection from them was too strong to capture the tracer images. The tip vortices are generated from the pressure difference between the suction and pressure sides at the blade tip region. The trailing edge of a blade produced the trailing vortices, which looked like a curved layer connected to a tip vortex. Figures 6 and 7 showed the particle images and the instantaneous velocity fields behind the propellers obtained at two tunnel pressures and 5 m/s free stream. The tip

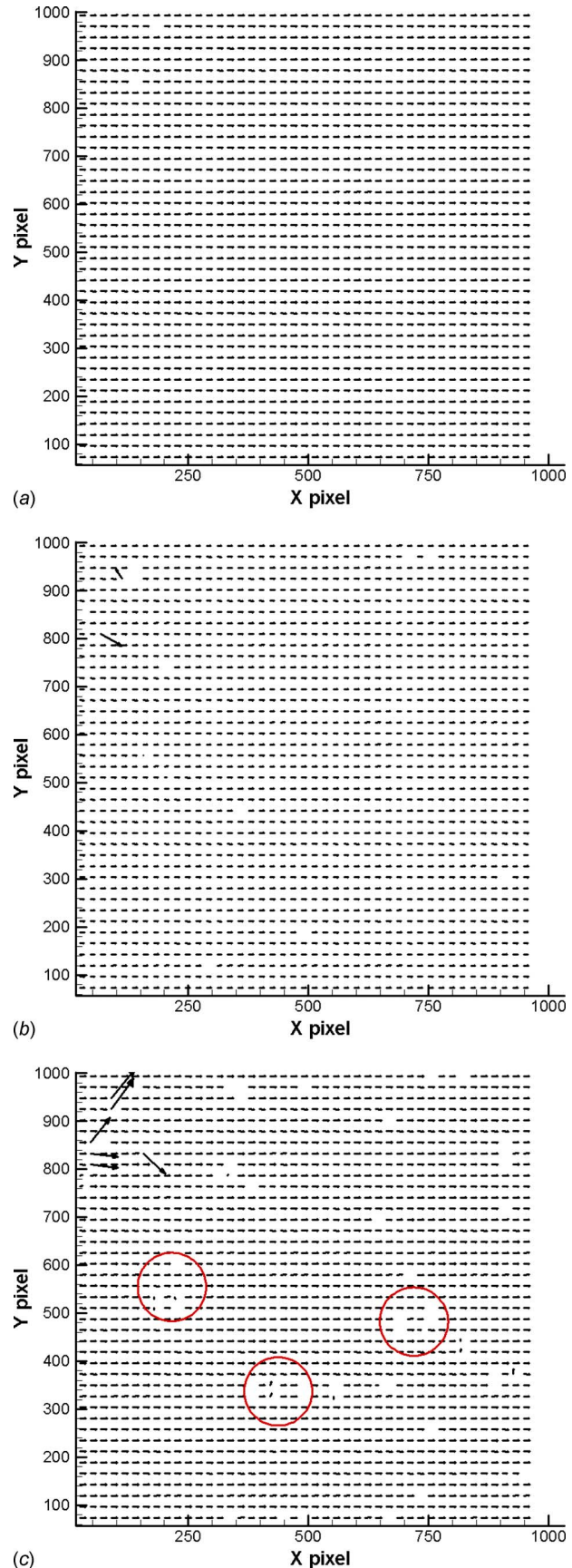
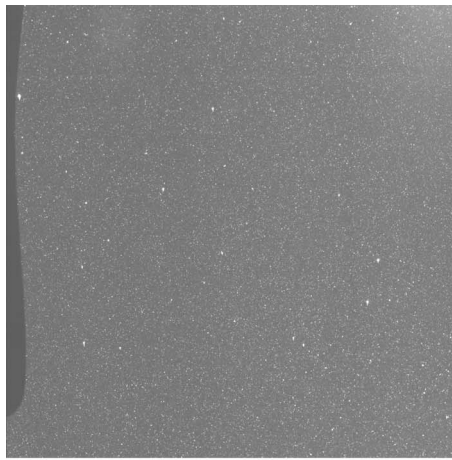
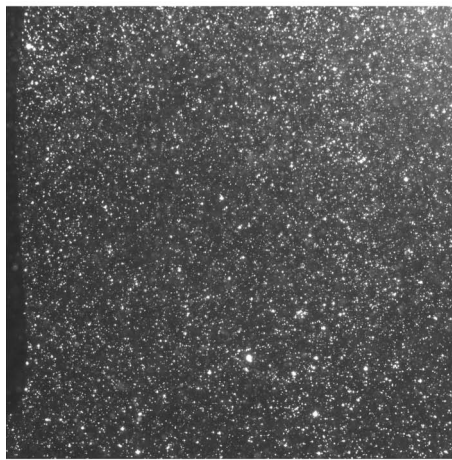


Fig. 5 Velocity fields at the tunnel pressure of 0.2 atm: (a) 3 m/s, (b) 5 m/s, and (c) 8 m/s



(a)



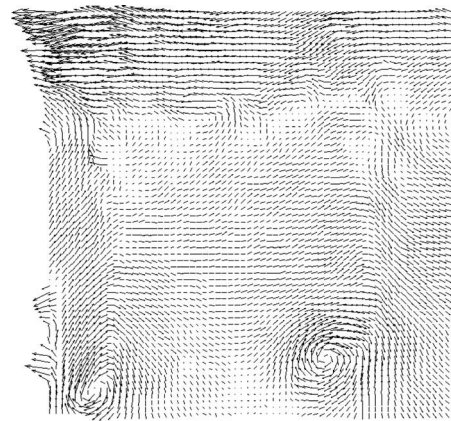
(b)

Fig. 6 Particle images of propeller wake at the same free stream velocity: (a) atmospheric pressure and (b) 0.25 atm

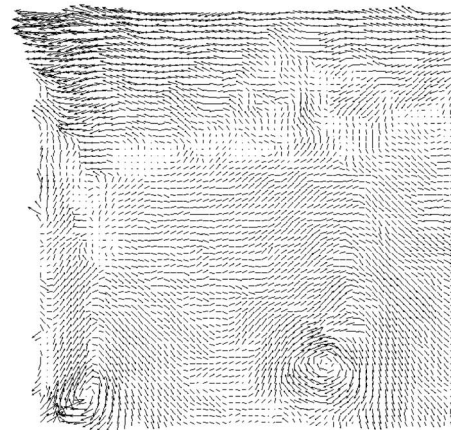
vortices and the wake sheets generated from the blade trailing resemble each other in both of the instantaneous velocity fields. At the atmospheric pressure, the aperture of the CCD camera was fully widened to capture the images of the tiny solid particles. On the other hand, the aperture was narrowed tightly so that it would not damage the CCD cells at the condition of 0.25 atm and cavitation number of 1.4 because the light intensity scattered from the bubbles was very strong.

Figure 8(a) shows the contour plots of phase-averaged axial velocity at $\phi=0$ deg when the solid particles are put into the tunnel water. The axial velocity component has large values in the slipstream, which means that the region has high axial momentum inside the trajectories of the tip vortices and relatively smaller values near the blade tip and the propeller axis. Along the tip region ($-0.5 < Y/D < -0.4$) of each blade, there are pairs of negative and positive isocontours with the shape of a circle because of the tip vortices. The velocity cores of Rankin type may give the information on vortex size from the characteristics of vortex. This tendency is very similar to the contour plots of bubble tracers (Fig. 8(b)). The result of the bubble tracers shows the contours' location and shapes similar to that of the solid particles. Although the magnitudes of axial velocity in the slipstream region are a little different between solid and bubble cases, the bubbles seem to show a trace ability as good as the solid tracers.

Figure 9 shows the axial velocity profile at several radial locations at $\phi=0$ deg. There was a velocity defect, which looks like a hump in the region $0.3 < r/R < 0.7$ around $X/D=0.3$ and 0.6, and



(a)



(b)

Fig. 7 Instantaneous fluctuating velocity fields subtracted by a convection velocity at the same free stream velocity: (a) atmospheric pressure and (b) 0.25 atm

it is originated from the merging of the boundary layers developed on two sides of the blade. As the viscous wake is influenced by a centrifugal force, the hump of velocity defect grew deeper with the increase in radial distance. However, there was a significant change in the axial velocity profile because of the influence of the tip vortices at $r/R=0.9$ in the case of both the solid and bubble tracers before the location of $X/D=0.35$. As the axial velocity of the slipstream is larger than that of the tip vortices and their rotational component reduces the axial velocity near $r/R=0.9$, the humps at $r/R=0.9$ show deep valleys and outbreak earlier than those at $0.3 \leq r/R \leq 0.7$.

Figure 9 shows the limitation of the bubble tracers in a high velocity gradient flow. In the region of $X/D \geq 0.35$, bubbles follow the wake flow behaviors such as the movement of the trailing vorticity and the tip vortices very well. On the other hand, bubbles could not trace the flow behaviors well in the region of $X/D < 0.35$, especially around the position of $r/R=0.9$ where the high velocity gradients appear. These experimental results led us to find that the bubble tracers would be useful in a wake region of $X/D \geq 0.35$ because the bubbles show rather good trace ability in terms of the axial velocity component compared with the solid particles. The solid tracers have a slightly larger axial velocity at the range of $0.3 \leq r/R \leq 0.7$ in the whole downstream area. Looking into the region of $X/D \geq 0.35$ where the bubbles seem to obtain the stability of its movement, the difference in axial velocity ranged from 0.63% to 2.10% in the radial distance $0.3 \leq r/R \leq 0.7$. The axial velocity difference gradually decreased as the radial distance in-

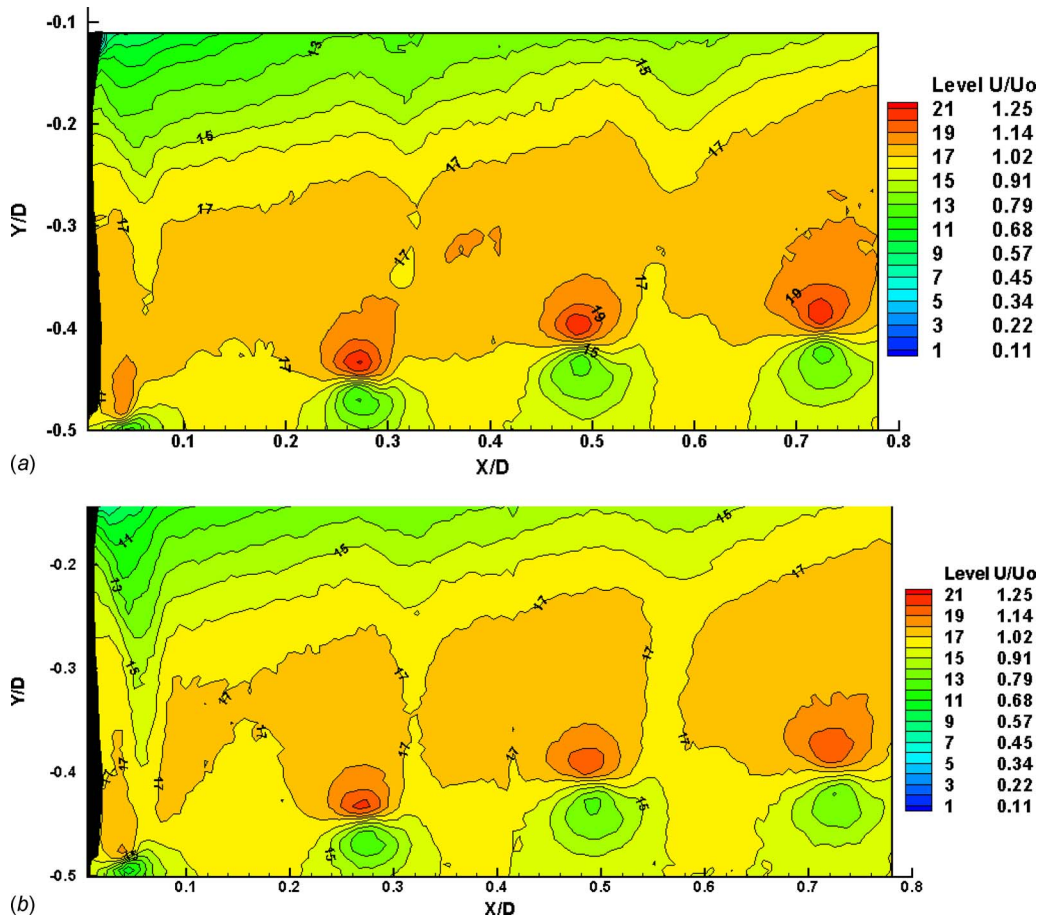


Fig. 8 The comparison of the phase-averaged axial velocity contours: (a) solid particles and (b) bubble tracers

creased from $r/R=0.3$ to $r/R=0.7$. The difference between both tracer cases was from 0.3% to 11.6% at $r/R=0.9$.

The difference in velocity magnitude between bubble and water is known as the slip velocity and is computed as follows:

$$U_{\text{mag}S} = \frac{(U_{\text{bubble}} - U_{\text{water}})}{U_{\text{free}}} \quad (1)$$

where U_{bubble} and U_{water} mean the total velocity magnitude of bubble and solid, and U_{free} is the free stream velocity measured by solid tracers. Figure 10(a) shows the contours of slip velocity $U_{\text{mag}S}$ regarding two propeller wake cases. In the slipstream region of $-0.35 < Y/D < -0.10$, the slip velocity was only 3% of the free stream velocity near the trailing vortices, and it has values ranging from 0.15% to 0.3% at the other areas. Reynolds number (based on the propeller diameter and fluid velocity) was around 10^6 in the present study, and the slip velocity was negligible at the region of small velocity gradient. This result is very similar to that of Murai et al. [10] who measured the slip velocity in the horizontal bubbly channel flow at the Reynolds number of 2×10^4 based on the channel height. To investigate the characteristics of a bubbly flow further in a high Reynolds number, another Reynolds number Re_S was defined by the slip velocity

$$Re_S = \frac{|U_{\text{bubble}} - U_{\text{water}}| D_{\text{bubble}}}{\nu} \quad (2)$$

Here, D_{bubble} and ν are the mean diameter of the bubbles and the kinematical viscosity of water, respectively. The slipstream region in Fig. 10(a) gives the range of $15 < Re_S < 75$ when D_{bubble} is supposed to be about 1 mm. This Reynolds number range is higher than that ($0 < Re_S < 9$) of the rising bubble case (see Ref. [1]) in spite of the similar diameter of bubbles. In the range $4 \leq Re_S \leq 100$, the drag coefficient reported by Clift et al. [11] is as follows:

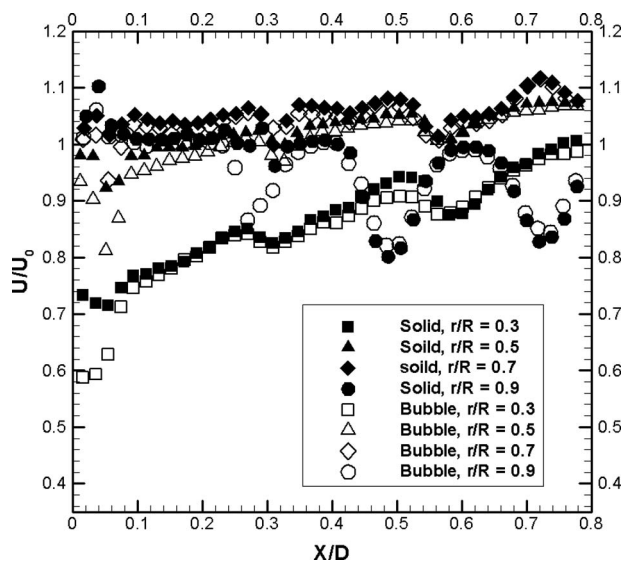


Fig. 9 The comparison of the phase-averaged axial velocity profiles at several radial locations

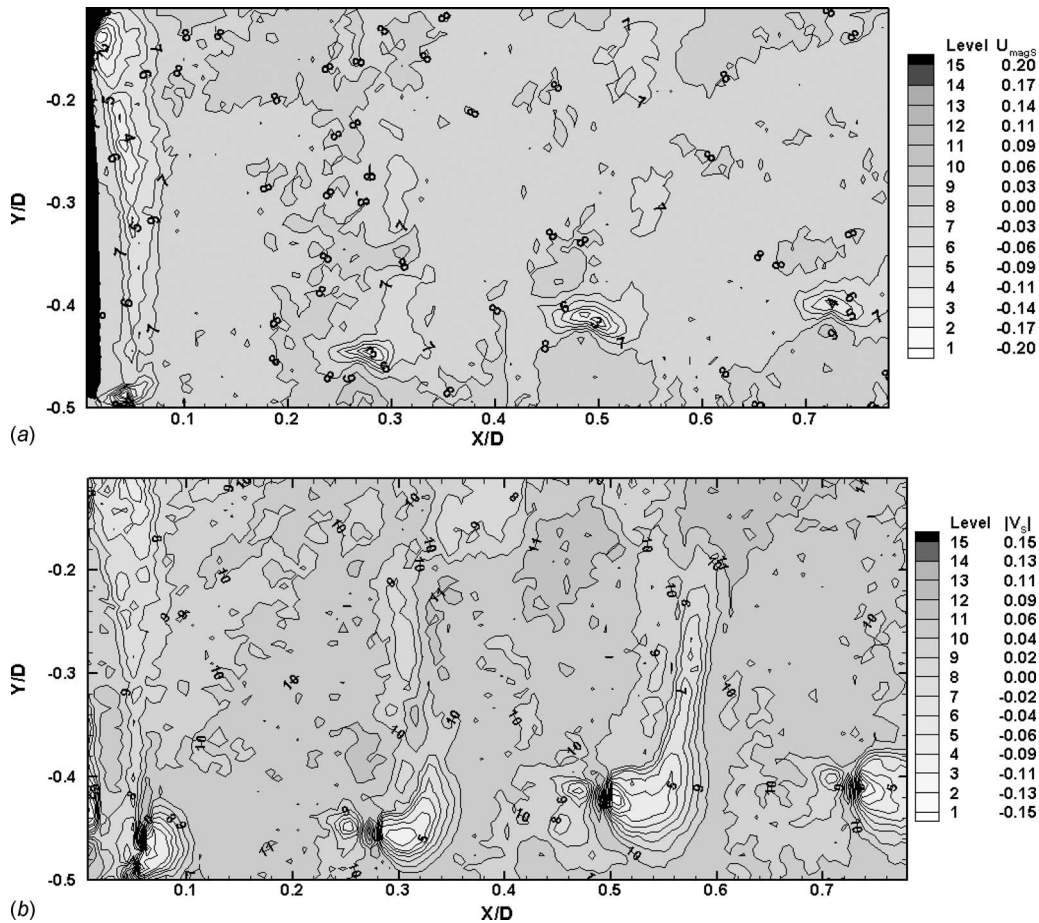


Fig. 10 Contour plots of slip velocity between bubble and solid tracers: (a) for velocity magnitude and (b) for vertical velocity

$$C_D = 13.725 \text{ Re}_S^{-0.74} \quad (3)$$

and the rising bubble case gives $1 < C_D < 20$. However, it decreased to a range of $0.56 < C_D < 1.85$ when a bubble appeared in a high Reynolds number flow above the transition region, experiencing a small velocity gradient.

In the case of the small velocity gradient flow, the drag force on the bubbles was too small to require serious correction of a bubbly flow into a real flow. On the other hand, the high velocity gradient, especially the tip vortex region ($-0.50 < Y/D < -0.35$) shown in Fig. 10(a), gives different characteristics of bubbles. The Re_S was about 1000 because the slip velocity magnitude increased to $0.2U_0$ at a tip vortex. The rotational velocity components were very strong around the core of a tip vortex. The solid tracers followed the rotational trace around the core better than the bubble tracers because the skin friction of the solid tracers is higher than that of bubbles, and it kept the inertial force continuously even at the region of very high velocity gradient. The lift force on individual bubble (see Ref. [12]) could be one potential source of the high slip velocity and it provides bubbles' slip in a shear and rotational region. The pressure gradient force owing to density effect could be another source because it accelerates bubbles in the radial direction of vortices. Those made bubbles not to follow the rotational trajectory exactly and have a rather low axial velocity component instead around the tip vortex core, which was different from the real flow behaviors.

In addition, each tip vortex has a similar vertical slip velocity V_S pattern though the wake moves downstream. The area in which the bubble has a more vertical velocity than water is sandwiched between those of $|V_S| < 0$ as shown in Fig. 10(b). The solid and

bubble tracers circulated around the core of the tip vortex tube because of significant rotational motion and centrifugal force. In particular, the bubbles have a greater vertical velocity magnitude because they may move more rapidly and more easily than the solids in the state of cavitating vortical flow. The region of the highest value of $|V_S|$ means the center of the tip vortex core, which can be confirmed in the Z-directional vorticity contours, as shown in Fig. 11.

The Z-directional vorticity values of the trailing vortices in the bubble tracer case are similar to those in solid tracers, and the contours in the bubble case show a slightly broader distribution than those of solids as shown in Fig. 11. Near the tip vortices, the vorticity values in the bubble case became smaller because it lost some of its trace ability owing to an increase in slip velocity. Actually, bubble concentration around tip vortices is different from that of the other regions. In the tip vortex region the bubble concentration was about $184/120^2$ pixels and it reduced to $75/120^2$ pixels at the sandwiched region between tip vortices. The bubbles accumulated near vortex cores and resulted with the reduction in velocity magnitudes of bubbles, which is closely related to the decrease in vorticity value at the tip vortex region of the bubble case. However, the locations of the tip and trailing vortices are very similar in both tracer cases. These findings led us to learn that a flow visualization using bubble tracers can be carried out in terms of the spatial configuration of a complicated flow. For example, the variation in the blade pitch of a propeller changes the spatial spacing between the tip and trailing vortices in a wake flow. Although the PIV technique using bubble tracers cannot measure the vorticity value accurately in a high velocity

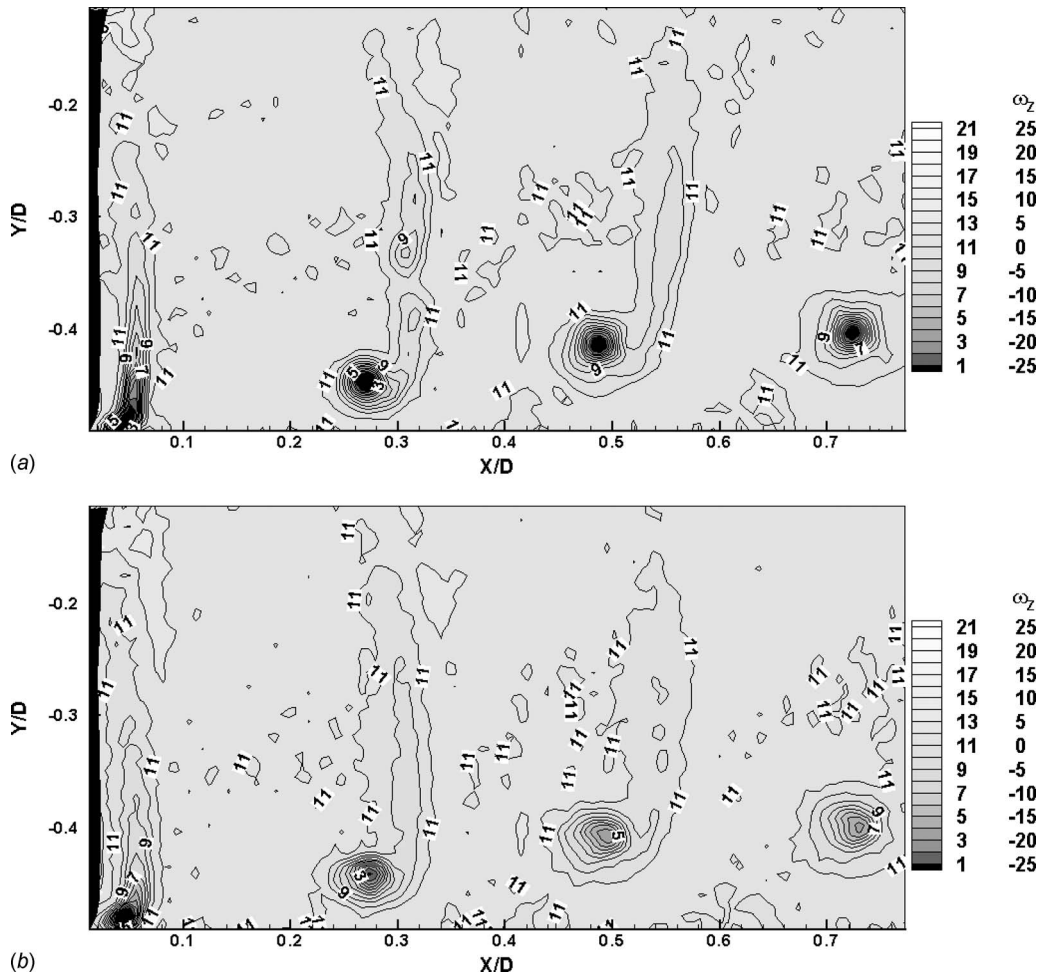


Fig. 11 The comparison of the phase-averaged vorticity contours: (a) solid particles and (b) bubble tracers

gradient region such as a vortex core, it would be helpful in diagnosing the parameters affecting the spatial evolution of the flows.

Figure 12 shows the phase-averaged vorticity profiles at several

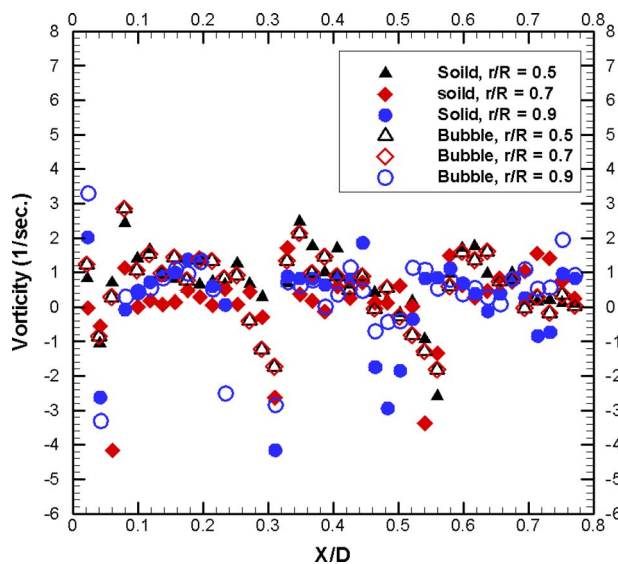


Fig. 12 The comparison of the phase-averaged vorticity profiles at several radial locations

radial locations. The vorticity distributions resembled one another except for the region of tip and trailing vortices in both tracer cases. Although both tracers displayed similar locations of trailing vortices at $r/R=0.7$ and 0.9 , the vorticity itself showed larger values in the solid tracers, and it increased as the radial distance increased. In particular, the locations of the trailing vortices varied according to the radial distance. The trailing vortices of $0.5 \leq r/R \leq 0.7$ appeared at more downstream locations than those of $r/R=0.9$ after the position of $X/D=0.4$ because the axial velocity in the slipstream is larger than that in the tip vortices.

The core of a tip vortex has the strongest vorticity value in the propeller wake except the hub vortices. The vorticity value in the cores decreased gradually up to the third tip vortex in the case of solid tracers, and the linear fitted line had an equation of $Y = 15.03X - 40.8$ as shown in Fig. 13, where Y and X mean vorticity and X/D axis, respectively. The reduction rate of vorticity value relaxed largely at the fourth tip vortex. In the case of bubble tracers, the reduction rate of vorticity increased significantly, and its equation became $Y = 34.02X - 37.0$ up to the third tip vortex. Both equations regarding the vorticity reduction rate would give some insight into how much vorticity value was underestimated when a PIV technique was employed in the measurements of high velocity gradient flow using bubble tracers. We found that the differences in the tip vortices' vorticity values between both tracers are attributed to the large slip velocity and Re_s in the high velocity gradient region, as shown in Fig. 10. The difference in the vorticity values between the two tracer cases was getting larger as the wake moved downstream. However, its difference

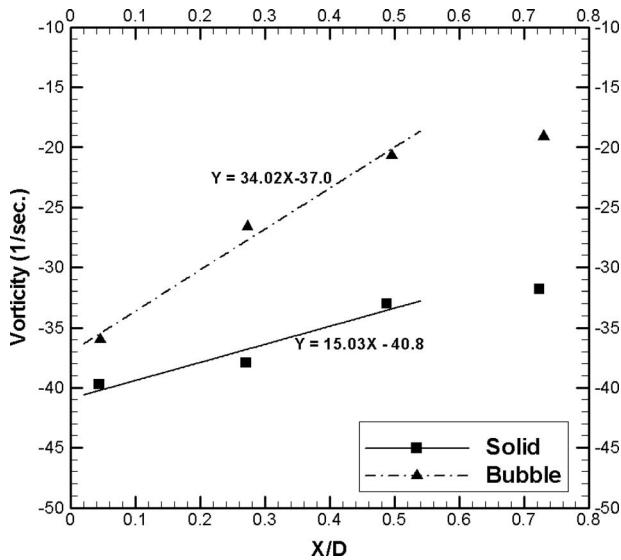


Fig. 13 The comparison of the vorticity values at the cores of tip vortices

maintained a constant value from the third tip vortex. In addition to the provision of criteria for the adoption of bubble tracers, these characteristics would be useful references for analyzing vortical flow with strong vortices.

In general, a bubble slip velocity is generated to make a balance between buoyancy and drag at the rising bubble in water without any acceleration. In a turbulent flow, however, a bubble experiences accelerations and decelerations continuously because of the vortical turbulence. The viscosity in the complicated turbulent flow is known to increase and the additional turbulent viscosity is known to affect the Reynolds shear stress (see Ref. [13]). The bubbles influenced the turbulent viscosity in the slipstream region of $r/R=0.5$ and 0.7 and increased the Reynolds shear stress as shown in Fig. 14. The humps and discontinuities indicate the existence of the trailing and tip vortices in the wake flow system. Although the absolute values of Reynolds shear stress of bubbles are higher than those of solid tracer, the distribution pattern and its amplitude are similar to each other, showing a biased trend owing to the slip velocity. Actually, Moriguchi and Kato [14] reported that the reduction in Reynolds shear stress induces the reduction in skin friction in the high shear rate flow when the bubbles appear on the wall without any dependency of the bubble size. The flow with a high shear rate on the wall was known to increase the bubbles' deformability and reduce the Reynolds shear stress. The present experiments also showed that the bubbles reduced the profile amplitude in Reynolds shear stress in the region of $r/R=0.8$ and 0.9 though they displayed a sort of biased trend of Reynolds shear stress. It seems that the high shear rate of the tip vortices provides the bubbles' excessive deformability and influences on the amplitude decrease in the Reynolds shear stress, showing an absolute value smaller than the solid case at the tip vortices. Actually, it was well known that bubbles experience an oscillatory deformation when the Weber number of bubbles is larger than

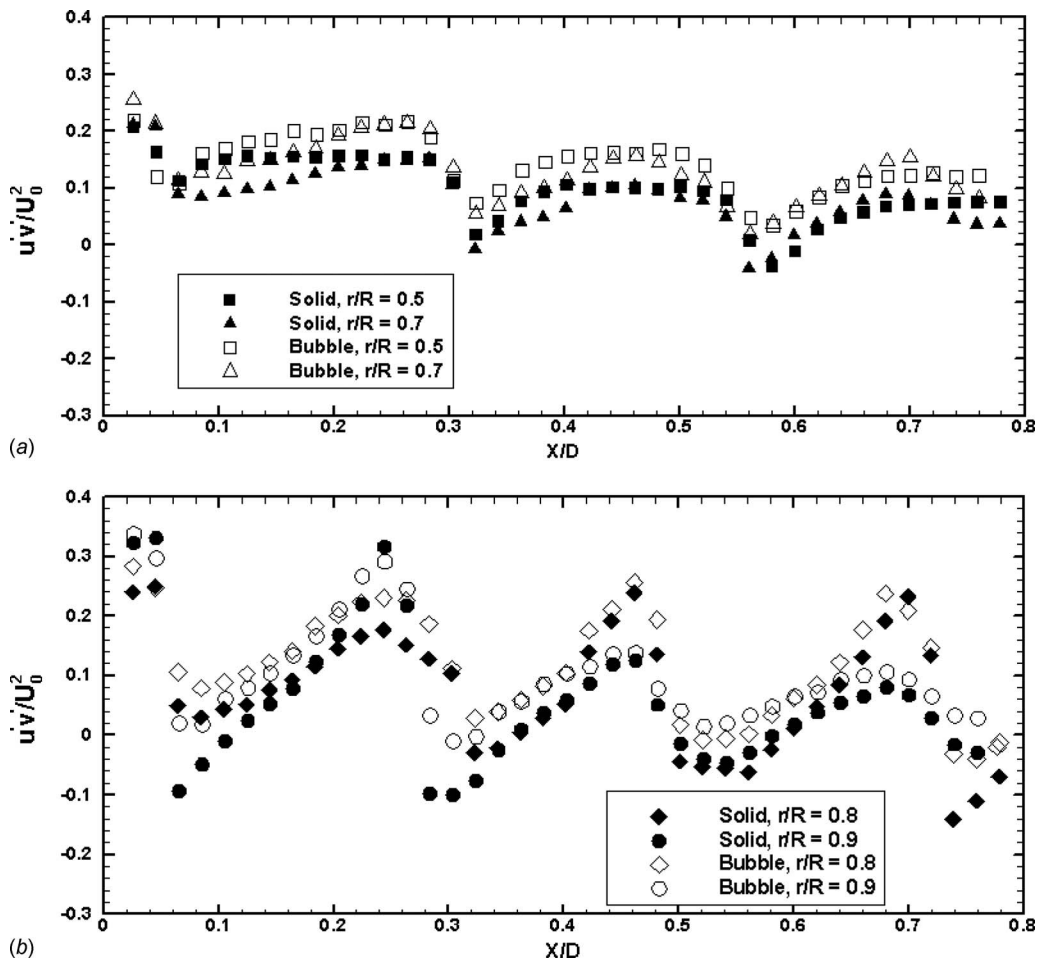


Fig. 14 The comparison of the Reynolds shear stress profiles at several radial locations

unity in a flow, especially rotating motion like vortex (see Ref. [15]). As the Weber number of bubbles was about 1.04 near a tip vortex core in the present study, the deformability of bubbles might be affecting the Reynolds shear stress around it.

The contour plots extracted from the ensemble-averaged velocity fields showed good trace ability from the viewpoint of locations of wake sheet and tip vortices. However, there are some discrepancies between the two results. For example, the vorticity values are different near the trailing vorticity and the tip vortices owing to the slip velocity variation. Additionally, an in-depth investigation of the bubbles as cavitation nuclei is called for because they might strengthen the cavitation or affect the cavitation pattern itself on the body surfaces. It would also be necessary to study the influences of error owing to the variation in bubble size in a high velocity gradient flow in the future though they could not be revealed in the present study because of the limitation of experimental environments.

4 Conclusions

The trace ability of the bubbles was investigated by using a two-frame PIV technique at high Reynolds number over 10^6 in the midsize cavitation tunnel. The velocity fields in the longitudinal planes were obtained both in uniform flows and in high velocity gradient flows of the propeller wake.

In the case of the uniform flow of 0.2 atm tunnel pressure, the bubbles about 1 mm in size produced good trace ability. The bubbles showed rather good trace ability in the high velocity gradient flow as well. The bubbles followed the behaviors of the propeller wake very well in the slipstream region. However, as the flow closes to a tip vortex in a high velocity gradient region, the bubbles showed some discrepancies on the flow behaviors.

A comparison of velocity field data in both tracer cases revealed the reason for the different results. The large slip velocity and Re_S provided a difference especially in the high velocity gradient region. The slipstream region gives a range of $15 < Re_S < 75$; however, Re_S is about 1000 at a high velocity gradient region of a tip vortex. Fitted equations regarding the vorticity reduction rate would give some reference that is useful for the PIV measurements of high velocity gradient flow using bubble tracers. The highest vertical slip velocity $|V_S|$ appears at the center of the tip vortex core, and the high shear flow seems to cause the bubbles' deformability to reduce the Reynolds shear stress.

Acknowledgment

This research was sponsored by the Ministry of Knowledge Economy, Korea under the project code PNS132B and also supported by the basic research project at the MOERI/KORDI (PES128B). In addition, the authors would like to thank Professor Yuichi Murai (Hokkaido University) for his valuable comments and kind advices.

References

- [1] Brenn, G., Braeske, H., and Durst, F., 2002, "Investigation of the Unsteady Two Phase Flow With Small Bubbles in a Model Bubble Column Using Phase-Doppler Anemometry," *Chem. Eng. Sci.*, **57**, pp. 5143–5159.
- [2] Lane, G. L., Schwarz, M. P., and Evans, G. M., 2005, "Numerical Modeling of Gas-Liquid Flow in Stirred Tanks," *Chem. Eng. Sci.*, **60**, pp. 2203–2214.
- [3] Guet, S., Ooms, G., Oliemans, R. V. A., and Mudde, R. F., 2004, "Bubble Size Effect on Low Liquid Input Drift-Flux Parameters," *Chem. Eng. Sci.*, **59**, pp. 3315–3329.
- [4] Lindken, R., and Merzkirch, W., 2002, "A Novel PIV Technique for Measurements in Multiphase Flows and Its Application to Two-Phase Bubbly Flows," *Exp. Fluids*, **33**, pp. 814–825.
- [5] Jansen, P. C. M., 1986, "Laboratory Observation of the Kinematics in the Aerated Region of Breaking Waves," *Coastal Eng.*, **9**, pp. 453–477.
- [6] Govender, K., Mocke, G. P., and Alport, M. J., 2002, "Video-Imaged Surf Zone Wave and Roller Structures and Flow Fields," *J. Geophys. Res.*, **107**, p. 3072.
- [7] Ryu, Y., Chang, K. A., and Lim, H. J., 2005, "Use of Bubble Image Velocimetry for Measurement of Plunging Wave Impinging on Structure and Associated Greenwater," *Meas. Sci. Technol.*, **16**, pp. 1945–1953.
- [8] Paik, B. G., Kim, K. Y., Ahn, J. W., and Kim, K. S., 2008, "Velocity Field Measurements Using Bubble Tracers in a Cavitation Tunnel," *Proceedings of the 18th International Offshore and Polar Engineering Conference*, Vancouver, BC, Canada, Jul. 6–11, pp. 198–203.
- [9] Raffel, M., Willert, C., and Kompenhans, J., 1998, *Particle Image Velocimetry*, Springer, New York.
- [10] Murai, Y., Oishi, Y., Takeda, Y., and Yamamoto, F., 2006, "Turbulent Shear Stress Profiles in a Bubbly Channel Flow Assessed by Particle Tracking Velocimetry," *Exp. Fluids*, **41**, pp. 343–352.
- [11] Clift, R., Grace, J. R., and Weber, M. E., 1978, *Bubbles, Drops and Particles*, Academic, New York.
- [12] Auton, T. R., 1984, "The Dynamics of Bubbles, Drops and Particles in Motion in Liquids," Ph.D. thesis, University of Cambridge, Cambridge, UK.
- [13] Kitagawa, A., Hishida, K., and Kodama, Y., 2005, "Flow Structure of Microbubble-Laden Turbulent Channel Flow Measured by PIV Combined With the Shadow Image Technique," *Exp. Fluids*, **38**, pp. 466–475.
- [14] Moriguchi, Y., and Kato, H., 2002, "Influence of Microbubble Diameter and Distribution on Frictional Resistance Reduction," *J. Mar. Sci. Technol.*, **7**, pp. 79–85.
- [15] Risso, F., and Fabre, J., 1998, "Oscillations and Breakup of a Bubble Immersed in a Turbulent Field," *J. Fluid Mech.*, **372**, pp. 323–355.

Yoshiki Yoshida¹

Kakuda Space Center,
Japan Aerospace Exploration Agency,
Koganezawa 1, Kimigaya,
Kakuda, Miyagi 981-1525, Japan
e-mail: yoshida.yoshiki@jaxa.jp

Yoshifumi Sasao

Institute of Fluid Science,
Tohoku University,
Katahira 2-1-1, Aoba,
Sendai, Miyagi 980-8577, Japan

Mitsuo Watanabe

Tomoyuki Hashimoto

Kakuda Space Center,
Japan Aerospace Exploration Agency,
Koganezawa 1, Kimigaya,
Kakuda, Miyagi 981-1525, Japan

Yuka Iga

Toshiaki Ikohagi

Institute of Fluid Science,
Tohoku University,
Katahira 2-1-1, Aoba,
Sendai, Miyagi 980-8577, Japan

Thermodynamic Effect on Rotating Cavitation in an Inducer

Cavitation in cryogenic fluids has a thermodynamic effect because of the thermal imbalance around the cavity. It improves cavitation performances in turbomachines due to the delay of cavity growth. The relationship between the thermodynamic effect and cavitation instabilities, however, is still unknown. To investigate the influence of the thermodynamic effect on rotating cavitation appeared in the turbopump inducer, we conducted experiments in which liquid nitrogen was set at different temperatures (74 K, 78 K, and 83 K) with a focus on the cavity length. At higher cavitation numbers, supersynchronous rotating cavitation occurred at the critical cavity length of $Lc/h \cong 0.5$ with a weak thermodynamic effect in terms of the fluctuation of cavity length. In contrast, synchronous rotating cavitation occurred at the critical cavity length of $Lc/h \cong 0.9-1.0$ at lower cavitation numbers. The critical cavitation number shifted to a lower level due to the suppression of cavity growth by the thermodynamic effect, which appeared significantly with rising liquid temperature. The unevenness of cavity length under synchronous rotating cavitation was decreased by the thermodynamic effect. Furthermore, we confirmed that the fluid force acting on the inducer notably increased under conditions of rotating cavitation, but that the amplitude of the shaft vibration depended on the degree of the unevenness of the cavity length through the thermodynamic effect. [DOI: 10.1115/1.3192135]

Keywords: thermodynamic effect, cavitating inducer, rotating cavitation, cavity length, fluid force

1 Introduction

In rocket engines, the turbopump inducer, which is actually a high-precision high-speed sophisticated rotating impeller, is one of the key components of a liquid propellant rocket engine. The inducer is installed upstream of the main impeller in the turbopump to achieve high suction performance. Rotating cavitation in inducers is known as one type of cavitation instability, in which an uneven cavity pattern propagates in the same direction as the rotor with a propagating speed ratio of 1.0–1.2. Unfortunately, this rotating cavitation generates shaft vibration arising from to the increase of the unsteady lateral load on the inducer [1,2].

On the other hand, the thermodynamic effect on cavitation is a favorable phenomenon in cryogenic fluids. It suppresses the growth of a cavity, since thermal imbalance appears around the cavity due to heat transfer for evaporation. Because of this heat transfer, saturated vapor pressure in the cavity decreases and the degree of cavity growth becomes smaller than that in water without the thermodynamic effect. Therefore, cavitation performance of the inducer in cryogenic fluids is improved.

However, the relationship between the thermodynamic effect and cavitation instabilities is poorly understood. To clarify this relationship, studies using refrigerant R114, hot water, and liquid nitrogen have been conducted by Franc et al. [3], Cervone et al.

[4], and Yoshida et al. [5], respectively. In the present study, we investigated the relationship between the thermodynamic effect and supersynchronous/synchronous rotating cavitation with a focus on the cavity length as an indication of cavitation. We conducted experiments with liquid nitrogen set at different temperatures (74 K, 78 K, and 83 K) in order to confirm the dependence of the thermodynamic effect on the temperature.

2 Experimental Facility and Apparatus

2.1 Experimental Facility. Experiments were conducted in the Cryogenic Inducer Test Facility (CITF) at Kakuda Space Center (KSC) of Japan Aerospace Exploration Agency (JAXA). Figure 1 shows a schematic of the test facility. This facility has two tanks, one upstream (run-tank) and one downstream (catch-tank), and the temperature of the liquid nitrogen can be varied by regulating the pressure in the run-tank. Thanks to this capability, liquid nitrogen set at different temperatures (74 K, 78 K, and 83 K) can be used as working fluid. Figure 2 shows the schematic diagram of the test inducer showing the installed pressure sensors and shaft displacement sensor. The inducer used in the present experiment has the same dimensions and geometric configurations as that in the previous experiment [5]. It has three blades with sweep cut-back at the leading edge, its solidity is about 2.1 at the tip. The inducer is driven by an electric motor at a rotation speed of 18,300 rpm, equal to that of an actual turbopump, and the flow rate is set at $Q/Q_d=1.06$ (Q_d : designed flow rate). In the previous study [5], test flow rate was set at $Q/Q_d=1.00$. Only synchronous rotating cavitation was observed, but supersynchronous rotating cavitation (super-SRC) did not appear at the flow rate of $Q/Q_d=1.00$. In addition, thermodynamic effect had scarcely any influence on the unevenness of the cavity length under the synchronous rotating

¹Contributing author.

Contributed by the Fluids Engineering Division of ASME for publication in the JOURNAL OF FLUIDS ENGINEERING. Manuscript received April 14, 2008; final manuscript received June 21, 2009; published online August 18, 2009. Review conducted by Joseph Katz. Paper presented at the 2007 ASME Fluids Engineering Division Summer Meeting and Exhibition (FEDSM2007), July 30–August 2, 2007, San Diego, CA.

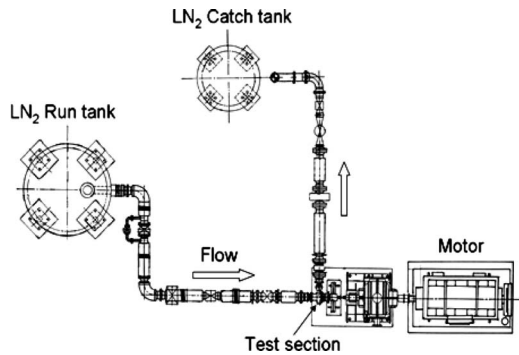


Fig. 1 Cryogenic Inducer Test Facility of JAXA

cavitation. To the contrary, in the present experiments at the flow rate of $Q/Q_d=1.06$, both supersynchronous and synchronous rotating cavitation were observed. And the thermodynamic effect affects the unevenness of the cavity length under the synchronous rotating cavitation. It could even be said that the flow rate of inducer has considerable influence concerning the occurrence of supersynchronous/synchronous rotating cavitation and thermodynamic effect on them.

2.2 Experimental Apparatus. To estimate the cavitating state of the inducer indirectly, eight pressure sensors (Pos. 1–8) are installed along the blade from the leading edge to the trailing edge on the casing, as shown in Figs. 2 and 3. The sensor is a charge mode pressure sensor (PCB Piezotronics Inc., model WH113A) with high resistance to shock (20,000 g), a wide range of the temperature for cryogenic fluid (33–477 K), linearity (<1%FS), and high resonance frequency (250 kHz). Uncertainty in ω/Ω (speed ratio of rotating cavitation) measured by the pressure sensors is 0.005. The pressure sensors detect the cavitation near the blade tip, i.e., tip leakage vortex cavitation. However, sensors are unable to detect the cavitation in the backflow upstream of the inducer, i.e., backflow vortex cavitation.

The methodology to observe the cavitating state in the inducer

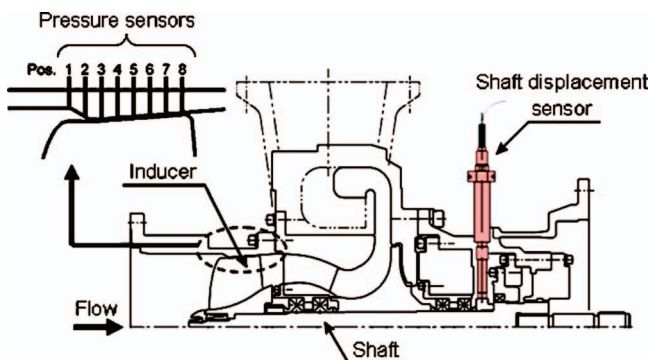


Fig. 2 Schematic diagram of the test inducer showing the installed pressure sensors and shaft displacement sensor

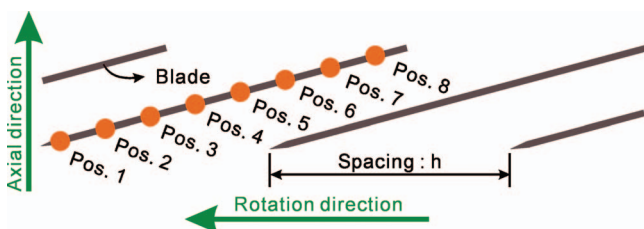


Fig. 3 Development view of the inducer showing location of pressure sensors along the inducer blade

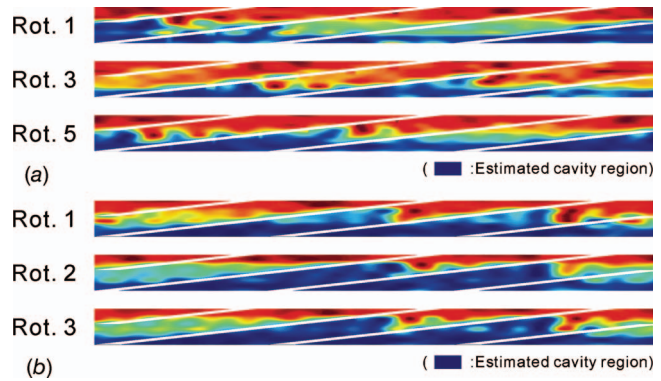


Fig. 4 (a) Estimated cavity region under supersynchronous rotating cavitation and (b) estimated cavity region under synchronous rotating cavitation

was basically the same as that mentioned in the previous experiment [5]. When cavitation develops on the suction side of the blade at the tip, the pressure sensor shows a particular wave form in which a flat region appears at the bottom. This region extends from the suction side to the pressure side within the interblade the cavitation number decreases. The pressure of this region can be considered to be the vapor pressure due to the cavitation. Thus, we judged this domain as the cavity region.

Figure 4 is drawn by the rearrangement of the wave forms of all the sensors. The dark area in these figures shows “estimated cavity region.” Using these figures at each cavitation number, the cavity length as an indication of cavitation can be observed by this indirect visualization. In a previous work [6], results of this indirect visualization using the pressure sensors agreed with the direct optical observation results in water. Uncertainty in Lc/h (nondimensional cavitation length) measured by these pressure sensors is 0.03.

The shaft displacement sensor is installed at the backend of the rotor, as shown in Fig. 2. The sensor for shaft vibration should be installed near the inducer. However, there is no space around the inducer due to the limitation of the pump structure

Rotating cavitation can be divided into two patterns based on the aspect of cavity fluctuations. Figure 4(a) indicates the cavity behavior for typical supersynchronous rotating cavitation, and Fig. 4(b) indicates typical synchronous rotating cavitation. Unevenness of the cavity length is observed in both figures. The longer/shorter cavity propagates from blade to blade on the sequence of rotation under supersynchronous rotating cavitation in Fig. 4(a). In contrast, the cavity length on each blade is uneven but not unsteady under synchronous rotating cavitation in Fig. 4(b). It is steady with no propagation during the sequence of rotation.

3 Rotating Cavitation and Thermodynamic Effect

3.1 Rotating Cavitation. As we have already mentioned, rotating cavitation is cavitation instability and has two patterns. Figure 5 shows examples of the cavitation state under conditions of supersynchronous (Fig. 5(a)) and synchronous rotating cavitation (Fig. 5(b)) by direct optical observation in water experiments [7]. In Fig. 5(a), the unevenness of cavity length (medium, short and long) on each blade (blades 1–3) can be clearly observed. However, supersynchronous rotating cavitation is an unsteady phenomenon in which the asymmetric pattern of the cavity length propagates from blade to blade at a speed 1.1–1.2 times higher than that of inducer rotation. In contrast, the unevenness of cavity length (long, long and short) on each blade (blades 1–3) can be also observed in Fig. 5(b). Though the cavitation state in the inducer is surely “asymmetric” and “uneven,” it does not change from blade to blade in rotation. From that viewpoint, synchronous

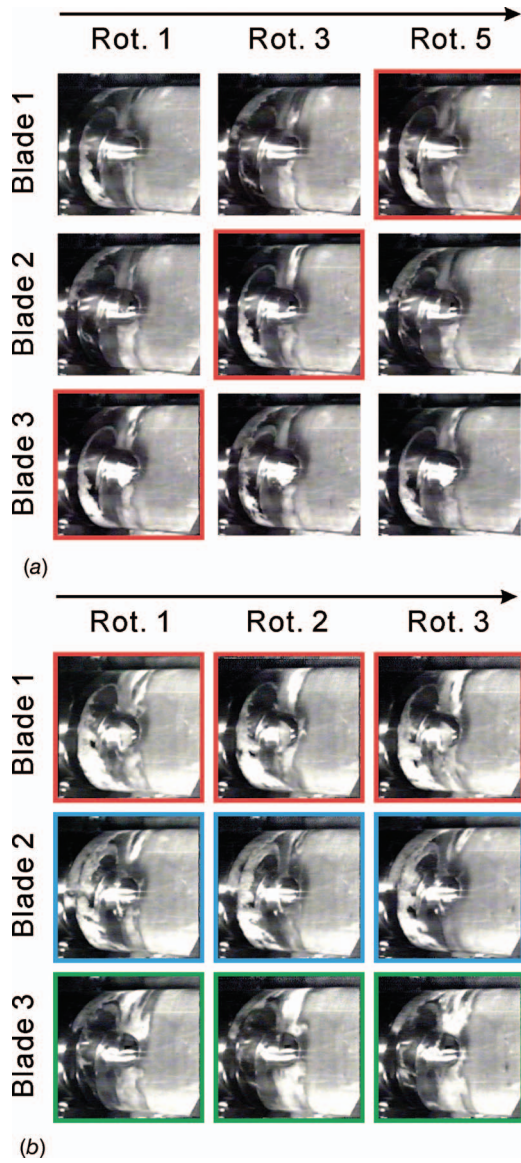


Fig. 5 (a) Photographs of supersynchronous rotating cavitation in water from Ref. [7]. (b) Photographs of synchronous rotating cavitation in water from Ref. [7].

rotating cavitation can be defined as a steady “anomalous” phenomenon. These direct optical observations in water agree with the indirect observations in liquid nitrogen shown in Figs. 4(a) and 4(b).

3.2 Thermodynamic Effect. The introduction of the temperature depression into the simple Rayleigh–Plesset equation for a spherical cavity yields [3]

$$\left[R\ddot{R} + \frac{3}{2}\dot{R}^2 \right] + \Sigma^* \dot{R} \sqrt{t} = \frac{p_v(T_\infty) - p}{\rho_l} \quad (1)$$

The third term on the left is the “thermal term” caused by the thermodynamic effect. Thermodynamic function Σ , which depends only on temperature T_∞ , was originally introduced by Brennen [8]. The dimension of thermodynamic function Σ is in $\text{m/s}^{3/2}$

$$\Sigma(T_\infty) = \frac{(\rho_v L)^2}{\rho_l^2 C_{pl} T_\infty \sqrt{\alpha_l}} \quad (2)$$

Equation (1) is made nondimensional using a chord C , inducer tip speed U , pressure coefficient C_p and cavitation number σ . The following equation is obtained (Franc et al. [3]):

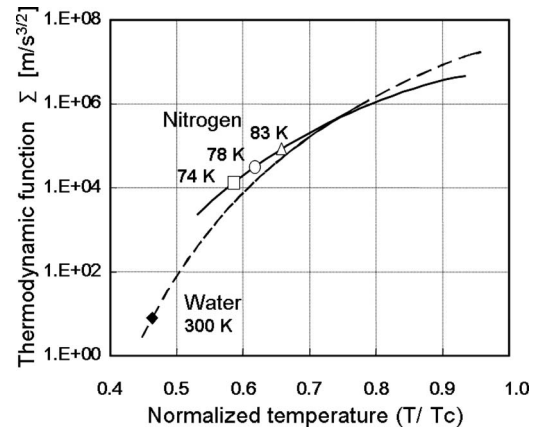


Fig. 6 Variation in the thermodynamic function $\Sigma(T)$ of nitrogen and water

$$\left[\bar{R}\ddot{R} + \frac{3}{2}\dot{\bar{R}}^2 \right] + \Sigma^* \dot{\bar{R}} \sqrt{\bar{t}} = -\frac{C_p + \sigma}{2} \quad (3)$$

where

$$\Sigma^* = \Sigma \sqrt{\frac{C}{U^3}} \quad (4)$$

When the nondimensional thermodynamic parameter $\Sigma^* = \Sigma(C/U^3)^{1/2}$ is larger, the thermodynamic effect becomes stronger and the cavity growth is suppressed. Watanabe et al. [9] analyzed the influence of nondimensional thermodynamic parameter Σ^* on cavity growth and cavitation instabilities in 2D-inducers. The trend of their analyzed results agreed well with 3D-inducer results reported by Franc et al. [3].

Figure 6 shows variations in thermodynamic function Σ for nitrogen and water against the normalized temperature T/T_c , where T_c is the temperature of the critical point. In addition, points for experimental conditions (74 K (\square), 78 K (\circ), and 83 K (\triangle)) and water at room temperature (300 K (\blacklozenge)) are also plotted in this figure. Comparisons of nondimensional thermodynamic parameter $\Sigma^* = \Sigma(C/U^3)^{1/2}$ of the experimental conditions are presented in Table 1. The range of Σ^* is 4.3 (at 74 K)–26.6 (at 83 K). Thus, the thermodynamic effect is expected to be larger in case of rising temperature at 83 K than that of falling temperature at 74 K.

4 Experimental Results

4.1 Head Coefficient and Cavity Length. We defined the length from the leading edge to the trailing edge of the estimated cavity region as the cavity length (L_c). In other words, the length of the dark region along the blade in Fig. 4 is the cavity length.

The diamond-shaped symbols (\diamond) in Fig. 7 show variations in nondimensional cavity length (L_c/h) normalized by blade spacing (h) for each channel of the inducer (i.e., three channels for the three-bladed inducer). The circles (\circ) in Fig. 7 show variations in the inducer head (ψ/ψ_0) normalized by the reference head coefficient (ψ_0). This figure contains results of two typical temperature conditions (74 K and 83 K). In addition, the triangle-shaped

Table 1 Comparison of the thermodynamic parameter Σ^*

	Temperature (K)	Rotation N (rpm)	Σ ($\text{m/s}^{3/2}$)	$\Sigma^* = \Sigma(C/U^3)^{1/2}$
Nitrogen	74	18,300	$1.4 \times 10^{+04}$	4.3
	78	18,300	$3.3 \times 10^{+04}$	10.2
	83	18,300	$8.6 \times 10^{+04}$	26.6

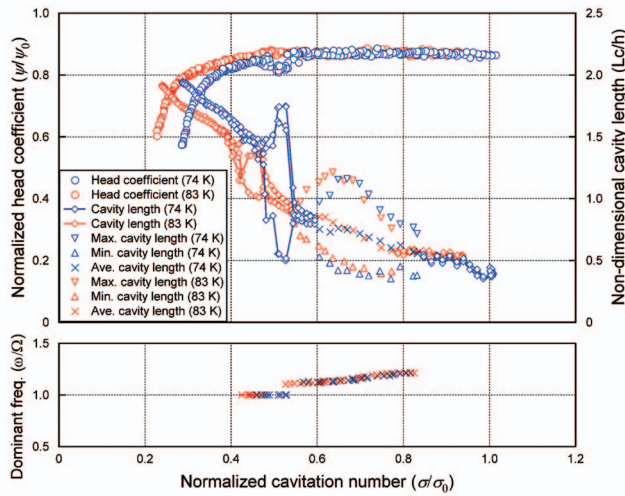


Fig. 7 Cavitation performances and cavity length of each channel (top), and variations in dominant frequency of shaft vibration (bottom) (uncertainty in $\psi/\psi_0=0.01$, $\sigma/\sigma_0=0.02$, $Lc/h=0.03$, and $\omega/\Omega=0.005$)

symbols (∇ , Δ) in Fig. 7 show the amplitude of the fluctuating cavity length (peak to peak) under the supersynchronous rotating cavitation, and cross-shaped symbols (\times) show the time-averaged cavity length.

As the cavitation number decreases, supersynchronous rotating cavitation occurs at a cavity length of about $Lc/h \cong 0.5$. Cavity length fluctuates on three blades with a certain phase lag. As a result, it can be seen that unevenness of cavity length propagates in the same direction as the rotor with a speed ratio of $\omega/\Omega = 1.1-1.2$ analyzed by fast Fourier transform (FFT), as shown at the bottom of Fig. 7. This aspect is similar to the visualization in the photographs in Fig. 5(a). Meanwhile, the averaged cavity length increases with decreasing cavitation number. The occurrence range of supersynchronous rotating cavitation at 83 K shifts

only a few cavitation numbers lower than that at 74 K due to the thermodynamic effect. The amplitude of cavity fluctuation and propagation speed ratio of the condition at 83 K are almost the same as those at 74 K. Watanabe et al. [9] analyzed the rotating cavitation using the singularity method with Kato's heat transfer model [10]. They reported that the propagation speed ratio of supersynchronous rotating cavitation becomes smaller due to the thermodynamic effect. On the other hand, Zoladz [11] observed from the comparison between the experimental results in liquid oxygen and in water that the thermodynamic effect affects the normalized amplitude of pressure fluctuations caused by rotating cavitation (which becomes larger in liquid oxygen than in water), but it does not affect the frequency of rotational speed of the cavity. Unfortunately, a full explanation of the difference between the present results and Watanabe's analytical results/Zoladz's experimental results has not been obtained in the present experiments. In order to explain, an extension of the experiment is underway in liquid nitrogen at several temperatures and flow rates.

In contrast, synchronous rotating cavitations occur at cavity length of $Lc/h \cong 0.9$ at 74 K and $Lc/h \cong 1.0$ at 83 K, and disappears at a cavity length of $Lc/h \cong 1.5$ in both temperature conditions. Under synchronous rotating cavitation, unevenness of the cavity length is manifested as three lengths (short, medium (or long), and long), similar to the photographs in Fig. 5(b). The degree of unevenness of the condition at 83 K is considerably less than that at 74 K, and beginning/closing cavitation numbers of synchronous rotating cavitation at 83 K shift to a lower point than those at 74 K due to the thermodynamic effect.

In addition, the circles (\circ) in Fig. 7 show the variations in the inducer head. Within the range of the occurrence of supersynchronous rotating cavitation, the inducer head has no effect on this cavitation instability. However, the inducer head temporarily decreases within the range of the occurrence of synchronous rotating cavitation only at the condition of 74 K. After breaking away from the synchronous rotating cavitation, cavity lengths become completely equal near $Lc/h=1.5$. Hereupon, inducer head drop begins to gradually occur for both temperature conditions, and the head drop is nearly equal at the same cavity length. This means that the inducer head is strongly dependent only on the cavity length. Fur-

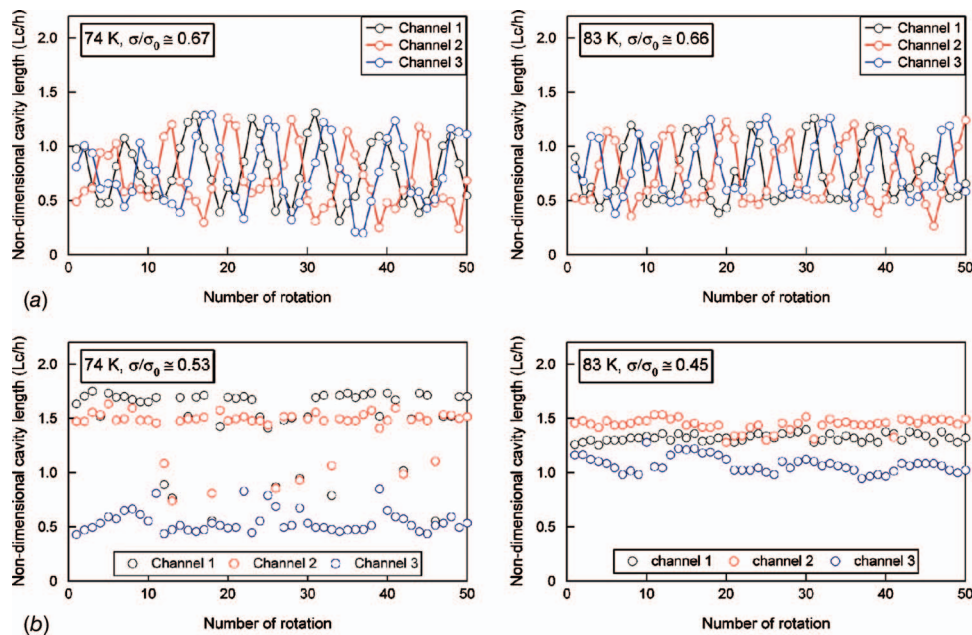


Fig. 8 (a) Fluctuations of cavity lengths for each channel in the case of supersynchronous rotating cavitation (left: 74 K, right: 83 K) (uncertainty in $Lc/h=0.03$) and (b) fluctuations of cavity lengths for each channel in the case of synchronous rotating cavitation (left: 74 K, right: 83 K) (uncertainty in $Lc/h=0.03$)

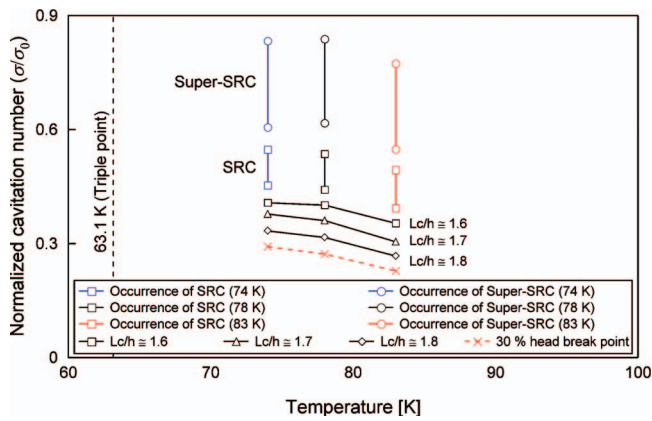


Fig. 9 Influence of temperature on cavity length and the region where the rotating cavitations occurs at 74 K, 78 K, and 83 K (uncertainty in $\sigma/\sigma_0=0.02$ and $Lc/h=0.03$)

thermore, as mentioned above, the onset of cavitation instability is also governed only by the cavity length through the liquid temperature, namely, the degree of the thermodynamic effect.

4.2 Behavior of Supersynchronous/Synchronous Rotating Cavitation. Figure 8 shows the fluctuations of the cavity length in each channel during supersynchronous (Fig. 8(a))/synchronous (Fig. 8(b)) rotating cavitation against the inducer rotation. For supersynchronous rotating cavitation in Fig. 8(a), the cavity length fluctuates within $Lc/h=0.4-1.2$ with $2\pi/3$ phase difference. The cavity propagates from blade 3 to blade 2, and finally to blade 1. After about eight rotations, the uneven pattern of cavity returns to the same situation. This means that the cavity propagates forward with a propagation speed ratio $\omega/\Omega=1.13$. This result agrees with the FFT analysis of the measurement of pressure fluctuations in Fig. 7. Comparing the conditions of 74 K and 83 K, not much difference between the behavior of the cavity fluctuation and that of the oscillating frequency is observed. From these results, it is inferred that the thermodynamic effect does not affect the behavior of cavity fluctuation during supersynchronous rotating cavitation at the higher cavitation numbers.

On the other hand, Fig. 8(b) shows that the cavity length for each channel exhibits breaking symmetry, such as supersynchronous rotating cavitation, but that unevenness is manifested against the inducer rotation during synchronous rotating cavitation. The cavity length of each channel is relatively steady. However, the differences in the unevenness of the cavity lengths (short, medium (or long), and long) are found between liquid temperatures of 74 K and 83 K. Although the unevenness of cavity length at 74 K is large, i.e., $Lc/h=0.5, 1.5,$ and 1.7 , that at 83 K is considerably small, i.e., $Lc/h=1.1, 1.3,$ and 1.5 . Thus, it is considered that the behavior of synchronous rotating cavitation at lower cavitation numbers is greatly affected by the thermodynamic effect. Although the averaged cavity length under the supersynchronous rotating cavitation is shorter than the blade spacing, i.e., $Lc/h < 1.0$, and the longer cavity lengths under the synchronous rotating cavitation are longer than the blade spacing, i.e., $Lc/h > 1.0$. On the other hand, we have observed in the previous work with another inducer [6] that the temperature depression increases rapidly when the cavity length, Lc/h , becomes longer than 1.1. When we consider a thermal time for heat transfer, a transit time, $\tau \equiv Lc/U$, is appropriate for a simple parameter, which indicates the interval from the bubble inception to the collapse. As the cavity length in synchronous rotating cavitation is longer than that in supersynchronous rotating cavitation, the transit time ($\tau=Lc/U$) of synchronous rotating cavitation is considerably longer than that of supersynchronous rotating cavitation. Thus, it seems that the amplitude to thermodynamic effect depends on the thermal time

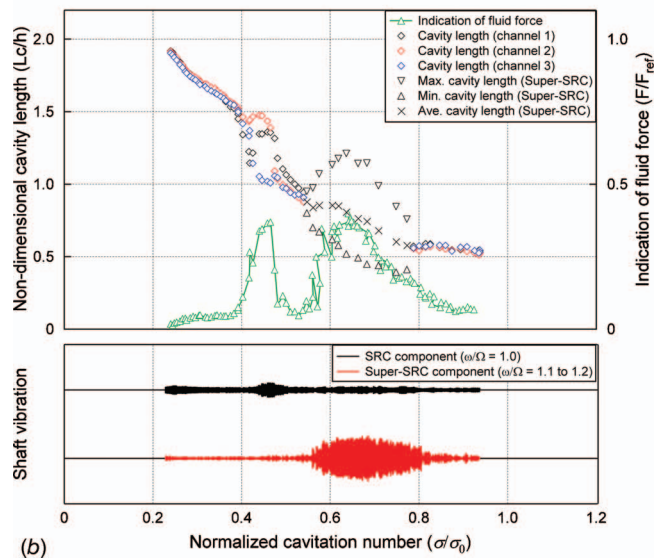
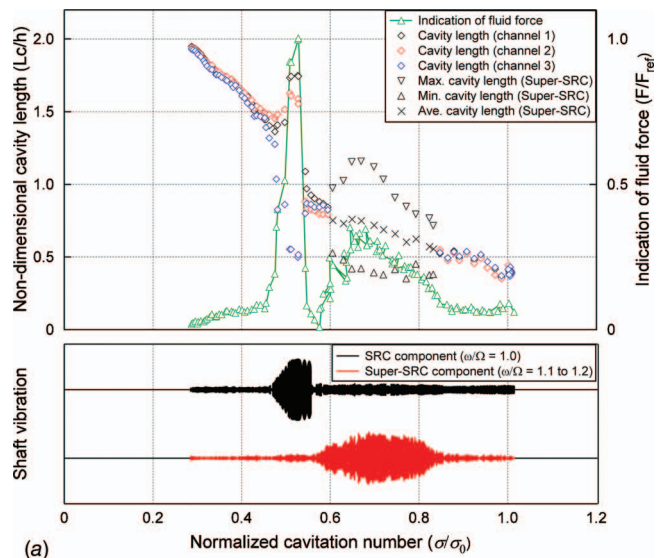


Fig. 10 (a) Variations in cavity length (top), fluid force (top), and shaft vibration (bottom) for 74 K (uncertainty in $\sigma/\sigma_0=0.02$, $Lc/h=0.03$, and $F/F_{ref}=0.03$) and (b) variations in cavity length (top), fluid force (top), and shaft vibration (bottom) for 83 K (uncertainty in $\sigma/\sigma_0=0.02$, $Lc/h=0.03$, and $F/F_{ref}=0.03$)

becomes larger in synchronous rotating cavitation than that in supersynchronous rotating cavitation. It might be the reason why the behavior of synchronous rotating cavitation at lower cavitation numbers is greatly affected by the thermodynamic effect.

It is remarked that thermodynamic effect on cavity unevenness under synchronous rotating cavitation was not prominent in the previous experiments at flow rate $Q/Q_d=1.00$ [5], although that is considerable large in the present experiments at flow rate $Q/Q_d=1.06$. When the flow rate decreases in the inducer, the tip leakage vortex cavitation increases due to the enlargement of the incidence angle. Also, vortex cavitation in the backflow upstream of the inducer becomes stronger due to the increase in the circulation at the inducer inlet [12]. These two vortex cavitations interact complexly on each other, and turbulence becomes stronger. Thus, it could be said that the change in these cavitation aspects through the decrease in flow rate has the sever influence on the degree of thermodynamic effect.

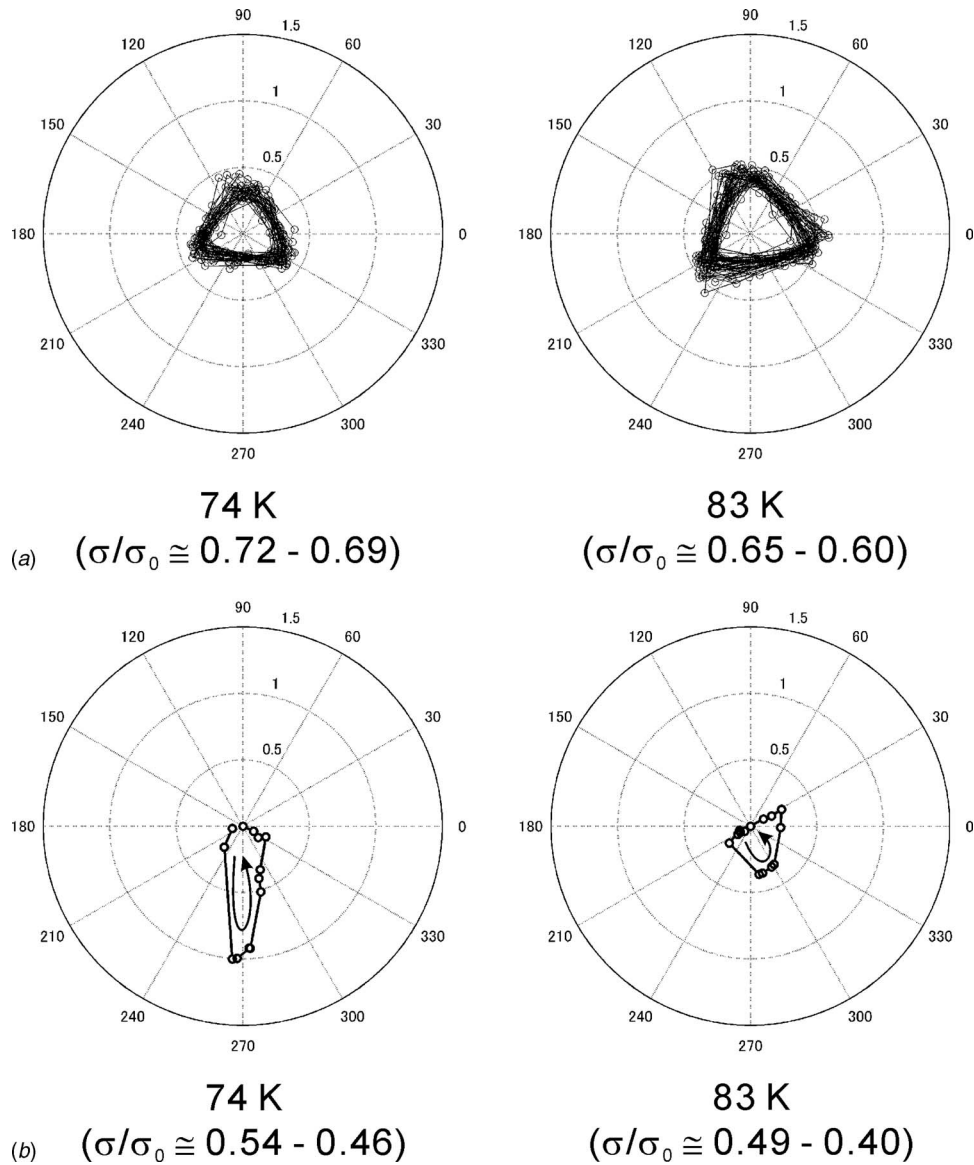


Fig. 11 (a) Instant vector orbits of fluid force under typical supersynchronous rotating cavitation at 74 K and 83 K (uncertainty in $F/F_{ref}=0.03$) and (b) time-averaged vector orbits of fluid force during synchronous rotating cavitation at 74 K and 83 K (uncertainty in $F/F_{ref}=0.03$)

5 Discussions

5.1 Liquid Temperature and Cavity Length. Figure 9 shows the relationships between the temperature of liquid nitrogen (74 K, 78 K, and 83 K) and the region of cavitation number where rotating cavitation occurs, and the cavitation number at a given cavity length. This figure indicates the dependence of cavitation number at the occurrence of the rotating cavitations (supersynchronous rotating cavitation and synchronous rotating cavitation) and at the given longer cavity length ($Lc/h=1.6, 1.7, 1.8$, and 30% head break) on the temperature. From this figure, it can be seen that the cavitation number at the onset of rotating cavitation and a given cavity length become smaller with the increase in the temperature of liquid nitrogen, since the thermodynamic effect is strengthened due to the increase in temperature. In addition, focusing on one cavity length, the difference of cavitation number for three temperatures tends to become smaller with falling temperature. It is considered that the temperature depression in the cavity (i.e., thermodynamic effect) decreases with decreasing ther-

modynamic function $\Sigma(T)$, and is restricted physically when it approaches the temperature (63.1 K) of triple point of nitrogen [6,13].

5.2 Fluid Force and Shaft Vibration. Figure 10 shows the variation in cavity length (Lc/h), indications of fluid force (F/F_{ref}) (top), and the component of the supersynchronous (super-SRC, $\omega/\Omega=1.1-1.2$)/synchronous (SRC, $\omega/\Omega=1.0$) shaft vibration (bottom) detected by the displacement sensors, for two temperatures 74 K (Fig. 10(a)) and 83 K (Fig. 10(b)). Fluid force was estimated by integrating the pressure distributions around the inducer casing. This estimated force is only an indication to evaluate the degree of fluid force acting on the inducer. The figure shows that the fluid force increases significantly during supersynchronous/synchronous rotating cavitation. Moreover, it can be found that the shaft vibrations are clearly amplified because of the action of the fluid force caused by supersynchronous/synchronous rotating cavitation. Thus, it has been considered that

the unbalanced fluid force caused by the rotating cavitation has a strong influence on the rotor dynamics in turbopumps [1,2,14].

Figure 11 presents the orbit of the fluid force vector under the typical supersynchronous rotating cavitations (Fig. 11(a)) and during the synchronous rotating cavitations (Fig. 11(b)) on the rotating coordinate. From this figure, the directions of instant force vectors under supersynchronous rotating cavitation are seen to change. The orbit of the force vector is exactly traced on an equilateral triangle due to the three blades. The degree of the equilateral triangle at 74 K (Fig. 11(a) left) is almost the same as that at 83 K (Fig. 11(b) right), and the component of the supersynchronous shaft vibration ($\omega/\Omega=1.1-1.2$) at 74 K (Fig. 10(a)) is also the same as that at 83 K (Fig. 10(b)). From these results, it can be concluded that there is no thermodynamic effect on the degree of supersynchronous shaft vibration, in which the averaged cavity length does not reach at the throat ($(Lc/h < 1.0)$).

In contrast, the orbit of the time-averaged force vector during synchronous rotating cavitation shows the increase in a certain direction. However, the fluid force at 83 K (Fig. 11(b) right) is less than that at 74 K (Fig. 11(b) left), and the component of the synchronous shaft vibration ($\omega/\Omega=1.0$) at 83 K (Fig. 10(b)) is also less than that at 74 K (Fig. 10(a)), respectively. Thus, it is considered that the thermodynamic effect on cavitation suppresses the synchronous shaft vibration through the decrease in the unevenness of the cavity length during the synchronous rotating cavitation. It could even be said that the thermodynamic effect on cavitation has not only a "thermal damping effect on the cavity growth," but also a "thermal damping effect on the shaft vibration" through the suppression of the cavitation instability at lower cavitation numbers, in which the cavity length extends over the throat ($Lc/h > 1.0$).

6 Conclusions

By experiments with liquid nitrogen set at different temperatures and considerations based on the cavity length as an indication of cavitation, the following points were clarified.

- (1) Rotating cavitation occurs at the same cavity length independent of temperature. The critical cavity length at the onset of supersynchronous rotating cavitation was $Lc/h \cong 0.5$, and that at the onset of synchronous rotating cavitation was $Lc/h \cong 0.9-1.0$ in the present inducer.
- (2) The thermodynamic effect suppresses the growth of cavity length. Growth of the cavity is distinctly suppressed with increasing liquid temperature.
- (3) Due to the above, the thermodynamic effect shifts the critical cavitation number of the rotating cavitations lower.
- (4) The differences in the behavior of the cavity fluctuation and oscillating frequency under supersynchronous rotating cavitation were not prominent at any of temperatures.
- (5) However, unevenness of the cavity length under synchronous rotating cavitation was greatly affected by the thermodynamic effect in the present experiments of flow rate $Q/Q_d=1.06$.
- (6) The favorable thermodynamic effect on cavitation instability becomes greater when the cavity length extends over the throat at lower cavitation numbers.
- (7) The fluid force acting on the inducer significantly increases under supersynchronous/synchronous rotating cavitation. The thermodynamic effect influences considerably the unevenness of the cavity length under synchronous rotating cavitation. Therefore, synchronous shaft vibration under synchronous rotating cavitation is much affected by the temperature of working fluid.

Acknowledgment

Authors would like to thank Mr. Yusuke Kazami of Tohoku University for his great help with data processing.

Nomenclature

C	= chord of inducer
C_p	= pressure coefficient
C_{pl}	= specific heat of liquid
F	= fluid force
F_{ref}	= reference value of fluid force
h	= blade spacing
L	= latent heat
Lc	= cavity length
p	= pressure
p_v	= vapor pressure
R	= radius of bubble
T_c	= critical temperature
T_∞	= ambient temperature
t	= time
U	= tip velocity of inducer
α_l	= thermal diffusivity of liquid
ρ_v	= vapor density
ρ_l	= liquid density
Σ	= thermodynamic function defined by Eq. (2)
Σ^*	= nondimensional thermodynamic parameter by Eq. (4)
σ	= cavitation number
σ_0	= reference value of cavitation number (upper limit of cavitation number in the present experiment)
τ	= transit time ($=Lc/U$)
ψ	= head coefficient
ψ_0	= reference value of head coefficient
Ω	= angular velocity of rotor
ω	= angular velocity of rotating cavitation

References

- [1] Rosenmann, W., 1965, "Experimental Investigations of Hydrodynamically Induced Shaft Forces With a Three-Bladed Inducer," *Proceedings of the Symposium on Cavitation in Fluid Machinery, Winter Annual Meeting*, ASME, New York, pp. 172-195.
- [2] Kamijo, K., Yoshida, M., and Tsujimoto, Y., 1993, "Hydraulic and Mechanical Performance of LE-7 LOX Pump Inducer," *AIAA J.*, **9**(6), pp. 819-826.
- [3] Franc, J. P., Rebattet, C., and Coulon, A., 2004, "An Experimental Investigation of Thermal Effects in a Cavitating Inducer," *ASME J. Fluids Eng.*, **126**, pp. 716-723.
- [4] Cervone, A., Testa, R., and d'Agostino, L., 2005, "Thermal Effects on Cavitation Instabilities in Helical Inducers," *AIAA J.*, **21**(5), pp. 893-899.
- [5] Yoshida, Y., Sasao, Y., Okita, K., Hasegawa, S., Shimagaki, M., and Ikohagi, T., 2007, "Influence of Thermodynamic Effect on Synchronous Rotating Cavitation," *ASME J. Fluids Eng.*, **129**(7), pp. 871-876.
- [6] Yoshida, Y., Kikuta, K., Hasegawa, S., Shimagaki, M., and Tokumasu, T., 2007, "Thermodynamic Effect on a Cavitating Inducer in Liquid Nitrogen," *ASME J. Fluids Eng.*, **129**(3), pp. 273-278.
- [7] Maekawa, Y., 1996, "Experimental Study of Unsteady Cavitation on an Inducer," MS thesis, Osaka University, Osaka (in Japanese).
- [8] Brennen, C. E., 1973, "The Dynamic Behavior and Compliance of a Stream of Cavitating Bubbles," *ASME J. Fluids Eng.*, **95**, pp. 533-541.
- [9] Watanabe, S., Hidaka, T., Horiguchi, H., Furukawa, A., and Tsujimoto, Y., 2007, "Analysis of Thermodynamic Effects on Cavitation Instabilities," *ASME J. Fluids Eng.*, **129**(9), pp. 1123-1130.
- [10] Kato, H., 1984, "Thermodynamic Effect on Incipient and Development of Sheet Cavitation," *Proceedings of International Symposium on Cavitation Inception* New Orleans, LA, Dec. 9-14, ASME, New York, Vol. 16, pp. 127-136.
- [11] Zoladz, T., 2000, "Observations on Rotating Cavitation and Cavitation Surge From the Development of the Fastrac Engine Turbopump," *Proceedings of the 36th AIAA/ASME/SAE/ASEE Joint Propulsion Conference*, Huntsville, AL, Jul. 17-19, Paper No. AIAA200-3403.
- [12] Kimura, T., Yoshida, Y., Hashimoto, T., and Shimagaki, M., 2008, "Numerical Simulation for Vortex Structure in a Turbopump Inducer: Close Relationship With Appearance of Cavitation Instabilities," *ASME J. Fluids Eng.*, **130**, p. 051104.
- [13] Watanabe, S., Furukawa, A., and Yoshida, Y., 2008, "Theoretical Analysis of Thermodynamic Effects on Cavitation in Cryogenic Inducer Using Singularity Method," *Proceedings of the 12th International Symposium on Transport Phenomena and Dynamics of Rotating Machinery*, Honolulu, HI, Feb. 17-22, Paper No. ISROMAC12-2008-20251.
- [14] Kobayashi, S., 2006, "Effects of Shaft Vibration on Occurrence of Asymmetric Cavitation in Inducer," *JSM Int. J.*, Ser. B, **49**(4), pp. 1220-1225.

Transition of Bubbly Flow in Vertical Tubes: New Criteria Through CFD Simulation

A. K. Das

e-mail: arup@mech.iitkgp.ernet.in

P. K. Das¹

e-mail: pkd@mech.iitkgp.ernet.in

Department of Mechanical Engineering,
IIT Kharagpur,
721302, India

J. R. Thome

LCTM,
EPFL,
Lausanne CH-1015, Switzerland
e-mail: john.thome@epfl.ch

The two fluid model is used to simulate upward gas-liquid bubbly flow through a vertical conduit. Coalescence and breakup of bubbles have been accounted for by embedding the population balance technique in the two fluid model. The simulation enables one to track the axial development of the voidage pattern and the distribution of the bubbles. Thereby it has been possible to propose a new criterion for the transition from bubbly to slug flow regime. The transition criteria depend on (i) the breakage and coalescence frequency, (ii) the bubble volume count below and above the bubble size introduced at the inlet, and (iii) the bubble count histogram. The prediction based on the present criteria exhibits excellent agreement with the experimental data. It has also been possible to simulate the transition from bubbly to dispersed bubbly flow at a high liquid flow rate using the same model. [DOI: 10.1115/1.3203205]

Keywords: bubbly flow, population balance, transition, coalescence, breakage

1 Introduction

Bubbly flow may be defined as a typical two phase flow pattern where a gaseous phase is dispersed in a liquid phase in the form of spherical, oblate spheroid, and small cap bubbles. Though bubbly flow often exhibits an apparently homogeneous structure, the hydrodynamics is sufficiently complex due to different velocities of two phases and dynamic processes such as coalescence and break up of bubbles.

There are numerous examples of bubbly flow covering a diverse range of applications. Chemical and biotechnological processes, operations for environmental pollution control, power generation, and cooling are only a few examples of such flow. Particularly in process applications, bubbly flow is often desirable as it is characterized by a thorough mixing of the dispersed phase in the carrier fluid. The large interface also provides improved rate of reaction and mass transfer. During gas-liquid two phase flow through a pipe line, bubbly flow is one of the common flow regimes, which may occur both in adiabatic and nonadiabatic situations. The designer should not only require the knowledge of the hydrodynamics, he should also have an adequate idea regarding the operating range of bubbly flow depending on the process parameters, flow geometry, and fluid properties.

Over the decades, untiring efforts have been made for the simulation of bubbly flow. Initially a homogeneous equilibrium model (HEM) was used in an attempt to treat bubbly flow as a single fluid whose properties were determined through different averaging rules. Drift flux model [1] can be considered as the next higher level model where the importance of slip between the phases was recognized. Various modifications [2–4] of this model have been proposed time to time in order to make it applicable for complex systems.

As the properties of the two phases are widely different and the slip between the phases could be considerable, it was appreciated that separate set of conservation equations are required for each of the phases. Additionally, the interaction between the phases also needs to be modeled. This gave rise to the methodology of the two

fluid model [5]. There have been many variations of this technique. An important idealization has been made by the researchers particularly for the cases when one phase is thoroughly dispersed in the other. This is known as interpenetrating continua or mixed continua [6]. According to the hypothesis of the interpenetrating continua, both the phases are simultaneously present at each and every point of the computational domain, while their influence on the hydrodynamics and the transport processes is given by the local phase fraction.

In multiphase flow, the phase distribution changes both with time and space even if the input and the operating conditions are kept invariant. Though the two fluid model is a considerable success toward the modeling of multiphase flow, it needs augmentation to take care of the variable phase distribution. Several methodologies have been suggested for this. The interfacial area transport equation was suggested by Ishii [7]. In 1998 Wu et al. [8] developed one grouped interfacial area transport equation for spherical bubbly flow pattern. Further, it is realized that the shape of the bubbles distorts during motion causing a change in the drag force and the fluid particle interaction mechanisms. Two-group (spherical/distorted bubble and cap/churn turbulent bubble) area transport equation was developed [9] to circumvent this.

An alternate approach of simulation through population balance model (PBM) [10] has also been adopted. PBM essentially considers the secondary phase as the assemblage of discrete class or subgroup having different characteristics lengths. Additionally, PBM can meticulously track the birth and death of the members of these subgroups. Various methodologies, such as method of discrete classes [10], quadrature method of moments [11], least square methods [12], etc., have been developed to implement PBM numerically.

As this model has a wide applicability with significant accuracy, a number of researchers [5,8,13] have adopted the technique for the simulation of bubbly flow with different modifications. Chen et al. [14] showed the applicability of the model in case of bubble columns of different diameters. Similarly, Yeoh and Tu [15] and Cheung et al. [16] solved the population balance equation along with the two fluid model using the method of discrete classes [10] for pipe flow. An extensive review of the works related to population balance modeling for bubbly flows in the bubble column can be found in Ref. [17], while Krepper et al. [18] reviewed the work for pipe flow.

¹Corresponding author.

Contributed by the Fluids Engineering Division of ASME for publication in the JOURNAL OF FLUIDS ENGINEERING. Manuscript received January 13, 2009; final manuscript received July 4, 2009; published online August 18, 2009. Assoc. Editor: Theodore Heindel.

Furthermore, for a better prediction of the assemblage of different sized entity multiple-sized group models (MUSIGs) has also been tried by different researchers [18–20]. In these models, different groups (based on size) of bubbles are assumed to have different velocities. A separate set of conservation equations are solved for each group of the bubbles, considering each one of them as one distinct continuum. However, the increase in computation time and the need for a large number of closure relationships cannot be overlooked in this type of simulations.

Efforts have also been made to directly solve the two phase interacting momentum balance equation by using sufficiently fine grids and smaller time steps in the problem domain. Esmaili and Tryggvason [21] applied “direct numerical simulation” (DNS) for laminar bubbly flow in a vertical channel. After that, continuous efforts [22–24] have been made to improve the numerical scheme for a better prediction. Nevertheless, due to the volume of computations involved, only small systems with fewer complexities can be modeled at present [25]. As a consequence, models based on averaging (both in time and space), such as the two fluid model, are very important for simulating problems of practical importance.

It is clear from the available literature that the application of a two fluid model along with PBM or interfacial area transport equation has produced reasonable success in the prediction of bubbly flow. However, to date not much effort has been made to predict the transition of cocurrent bubbly flow through a circular conduit using computational fluid dynamics (CFD). On the other hand, CFD is rigorously used by researchers [26–29] to determine the transition of homogeneous to heterogeneous regime for bubble column reactors. This motivated us for the numerical investigations of transition regimes of bubbly flow situations. Bubbly flow through a vertical tube is bound by two neighboring flow regimes. At the low and moderate liquid flow rate, bubbly flow transforms into slug flow with the increase in air flow rate, whereas transition from bubbly to dispersed bubbly flow is observed at high liquid flow rates [30]. Classically, these transition criteria have been derived from the control volume approach using a number of simplifying assumptions [31,32]. From these criteria of transition are predicted based on the phase superficial velocities without taking other process parameters (such as tube diameter, inlet bubble size distribution, etc.) into cognition. Furthermore, a considerable variation has been reported in the transition boundaries observed in different experiments. This has motivated the present work to apply CFD technique to identify the suitable transition criteria, which are rigorously based on hydrodynamics. The bubbly flow has been simulated using the two fluid model along with the population balance technique. Though the basic structure of the model has been retained, a few important modifications have been made to simplify the computation and to improve the simulation. The model simulation has been used to investigate the dynamic development of coalescence and to break up processes along the axial direction. This has been studied noting the breakage and coalescence frequency, bubble volume account below and above the bubble size at the inlet, and bubble count histogram. It has been possible to propose unique transition criteria from bubbly to slug flow. The transition boundary predicted by the present model matches very well with the experimental data. Finally, the present model has been extended to the zone of high liquid flow rate to predict the transition to dispersed bubbly flow. Experimentally observed bubbly to dispersed bubbly transition is predicted satisfactorily.

1.1 Model Development. Figure 1 depicts the typical up flow of gas-liquid mixture with low superficial velocities, where the lighter phase is dispersed in the form of bubbles of different sizes in a round vertical conduit. The constitutive equations of each phase are developed based on the volume average properties of the phase. The total population of bubbles is discretized into subgroups based on volume to avoid intermediate bubble generation during coalescence. In the present model each group of bubbles

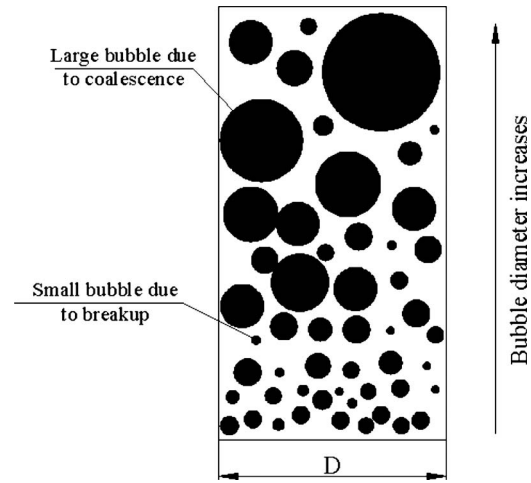


Fig. 1 Schematic representation of bubbly flow

has its characteristic length and occupies a fixed space at any instant. At any location, the number of bubbles in each group can be individually estimated considering their breakage and coalescence with other bubbles.

A Eulerian technique, known as the two fluid model [33], has been used for simulating the hydrodynamics. In this model, two competing phases are considered as interpenetrating continua by introducing the instantaneous phase fraction α_i . The approach gives the freedom to use coarser nodes and longer time steps compared with the Eulerian–Lagrangian approach.

Isothermal bubbly flow in the absence of any phase change can be described by the conservation of mass and momentum in each of the phases. Furthermore, cocurrent vertical upflow can be considered to be axisymmetric. The conservation equations in the r - z coordinate system are given below based on the formalism of two fluid model.

For continuity equation,

$$\frac{\partial}{\partial t}[\rho_i \alpha_i] + \frac{1}{r} \frac{\partial}{\partial r}[r \rho_i \alpha_i u_i] + \frac{\partial}{\partial z}[\rho_i \alpha_i w_i] = 0 \quad (1)$$

For r momentum,

$$\begin{aligned} \frac{\partial}{\partial t}[\rho_i \alpha_i u_i] + \frac{\partial}{\partial r}[\rho_i \alpha_i u_i^2] + \frac{\partial}{\partial z}[\rho_i \alpha_i u_i w_i] = & -\alpha_i \frac{\partial P}{\partial r} + \alpha_i \rho_i g_r \\ & + \mu_i \frac{\partial^2}{\partial r^2}(\alpha_i u_i) + \frac{\mu_i \alpha_i u_i}{r^2} + \frac{\mu_i}{r} \frac{\partial}{\partial r}(\alpha_i u_i) + \mu_i \frac{\partial^2}{\partial z^2}(\alpha_i u_i) \\ & - F_{wir} \mp F_{LGr} \pm F_{dispr} \end{aligned} \quad (2)$$

For z momentum,

$$\begin{aligned} \frac{\partial}{\partial t}[\rho_i \alpha_i w_i] + \frac{\partial}{\partial r}[\rho_i \alpha_i u_i w_i] + \frac{\partial}{\partial z}[\rho_i \alpha_i w_i^2] = & -\alpha_i \frac{\partial P}{\partial z} + \alpha_i \rho_i g_z \\ & + \mu_i \frac{\partial^2}{\partial r^2}(\alpha_i w_i) + \frac{\mu_i}{r} \frac{\partial}{\partial r}(\alpha_i w_i) + \mu_i \frac{\partial^2}{\partial z^2}(\alpha_i w_i) \\ & - F_{wiz} \mp F_{LGz} \pm F_{dispz} \end{aligned} \quad (3)$$

Here $i=l$ stands for liquid phase, and $i=g$ stands for gas phase. P is assumed as the average pressure of the mixture, and it can be evaluated using the equation of state in the following manner:

$$P = (\rho_l \alpha_l + \rho_g \alpha_g) RT \quad (4)$$

Constitutive relationships for the force terms used in the momentum equations are selected from the published literature. As the generic nature of the radial and axial forces is the same, directions of the forces are omitted in the respective equations (Eqs. (5)–(10)). For the vector quantities associated with the forces, we

have used their nondirectional forms by putting a bar over the symbols of the respective vectors. For the directional equation of the forces the quantities under the bar will be substituted by the respective directional form of the vectors.

F_{LG} is the interfacial drag force that can be expressed as [34]

$$\overline{F_{LG}} = \frac{2C_{FL}}{D} \sqrt{\alpha \rho_g (\overline{u_g} - \overline{u_l})} |\overline{u_g} - \overline{u_l}| + \frac{\alpha}{2} \rho_l \overline{u_g} \frac{\partial}{\partial r} (\overline{u_g} - \overline{u_l}) \quad (5)$$

The first term of the force represents the drag force, and the second term is the apparent mass force due to the change in kinetic energy induced by the bubble motion in the liquid.

In the above expression C_{FL} is the interfacial friction factor and is given by

$$C_{FL} = C_D \sqrt{\alpha (1 - \alpha)^{-1.7} \frac{\rho_l}{\rho_g} \frac{D}{D_B}} \quad (6)$$

C_D is drag coefficient for a single bubble, and D_B is average bubble diameter at a particular location. This is determined through the population balance technique and constitutes one of the interfaces between the two fluid model and population balance technique.

Based on Chisholm's [35] correlation wall liquid friction force F_{WL} (Eqs. (2) and (3)) can be expressed as

$$F_{WL} = [1 + (Y_c^2 - 1)(B(X_c(1 - X_c))^{(2-n)/2} + X_c^{2-n})] \Delta P_{L0} \quad (7)$$

Here, ΔP_{L0} is the single phase pressure drop due to friction and $n=0.25$ for air water system. In Eq. (7) the empirical constant B is dependent on the fluid pair associated. It can be calculated as follows:

$$B = \frac{CY_c - 2^{2-n} + 2}{Y_c^2 - 1} \quad (8)$$

where

$$C = \frac{\overline{u_l}}{\overline{u_g}} \sqrt{\frac{\rho_l}{\rho_g} \left(1 - \frac{\overline{u_g}^2 \rho_g}{\overline{u_l}^2 \rho_l}\right)}$$

For various combinations of superficial velocities within the reported range, it varies between 11,000 and 14,000 for air water combination. For calculation of the values of B in the present model, an average of the possible values of B has been considered, which came out near to 12,500. X_c and Y_c can be expressed as follows:

$$X_c = \frac{1}{1 + \frac{1 - \alpha}{\alpha} \frac{\rho_l \overline{u_l}}{\rho_g \overline{u_g}}} \quad \text{and} \quad Y_c = \left(\frac{f_{G0} \rho_l}{f_{L0} \rho_g}\right)^{0.5} \quad (9)$$

The wall friction factor for the gaseous phase is also calculated using Eq. (7) after employing the gaseous phase frictional pressure drop (ΔP_{G0}) as the multiplier in place of ΔP_{L0} .

The turbulent dispersion force of gaseous phase is considered in the form of Favre averaged variables [36]

$$F_{disp} = C_{TD} C_D \frac{\gamma_{lg}}{Sc_{lg}} \left[\frac{\nabla \alpha_l}{\alpha_l} - \frac{\nabla \alpha_g}{\alpha_g} \right] \quad (10)$$

C_{TD} and C_D are the turbulent dispersion force coefficient and the drag force coefficient for a single bubble. C_{TD} is taken as 1.0 in the present simulation. γ_{lg} is the turbulence kinetic viscosity, and Sc_{lg} is the turbulent Schmidt number of the gaseous phase.

A population balance [37] has been incorporated in the present model to keep account of bubble evolution in the bulk of continuous phase due to coalescence and breakup. As a result of these processes, bubbles of new groups may appear (birth) and those of existing groups may disappear (death). Accordingly, the population balance can be obtained in terms of the birth and death rate

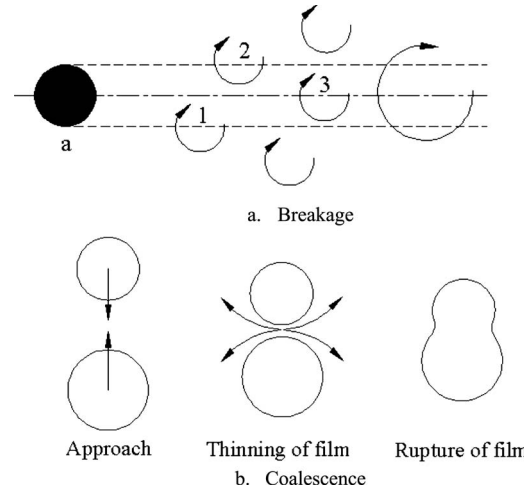


Fig. 2 Steps of the breakage and coalescence process

$$\frac{\partial n(r, z, t; d)}{\partial t} + u_g \frac{\partial n(r, z, t; d)}{\partial r} + w_g \frac{\partial n(r, z, t; d)}{\partial z} = B_B(r, z, t; d) - D_B(r, z, t; d) + B_C(r, z, t; d) - D_C(r, z, t; d) \quad (11)$$

In the present model, the entire population of bubble is discretized into different subgroups of equal volume interval. Each subgroup has its own span of bubble characteristic length. The mean of this span is considered to be the pivotal length scale associated with the subgroup. As the bubbles are equispaced in volume, a newly born bubble during coalescence explicitly falls in one of the subgroup nodes. This exactly satisfies the conservation of bubble volume. On the other hand, during breakage the daughter bubbles may not have a size corresponding to the pivotal length scale. Such bubbles are distributed among the neighboring subgroups, keeping the bubble mass and number fixed. Nucleation of new bubbles, evaporation, condensation, shrinkage, and elongation are not considered in the present model. Present model only recognizes the appearance of newly born bubbles and the disappearance of the extinct bubbles due to dynamic interactions in a fixed control volume. However, their redistribution is considered to be random and solely guided by the advection of two phase mixture. Furthermore, only binary coalescence and binary breakage of the bubbles are considered.

Collision with turbulent eddies are considered as the mechanism of breakup and is schematically shown in Fig. 2(a). Breakage of a bubble is possible only when the turbulence kinetic energy of the striking eddy supersedes the effect of surface energy of the interacting bubble [38]. This leads to the surface rupture of the bubbles and the formation of daughter bubbles. Moreover, breakup occurs when an eddy of size comparable to the bubble characteristic length collides with it. If the eddy size is larger than the bubble characteristic length, collision between them is unable to make any craters on the bubble. Thus, in Fig. 2(a) only eddies denoted by 1, 2, and 3 are effective for the breakup process. The size of the daughter bubbles due to breakage depends on the strength of the eddies [39], which, in turn, depend on the local hydrodynamics.

Birth and death of bubbles due to the breakup process can be calculated as follows:

$$B_B(r, z, t; d) = \int_d^\infty \eta(d' - d, d) \nu(d') g(d') n(r, z, t; d') dd' \quad (12)$$

$$D_B(r, z, t; d) = n(r, z, t; d) g(d) \quad (13)$$

Based on the model proposed by Kostoglou and Karabelas [40] bubble breakup frequency can be expressed as

$$g(d) = k(1 - \alpha) \times \left(\frac{\varepsilon}{d^2}\right)^{1/3} \int_0^1 \int_{\xi_{\min}}^1 \frac{(1 + \xi)^2}{\xi^{11/3}} e^{-(12c_1\sigma)/(2.04\rho_c\varepsilon^{2/3}d^{5/3}\xi^{11/3})} d\xi df_v \quad (14)$$

Here f_v is the ratio of the volume of mother and daughter bubbles, and ε is the energy dissipation rate per unit mass. ε can be written in the following fashion [41], in terms of pipe diameter (D) and mixture velocity (U_m):

$$\varepsilon = \frac{f_v U_m^3}{2D} \quad (15)$$

U_m is calculated as follows:

$$U_m = \sqrt{(u_g^2 + w_g^2)^2 + \sqrt{(u_l^2 + w_l^2)^2}} \quad (16)$$

C_1 is an empirical constant and can be expressed in terms of f_v as follows:

$$C_1 = f_v^{2/3} + (1 - f_v)^{2/3} - 1 \quad (17)$$

ξ_{\min} is the nondimensional minimum daughter bubble size that can be obtained from the Kolmogoroff microscale, as described by Tsouris and Tavlarides [42].

The minimum size of the bubble that can be fragmented by a colliding eddy of strength ε is calculated as follows using the conjecture of Troshko and Zdravistch [43]:

$$d_{\min} = 1.15 \frac{\sigma^{3/5}}{\rho_l^{3/5} \varepsilon^{2/5}} \quad (18)$$

For bubbles of size larger than a critical value, instantaneous break up may take place because of the instability of the gas-liquid interface. According to Carrica and Clausse [44] the probability is given by

$$g(d) = b^* \frac{(d - d_c)^m}{(d - d_c)^m + d_c^m} \quad (19)$$

where d_c is the critical bubble diameter, set as 27 mm, and b^* and m are model parameters set as 100 s⁻¹ and 6.0, respectively [44].

Daughter distribution probability $\eta(d_1, d_2)$ proposed by Kostoglou and Karabelas [45] is used in the present model.

$$\eta(d_1, d_2) = \left(\frac{1}{\frac{d_1}{d_2} + a} + \frac{1}{1 - \frac{d_1}{d_2} + b} + \frac{2(z-1)}{b+0.5} \right) \frac{6I}{\pi d_2^3} \quad (20)$$

where I is the normalization coefficient and is expressed as

$$I = \frac{0.5}{\ln(1+a) - \ln(b) + \frac{z-1}{b+0.5}} \quad \text{and} \quad z = \frac{a}{4b(1+b)(1-a)}$$

a and b are parameters that define the shape of the daughter drop size distribution function. In the present model, the values $a = 0.1$ and $b = 1$ [45] are used that signifies "U" shaped bubble size distribution.

For coalescence of bubbles to occur in the turbulent flow field of a gas-liquid mixture, the bubbles must first collide with each other and then remain in contact for sufficient time so that the processes of liquid film drainage, film rupture, and finally coalescence may occur. After the collision between two bubbles, a successful coalescence through film rupture is depicted in Fig. 2(b). The following expressions can be taken for the birth and death due to coalescence process, respectively

$$B_C(r, z, t; d) = \frac{1}{2} \int_0^{v(d)/2} \lambda(d_{v-v'}, d_{v'}) n(r, z, t; d_{v-v'}) n(r, z, t; d_{v'}) dv' \quad (21)$$

$$D_C(r, z, t; d) = n(r, z, t; d_v) \int_0^\infty \lambda(d_v, d_{v'}) n(r, z, t; d_{v'}) dv' \quad (22)$$

Binary coalescence of two equal sized bubbles generates a daughter bubble having 1.26 times diameter of its parents. Therefore, two bubbles having the dimension greater than 0.8D (D is tube diameter) will result a coalesced bubble of diameter greater than D . This obviously goes beyond the computational domain. Further, it has been reported [46] that bubbles with diameter 0.6D represent a transition to cap bubble or a Taylor bubble. With all these considerations, the maximum bubble diameter is restricted up to the half of the diameter of the pipe through which the flow occurs to attain transition between bubble and slug flow.

Coalescence frequency $\lambda(d_1, d_2)$ is the product of the effective swept volume rate, $h(d_1, d_2)$ and film rupture efficiency $p(d_1, d_2)$. Effective swept volume rate is calculated using the analogy between kinetic theory of gasses and bubble coalescence phenomena. According to Coualoglou and Tavlarides [47], effective swept volume rate is calculated as:

$$h(d_1, d_2) = c_2 \frac{\varepsilon}{1 + \alpha} (d_1 + d_2)^2 (d_1^{2/3} + d_2^{2/3})^{1/2} \quad (23)$$

Film drainage is controlled by inertia and surface tension forces [48]. For two bubbles of diameter d_1 and d_2 Coualoglou and Tavlarides [47] proposed the film rupture efficiency as follows:

$$p(d_1, d_2) = \exp \left[- \frac{c_3 \rho_l \mu_l \varepsilon}{\sigma^2 (1 + \alpha)^3} \left(\frac{d_1 d_2}{d_1 + d_2} \right)^4 \right] \quad (24)$$

The numerical constants C_2 and C_3 are related to the collision frequency and the rupture efficiency, respectively. Values of C_2 and C_3 are taken as $0.0055 \phi^{-1.3404}$ and 5.4×10^8 , as referred by Ioannou et al. [41]. They used the experimental data of Lovick [49] to fit the values of the above constants.

Finally, we like to make a couple of comments regarding the present simulation. First, no rigorous turbulence closure has been used. Taking the queue from the single phase flow, number of researchers has used the k - ε formulation for turbulence modeling even in case of two phase flow [50,51]. The empirical constants needed for such formulation were determined from single phase experiments though there is no guarantee that they are applicable also for the two phase hydrodynamics [52]. We have used a rather simple relationship for turbulent energy dissipation (Eq. (15)). It goes without saying that a better physical model may improve the prediction substantially.

Second, for the sake of simplicity, we have assumed identical velocities for bubbles of all the subgroups. Strictly speaking this is a simplification. For a better prediction, different groups of bubbles may be assigned different characteristic velocities and closure laws for drag, lift, etc. [53]. Within the same framework of population balance model the above may be implemented.

2 Boundary Condition and Solution Procedure

The following boundary conditions are employed for the present simulation.

- For both the phases, at the inlet uniform velocity profile in stream wise direction and zero velocity at the crosswise direction is assumed. No slip condition is prescribed at the wall of the conduit.
- Void fraction of gaseous phase (α) and pressure at the inlet are specified.
- For a better simulation of the flow field finer node have been used near the wall. A small velocity as per the logarithmic law of buffer layer is implemented at a very small distance from the conduit wall [54].
- Uniform distribution of equal sized bubble is considered at the inlet whereas initially ($t=0$) the conduit is filled up only with the carrier phase

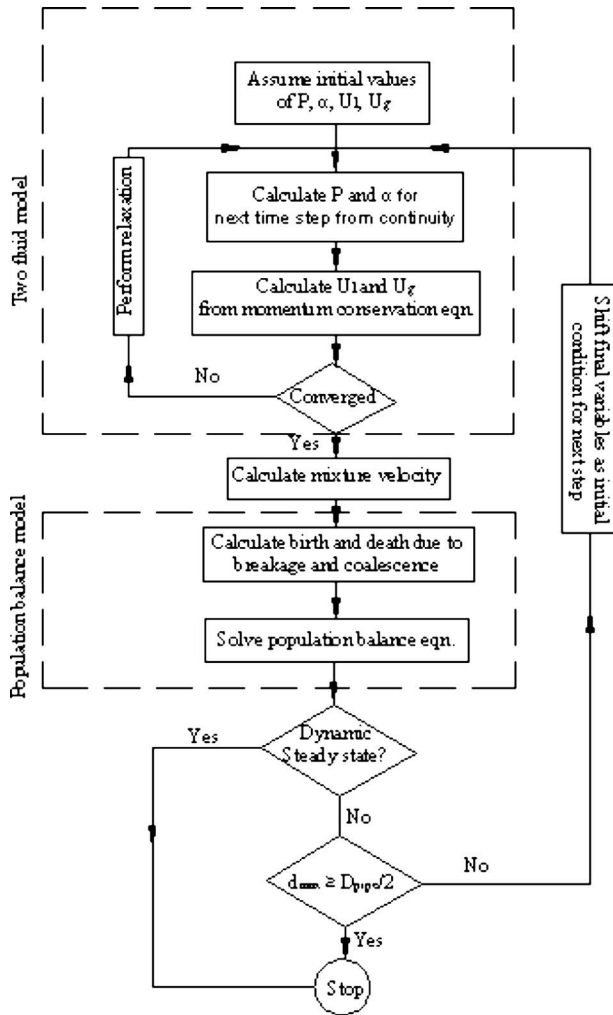


Fig. 3 Solution methodology of the proposed model

$$n(r, 0, t; d) = \begin{cases} N_{d, \text{node}} & \text{for } d = d_{\text{in}} \\ 0 & \text{for } d \neq d_{\text{in}} \end{cases} \quad (25)$$

and

$$n(r, z, 0; d) = 0 \quad (26)$$

where d_{in} is the bubble size entering at the inlet plane and can be selected as desired. This mimics a situation where the gas phase is introduced into the conduit by a large number of nozzles uniformly distributed at the inlet section.

- v. Overall possible bubble sizes ($\xi_{\text{min}} \leq d/2 \leq D/2$) are divided into 40 equal volumes to simulate a realistic flow phenomenon.

Solving Eqs. (1)–(3), the velocity field at each node point is calculated with 1% convergence criteria and is subsequently used for determining the mixture velocity at that particular position. Mixture velocity is used to determine the distribution of bubble size for the next instant based on the population balance equation (Eq. (11)). Figure 3 shows the solution methodology of the proposed model. Simulation is forward marched until either a steady dynamic solution ($(\partial/\partial t)n(r, z, t; d) \approx 0$ for all d) is reached or the hydrodynamics gives a clear indication toward the transition into slug flow. The criteria for such transition will be described in detail in Secs. 3 and 4.

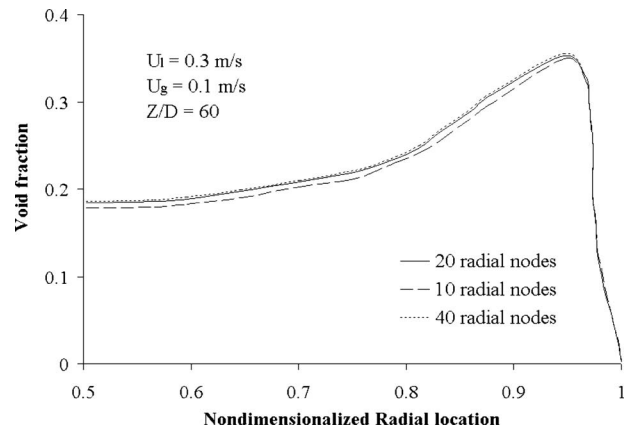


Fig. 4 Effect of radial mesh refinement on void distribution

3 Validation of the Model

Solution of the model based on the algorithm shown in Fig. 3 gives the phase velocity and void fraction at any particular point of conduit. Computations have been done selecting different mesh sizes and time steps to check the node independence and to find out optimal values of node spacing and time step. Results on the effect of mesh size on void distribution are depicted in Fig. 4. From this study it is decided that 20 radial nodes will be sufficient for a compromise between the accuracy and the computational time. For the flow field to become fully developed total length of the pipe is assumed to be a minimum of $100D$. Grid independent studies have also been made for the axial direction, and 1000 nodes were found to be sufficient for that. Total number of cells then turns out to be 18,981.

There is a considerable volume of gas-liquid bubbly two phase flow data in open literature. Among them one pioneering work by Serizawa et al. [55] and one recent work by Ohnuki and Akimoto [56] are selected for the verification of the present model. Comparisons of the present simulation against these data are described below.

In Fig. 5 computational results are compared with the data of Serizawa et al. [55] for various inlet qualities and reported bubble diameters. Simulation results are taken at a considerable distance ($30D$) from the inlet plane to avoid the effect of entrance region. Liquid velocity is kept at 1.03 m/s, same as that in Ref. [55]. Void fractions at different qualities are presented with respect to non-dimensional radial position. The velocity of the air at the inlet plane is calculated by multiplying liquid velocity at the inlet with void fraction. Though there is a mismatch in the profiles near the

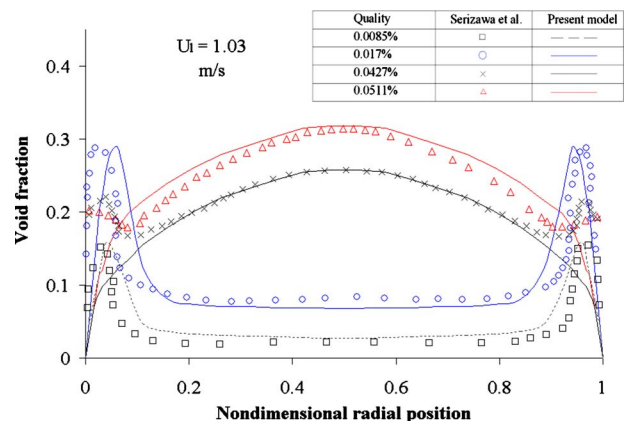


Fig. 5 Comparison of void fraction of present model and experimental data of Serizawa et al. [50]

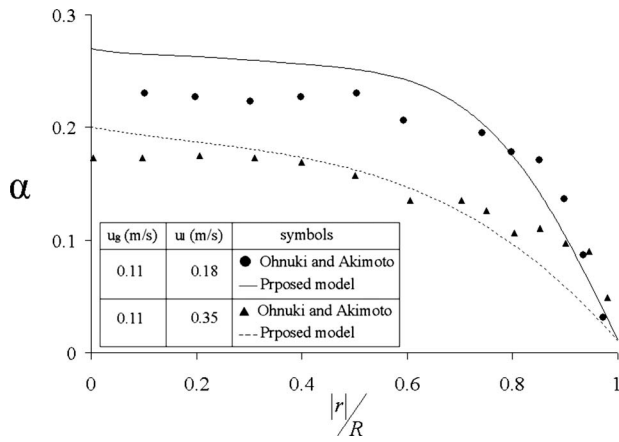


Fig. 6 Comparison of void fraction with the present model and experimental data of Ohnuki and Akimoto [51]

wall, it is clear from Fig. 5 that the model predicts the radial void fraction distribution satisfactorily. Near the wall, an improved modeling of the motion of the continuous phase, including the effect of boundary layer and buffer layer, is expected to give a better result without the stringent requirement of the finer grids everywhere in the computational domain.

Ohnuki and Akimoto [56] used an optical probe for the measurement of void fraction and a dual sensor resistivity probe for the measurement of bubble velocity and its fluctuation. In Fig. 6, radial distribution of void fraction obtained by numerical simulation is compared with the results of Ohnuki and Akimoto [56] for identical conditions (liquid velocity of 0.18 m/s and gas velocity of 0.11 m/s). A satisfactory agreement has been observed. Estimated void fraction profile for a higher liquid flow rate of 0.35 m/s keeping the air flow rate the same (0.11 m/s) is also depicted in the same figure. The same phase velocities were used by Ohnuki and Akimoto [56]. A good agreement has also been obtained in this case.

Comparisons of the predicted radial profile of volume averaged bubble diameter with experiment at same initial situations [56] are depicted in Fig. 7. The developed model predicts the correct trend though it underpredicts the average bubble diameter toward the tube wall. Present model is also used to investigate the distribution of bubble Sauter mean diameter in a radial plane. When the surface area and the volume of the averaged diameter bubbles are equal to those of the polydisperse bubbles, this averaged diameter is called the Sauter diameter (volume-surface area mean diam-

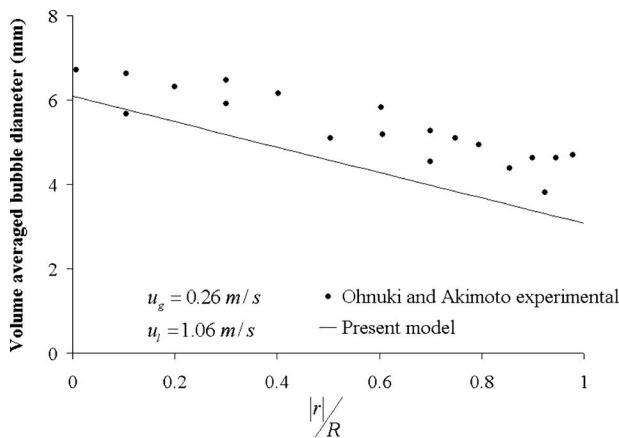


Fig. 7 Radial distribution of volume averaged bubble diameter; a comparison between present model and experimental data of Ohnuki and Akimoto [51] at high flow rates

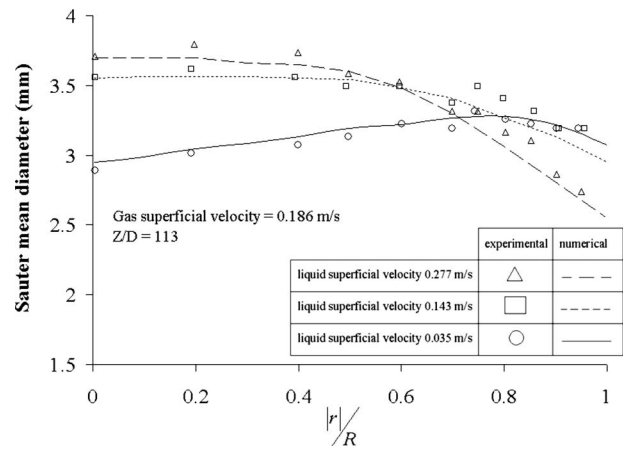


Fig. 8 Comparison of the computed bubble Sauter diameter along a radial plane with the experimental result of Shen et al. [52]; low gas superficial velocity

eter). It can be calculated based on the values of the scalar fraction (f_i) of the volume of a particular sized bubble with respect to the overall gaseous phase and the corresponding discrete bubble diameter d_i is obtained as

$$d_{32} = \frac{1}{\sum_{i=1}^N \frac{f_i}{d_i}} \quad (27)$$

The computed result of the bubble Sauter diameter is compared with the experimental observation of Shen et al. [57] for air water flow through a tube diameter of 200 mm. Figure 8 shows a very good prediction of the Sauter mean diameter at a gas superficial velocity of 0.186 m/s for three different liquid superficial velocities covering a wide range, as considered by Shen et al. [57] in their experiment. The prediction is also satisfactory for higher gas superficial velocity, as depicted in Fig. 9. With the confidence gained from the above comparisons, the present model has been employed to investigate the development of flow along the axial direction and the transition from bubbly to slug flow.

4 Axial Development of the Phase Distribution

It has been mentioned earlier that the gas phase at the inlet boundary is considered as a uniform distribution of equal sized bubbles. Therefore, it is obvious that any transformation from

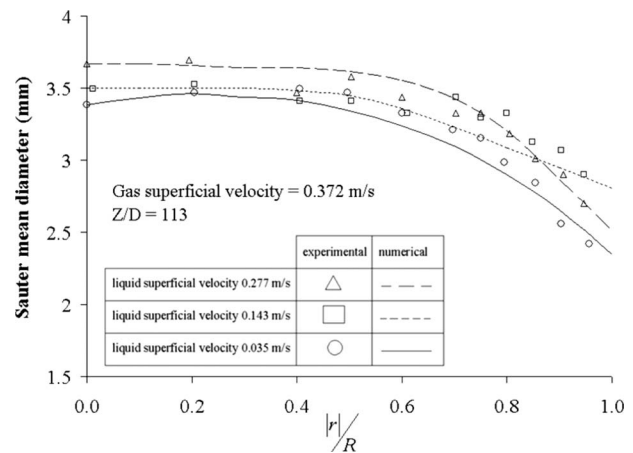


Fig. 9 Comparison of the computed bubble Sauter diameter along a radial plane with the experimental result of Shen et al. [52]; high gas superficial velocity

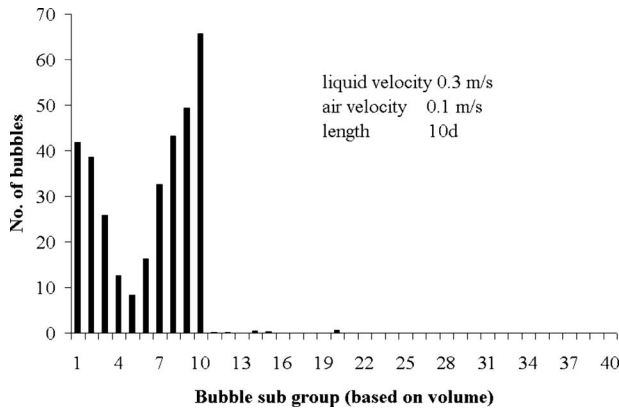


Fig. 10 Radial bubble count histogram at an axial distance of 10D for low flow rates

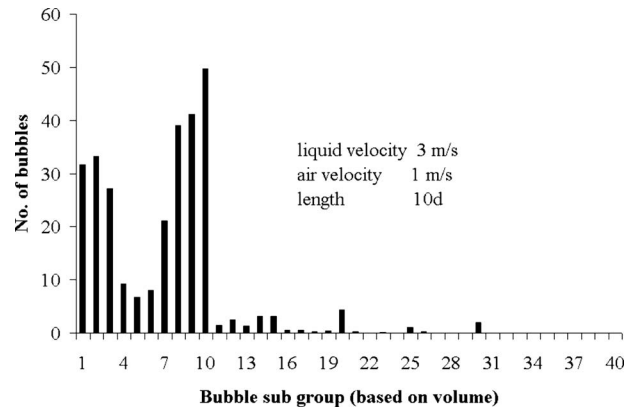


Fig. 13 Radial bubble count histogram at an axial distance of 10D for high flow rates

bubbly flow is due to the development of the flow of the two phase mixture downstream of the inlet plane. Due to the coalescence and breakup of the bubbles during their random motion, the number of bubbles in a particular subgroup may increase or decrease in the downstream. This is solely guided by the hydrodynamics. Some interesting cases are discussed below.

In Figs. 10–12 the bubble count of different subgroups in a radial plane is shown for different axial positions. The bubbles of tenth subgroup are introduced at the inlet with a liquid velocity of 0.3 m/s and an air velocity of 0.1 m/s. To track the generation of bubbles bigger than the size entered at the inlet, the tenth sub-

group has been entered. Moreover, a wide gap between the maximum possible bubble sizes and the bubbles to be entered will not bias the transition criteria. There is bubble growth due to coalescence; rather smaller size bubbles are formed as one moves toward the downstream. This is clear from the bubble count histograms estimated at 10D (Fig. 10), 30D (Fig. 11), and 60D (Fig. 12). The number of tenth subgroup bubbles (introduced at the inlet) reduces, while the number of bubbles belonging to smaller subgroups increases gradually. The coalescence of bubbles is clearly discernable from Figs. 13–15 at a high phase velocities (liquid velocity of 3 m/s and gas velocity of 1 m/s) even at an axial length of 10D. At this position one can see formation of bubble up to a subgroup of 30 that is considerably larger compared with the bubbles introduced at the inlet plane (tenth subgroup). The number of bubbles just double and triple of inlet bubble size group is high compared with the other higher sized bubble group as there is a rich tendency of coalescence of two inlet sized bubbles. At further downstream the number of large size bubbles ($V_i > V_p$) increases and new bubbles with even larger diameter come into existence.

To confirm the generation of larger bubbles at higher gas and liquid flow rates, a total volume count of bubbles above and below those introduced at the inlet are depicted in Table 1. The generation of larger bubbles at higher phase flow rates can also be confirmed by taking an account of the volume of the bubbles of different subgroups. For these a nondimensional parameter, namely, V_{high} has been defined as follows:

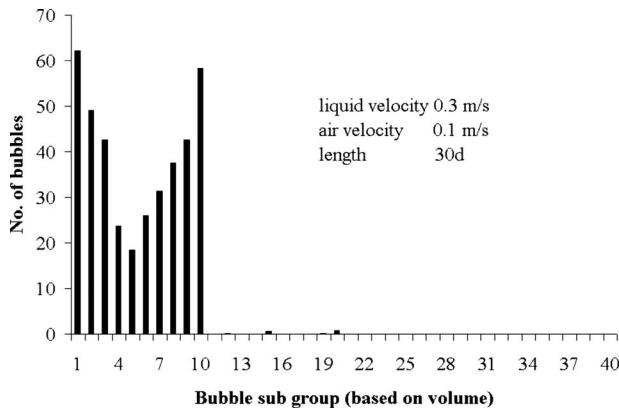


Fig. 11 Radial bubble count histogram at an axial distance of 30D for low flow rates

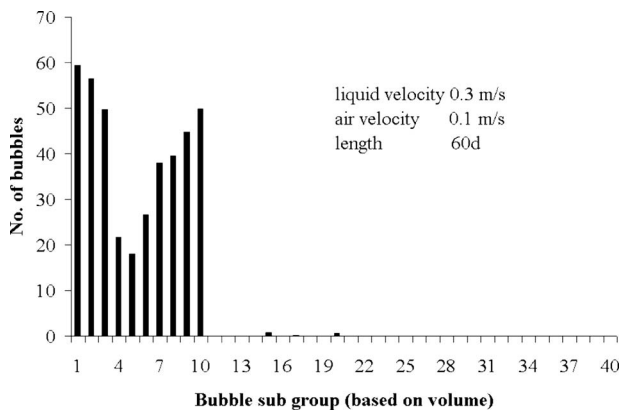


Fig. 12 Radial bubble count histogram at an axial distance of 60D for low flow rates

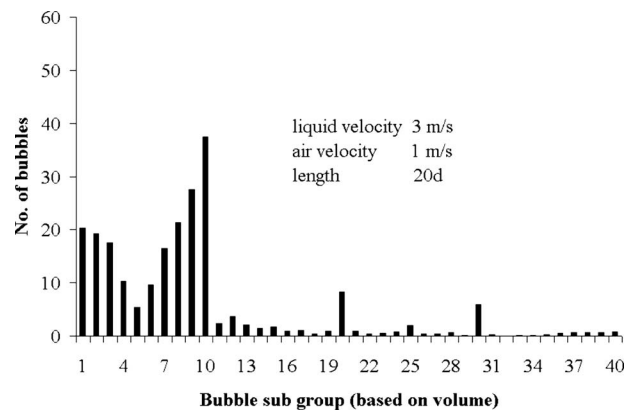


Fig. 14 Radial bubble count histogram at an axial distance of 20D for high flow rates

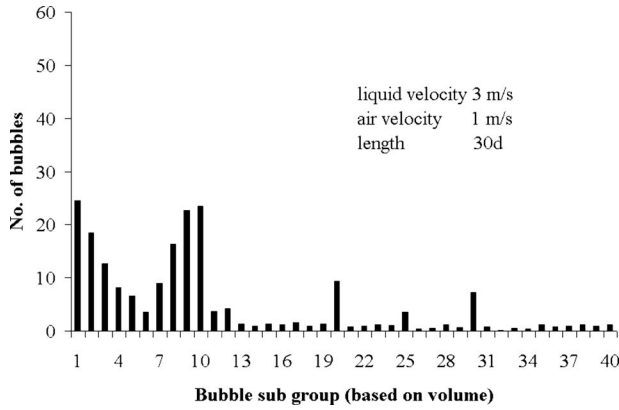


Fig. 15 Radial bubble count histogram at an axial distance of 30D for high flow rates

$$V_{\text{high}} = \frac{\sum_{i=p+1}^m v_i n_i}{\sum_{i=1}^m v_i n_i} \quad (28)$$

where p th subgroup of bubbles enters at the inlet. V_{high} at different axial planes for low and high phase flow rates are presented in Tables 1 and 2. At low phase flow rates (Table 1) the value of V_{high} is relatively low and assumes a constant value after some distance from the inlet plane. This indicates the existence of a steady bubbly flow for the given hydrodynamic parameters. As the flow develops, downstream of the inlet plane coalescence and breakup occurs, the process of break up being more dominant compared with coalescence. However, these two competing processes reach a dynamic steady state, where the maximum bubble size can never cross a certain limit to perturb the flow toward the slug flow regime. The flow essentially remains bubbly though there is a readjustment of bubble size and void distribution compared with the inlet plane.

Table 2 presents a different picture. V_{high} increases continuously along the downstream. This signifies the domination of coalescence over break up. Importantly, it indicates gradual growth of some bubbles as they move up. This is conducive for the generation of cap bubbles to start with and for the formation of the Taylor bubble finally.

To investigate the bubble size evolution with axial length, a cumulative estimate of bubble volume over the input sized bubble is shown in Fig. 16. The inlet velocity of air is taken as 0.1 m/s, and the inlet velocity of liquid is 0.3 m/s. The figure clearly supports the statement made above from the observations in Table 2.

Table 1 Liquid velocity 0.3 m/s and gas velocity 0.1 m/s

Axial location	Total volume above inlet diameter (m ³)	Total volume below inlet diameter (m ³)	V_{high}
10D	0.00004588	0.002962	0.01525
30D	0.00004689	0.00296	0.01559
60D	0.00004701	0.00298	0.015526

Table 2 Liquid velocity 3 m/s and gas velocity 1 m/s

Axial location	Total volume above inlet diameter (m ³)	Total volume below inlet diameter (m ³)	V_{high}
10D	0.000667	0.002331	0.2225
20D	0.001399	0.001609	0.4663
30D	0.001895	0.001104	0.6317

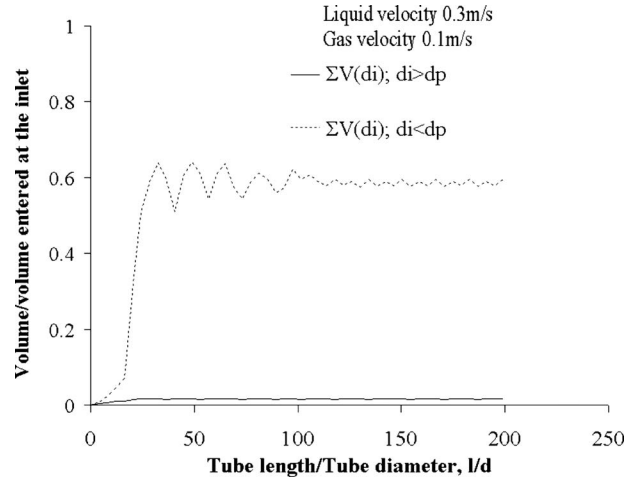


Fig. 16 Volume of bubbles above tenth subgroup (size at inlet) as a function of axial length; low superficial velocities

Though coalescence is present, it is not strong enough to generate new bubbles of larger diameter ($d_i > d_p$) in sufficient quantity. On the other hand, the process of breakup is more significant and is able to create smaller bubbles ($d_i < d_p$). Another interesting feature may be noted from the figure. Beyond a l/D of 100, the volume count above and below the bubble size introduced at the inlet does not change with the pipe length. This gives an idea regarding the pipe length required for the development of the flow. There is enough controversy regarding the developing length in the case of two phase flow. CFD simulation is capable of resolving this issue. Obviously the criterion for the developing length depends on the operating conditions, as will be clear from the results presented below.

In Fig. 17 an assessment of the breakage and coalescence process along the axial direction has been made by taking an account of the bubbles with size below and above those ($d = d_p$) entering the inlet plane. At a liquid velocity of 0.3 m/s and a gas velocity of 0.1 m/s, the coalescence rate is very low and remains more or less constant along the axial length. On the other hand, downstream of the inlet plane, the local breakage rate undergoes a large fluctuation. The fluctuation continues along the axial direction with diminishing amplitude and ultimately stabilizes into a steady periodic nature. Referring back to Figs. 10–12, one can appreciate the presence of a stronger breakup process compared with the process of coalescence for the selected phase velocities. It is also evident in Figs. 16 and 17 that the flow of the two phase mixture assumes

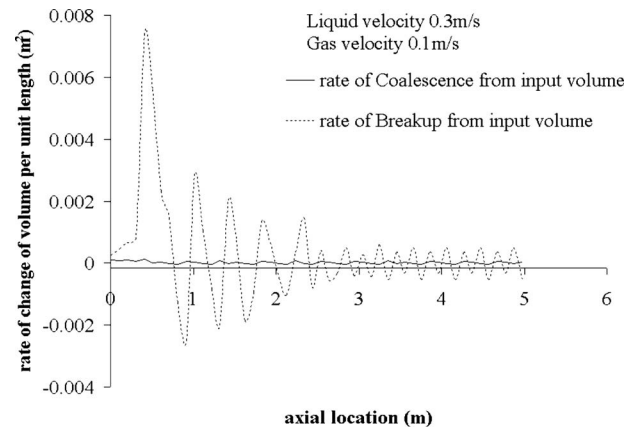


Fig. 17 Evolution of breakage and coalescence with axial location at lower flow rates

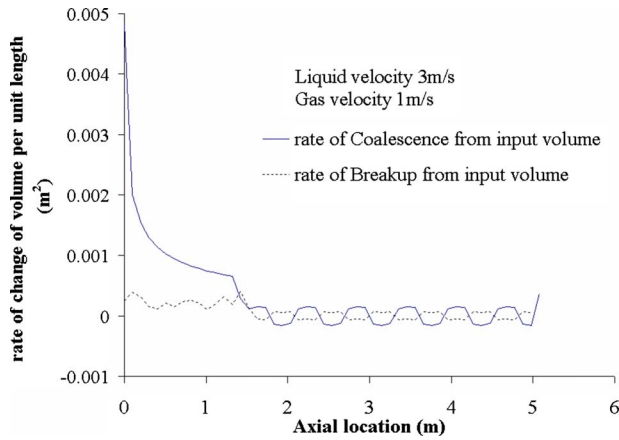


Fig. 18 Evolution of breakage and coalescence with axial location at higher flow rates

a dynamic steady state downstream of the inlet plane where the time averaged flow characteristics do not change axially.

The morphology of the dispersed phase goes through a different developmental pattern at higher phase flow rates. Figure 18 shows that a vigorous process of coalescence starts immediately after the bubbles enter the conduit. However, the coalescence rate reduces and ultimately stabilizes to a fluctuating pattern with a small amplitude. The process of break up on the other hand is rather insignificant. The net effect of coalescence and breakup on the bubble size distribution is depicted in Fig. 19, which clearly indicates the zone for flow development.

The evolution of bubble size along the conduit length as a function of inlet flow rates is depicted in Fig. 20. From the figure it is evident that at lower flow rates of gas and liquid (0.1 m/s and 0.3 m/s, respectively), the maximum bubble size remains unaltered (more or less identical to the bubbles at the inlet). This clearly shows that in the flow field, bubble break up is dominant leading toward the flow of different sized spherical bubbles, i.e., bubbly flow. At a higher flow rate the bubble size reaches the prescribed maximum limit of bubble diameter. This definitely indicates a possible transition from bubbly flow.

4.1 Transition From Bubbly Flow. To date, the identification of flow regime boundary has been achieved either through experimental [58,59] or by control volume based analytical modeling [60]. Assuming the transition to slug flow takes place due to high frequency of collisions at an increased density of dispersed

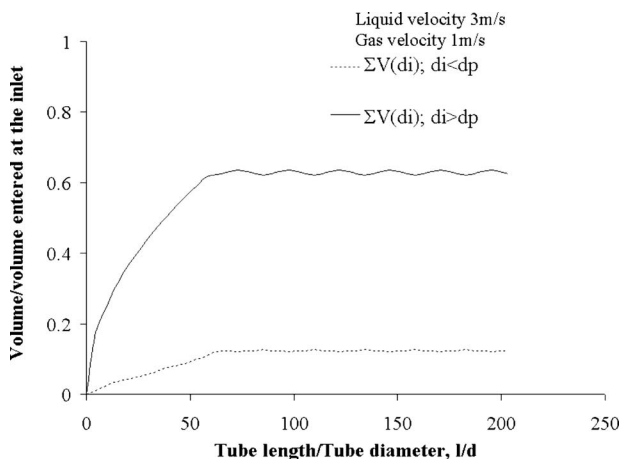


Fig. 19 Volume of bubbles above the tenth subgroup (size at inlet) as a function of axial length; high superficial velocities

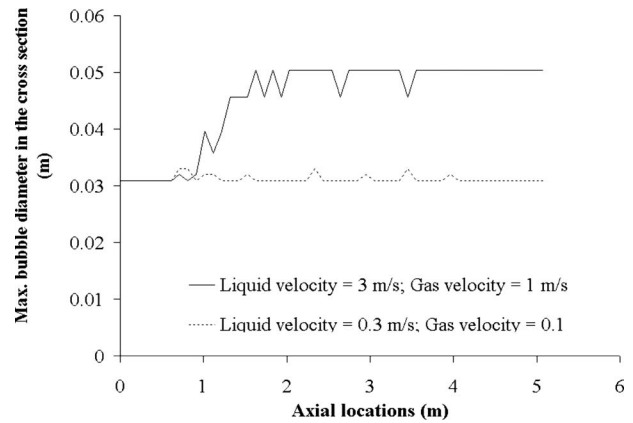


Fig. 20 Change of maximum bubble diameter along axial length for air water two phase flow

bubble Radovicich and Moissis [60] proposed a semitheoretical analysis. They have considered a cubic lattice of spherical bubbles fluctuating around their mean position and suggested that the transition occurs at a maximum limiting void fraction of 0.3 for bubbly flow. This physical model has also been supported by Dukler and Taitel [31] and Mishima and Ishii [32]. However, there is a controversy regarding the value of the maximum limiting void fraction, and a value of 0.25 is well accepted in the literature.

A slightly different view is proposed by Bilicki and Kestin [61]. The spherical bubbles dispersed in a bubbly flow do not move with identical velocities. The wake of a preceding bubble induces acceleration to its successors. A bubble may catch up to its predecessors and may coalesce to form a larger bubble. According to them this is the root cause of transition. For the success of the coalescence process, the distance between the two bubbles should be below a characteristics length, which is stochastic in nature depending on the flow phenomena. Based on this argument they proposed a transition criterion, which depends on a limiting void fraction, phase superficial velocities, "local friction velocity," and some numerical constants. The numerical constants were determined by experiments.

Different researchers have proposed void fraction wave as the cause of transition from bubbly to slug flow. Marcedier [62] observed that void fraction waves are damped in bubbly flows where the damping decreases with the increase in the mean void fraction. It has further been hypothesized that at some value of mean void fraction, the damping could disappear and the instability of the void fraction wave may give rise to bubble-slug transition. Matuszkiewicz et al. [63] took the queue from this postulation and experimentally demonstrated that transition from bubbly to slug flow occurs for a range of average void fraction $0.1 < \alpha_{\text{mean}} < 0.45$. It may be noted that this value is different from the limiting void fraction reported by Taitel et al. [30].

Sun et al. [64] conducted an experiment on the gas-liquid two phase up flow in a tube diameter of 112.5, mm where the disturbance was created by a swinging metallic plate at the upstream of the flow. Bubbly flow was observed up to a mean void fraction of 19.2%. The sudden emergence of Taylor bubble was observed at a gas concentration of 21.5%. This induces a transition to slug flow. They also observed at high liquid velocity that the intense turbulence suppresses the formation of Taylor bubbles. As a result an increase in mean void fraction transforms the bubbly flow directly to churn flow.

Alternatively, efforts have been made to characterize the termination of bubbly flow based on the maximum bubble diameter. Again different criteria have been used. Tomiyama et al. [46] considered a bubble to be a slug bubble when its equivalent diameter

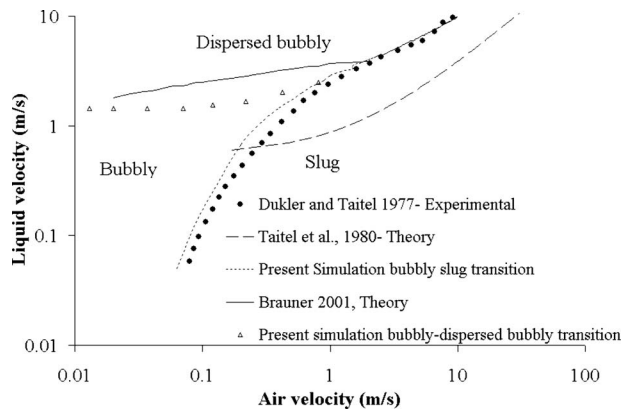


Fig. 21 Transition of bubbly flow; present simulation and experimental results of Olmos et al. [27] and Mercadier [62]

was 0.6 of the tube diameter. Krussenberg et al. [65] and Lucas et al. [59] also suggested a differentiation between the bubbly flow and slug flow based on the equivalent diameter of the largest bubble.

It may be noted that the transition criteria predicted from experimental observations are system specific and are dependent on operating conditions. On the other hand theoretical predictions developed so far uses mechanistic models on suitable “control volumes.” They typically rely on a specific mechanism and a number of simplified assumptions. To date little effort has been made to apply CFD simulation for the identification of flow regime boundary. In the present work we present a methodology for the same.

It has been accepted beyond doubt that coalescence is the mechanism for the transition from bubbly to slug flow. However, coalescence is a spatio-temporal process. It is necessary to investigate the hydrodynamics both locally and axially to bring out a clear picture about the transition. Furthermore, as coalescence and breakup simultaneously occur, we propose monitoring of the three different characteristics.

The formation of a large size bubble is of crucial importance.

The number of large bubbles should increase, and individual large bubbles should further grow in size

Finally, the consistency of the above two process should also be reflected in a diminishing rate of bubble breakup.

To monitor these three aspects, we have studied (i) the bubble histogram at different axial levels, (ii) bubble volume account below and above the bubble size introduced at the inlet, and (iii) breakage and coalescence frequency along axial length.

Based on the above criteria transition from bubbly to slug flow has been predicted and compared with the experimental observation of Dukler and Taitel [31] in Fig. 21. An excellent match between our prediction and experimental result has been observed. It can also be noted that the prediction by the present method is better than that of Taitel et al. [30].

A second type of transition from bubbly flow at high liquid velocity was proposed by Taitel et al. [30]. This flow regime is different from bubbly flow at low liquid velocity and is termed as dispersed bubbly flow. Hinze [66] proposed a mechanism for estimating the maximum bubble size from a balance between turbulence kinetic energy and drop surface energy. Hinze’s [66] analysis is applicable for dilute suspension. Brauner [67] extended Hinze’s [66] model for dense dispersion and obtained a modified expression for maximum bubble diameter. They have further suggested considering the largest of the diameter value calculated by the original Hinze [66] theory and its extension. For the present system the diameter of the largest dispersed bubble is given by the following equation:

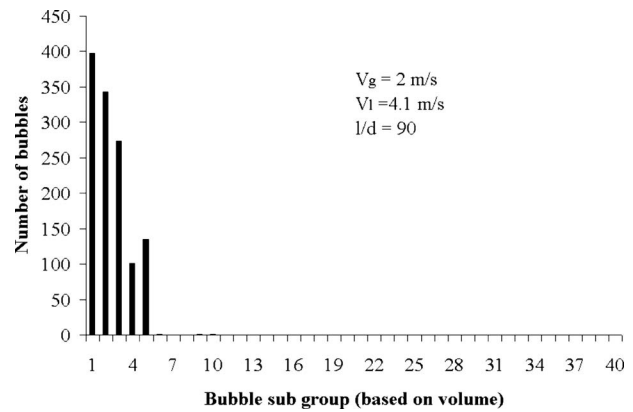


Fig. 22 Radial bubble count histogram for the high liquid flow rate showing dispersed bubbly flow

$$\frac{D_{surf}}{D_P} = 0.55 \left(\frac{\rho_c U_c^2 D_P}{\sigma} \right)^{-0.6} \left(\frac{\rho_{mf}}{\rho_c (1 - \epsilon)} \right)^{-0.4} \quad (29)$$

To investigate the bubbly to dispersed bubbly transition in the perspective of the present CFD model, the simulations have been done for higher liquid flow rates. A typical result of bubble count histogram can be seen in Fig. 22. The prediction shows a good concurrence with the model of Taitel et al. [30]. Almost complete disappearance of tenth subgroup bubbles indicate that the bubbles introduced at the inlet plane undergoes a thorough disintegration process due to high rate of turbulent dissipation. As a result, bubbly flow at the channel inlet transforms into dispersed bubbly flow further downstream.

To get an overall picture of the flow development with the change in liquid velocity, one may refer to Fig. 23, where simulation results for a single gas velocity at three different liquid velocities have been shown. The volume histogram clearly indicates slug flow, bubbly flow, and dispersed bubbly flow with the increase in liquid flow rates. Finally, the occurrence of critical dispersed bubble (Eq. (29)) as a function of phase superficial velocities has been depicted in Fig. 21. The simulation result shows a close match with the regime boundary mechanistically predicted by Brauner [67].

5 Conclusion

In the present paper the population balance equation coupled with two fluid model is used for the prediction of bubble evolution in gas-liquid two phase flow through a vertical conduit. Coales-

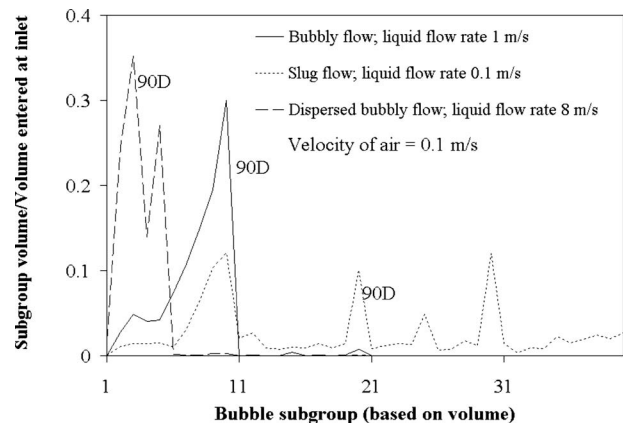


Fig. 23 Indication of different flow regimes by the bubble volume histogram obtained with a variation in liquid velocity for a fixed gas flow rate

cence of two similar or different sized bubbles and homogeneous and nonhomogeneous binary break up of a bubble has been considered in the PBM. The model has been validated rigorously against experimental results from various sources.

Using the present model an effort has been made to propose a new transition criterion from bubbly flow to slug flow. By tracking the coalescence frequency and breakup frequency along the conduit axis, the dominance of any of the processes over the other at a given condition of flow superficial velocities can easily be made. Volume count of the bubbles over and below the bubble size introduced at the inlet can be used as a criterion for the above. Additionally, the bubble count histogram obtained from the present model at different axial locations also helps to ascertain the transition from bubbly to slug flow. The transition boundary obtained by such procedure gives an excellent match with the published experimental data. At a higher liquid velocity the simulation results show a suppression of coalescence and a dominance of breakup process—a situation conducive for dispersed bubbly flow. Simulation results have been generated to obtain the maximum bubble size (Eq. (29)) needed for a transition to disperse bubbly flow. A good agreement has been obtained with the model of Brauner [67].

The present work demonstrates the strength of CFD simulation for the identification of flow regime. Even though no special turbulence model has been considered in the formulation, the model successfully defines the boundaries of bubbly flow. Furthermore, as the axial development of the flow phenomena can be studied, the model can be utilized for determining the developing length for flow through a conduit.

Nomenclature

- b^* = empirical constant of Eq. (19)
 B = empirical constant of Eq. (7)
 B_B = number of new born bubbles due to break up
 B_C = number of new born bubbles due to coalescence
 c_1 = constant in Eqs. (14) and (17)
 c_2 = empirical constant in Eq. (23)
 c_3 = empirical constant in Eq. (24)
 C_D = drag coefficient for a single bubble
 C_{FL} = interfacial friction factor
 C_{TD} = turbulent dispersion force coefficient
 d_c = critical bubble diameter for bubble breakup frequency (m)
 D_B = number of dying bubbles due to break up
 D_C = number of dying bubbles due to coalescence
 D = pipe diameter (m)
 d = diameter of the bubbles (m)
 f_{Go} = wall friction factor of gaseous phase
 f_{Lo} = wall friction factor of liquid phase
 f_v = volume fraction of daughter bubble to mother bubble
 F_{dispr} = turbulent dispersion force in the radial direction (kg m s⁻²)
 F_{dispz} = turbulent dispersion force in the axial direction (kg m s⁻²)
 F_{LGz} = interfacial force to gaseous phase in the axial direction (kg m s⁻²)
 F_{LGr} = interfacial force to gaseous phase in the radial direction (kg m s⁻²)
 F_{GLz} = mass transfer force to gaseous phase in the axial direction (kg m s⁻²)
 F_{GLr} = mass transfer force to gaseous phase in the radial direction (kg m s⁻²)
 F_{LLz} = mass transfer force to liquid phase in the axial direction (kg m s⁻²)
 F_{LLr} = mass transfer force to liquid phase in the radial direction (kg m s⁻²)

- F_{WGz} = wall gas friction force in the axial direction (kg m s⁻²)
 F_{WGr} = wall gas friction force in the radial direction (kg m s⁻²)
 F_{WLz} = wall liquid friction force in the axial direction (kg m s⁻²)
 F_{WLR} = wall liquid friction force in the radial direction (kg m s⁻²)
 g_x = gravitational acceleration in the x direction (m s⁻²)
 $g(a)$ = breakage frequency of the bubbles of diameter a (s⁻¹)
 $h(a, b)$ = effective swept volume rate for bubble diameter a and b (s⁻¹)
 k = empirical constant in Eq. (14)
 m = empirical constant in Eq. (19)
 n = empirical constant in Eq. (7)
 $n(r, z, t; d)$ = number of bubbles at (r, z) of size d at time t
 $p(a, b)$ = film rupture efficiency of bubbles of diameter a and b
 P = pressure of the mixture phase (kg m s⁻²)
 R_B = average bubble diameter (m)
 Sc_{ig} = turbulent Schmidt number for gaseous phase
 t = time (s)
 U_m = mixture velocity (m s⁻¹)
 w_g = axial velocity of dispersed phase (m s⁻¹)
 w_l = axial velocity of continuous phase (m s⁻¹)
 $v(d)$ = volume of the bubble of diameter d (m³)
 u_g = radial velocity of dispersed phase (m s⁻¹)
 u_l = radial velocity of continuous phase (m s⁻¹)
 z = axial direction of the conduit (m)
 r = radial direction of the conduit (m)

Greek Alphabet

- α = dispersed phase void fraction
 ΔP_{LO} = single phase frictional pressure drop (kg m s⁻²)
 ϵ = energy dissipation rate per unit mass (m² s⁻³)
 γ_{ig} = turbulent kinetic viscosity (m² s⁻¹)
 $\eta(a, b)$ = daughter bubble probability distribution
 $\lambda(a, b)$ = coalescence frequency of bubble diameter a and b (s⁻¹)
 μ_g = viscosity of discrete phase (kg m⁻¹ s⁻¹)
 μ_l = viscosity of continuous phase (kg m⁻¹ s⁻¹)
 $\nu(a)$ = number of bubbles formed from the breakage of a bubble diameter a
 ξ_{min} = nondimensional minimum daughter bubble size
 ρ_l = density of continuous phase (kg m⁻³)
 ρ_g = density of dispersed phase (kg m⁻³)
 σ = surface tension (kg s⁻²)

References

- Zuber, N., and Findlay, J. A., 1965, "Average Volumetric Concentration in Two Phase Flow Systems," ASME J. Heat Transfer, **87**, pp. 453–468.
- Ishii, M., and Zuber, N., 1970, "Thermally Induced Flow Instabilities in Two-Phase Mixtures," Proceedings of the Fourth International Heat Transfer Conference, Paris, France.
- Saha, P., and Zuber, N., 1978, "An Analytical Study of the Thermally Induced Two Phase Flow Instabilities Including the Effects of Thermal Non-Equilibrium," Int. J. Heat Mass Transfer, **21**, pp. 415–426.
- Kim, C., and Roy, R. P., 1981, "Two Phase Flow Dynamics by a Five Equation Drift Flux Model," Lett. Heat Mass Transfer, **8**, pp. 57–68.
- Hibiki, T., and Ishii, M., 2000, "Two-Group Interfacial Area Transport Equations at Bubbly-to-Slug Flow Transition," Nucl. Eng. Des., **202**, pp. 39–76.
- Rakhmatulin, K. A., 1956, "Fundamentals of Gas Dynamics of Interpenetrating Motions of Compressible Media," Prikl. Mat. Mekh., **20**(2), pp. 184–195.
- Ishii, M., 1977, "One Dimensional Drift Flux Model and Constitutive Equations for Relative Motion Between Phases in Various Two-Phase Flow Regimes," Argonne National Laboratory, Technical Report No. ANL-77-47.
- Wu, Q., Ishii, M., and Uhle, J., 1998, "Frame Work of Two-Group Model for

- Interfacial Area Transport in Vertical Two-Phase Flows," *Trans. Am. Nucl. Soc.*, **79**, pp. 351–352.
- [9] Fu, X. Y., and Ishii, M., 2003, "Two-Group Interfacial Area Transport in Vertical Air-Water Flow I. Mechanistic Model," *Nucl. Eng. Des.*, **219**, pp. 143–168.
- [10] Kumar, S., and Ramkrishna, D., 1996, "On the Solution of Population Balance Equations by Discretization—I. A Fixed Pivot Technique," *Chem. Eng. Sci.*, **51**(8), pp. 1311–1332.
- [11] Marchisio, D. L., Vigil, R. D., and Fox, R. O., 2003, "Quadrature Method of Moments for Aggregation-Breakage Processes," *J. Colloid Interface Sci.*, **258**, pp. 322–334.
- [12] Dorao, C. A., and Jakobsen, H. A., 2006, "A Least Squares Method for the Solution of Population Balance Problems," *Comput. Chem. Eng.*, **30**, pp. 535–547.
- [13] Yao, W., and Morel, C., 2004, "Volumetric Interfacial Area Prediction in Upwards Bubbly Two-Phase Flow," *Int. J. Heat Mass Transfer*, **47**, pp. 307–328.
- [14] Chen, P., Sanyal, J., and Duduković, M. P., 2005, "Numerical Simulation of Bubble Columns Flows: Effect of Different Breakup and Coalescence Closures," *Chem. Eng. Sci.*, **60**(4), pp. 1085–1101.
- [15] Yeoh, G. H., and Tu, J. Y., 2006, "Two-Fluid and Population Balance Models for Subcooled Boiling Flow," *Appl. Math. Model.*, **30**, pp. 1370–1391.
- [16] Cheung, S. C. P., Yeoh, G. H., and Tu, J. Y., 2007, "On the Modelling of Population Balance in Isothermal Vertical Bubbly Flows—Average Bubble Number Density Approach," *Chem. Eng. Process.*, **46**, pp. 742–756.
- [17] Jakobsen, H. A., Lindborg, H., and Dorao, C. A., 2005, "Modeling of Bubble Column Reactors: Progress and Limitations," *Ind. Eng. Chem. Res.*, **44**, pp. 5107–5151.
- [18] Krepper, E., Lucas, D., and Prasser, H. M., 2005, "On the Modelling of Bubbly Flow in Vertical Pipes," *Nucl. Eng. Des.*, **235**, pp. 597–611.
- [19] Lo, S., 1996, "Application of the MUSIG Model to Bubbly Flows," AEA Technology, Technical Report No. AEAT-1096.
- [20] Lucas, D., Krepper, E., and Prasser, H. M., 2001, "Prediction of Radial Gas Profiles in Vertical Pipe Flow on Basis of the Bubble Size Distribution," *Int. J. Therm. Sci.*, **40**, pp. 217–225.
- [21] Esmaceli, A., and Tryggvason, G., 1998, "Direct Numerical Simulations of Bubbly Flows. Part 1—Low Reynolds Number Arrays," *J. Fluid Mech.*, **377**, pp. 313–345.
- [22] Bunner, B., and Tryggvason, G., 2002, "Dynamics of Homogeneous Bubbly Flows: Part 1. Rise Velocity and Microstructure of the Bubbles," *J. Fluid Mech.*, **466**, pp. 17–52.
- [23] Bunner, B., and Tryggvason, G., 2002, "Dynamics of Homogeneous Bubbly Flows: Part 2. Velocity Fluctuations," *J. Fluid Mech.*, **466**, pp. 53–84.
- [24] Bunner, B., and Tryggvason, G., 2003, "Effect of Bubble Deformation on the Properties of Bubbly Flows," *J. Fluid Mech.*, **495**, pp. 77–118.
- [25] Biswas, S., Esmaceli, A., and Tryggvason, G., 2005, "Comparison of Results From DNS of Bubbly Flows With a Two Fluid Model for the Two-Dimensional Laminar Flows," *Int. J. Multiphase Flow*, **31**, pp. 1036–1048.
- [26] Shnip, A. I., Kolhatkar, R. V., Swamy, D., and Joshi, J. B., 1992, "Criteria for Transition From the Homogeneous to Heterogeneous Regime in Two-Dimensional Bubble Column Reactors," *Int. J. Multiphase Flow*, **18**(5), pp. 705–726.
- [27] Olmos, E., Gentric, C., Vial, C., Wild, G., and Midoux, N., 2001, "Numerical Simulation of Multiphase Flow in Bubble Column Reactors. Influence of Bubble Coalescence and Break-Up," *Chem. Eng. Sci.*, **56**, pp. 6359–6365.
- [28] Olmos, E., Gentric, C., Ponsin, S., and Midoux, N., 2003, "Description of Flow Regime Transitions in Bubble Columns Via Laser Doppler Anemometry Signal Processing," *Chem. Eng. Sci.*, **58**, pp. 1731–1742.
- [29] Sankaranarayanan, K., and Sundaresan, S., 2002, "Lift Force in Bubbly Suspensions," *Chem. Eng. Sci.*, **57**, pp. 3521–3542.
- [30] Taitel, Y., Bornea, D., and Dukler, A. E., 1980, "Modelling Flow Pattern Transitions for Steady Upward Gas-Liquid Flow in Vertical Tubes," *AIChE J.*, **26**(3), pp. 345–354.
- [31] Dukler, A. E., and Taitel, Y., 1977, "Flow Regime Transitions for Vertical Upward Gas Liquid Flow," Houston University, Progress Report No. 2, NUREG-0163.
- [32] Mishima, K., and Ishii, M., 1984, "Flow Regime Transition Criteria for Upward Two-Phase Flow in Vertical Tubes," *Int. J. Heat Mass Transfer*, **27**, pp. 723–737.
- [33] Anderson, T. B., and Jackson, R., 1967, "A Fluid Mechanical Description of Fluidized Beds: Equations of Motion," *Ind. Eng. Chem. Fundam.*, **6**, pp. 527–539.
- [34] Richter, H. J., 1983, "Separated Two-Phase Flow Model: Application to Critical Two Phase Flow," *Int. J. Multiphase Flow*, **9**(5), pp. 511–530.
- [35] Chisholm, D., 1973, "Pressure Gradient Due to Friction During the Flow of Evaporating Two Phase Mixtures in Smooth Tubes and Channel," *Int. J. Heat Mass Transfer*, **16**, pp. 347–358.
- [36] Burns, A. D., Frank, T., Hamill, I., and Shi, J., 2004, "The Farve Averaged Drag Model for Turbulent Dispersion in Eulerian Multi-Phase Flows," Proceedings of the Fifth International Conference on Multiphase Flow, Yokohama, Japan.
- [37] Ramkrishna, D., 2000, *Population Balances—Theory and Applications to Particulate Systems in Engineering*, Academic, San Diego, CA.
- [38] Wang, T., Wang, J., and Jin, J., 2003, "A Novel Theoretical Breakup Kernel Function for Bubbles/Droplets in a Turbulent Flow," *Chem. Eng. Sci.*, **58**, pp. 4629–4637.
- [39] Luo, H., and Svendsen, H. F., 1996, "Theoretical Model for Drop and Bubble Breakup in Turbulent Dispersions," *AIChE J.*, **42**, pp. 1225–1233.
- [40] Kostoglou, M., and Karabelas, A. J., 2005, "Towards a Unified Framework for the Derivation of Breakage Functions Based on the Statistical Theory of Turbulence," *Chem. Eng. Sci.*, **60**, pp. 6584–6595.
- [41] Ioannou, K., Hu, B., Matar, O. K., Hewitt, G. F., and Angeli, P., 2004, "Phase Inversion in Dispersed Liquid-Liquid Pipe Flows," Proceedings of the Fifth International Conference on Multiphase Flow, Yokohama, Japan.
- [42] Tsouris, C., and Tavlirides, L. L., 1994, "Breakage and Coalescence Models for Drops in Turbulent Dispersions," *AIChE J.*, **40**, pp. 395–406.
- [43] Troshko, A. A., and Zdravistch, F., 2009, "CFD Modeling of Slurry Bubble Column Reactors for Fisher-Tropsch Synthesis," *Chem. Eng. Sci.*, **64**, pp. 892–903.
- [44] Carrica, P. M., and Clause, A. A., 1993, "Mathematical Description of the Critical Heat Flux as Nonlinear Dynamic Instability," *Instabilities in Multiphase Flow*, G. Gouesbet and A. Berlemont, eds., Plenum, New York.
- [45] Kostoglou, M., and Karabelas, A. J., 1998, "Theoretical Analysis of Steady State Particle Size Distribution in Limited Breakage Process," *J. Phys. A*, **31**, pp. 8905–8921.
- [46] Tomiyama, A., Nakahara, Y., Adachi, Y., and Hosokawa, S., 2003, "Shapes and Rising Velocities of Single Bubbles Rising Through an Inner Subchannel," *J. Nucl. Sci. Technol.*, **40**, pp. 136–142.
- [47] Coualoglou, C. A., and Tavlirides, L. L., 1977, "Description of Interaction Processes in Agitated Liquid-Liquid Dispersions," *Chem. Eng. Sci.*, **32**, pp. 1289–1297.
- [48] Chesters, A. K., 1991, "The Modelling of Coalescence Processes in Fluid-Liquid Dispersions: A Review of Current Understanding," *Trans. Inst. Chem. Eng.*, **69**, pp. 259–270.
- [49] Lovick, J., 2004, "Horizontal Oil-Water Flows in the Dual Continuous Flow Regime," Ph.D. thesis, University College London, England.
- [50] Hu, H. G., and Zhang, C., 2007, "A Modified $k-\epsilon$ Turbulence Model for the Simulation of Two-Phase Flow and Heat Transfer in Condensers," *Int. J. Heat Mass Transfer*, **50**, pp. 1641–1648.
- [51] Ekambara, K., Sanders, R. S., Nandakumar, K., and Masliyah, J. H., 2008, "CFD Simulation of Bubbly Two-Phase Flow in Horizontal Pipes," *Chem. Eng. J.*, **144**, pp. 277–288.
- [52] Prosperetti, A., and Tryggvason, G., 2007, "Introduction: A Computational Approach to Multiphase Flow," A. Prosperetti and G. Tryggvason, eds., *Computational Methods for Multiphase Flow*, Cambridge University Press, Cambridge, England.
- [53] Tomiyama, A., and Shimada, N., 2001, "A Numerical Method for Bubbly Flow Simulation Based on a Multi-Fluid Model," *ASME J. Pressure Vessel Technol.*, **123**, pp. 510–516.
- [54] Schumann, U., 1975, "Subgrid Scale Model for Finite Difference Simulations of Turbulent Flows in Plane Channels and Annuli," *J. Comput. Phys.*, **18**, pp. 376–404.
- [55] Serizawa, A., Kataoka, I., and Michiyoshi, I., 1975, "Turbulence Structure of Air-Water Bubbly Flow—II. Local Properties," *Int. J. Multiphase Flow*, **2**, pp. 235–246.
- [56] Ohnuki, A., and Akimoto, H., 2000, "Experimental Study on Transition of Flow Pattern and Phase Distribution in Upward Air-Water Two-Phase Flow Along a Large Vertical Pipe," *Int. J. Multiphase Flow*, **26**(3), pp. 367–386.
- [57] Shen, X., Mishima, K., and Nakamura, H., 2005, "Two-Phase Flow Distribution in a Vertical Large Diameter Pipe," *Int. J. Heat Mass Transfer*, **48**(1), pp. 211–225.
- [58] Nakoryakov, V. E., Kashinsky, O. N., Randin, V. V., and Timkin, L. S., 1996, "Gas Liquid Bubbly Flow in Vertical Pipes. Data Bank Contribution," *ASME J. Fluids Eng.*, **118**, pp. 377–382.
- [59] Lucas, D., Krepper, E., and Prasser, H. M., 2005, "Development of Co-Current Air-Water Flow in a Vertical Pipe," *Int. J. Multiphase Flow*, **31**, pp. 1304–1328.
- [60] Radovicich, N. A., and Moissis, R., 1962, "The Transition From Twophase Bubble Flow to Slug Flow," MIT Technical Report No. 7-7633-22.
- [61] Bilicki, Z., and Kestin, J., 1987, "Transition Criteria for Two Phase Flow Patterns in Vertical Upward Flow," *Int. J. Multiphase Flow*, **13**, pp. 283–294.
- [62] Mercadier, Y., 1981, "Contribution à l'étude des propagations de perturbations de taux de vide dans les écoulements diphasiques eau-air à bulles," Ph.D. thesis, Institut National Polytechnique de Grenoble, Université Scientifique et Médicale, France.
- [63] Matuszkiewicz, A., Flamand, J. C., and Boure, J. A., 1987, "The Bubble Slug Flow Pattern Transition and Instabilities of Void Fraction Waves," *Int. J. Multiphase Flow*, **13**, pp. 199–217.
- [64] Sun, B., Wang, R., Zhao, X., and Yan, D., 2002, "The Mechanism for the Formation of Slug Flow in Vertical Gas-Liquid Two Phase Flow," *Solid-State Electron.*, **46**, pp. 2323–2329.
- [65] Krussenberg, A. K., Prasser, H. M., and Schaffrath, A., 1999, "A New Criterion for the Bubble Slug Transition in Vertical Tubes," Proceedings of the Ninth International Topical Meeting on Nuclear Reactor Thermal Hydraulics (NURETH-9), San Francisco, CA.
- [66] Hinze, J., 1955, *Turbulence*, McGraw-Hill, New York.
- [67] Brauner, N., 2001, "The Prediction of Dispersed Flows Boundaries in Liquid-Liquid and Gas-Liquid Systems," *Int. J. Multiphase Flow*, **27**, pp. 885–910.

Transition of Bubbly Flow in Vertical Tubes: Effect of Bubble Size and Tube Diameter

A. K. Das

e-mail: arup@mech.iitkgp.ernet.in

P. K. Das¹

e-mail: pkd@mech.iitkgp.ernet.in

Department of Mechanical Engineering,
IIT Kharagpur,
721302, India

J. R. Thome

LCTM,
EPFL,
Lausanne CH-1015, Switzerland
e-mail: john.thome@epfl.ch

In a companion paper ("Modelling Bubbly Flow by Population Balance Technique Part I: Axial Flow Development and Its Transitions," ASME J. Fluids Eng), a two fluid model along with a multiclass population balance technique has been used to find out comprehensive criteria for the transition from bubbly to slug flow, primarily through a study of axial flow development. Using the same basic model the transition mechanism has been investigated in the present paper covering a wide range of process parameters. Though the dominating rate of bubble coalescence during the axial development of the flow acts as the main cause for the transition to slug flow, the simultaneous transformation of the radial voidage pattern cannot be overlooked. Appearance of core, intermediate, wall, and two peaks are observed in the radial voidage distribution depending on the phase superficial velocities. A map has been developed indicating the boundaries of the above sub-regimes. It has been observed that not only the size of the bubbles entering the inlet plane but also the size distribution (monodispersion or bidispersion) changes the voidage peak and shifts the transition boundary. It is interesting to note that the bubbly flow only with a core peak void distribution transforms into slug flow with a change in the operating parameters. Transition boundary is also observed to shift with a change in the tube diameter. The simulation results have been compared with experimental data taken from different sources and very good agreements have been noted. [DOI: 10.1115/1.3203206]

Keywords: bubbly flow, population balance, transition, wall peaking, core peaking

1 Introduction

A bubbly flow often appears as a homogeneous dispersion of gas bubbles in a liquid medium. In reality, the flow regime is rather complex due to the presence of different spatial-temporal structures and the interplay of various complex mechanisms. The motion of a bubble is the result of a large number of forces, namely fluid-fluid interaction, bubble transverse dispersion, wall lubrication, Magnus force, etc. Depending on the relative magnitude of these forces, different variations are possible in the bubbly flow. It is well known that the pattern of void distribution in a cross sectional plane could be wall peaked or core peaked depending on the operating conditions [1–4]. It has also been reported that the conduit size has a distinct effect on the bubbly flow pattern. Further, the bubbly flow is influenced by the characteristics of the bubble inputs. Development of the void profile is not identical in the case of monodispersed and polydispersed bubble inputs.

Modeling of the bubbly flow with all its complexities is a formidable task. Nevertheless, due to the occurrence of the bubbly flow in widespread industrial application, numerous efforts have been made to model it. Based on generalized two fluid approach [5,6], Antal et al. [7] developed a model for two-phase bubbly flow. Troshko and Hassan [8] presented a two-phase flow model including the near wall region and developed a two-phase wall law. To model the turbulence, they extended the single-phase standard k - ϵ model for two-phase flow, neglecting the turbulence in the dispersed phase. But their model is valid only for monodispersed flow of gaseous bubbles in the bulk liquid. Politano et al. [9] used the two fluid model, considering the bubble size distribution

with groups of constant mass. Their model can predict the presence of wall and core peakings but remains silent about the possibility of any other voidage profile. Carrica and Clausse [10] solved the behavior of polydispersed bubble formation using a multigroup model along with a two fluid model. Recently, Kreeper et al. [11] used the N - M MUSIG model for solving bubbly flow having N velocity group and M bubble group size. Yeoh and Tu [12] solved the population balance equation in axial direction along with a two fluid model using the method of discrete classes in order to incorporate the effect of bubble size.

In a companion paper [13], using the two-fluid model and the population balance technique, the hydrodynamics of bubbly flow has been simulated. Emphasis has been given on the analysis of axial flow development. The population balance technique enables one to detect the bubble population at any axial level and to assess the process of coalescence and breakage. An objective and comprehensive criterion for the transition from bubbly to slug flow has been proposed. The simulation shows excellent agreement with published results.

Certainly the importance of axial development cannot be overlooked as it has direct bearing to the transition. Nevertheless, hydrodynamics of bubbly flow strongly depends also on the phase distribution and bubble population along the radial direction. This gives rise to different peaked structure [1,3,14] of the void fraction and also influences the transition. To date the prediction of bubbly-slug transition based on superficial phase velocities [15,16] is well accepted by many researchers. However, such a criterion does not take into cognition the effect of inlet bubble size [17] and tube diameter [18] on the transition from bubbly to slug flow. In the present paper, the basic two fluid and population balance model [13] for bubbly flow has been employed to investigate the above issues. In the first part of the paper, we have made a thorough study on the radial distribution of dispersed phase. In the second part, the effect of operating variables other than the phase velocities on the flow regime transition has been investigated.

¹Corresponding author.

Contributed by the Fluids Engineering Division of ASME for publication in the JOURNAL OF FLUIDS ENGINEERING. Manuscript received January 13, 2009; final manuscript received June 23, 2009; published online August 18, 2009. Assoc. Editor: Theodore Heindel.

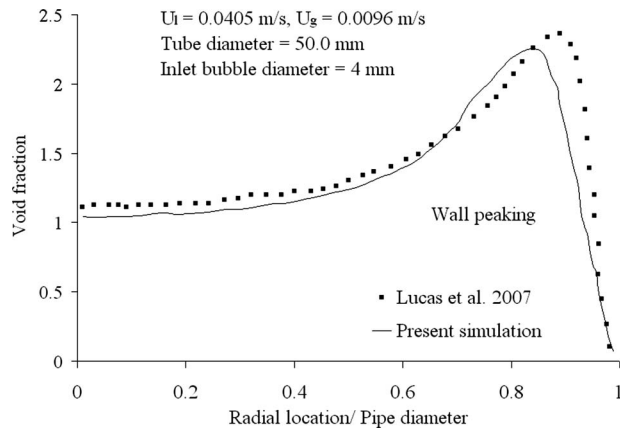


Fig. 1 Comparison of the void distribution of the present model and the experimental observations of Lucas et al. [20] at low phase flow rates

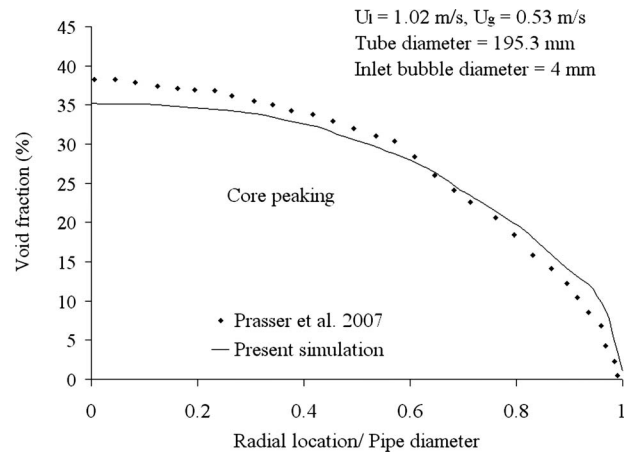


Fig. 2 Comparison of the void distribution of the present model and the experimental observations of Prasser et al. [21] at high phase flow rates

Excellent agreement has been obtained between the simulation and the experimental data obtained from various sources.

2 Results and Discussion

In a number of experiments on gas liquid upflow through vertical conduits, nonuniform void distribution has been observed at the downstream while gas bubbles were introduced uniformly at the inlet plane. Theoretical simulations of the bubbly flow also corroborate the peaked characteristic of the void profile [15,19]. It is important to note that not only the absolute value of the void fraction varies in the different flow regimes, each of the regimes has a typical pattern for radial distribution of the void fraction. Therefore, in the present paper, we want to investigate further into the transformation of the void profile due to the operating and inlet conditions.

The present model is compared with the experimental void fraction obtained by Zun [3], Song et al. [4], and Lucas et al. [20] in the case of a two-phase flow mixture of air and water in vertical ducts. To simulate the experiments, the ducts were discretized into 40 radial nodes with finer discretization near the wall of the tube. In the axial direction 500 uniform spaced grids were generated to track the evolution of the bubbly flow. Bubble mass is divided into 40 equal groups by volume to eradicate the complexity of the volume discretization during the coalescence of bubbles. In case of bubble breakage, if the daughter bubbles do not fall in an exact size group they are distributed among its immediate neighbors, maintaining the conservation of mass and number.

An extensive study of the bubbly flow [20] has been made in the MTL loop facility. The test section in this loop has an inner diameter of 52.3 mm and a length of 3.5 m. Wire mesh sensors have been used for the measurement of void fractions at a distance of $60D$ from the inlet. Figure 1(a) shows the simulation results at an air flow rate of 0.0096 m/s and a water flow rate of 0.0405 m/s as has been used by Lucas et al. [20]. Most of the bubbles are gathered near the wall of the tube. Results from the present model also show a similar pattern of the void fraction distribution. Similar experimental studies were made by Prasser et al. [21]. They used a larger tube with 195.3 mm diameter and 8.78 m length. At an air flow rate of 0.53 m/s and water flow rate of 1.02 m/s, they observed that the void distribution pattern changed (Fig. 2) into a parabolic shape exhibiting core peak. Simulation results for the same conditions satisfactorily agree (Fig. 2) with the experimental observations. This shows that the present model can handle both inward and outward lateral migrations of the bubbles, depending on the flow velocities and tube diameter.

Zun [3] proposed that uniform input of big bubbles at the inlet produces a core peak while smaller bubbles at the inlet produce a wall peak. Interestingly, when a mixture of big and small bubbles

is introduced at the inlet, simultaneous occurrence of wall and core peaks is possible at further downstream. According to Zun [3], the bubbles, having high intrinsic oscillatory motion, stay near the wall and the others settle at the core of the conduit as the amplitude of the oscillation is a strong function of the bubble diameter. To demonstrate this, Zun [3] conducted an experiment using a vertical conduit of square cross section having 25.4 mm sides. Downstream gas void fraction was measured using micro-sensitivity probes. Experiments were conducted for different inlet bubble sizes and void fractions. In general, experiments were conducted for low gas flow rates. Results are depicted in Fig. 3. As the present model is an axisymmetric one, an exact simulation of the results of Zun [3] is not possible. However, simulations have been done for a circular tube using identical operating conditions. Simulation results exhibit excellent trend matched with the experimental results of Zun [3].

The shape of the void distribution in the downstream due to the injection of two different bubble sizes at the inlet has also been investigated by Song et al. [4]. They used a vertical tube with 29 mm inner diameter and 3.7 m length to study the development of the voidage profile in a mineral oil-air flow. Nozzles of different sizes were used to produce bubbles of two different diameters. 3D photographic method was used for measuring the position of the bubbles and the void fraction profile was derived from it. Figure 4 shows the comparison of the estimated void distribution against the experimental observation by Song et al. [4] for the simultaneous entry of 3.4 mm and 2.5 mm diameter bubbles. Liquid flow

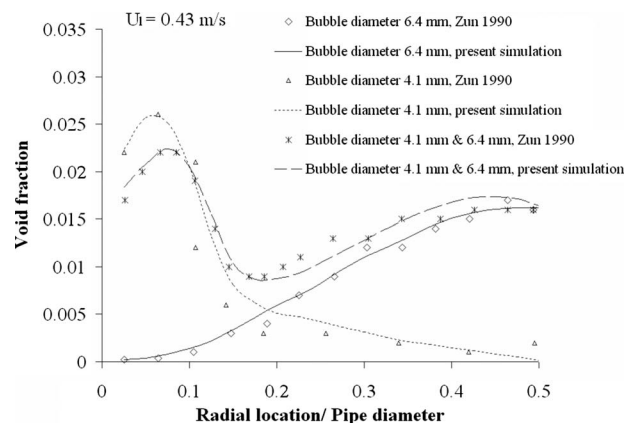


Fig. 3 Comparison of the two peak void distributions; present model versus experimental observations of Zun [3]

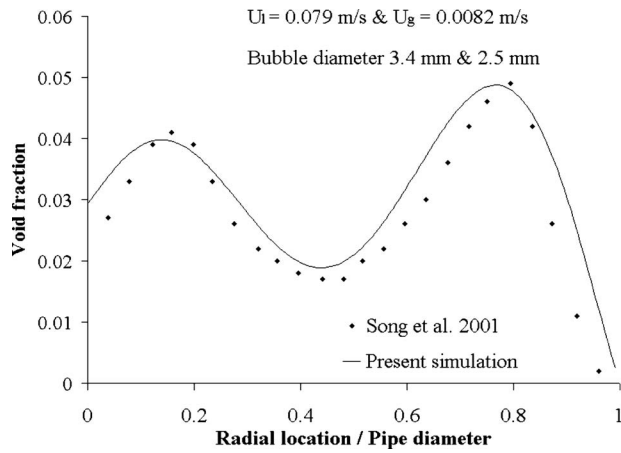


Fig. 4 Comparison of the two peak void distributions; present model versus experimental observations of Song et al. [4]

rate is kept at 0.079 m/s and air flow rate is maintained at 0.0082 m/s, which are identical to the experimental conditions of Song et al. [4]. Generated results at an axial length of $60D$ were presented to minimize the entrance effect. Agreement between the simulation and experiment is reasonably well.

Occurrence of different peaked structures of the voidage profile in the bubbly flow has been observed in different independent experiments [1]. The reason for this has loosely been attributed to the forces acting on individual bubbles and the interactions between neighboring bubbles. As the evolution of the voidage profile is a result of the interplay of various complex phenomena, its prediction is not possible through a control volume based model (prevalent in the analysis of the two-phase flow). On the contrary, a computational fluid dynamics (CFD) simulation with an inbuilt capability to model the bubble interactions can simulate this phenomenon reasonably well. The capability of the present model for predicting bubbly-slug transition has been presented in an earlier communication [13]. The model prediction depicts a good match with the regime boundary proposed by Taitel et al. [22] experimentally. It is interesting to note that a unique regime boundary was not observed by different investigators. In Fig. 5 bubbly-slug transitions as observed in different experiments point out a substantial difference between themselves. While the trend of the transition boundary of Griffith and Wallis [23], Dukler and Taitel [15], and Mishima and Ishii [24] are similar (which also matches with the prediction of the present simulation), the nature of the other transition boundaries [22,25–28] are different. It may be quite possible that the difference in the inlet condition of the spe-

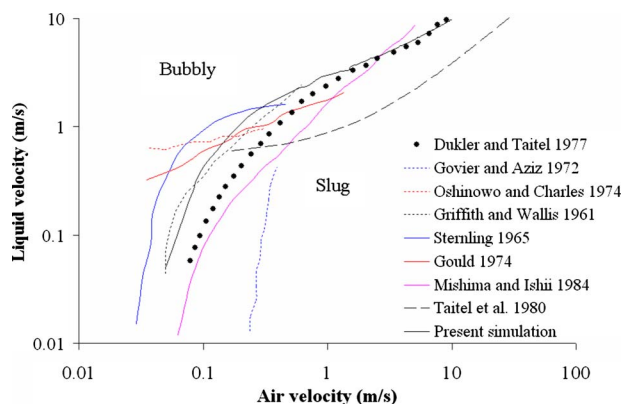


Fig. 5 Comparison of the existing flow pattern maps with the present prediction

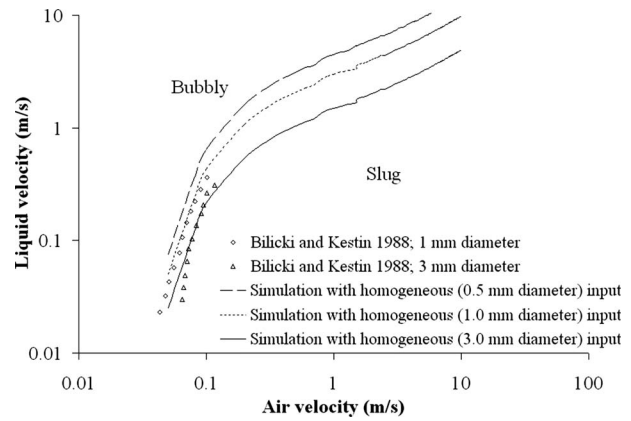


Fig. 6 Effect of bubble size (homogeneous distribution) at the inlet on the flow pattern map

cific experiments is mainly responsible for this mismatch. Unfortunately, in most of the experimental results the inlet conditions, particularly the bubble size distribution, have not been specified explicitly. Therefore, it is difficult to substantiate the above proposition directly. As an alternative, we have tried to predict the transition boundary for different inlet conditions. The results are discussed below.

To see the effect of bubble size at the inlet on the flow pattern map, results were generated using the present model for homogeneous inputs of various bubble sizes. Figure 6 shows the change in the flow regime map due to the change in the bubble size at the inlet from 0.5 mm to 1 mm and then to 3 mm. Bubbly flow turns into slug flow at a lower flow rate of liquid for a fixed gas flow rate with the increase in inlet bubble size. It is obvious that bubbles of higher size at the input takes less effort to merge into a big gaseous slug. Results generated from the developed model efficiently support the intuitive concept about bubble coalescence. Flow pattern map of Bilicki and Kestin [29] for different sized bubble inputs are also plotted in Fig. 6 to support the results generated from the present model. A plexiglass tube with 20 mm diameter and 1.5 m length has been used in Ref. [29] to view the two-phase flow patterns for air and water. Tests were carried out for bubble diameters of 1 mm and 3 mm. The observations are in close concordance with the simulation results.

In most of the experiments monosized bubbles are rarely injected at the inlet. In general there could be a distribution of bubble size. Simulations are made to study the effect of a mixed bubble population at the inlet on the flow regime transition. Different inlet populations consisting mainly of (a) 0.5 mm bubble diameter, (b) 1 mm bubble diameter and (c) 2 mm bubble diameter as well as (d) 50% bubbles of 0.5 mm diameter+50% of 1 mm diameter, and (e) 50% bubbles of 1 mm diameter+50% of 2 mm diameter were considered at the inlet, as shown in Fig. 7. In all the cases, the inlet volume fraction is kept constant. It can be seen that with the mixing of higher sized bubbles the flow pattern map for 1 mm diameter bubbles at the inlet shifts downward, causing the transition at a lower air flow rate. Similarly, when 0.5 mm diameter bubbles are mixed with 1 mm diameter bubbles, slug bubbles appear at a higher gas flow rate for a fixed liquid flow rate compared with the homogeneous input of 1 mm diameter bubbles. This analysis can be extended further to investigate the effect of polydispersed bubble input at the inlet plane on the void distribution profiles and flow pattern map. It is also clear from the results generated from the simulation that along with the superficial velocities, the bubble diameter is an important parameter for the transition of bubbly flow to slug flow. It is interesting to note that curves a and d, and curves c and e intersect each other, indicating an implicit effect of the inlet bubble size on the transition boundary. Effect of mixing two different bubble sizes cannot

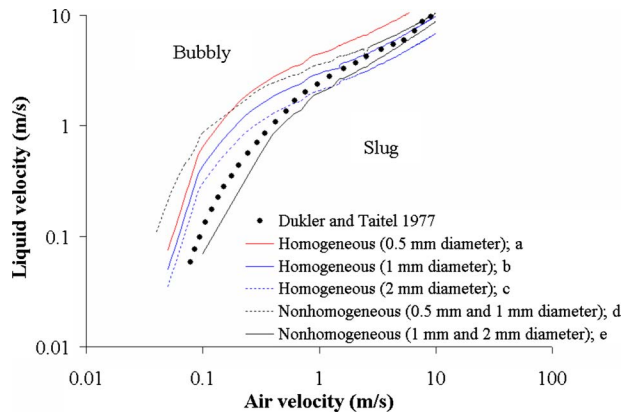


Fig. 7 Effect of bubble size (nonhomogeneous distribution) at the inlet on the flow pattern map

be predicted (even qualitatively) from the logic of linear averaging. The input bubble diameter distribution influences the hydrodynamics in a number of ways. It has got direct effects on the rate of breakage and coalescence as well as on the drag force. The laws governing these phenomena are strongly nonlinear. The regime boundaries depicted in Fig. 7 is a reflection of that fact.

It is a well recognized fact that flow regime transition is not a discrete event. It is more likely that a fully developed bubbly flow transforms into a fully developed slug flow through a gradual change. In this regard the different peaked structures of the voidage distributions in bubbly flow may have a role to play. The present model has been used to investigate this. For a case study, uniform distribution of bubbles of $0.05D$ has been considered at the inlet plane and the void fraction profile is investigated at $60D$ from the inlet. Figure 8 shows the boundary obtained between the wall and core peaking void fraction profiles based on the liquid and gaseous phase flow velocities. To make a comparison with the available void distribution, map results of Serizawa and Kataoka [30], Ohnuki and Akimoto [14], and Lucas et al. [31] are depicted in the same figure. Serizawa and Kataoka [30] proposed a band of flow velocities beyond which a void fraction profile with core peaking changes into a profile with wall peaking. Present results of the simulation falls well in the band proposed by Serizawa and Kataoka [30]. The boundaries proposed by Ohnuki and Akimoto [14] and Lucas et al. [31], though fall within the band, do not match well with the present simulation. In their model, Lucas et al. [31] assumed that the whole bubble mass is divided into three separate bubble groups, whereas in the present simulation 40 sub-groups have been considered. This may be one of the reasons in the discrepancy of the results.

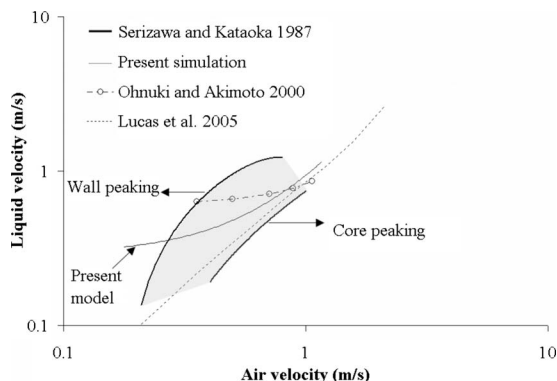


Fig. 8 Ranges of wall and core peakings

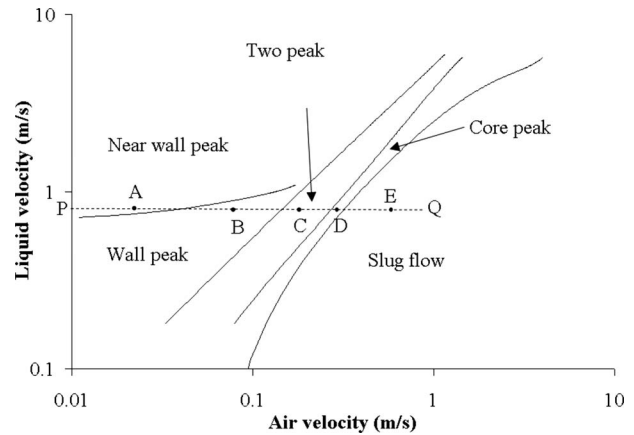


Fig. 9 Subregimes in the bubbly flow based on the voidage profile

To appreciate further the development of the voidage profile and its effect on the flow regime transition, one may refer to Fig. 9. Here, a line PQ drawn parallel to the abscissa, indicating increasing gas superficial velocities at a constant liquid superficial velocity, is tracked. Point A on this curve indicates a peak very near the wall at a low gas flow rate. With the increase in gas flow rate (point B) the peak shifts away from the wall. With a further increase in gas flow rate (point C), two peaks—one at the pipe center and another near the wall—appears. Subsequent increase in gas superficial velocity (point D) strengthens the core peak while the wall peak disappears. Finally, one gets slug flow by increasing the air velocity further (point E). This also reveals the physics of flow regime transition. Slug flow constitutes of a pseudoperiodic movement of Taylor bubbles and spherical bubble laden liquid slugs through any cross sections. From the above observation it can be said that the formation of the Taylor bubbles is pre-empted by a dense voidage (as well as larger bubbles) at the core of the conduit. This is also supported by experimental observations [32].

Over the years, numerous efforts [22,33,34] have been made to predict the bubbly-slug transition criteria for concurrent upflow through a vertical tube. Different dimensional and nondimensional parameters have been selected as the coordinate axes for representing the flow regime boundary on a two dimensional plane. Out of all such efforts the model of Dukler and Taitel [35] is one of the most popular. Based on the argument of maximum packing density of the spherical bubbles, the maximum void fraction has been predicted in this model. While doing so, a uniform distribution of bubbles in an infinite mixture medium has been considered without taking any cognition of the tube wall effect. With a simplifying assumption, the limiting void fraction achieved was 25%. The authors have further used the material conservation and the relationship for slip velocity to obtain the transition criteria in terms of the phase superficial velocities. This is a simple yet elegant derivation, which showed reasonable agreements with a number of experimental results. The idealizations made in the model, namely, one dimensionality and invariance with bubble and tube diameters were essential for obtaining a simple closed form expression as the transition criteria.

It has already been demonstrated that the bubble size influences the transition boundary. Evidence is also available in the literature indicating different flow structure and transition boundaries for different tube diameters. To examine exclusively the effect of the tube diameter on the transition boundary, one needs to conduct experiments with different tube sizes and identical inlet bubble populations. However, such results are readily not available. We have simulated bubbly flow for different conduit diameters (25.4 mm, 50.8 mm, and 76.2 mm) with uniform distribution of 2.54 mm diameter bubbles at the inlet. For 25.4 mm and 50.8 mm pipe geometries, 40 grids have been taken in radial direction whereas

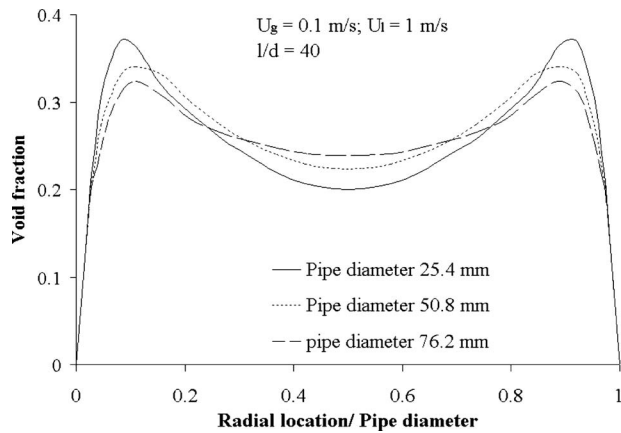


Fig. 10 Effect of tube diameter on the void fraction profile at low phase velocities

60 grids have been taken for the 76.2 mm diameter tube. Axial length is kept constant for all the tube diameters at 5 m. All the results depicted in the present paper are taken at a distance of $40D$ from the inlet plane. Results are depicted in Figs. 10–12. Void fraction distribution at an air flow rate of 0.1 m/s and a liquid flow rate of 1 m/s is depicted in Fig. 10 for all the three tube sizes. In all the cases, sharp peak can be visible at the wall of the conduit. At a 25.4 mm diameter the rise of the peak is highest at the vicinity of the wall while the deepest valley is observed at the central region. With the increase in the diameter the peak sharpness decreases, making the voidage profile relatively uniform. The position of the peak near the wall also shifts toward the center of the tube geometry. Results of the void fraction distribution for various tube diameters at higher liquid (3 m/s) and air (2 m/s) flow rates are depicted in Fig. 11. In all the cases, core peaking is observed. However, the profile becomes flatter with the increase in the tube diameter. The figures bring out the diminishing wall effect on the gaseous phase with the increase in the tube diameter.

As the change in tube diameter causes a change in the voidage profile, it is not unwise to expect that the tube diameters may have an effect on the flow regime transition. Flow regime boundary has been constructed using the present simulation for the three different tube diameters, as shown in Fig. 12. There is a distinct upward shift of the transition line with the increase in the conduit size. The data available for the 25.4 mm [18] and 50.8 mm [22] tube diameters exhibit reasonable agreement with the simulation results.

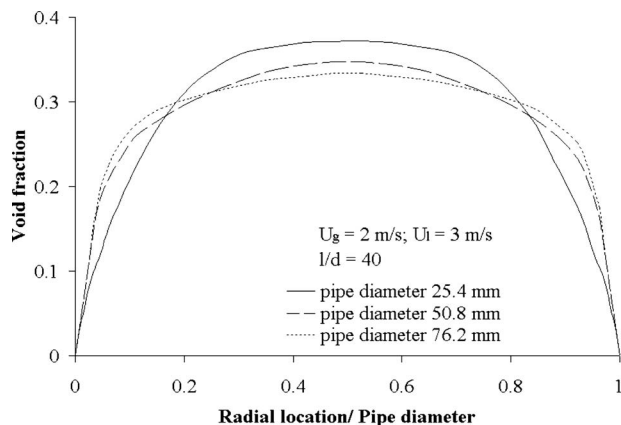


Fig. 11 Effect of tube diameter on the void fraction profile at high phase velocities

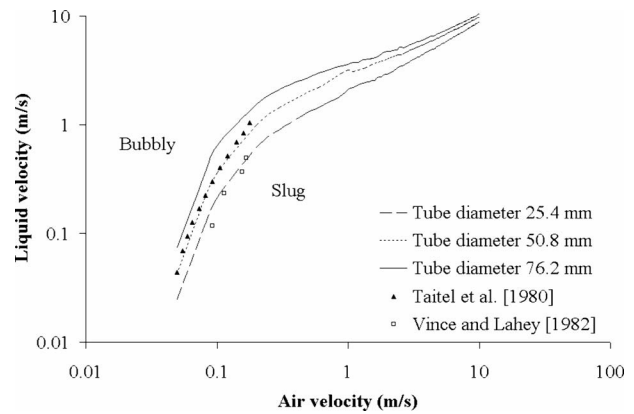


Fig. 12 Bubbly to slug transition boundary for different tube diameters

3 Conclusion

A two fluid model along with a population balance technique [13] has been employed for an in depth study of the hydrodynamics of the bubbly flow in a vertical conduit. The observations are reported in two papers. In the present paper, the distribution of the dispersed phase in radial plane and the effect of the inlet bubble size and tube diameter on the transition to slug flow have been investigated in details. The salient observations are enumerated below as follows:

1. The capability of the model for predicting different peaked structures of the void distribution in the bubbly flow has been demonstrated. A regime map has been constructed, showing near wall, wall, two, and core peaks with a gradual increase in the superficial gas velocity. This diagram makes a clear demonstration of the formation of slug flow from a core peak rich in gas concentration.
2. The model has convincingly demonstrated that the phase superficial velocities are not the sole parameters to dictate the transition of the flow regimes. The inlet bubble size plays a crucial role in the axial development of the bubbly flow and its transition to slug flow. When uniform sized bubbles are introduced at the inlet, the regime boundary experiences an upward shift with a decrease in the bubble size.
3. When bubbles of different sizes are considered at the inlet plane, the shift in regime boundary becomes complex, as can be seen from Fig. 7. The crossover between the different regime boundaries probably indicates a change in the bubble hydrodynamics at various ranges of the phase velocities.
4. Present simulation also depicts that the tube diameter has an influence on both the void distribution and transition boundary.

The present paper (along with the companion paper [13]) establishes the strength of the CFD technique in the simulation of complex two-phase hydrodynamics. Though the simulation is based on an averaged formulation and uses no special model for turbulence, the results agree well with experimental data taken from a diverse source. The simulation brings out a better physical picture of the bubbly flow, which was hitherto impossible through control volume based or one dimensional model. Though there is a scope for the improvisation of the model, the need for new experimental data for its validation cannot be overlooked.

References

- [1] Serizawa, A., Kataoka, I., and Michiyoshi, I., 1975, "Turbulence Structure of Air-Water Bubbly Flow—II Local Properties," *Int. J. Multiphase Flow*, **2**, pp. 235–246.
- [2] Sekoguchi, K., Fukui, H., and Sato, Y., 1981, "Flow Characteristics and Heat Transfer in Vertical Bubble Flow," *Proceedings of Japan-U.S. Seminar on*

- Two-Phase Flow Dynamics*, Hemisphere, Washington, DC, pp. 59–74.
- [3] Zun, I., 1990, “The Mechanism of Bubble Non-Homogeneous Distribution in Two-Phase Shear Flow,” *Nucl. Eng. Des.*, **118**, pp. 155–162.
- [4] Song, Q., Luo, R., Yang, X. Y., and Wang, Z., 2001, “Phase Distributions for Upward Laminar Dilute Bubbly Flows With Non-Uniform Bubble Sizes in Vertical Pipe,” *Int. J. Multiphase Flow*, **27**, pp. 379–390.
- [5] Ishii, M., 1977, “One Dimensional Drift Flux Model and Constitutive Equations for Relative Motion Between Phases in Various Two-Phase Flow Regimes,” Argonne National Laboratory, Technical Report No. ANL-77-47.
- [6] Drew, D. A., and Lahey, R. T., 1979, “Application of General Constitutive Principles to the Derivation of Multidimensional Two-Phase Flow Equations,” *Int. J. Multiphase Flow*, **5**, pp. 243–264.
- [7] Antal, S. P., Lahey, R. T., Jr., and Flaherty, J. E., 1991, “Analysis of Phase Distribution in Fully Developed Laminar Bubbly Two-Phase Flow,” *Int. J. Multiphase Flow*, **17**, pp. 635–652.
- [8] Troshko, A. E., and Hassan, Y. A., 2001, “A Two-Equation Turbulence Model of Turbulent Bubbly Flows,” *Int. J. Multiphase Flow*, **27**, pp. 1965–2000.
- [9] Politano, M. S., Carrica, P. M., and Converti, J., 2003, “A Model for Turbulent Polydisperse Two Phase Flow in Vertical Channels,” *Int. J. Multiphase Flow*, **29**, pp. 1153–1182.
- [10] Carrica, P. M., and Clause, A. A., 1993, “Mathematical Description of the Critical Heat Flux as Nonlinear Dynamic Instability,” *Instabilities in Multiphase Flow*, G. Gouesbet and A. Berlemont, eds., Plenum, New York.
- [11] Krepper, E., Lucas, D., and Prasser, H. M., 2005, “On the Modelling of Bubbly Flow in Vertical Pipes,” *Nucl. Eng. Des.*, **235**, pp. 597–611.
- [12] Yeoh, G. H., and Tu, J. Y., 2006, “Two-Fluid and Population Balance Models for Subcooled Boiling Flow,” *Appl. Math. Model.*, **30**, pp. 1370–1391.
- [13] Das, A. K., Das, P. K., and Thome, J. R., 2009, “Transition of Bubbly Flow in Vertical Tubes: New Criteria Through CFD Simulation,” *ASME J. Fluids Eng.*, In Press.
- [14] Ohnuki, A., and Akimoto, H., 2000, “Experimental Study on Transition of Flow Pattern and Phase Distribution in Upward Air-Water Two-Phase Flow Along a Large Vertical Pipe,” *Int. J. Multiphase Flow*, **26**(3), pp. 367–386.
- [15] Dukler, A. E., and Taitel, Y., 1977, “Flow Regime Transitions for Vertical Upward Gas Liquid Flow,” Houston University, Technical Report No. 2, NUREG-0163.
- [16] Fu, X. Y., and Ishii, M., 2003, “Two-Group Interfacial Area Transport in Vertical Air-Water Flow I. Mechanistic Model,” *Nucl. Eng. Des.*, **219**, pp. 143–168.
- [17] Bilicki, Z., and Kestin, J., 1988, “Experimental Investigation of Certain Aspects of Upward Vertical Bubble and Slug Flows,” *Exp. Fluids*, **6**, pp. 455–460.
- [18] Vince, M. A., and Lahey, R. T., 1982, “On the Development of an Objective Flow Regime Indicator,” *Int. J. Multiphase Flow*, **8**, pp. 93–124.
- [19] Cheung, S. C. P., Yeoh, G. H., and Tu, J. Y., 2007, “On the Modelling of Population Balance in Isothermal Vertical Bubbly Flows—Average Bubble Number Density Approach,” *Chem. Eng. Process.*, **46**, pp. 742–756.
- [20] Lucas, D., Krepper, E., and Prasser, H. M., 2007, “Use of Models for Lift, Wall and Turbulent Dispersion Forces Acting on Bubbles for Poly-Disperse Flows,” *Chem. Eng. Sci.*, **62**(15), pp. 4146–4157.
- [21] Prasser, H. M., Beyer, M., Carl, H., Gregor, S., Lucas, D., Pietruske, H., Schütz, P., and Weiss, F. P., 2007, “Evolution of the Structure of a Gas-Liquid Two Phase Flow in a Large Vertical Pipe,” *Nucl. Eng. Des.*, **237**, pp. 1848–1861.
- [22] Taitel, Y., Bornea, D., and Dukler, A. E., 1980, “Modelling Flow Pattern Transitions for Steady Upward Gas-Liquid Flow in Vertical Tubes,” *AIChE J.*, **26**(3), pp. 345–354.
- [23] Griffith, P., and Wallis, G. B., 1961, “Two-Phase Slug Flow,” *ASME J. Heat Transfer*, **83**, pp. 307–320.
- [24] Mishima, K., and Ishii, M., 1984, “Two-Fluid Model and Hydrodynamic Constitutive Relations,” *Nucl. Eng. Des.*, **82**(2–3), pp. 107–126.
- [25] Sterlino, V. C., 1965, “Two-Phase Theory and Engineering Decision,” Award Lecture, AIChE Annual Meeting.
- [26] Govier, G. W., and Aziz, K., 1972, *The Flow of Complex Mixtures in Pipes*, Van Nostrand Reinhold, New York, pp. 388–389.
- [27] Gould, T. L., 1974, “Vertical Two-Phase Steam Water Flow in Geothermal Wells,” *J. Pet. Technol.*, **26**, pp. 833–842.
- [28] Oshinowo, T., and Charles, M. E., 1974, “Vertical Two-Phase Flow. Part 1: Flow Pattern Correlations,” *Can. J. Chem. Eng.*, **52**, pp. 25–35.
- [29] Bilicki, Z., and Kestin, J., 1987, “Transition Criteria for Two Phase Flow Patterns in Vertical Upward Flow,” *Int. J. Multiphase Flow*, **13**, pp. 283–294.
- [30] Serizawa, A., and Kataoka, I., 1987, “Phase Distribution in Two-Phase Flow,” Proceedings of ICHMT International Seminar on Transient Two-Phase Flow, Dubrovnik, Yugoslavia, pp. 24–30.
- [31] Lucas, D., Krepper, E., and Prasser, H. M., 2005, “Development of Co-Current Air-Water Flow in a Vertical Pipe,” *Int. J. Multiphase Flow*, **31**, pp. 1304–1328.
- [32] Rao, N. M., 2002, “Investigations on Buoyancy Induced Circulation Loops,” Ph.D. thesis, IIT, Kharagpur, India.
- [33] Serizawa, A., and Kataoka, I., 1988, “Phase Distribution in Two Phase Flow,” *Transient Phenomena in Multiphase Flow*, N. Afgan ed., Hemisphere, Washington, DC, pp. 179–224.
- [34] Hibiki, T., and Ishii, M., 2000, “Two-Group Interfacial Area Transport Equations at Bubbly-to-Slug Flow Transition,” *Nucl. Eng. Des.*, **202**, pp. 39–76.
- [35] Dukler, A. E., and Taitel, Y., 1986, “Flow Pattern Transitions in Gas-Liquid Systems: Measurement and Modeling,” *Multiphase Science and Technology*, Vol. 2, G. F. Hewitt, J. M. Delhay, and N. Zuber, eds., Hemisphere, Washington, DC, pp. 1–94.

Analytical Solution for Newtonian Laminar Flow Through the Concave and Convex Ducts

M. Firouzi

S. H. Hashemabadi

e-mail: hashemabadi@iust.ac.ir

Computational Fluid Dynamics Research Laboratory,
School of Chemical Engineering,
Iran University of Science and Technology,
Narmak, Tehran 16846, Iran

In this paper, the motion equation for steady state, laminar, fully developed flow of Newtonian fluid through the concave and convex ducts has been solved both numerically and analytically. These cross sections can be formed due to the sedimentation of heavy components such as sand, wax, debris, and corrosion products in pipe flows. The influence of duct cross section on dimensionless velocity profile, dimensionless pressure drop, and friction factor has been reported. Finally based on the analytical solutions three new correlations have been proposed for the product of Reynolds number and Fanning friction factor ($C_f Re$) for these geometries. [DOI: 10.1115/1.3184026]

Keywords: analytical, numerical, Newtonian, concave, convex, noncircular passage, Fanning friction factor, sedimentation

1 Introduction

A range of noncircular duct configurations is employed for internal flow and heat transfer applications in chemical, petroleum, pharmaceutical, food, and plastics industries. It is of great practical interest to be able to predict the pressure drop and heat transfer characteristics of fluid flows in different duct geometries. One of the applications of fluid flow in irregular ducts is in the piping systems that encountered with sedimentation, and most fluid flows in environmental and industrial applications are directly influenced by sediment. Sediment transport is important to river, shoreline, and harbor projects in piping systems. It can cause to form geometric domains that are far from ideal in shape. It is not difficult to imagine subsea pipelines blocked by accumulated wax or by hydrate plugs, bundled pipes with debris settlement, or heavily clogged cross sections with grease or hard water scaling (Fig. 1) [1]. Few exact solutions are available only for simple fluid models and circular pipe cross sections. Many attempts were made in modeling Newtonian and non-Newtonian fluids in various noncircular cross sectional ducts, which most of them are numerical or experimental. Several investigations have been reported for flow characteristics in trapezoidal cross section [2–4], in rectangular cross section [5–7], non-Newtonian fluid flow through triangular channels [8,9], friction factor, pressure drop, and Nusselt number of Newtonian fluid flowing in ducts of arbitrary cross sections [10], and an approximate solution for determining the pressure drop in microchannels of arbitrary cross section [11].

Here we focused on analytical solution for laminar fully developed Newtonian fluid flow through a family of noncircular passage with concave and convex cross sections, which is selected

for the solid buildup boundary family of curves, since some of solids such as wax surfaces are expected to be more curved than flat and this buildup increases with time.

2 Mathematical Modeling

2.1 Analytical Solution

2.1.1 Velocity Profile. Figure 2(a) shows cross section of three different noncircular horizontal ducts. The appropriate coordinate system for solving the flow problem in this case is the well-known bipolar coordinate system. Coordinate φ represents the view angle of the two poles from an arbitrary point in the flow domain, and coordinate ξ relates to the ratio of the radius vectors r_1 and r_2 , $\xi = \ln(r_1/r_2)$, where r_1 and r_2 , as illustrated in Fig. 2(b), are distances of arbitrary point to two poles. The transformation functions for Cartesian and bipolar coordinates are [12] as follows:

$$x = \frac{R \sin \varphi_1 \sinh \xi}{\cosh \xi - \cos \varphi}, \quad y = \frac{R \sin \varphi_1 \sin \xi}{\cosh \xi - \cos \varphi}$$

For steady state, laminar, and fully developed Newtonian fluid flow, while all body forces are negligible the motion equation can be simplified as follows [13]:

$$\left[\frac{\cosh \xi - \cos \varphi}{\sin \varphi_1} \right]^2 \left(\frac{\partial^2 v^*}{\partial \varphi^2} + \frac{\partial^2 v^*}{\partial \xi^2} \right) = -4 \quad (1)$$

where the velocity has been nondimensionalized by the maximum velocity of Newtonian fluid flow through the pipe ($v_{\max} = (R^2/4\mu)(dp/dz)$). No-slip condition on boundaries can be defined as follows:

$$v^*|_{\varphi_1} = v^*|_{\varphi_2} = v^*|_{\xi=\pm\infty} = 0 \quad (2)$$

where φ_2 is the bottom wall angle (Fig. 2(a)). Equation (1) is nonhomogeneous, so the general solution of dimensionless velocity profile v^* is composed of particular solution v^{*p} and the homogeneous solution v^{*h} :

$$v^* = v^{*h} + v^{*p} \quad (3)$$

The velocity profile of Newtonian fluid through the circular pipe is used as a particular solution. Therefore the particular solution v^{*p} in the bipolar coordinate is [15]

$$v^{*p} = \frac{2 \sin(\varphi - \varphi_1) \sin(\varphi_1)}{(\cosh \xi - \cos \varphi)} \quad (4)$$

By substituting the particular solution into Eq. (1), the following homogeneous equation can be obtained:

$$\frac{\partial^2 v^{*h}}{\partial \varphi^2} + \frac{\partial^2 v^{*h}}{\partial \xi^2} = 0 \quad (5)$$

And for boundary conditions, we have

$$v^{*h}|_{\varphi=\varphi_1} = 0 \quad (6)$$

$$v^{*h}|_{\xi=\pm\infty} = 0 \quad (7)$$

$$v^{*h}|_{\varphi=\varphi_2} + \frac{2 \sin(\varphi_2 - \varphi_1) \sin(\varphi_1)}{(\cosh \xi - \cos \varphi_2)} = 0 \quad (8)$$

The homogeneous solution v^h can be obtained by using Fourier integral method [14]:

$$v^{*h} = \int_0^\infty \phi(\omega) \sinh[\omega(\varphi - \varphi_1)] \cos(\omega\xi) d\omega \quad (9)$$

Obviously this solution satisfies Eqs. (5) and (6). Equation (7) is an underlying requirement for the legitimate use of Fourier integral in obtaining the solution. By substituting Eq. (9) into Eq. (8) we have

Contributed by the Fluids Engineering Division of ASME for publication in the JOURNAL OF FLUIDS ENGINEERING. Manuscript received May 20, 2008; final manuscript received June 21, 2009; published online August 14, 2009. Assoc. Editor: Ye Zhou.

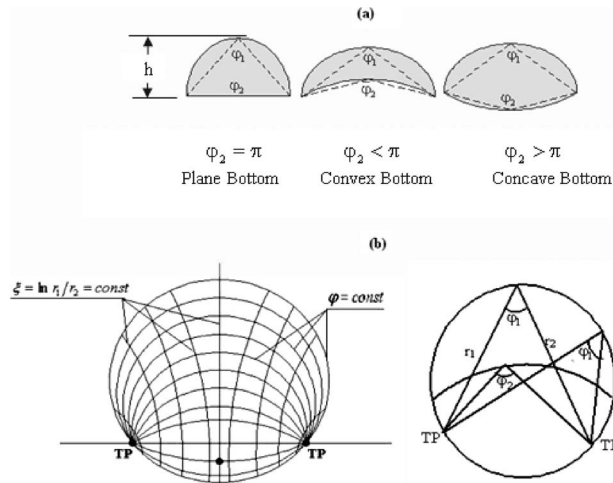


Fig. 1 Schematic descriptions of (a) flow passage cross section and (b) bipolar coordinate

$$\int_0^{\infty} \phi^*(\omega) \sinh[\omega(\varphi_2 - \varphi_1)] \cos(\omega\xi) d\omega + \frac{2 \sin(\varphi_2 - \varphi_1) \sin(\varphi_1)}{(\cosh \xi - \cos \varphi_2)} = 0 \quad (10)$$

This can be simplified to

$$\int_0^{\infty} \tilde{\phi}(\omega) \cos(\omega\xi) d\omega = 1 \quad (11)$$

where

$$\tilde{\phi}(\omega) = \frac{\phi(\omega)^* \sinh[\omega(\varphi_2 - \varphi_1)]}{K^*}, \quad K^* = -\frac{2 \sin(\varphi_2 - \varphi_1) \sin(\varphi_1)}{(\cosh \xi - \cos \varphi_2)} \quad (12)$$

To calculate the spectral function $\tilde{\phi}(\omega)$ for curved bottom ($\varphi_2 \neq \pi$), the following definite integral is used [12]:

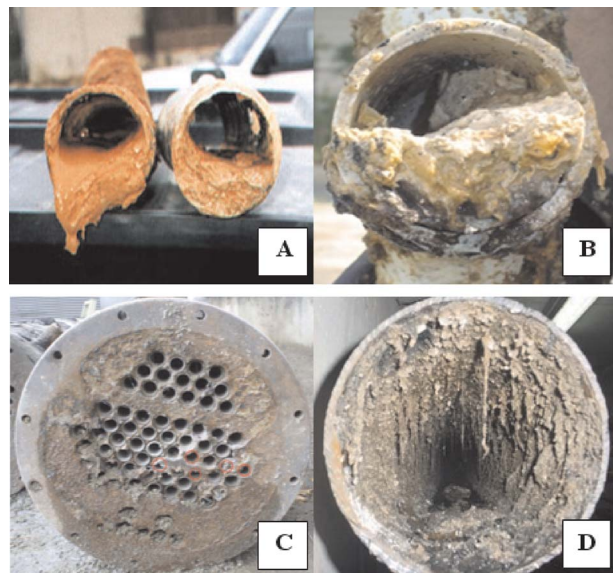


Fig. 2 Some examples of the clogged pipe: (a) mud sediment in pipes, (b) clogged pipe with grease, (c) fouling in heat exchangers, and (d) deposit of the sludge pipe [2]

$$\int_0^{\infty} \frac{-2 \sinh[(\varphi - \pi)\omega] (\cosh \xi - \cos \varphi)}{\sin \varphi \sinh(\omega\pi)} \cos(\omega\xi) d\omega = 1 \quad (13)$$

which for the special case of flat bottom ($\varphi_2 = \pi$):

$$\int_0^{\infty} \frac{2\omega (\cosh \xi - \cos \varphi)}{\sinh(\pi\omega)} \cos(\omega\xi) d\omega = 1 \quad (14)$$

While the bottom is convex or concave ($\varphi_2 \neq \pi$), by comparing Eq. (11) with Eqs. (13) and (14), the nondimensionalized spectral function can be derived as follows:

$$\phi^*(\omega) = -\frac{2K^* \sinh[\omega(\varphi_2 - \pi)] (\cosh \xi - \cos \varphi_2)}{\sin \varphi_2 \sinh(\pi\omega) \sinh[\omega(\varphi_2 - \varphi_1)]} \quad (15)$$

and for plane bottom ($\varphi_2 = \pi$),

$$\phi^*(\omega) = \frac{2K^* \omega (1 + \cosh \xi)}{\sinh(\pi\omega) \sinh[\omega(\pi - \varphi_1)]} \quad (16)$$

Finally the dimensionless velocity distribution can be obtained:

$$v^*(\xi, \varphi) = \int_0^{\infty} \phi^*(\omega) \sinh[\omega(\varphi - \varphi_1)] \cos(\omega\xi) d\omega + 2 \sin(\varphi_1) \frac{\sin(\varphi - \varphi_1)}{(\cosh \xi - \cos \varphi)} \quad (17)$$

2.1.2 Pressure Drop. The corresponding flow rates of fluid can be obtained by integrating the velocity over the flow area; to calculate the pressure drop, the flow rate is assumed to be equal to the flow rate of Newtonian flow in the circular cross section duct:

$$Q = \int_{-\infty}^{\infty} \int_{\varphi_1}^{\varphi_2} v(\xi, \varphi) \left(\frac{R \sin \varphi_1}{\cosh \xi - \cos \varphi} \right)^2 d\varphi d\xi = \frac{R^4 \sin^2 \varphi_1}{4\mu} \frac{dp}{dz} F(\varphi_1, \varphi_2) \quad (18)$$

where

$$F(\varphi_1, \varphi_2) = \int_{-\infty}^{+\infty} \int_{\varphi_1}^{\varphi_2} \frac{v^*(\xi, \varphi)}{(\cosh \xi - \cos \varphi)^2} d\varphi d\xi \quad (19)$$

The flow pressure drop through the noncircular ducts can be calculated from Eq. (18):

$$\frac{dp}{dz} = \frac{4\mu Q}{R^4 \sin^2 \varphi_1} F(\varphi_1, \varphi_2) \quad (20)$$

The pressure gradient, Eq. (20), can be nondimensionalized with Hagen–Poiseuille relationship for the pressure drop of Newtonian fluid flow through the pipes:

$$\frac{dp^*}{dz} = \frac{\left(\frac{dp}{dz} \right)}{\left(\frac{dp}{dz} \right)_{\text{pipe}}} = \frac{\pi}{2 \sin^2(\varphi_1) F(\varphi_1, \varphi_2)} \quad (21)$$

2.1.3 Friction Factor Calculation. Once the problem is solved for the velocity profile, the local shear stress can be derived, the pipe walls are described by surfaces where $\varphi = \text{const}$, or in other words in the bipolar coordinate system, this boundary is isolines of coordinate φ [14,15], hence the shear stress can be calculated as

$$\tau_{\varphi z}^* = \frac{1}{2} \left(\frac{\cosh \xi - \cos \varphi}{\sin \varphi_1} \right) \frac{\partial v^*(\xi, \varphi)}{\partial \varphi} \quad (22)$$

where the shear stress is nondimensionalized by $(R/2)(dp/dz)$. By substituting the dimensionless velocity derivative, the following can be obtained:

$$\begin{aligned} \tau_{\varphi z}^* = & \cos(\varphi - \varphi_1) - \frac{\sin \varphi \sin(\varphi - \varphi_1)}{\cosh \xi - \cos \varphi} \\ & + \frac{\cosh \xi - \cos \varphi}{2 \sin \varphi_1} \int_0^\infty \varphi(\omega) \omega \cosh[\omega(\varphi - \varphi_1)] d\omega \quad (23) \end{aligned}$$

Then the friction factor, which is one of the most important characteristics in fluid flows, can be calculated. The definition of Fanning friction factor is [13] as follows:

$$C_f \text{ Re} = \left(\frac{D_h^2}{R} \right) \left(\frac{\int_{-\infty}^{+\infty} \tau_{\varphi z}^*(\xi, \varphi_1) \left(\frac{R \sin \varphi_1}{\cosh \xi - \cos \varphi} \right) d\xi + \int_{-\infty}^{+\infty} \tau_{\varphi z}^*(\xi, \varphi_2) \left(\frac{R \sin \varphi_1}{\cosh \xi - \cos \varphi} \right) d\xi}{\int_{-\infty}^{+\infty} \int_{\varphi_1}^{\varphi_2} v^*(\xi, \varphi) \left(\frac{R \sin \varphi_1}{\cosh \xi - \cos \varphi} \right)^2 d\varphi d\xi} \right) \quad (27)$$

For flat bottom ($\varphi_2 = \pi$), the hydraulic diameter can be calculated as follows:

$$D_h = \frac{2R[\pi - \varphi_1 + 1/2 \sin(2\varphi_1)]}{\pi - \varphi_1 + \sin(\varphi_1)} \quad (28)$$

and for curved bottom ($\varphi_2 \neq \pi$),

$$D_h = \frac{2R \left(\pi - \varphi_1 + \frac{1}{2} \sin(2\varphi_1) - \left(\frac{\sin \varphi_1}{\sin \varphi_2} \right)^2 \left(\pi - \varphi_2 + \frac{1}{2} \sin(2\varphi_2) \right) \right)}{\pi - \varphi_1 + (\pi - \varphi_2) \frac{\sin \varphi_1}{\sin \varphi_2}} \quad (29)$$

2.2 Numerical Solution. In this section, to recheck the results of the analytical solution because of insufficiency of related established results for more validation of obtained analytical results, the momentum equation is solved numerically with finite element method (FEM). The momentum equation is preferred to be solved in the Cartesian coordinate system, which, by considering the mentioned assumptions in analytical solution, can be simplified as follows:

$$\frac{\partial \tau_{zx}}{\partial x} + \frac{\partial \tau_{zy}}{\partial y} + \frac{dp}{dz} = 0 \quad (30)$$

The nondimensional form of the motion equation (Eq. (30)) for Newtonian fluid is as follows:

$$\frac{\partial}{\partial x^*} \left(\frac{\partial v^*}{\partial x^*} \right) + \frac{\partial}{\partial y^*} \left(\frac{\partial v^*}{\partial x^*} \right) = -16 \quad (31)$$

where

$$C_f \text{ Re} = 4 \left(\frac{\bar{\tau}_w^*}{\bar{v}^*} \right) \left(\frac{D_h}{R} \right) \quad (24)$$

Here $\bar{\tau}_w^*$ and \bar{v}^* are the average dimensionless wall shear stress and average dimensionless velocity, respectively, and can be obtained as follows:

$$\begin{aligned} \bar{\tau}_w^* = & \frac{1}{P} \left[\int_{-\infty}^{+\infty} \tau_{\varphi z}^*(\xi, \varphi_1) \left(\frac{R \sin \varphi_1}{\cosh \xi - \cos \varphi_1} \right) d\xi \right. \\ & \left. + \int_{-\infty}^{+\infty} \tau_{\varphi z}^*(\xi, \varphi_2) \left(\frac{R \sin \varphi_1}{\cosh \xi - \cos \varphi_2} \right) d\xi \right] \quad (25) \end{aligned}$$

$$\bar{v}^* = \frac{1}{A} \int_{-\infty}^{+\infty} \int_{\varphi_1}^{\varphi_2} v^*(\xi, \varphi) \left(\frac{R \sin \varphi_1}{\cosh \xi - \cos \varphi} \right)^2 d\varphi d\xi \quad (26)$$

where A and P are the area and the perimeter of the duct cross section, respectively. By substituting Eqs. (25) and (26) into Eq. (24), it yields the following:

$$v^* = \frac{v}{R^2 \frac{dp}{dz}}, \quad x^* = \frac{x}{D}, \quad y^* = \frac{y}{D} \quad (32)$$

The top and bottom walls are subjected to no-slip condition.

3 Results and Discussion

Figures 3 and 4 show the comparison of dimensionless velocity profile that is obtained from numerical and analytical solutions for two different cross sections ($\varphi_1 = \pi/3$ and $\varphi_2 = \pi$ and semicircular cross section duct $\varphi_1 = \pi/2$ and $\varphi_2 = \pi$) as expected by increasing ξ (Fig. 4); the velocity approaches zero in the vicinity of the wall.

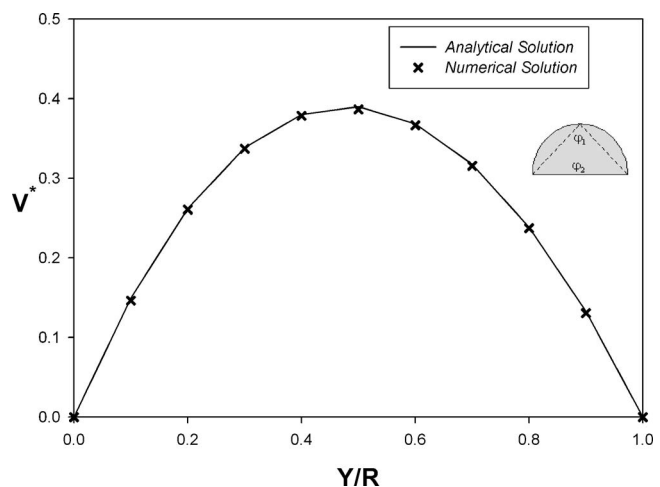


Fig. 3 Comparison of numerical and analytical dimensionless velocity profiles for the case of the semicircle cross section ($\varphi_1 = \pi/2$ and $\varphi_2 = \pi$) at $\xi = 0$ (along the meridian)

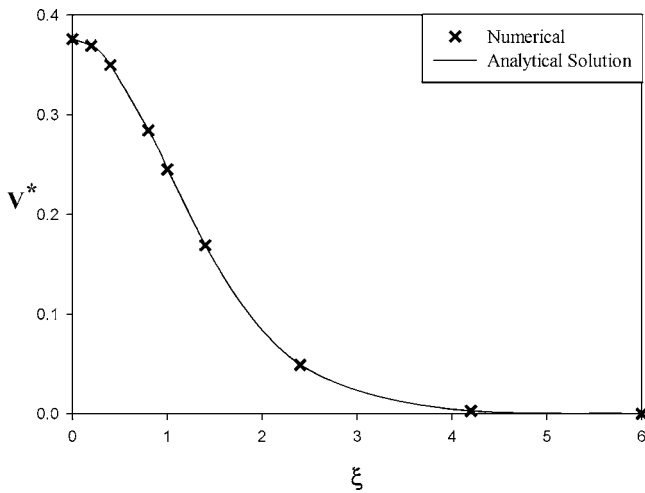


Fig. 4 Comparison of numerical and analytical solutions for the dimensionless velocity profile at $\varphi=2\pi/3$ with cross section specification: $\varphi_1=\pi/3$ and $\varphi_2=\pi$

The analytical and numerical results illustrate a good agreement. Figure 5 shows the comparison of numerical and analytical solutions for dimensionless axial velocity profile in different cross section ducts (concave, plane, and convex); as is distinct they are also in good agreement with the analytical solution (less than 0.8% of error on the average). As well, the results show that by increasing the concavity the velocity promotes and it decreases by changing the lower wall shape to convexity. Figure 6 depicts the axial nondimensional velocity profile variation with ξ ; as expected the maximum dimensionless velocity occurs at $\xi=0$ and the velocity decreases by increasing ξ and finally it approaches zero and indeed it validates the no-slip boundary condition at poles.

Figure 7 illustrates the dimensionless pressure drop versus duct aspect ratio (h/D) in different cross section shapes. The duct aspect ratio (h/D) can be related to φ_1 and φ_2 as follows:

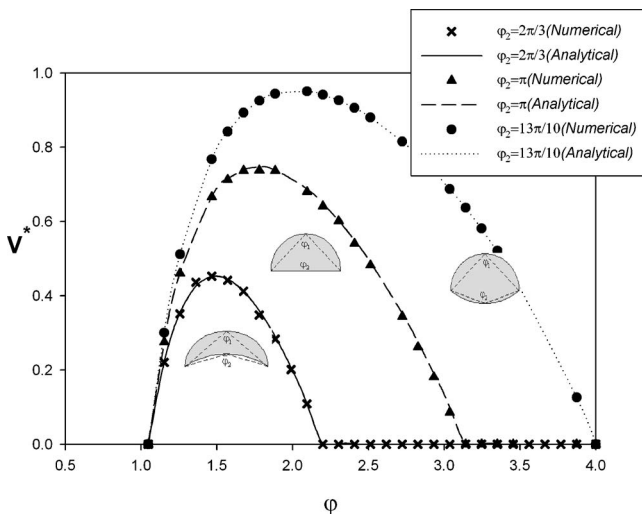


Fig. 5 Comparison of numerical and analytical solutions for various duct cross sections due to different bottom wall shapes: $\varphi_1=\pi/3$ and $\xi=0$

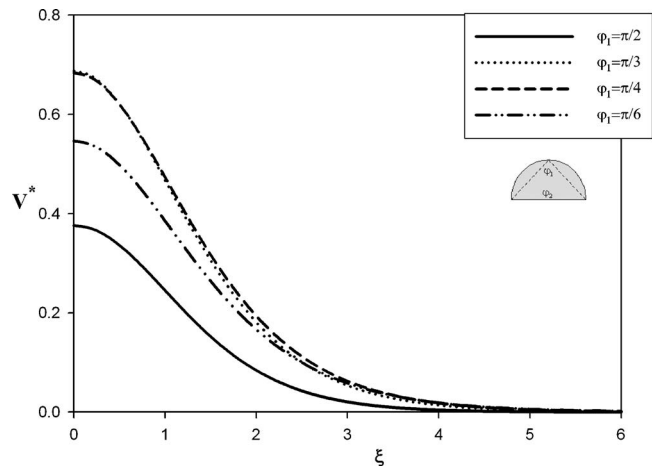


Fig. 6 Velocity variation with ξ for different upper wall shapes, $\varphi_2=2\pi/3$

$$\frac{h}{D} = -0.5 \left(\frac{\sin \varphi_1 \sin \varphi_2}{1 - \cos \varphi_2} - \frac{\sin \varphi_1}{\tan \frac{\varphi_1}{2}} \right) \quad (33)$$

Obviously while the duct aspect ratio is equal to 1 (circular cross section) the dimensionless pressure drop approaches 1, and the reduction in aspect ratio (decreasing flow area) for a given flow rate affects an increase in the pressure drop and this promotion is more noticeable for the concave lower wall. 20% irregularity in the cross section ($h/D=0.8$) for the case of $\varphi_2=2\pi/3$ compared to a circular cross section causes an approximately 30% increase in pressure drop, which is important in analyzing the pressure drop of the flow through the clogged pipe.

The product of Reynolds number and Fanning friction factor ($C_f Re$) can be obtained for different cross sections by using Eq. (27). For the special case of a circular cross section ($\varphi_1=0$) $C_f Re$ equals to 16 and for the case of semicircle ducts ($\varphi_1=\pi/2$ and $\varphi_2=\pi$) the product of Reynolds number and Fanning friction factor ($C_f Re$) is calculated to be 15.768891, which matches well with the reported numerical solution ($C_f Re=15.768832$) [16]. Tables 1 and 2 illustrate the product of Reynolds number and Fanning friction factor ($C_f Re$) for some of these cross sections. While the upper wall view angle (φ_1) of flat bottom ducts (φ_2

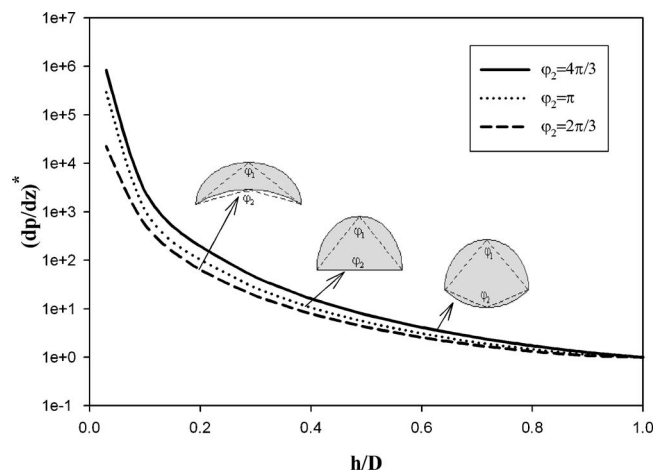
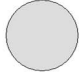
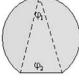
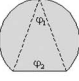
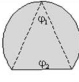
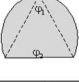
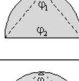

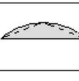


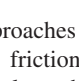


Fig. 7 Variation in the dimensionless pressure drop with aspect ratio (h/D) for various duct cross sections (different φ_1 and φ_2)

Table 1 C_f Re for some of duct cross section with plane bottom ($\varphi_2 = \pi$)

Cross Section Shape	φ_1	C_f Re
	0	16.0000
	$\frac{\pi}{10}$	15.9723
	$\frac{\pi}{6}$	15.9242
	$\frac{\pi}{4}$	15.8634
	$\frac{\pi}{3}$	15.8219
	$\frac{\pi}{2}$	15.7689
	$\frac{3\pi}{4}$	15.6575
	$\frac{4\pi}{5}$	15.6625
	$\frac{14\pi}{15}$	17.0044
	$\frac{15\pi}{16}$	19.7386
	$\frac{16\pi}{17}$	21.0787

$= \pi$) approaches π (Table 1), the product of Reynolds number and Fanning friction factor (C_f Re) tends to the value for the two parallel plates that equals to 24.

Due to the complexity of analytically solving the integrals into Eq. (27), two simple correlations for calculating the Fanning friction factor for the Newtonian fluid flow through the ducts with an irregular cross section are proposed, which is applied by process designers and analyzers. For the case of the lower plane wall ($\varphi_2 = \pi$),

$$C_f \text{ Re} = 16 \left(1 + \sum_{n=1}^8 a_n \varphi_1^n \right) \quad (34)$$

and for the curved bottom wall ($\varphi_2 \neq \pi$),












$$C_f \text{ Re} = 16 \left(1 + \sum_{n=1}^3 a_n \varphi_1^n + \varphi_1 \varphi_2 (a_4 + a_5 \varphi_2 + a_6 \varphi_1) \right) \quad (35)$$

Table 3 shows all coefficients of Eqs. (34) and (35). In other words, we have proposed two geometry correction factors that can convert the product of Reynolds number and Fanning friction factor (C_f Re) for the laminar flow through the pipes to the laminar flow through the concave and convex ducts. Figure 8 depicts the correlation (Eqs. (34) and (35)) accuracy with respect to analytical solution results; as seen, they are in very good agreement.

4 Conclusion

An analytical study was carried out to calculate the velocity profile, pressure drop, and friction factor of steady state, laminar,

Table 2 C_f Re for some of duct cross section with concave ($\varphi_2 > \pi$) and convex ($\varphi_2 < \pi$) bottoms

Cross Section Shape	φ_1	φ_2	C_f Re
	$\frac{3\pi}{4}$	$\frac{7\pi}{6}$	11.9343
	$\frac{\pi}{2}$	$\frac{7\pi}{6}$	15.0948
	$\frac{\pi}{2}$	$\frac{4\pi}{3}$	14.3730
	$\frac{\pi}{3}$	$\frac{7\pi}{6}$	15.7672
	$\frac{\pi}{6}$	$\frac{11\pi}{10}$	15.9802
	$\frac{3\pi}{4}$	$\frac{5\pi}{6}$	5.4775
	$\frac{\pi}{2}$	$\frac{5\pi}{6}$	13.3243
	$\frac{\pi}{2}$	$\frac{2\pi}{3}$	6.4044
	$\frac{\pi}{3}$	$\frac{2\pi}{3}$	11.4158
	$\frac{\pi}{6}$	$\frac{4\pi}{5}$	15.4084
	$\frac{\pi}{6}$	$\frac{\pi}{5}$	5.4581

and fully developed flow of Newtonian fluid through the concave and convex ducts. The analytical solution has been validated by the numerical solution of the simplified motion equation with above mentioned assumptions. The results show that the dimensionless velocity profiles are in good agreement with the analytical solution. As a result, by increasing the concavity of the lower wall for a given upper wall angle, the velocity profile increases and by increasing the lower wall convexity the velocity decreases. The product of Reynolds number and Fanning friction factor (C_f Re) has been calculated for the different duct geometries, which for the special case of a circular cross section ($\varphi_1 = 0$) C_f Re equals to 16 and by increasing the upper wall view angle ($\varphi_1 \rightarrow \pi$) for flat bottom ducts, the results show that C_f Re approaches 24, which is the C_f Re value for the two parallel plates. For simple application of this work, three analytical based correlations have been proposed for three different cross sections (flat, concave, and convex bottom). The prediction of correlations has good accuracy with respect to analytical solution results.

Nomenclature

- A = flow area
- C_f = Fanning friction factor
- D = pipe diameter
- D_h = hydraulic diameter
- F = defined by Eq. (19)
- h = duct height
- L = pipe length
- p = pressure
- P = perimeter of the duct
- Q = flow rate

Table 3 Coefficients of Eqs. (34) and (35)

Bottom angle	<i>a</i>							
	1	2	3	4	5	6	7	8
$\varphi_2 = \pi$	-0.180	1.576	-4.970	7.467	-6.021	2.673	-0.616	0.057
$\varphi_2 < \pi$	-2.170	-0.216	-0.096	1.449	-0.252	0.136	-	-
$\varphi_2 > \pi$	0.191	0.356	0.003	-0.200	0.043	-0.112	-	-

R = pipe radius
Re = Reynolds number
v = velocity
x = related to the Cartesian coordinate
y = related to the Cartesian coordinate
Y = distance from the bottom wall
z = axial direction

- = average value
h = homogeneous
p = particular

Greek Symbols

μ = dynamic viscosity
 ξ = ratio of the radius vectors in the bipolar coordinate
 ρ = density
 τ = stress
 φ = view angle of the interface in the bipolar coordinate

Subscripts

1 = upper wall
 2 = bottom wall
 max = maximum

Superscripts

* = dimensionless property

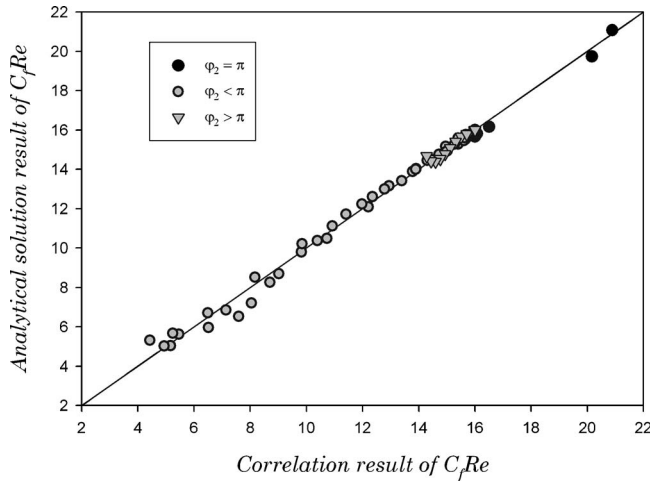


Fig. 8 Comparison of analytical solution and correlation results for $C_f Re$

References

[1] Barat, R., Bouzas, A., Marti, N., Ferrer, J., and Seco, A., 2009, "Precipitation Assessment in Wastewater Treatment Plants Operated for Biological Nutrient Removal: A Case Study in Murcia, Spain," *J. Environ. Manage.*, **90**, pp. 850–857.
 [2] Wu, P. Y., and Little, W. A., 1983, "Measurement of Friction Factor of the Flow of Gases in Very Fine Channels Used for Microminiaturize Joule-Thomson Refrigerators," *Cryogenics*, **24**(8), pp. 273–277.
 [3] Wu, H. Y., and Cheng, P., 2003, "Friction Factors in Smooth Trapezoidal Silicon Microchannels With Different Aspect Ratios," *Int. J. Heat Mass Transfer*, **46**, pp. 2519–2525.
 [4] Weilin, Q., Mala, G. M., and Dongqing, L., 2000, "Pressure-Driven Water Flows in Trapezoidal Silicon Microchannels," *Int. J. Heat Mass Transfer*, **43**(3), pp. 353–364.
 [5] Peng, X. F., Peterson, G. P., and Wang, B. X., 1994, "Frictional Flow Characteristics of Water Flowing Through Microchannels," *Exp. Heat Transfer*, **7**(4), pp. 249–264.
 [6] Pfund, D., Rector, D., Shekarriz, A., Popescu, A., and Welty, J., 2000, "Pressure Drop Measurements in a Micro Channel," *AIChE J.*, **46**(8), pp. 1496–1507.
 [7] Hrnjak, P., and Tu, X., 2007, "Single Phase Pressure Drop in Microchannels," *Int. J. Heat Fluid Flow*, **28**(1), pp. 2–14.
 [8] Etemad, S. Gh., Mujumdar, A. S., and Nassef, R., 1996, "Simultaneously Developing Flow and Heat Transfer of Non-Newtonian Fluids in Equilateral Triangular Duct," *Appl. Math. Model.*, **20**(12), pp. 898–908.
 [9] Hashemabadi, S. H., Etemad, S. Gh., Golkar Naranji, M. R., and Thibault, J., 2003, "Laminar Flow of Non-Newtonian in Right Triangular Ducts," *Int. Commun. Heat Mass Transfer*, **30**(1), pp. 53–60.
 [10] Etemad, S. Gh., and Bakhtiari, F., 1999, "General Equations for Fully Developed Fluid Flow and Heat Transfer Characteristics in Complex Geometries," *Int. Commun. Heat Mass Transfer*, **26**(2), pp. 229–238.
 [11] Bahrami, M., Yovanovich, M., and Richard Culham, J., 2007, "A Novel Solution for Pressure Drop in Singly Connected Microchannels of Arbitrary Cross-Section," *Int. J. Heat Mass Transfer*, **50**(13–14), pp. 2492–2502.
 [12] Firouzi, M., and Hashemabadi, S. H., 2008, "Analytical Solution for Newtonian-Bingham Plastic Two-Phase Pressure Driven Stratified Flow Through the Circular Ducts," *Int. Commun. Heat Mass Transfer*, **35**, pp. 666–673.
 [13] Bird, R. B., Armstrong, R. C., and Hassager, O., 1978, *Dynamics of Polymeric Liquids*, Vol. 1, Wiley, New York, pp. 592–595.
 [14] Brauner, N., Rovinsky, J., and Maron, D. M., 1996, "Analytical Solution for Laminar-Laminar Two Phase Stratified Flow in Circular Conduit," *Chem. Eng. Sci.*, **141**, pp. 103–143.
 [15] Biberg, D., and Halvorsen, G., 2000, "Wall and Interfacial Shear Stress in Pressure Driven Two-Phase Laminar Stratified Pipe Flow," *Int. J. Multiphase Flow*, **26**(10), pp. 1645–1673.
 [16] Syrjälä, S., 2002, "Accurate Prediction of Friction Factor and Nusselt Number for Some Duct Flows of Power-Law Non-Newtonian Fluid," *Numer. Heat Transfer, Part A*, **41**(1), pp. 89–100.